Roya Dehghan-Niri

Advanced Transmission Electron Microscopy Studies of Cobalt Fischer-Tropsch Catalysts

Thesis for the degree of Philosophiae Doctor

Trondheim, August 2012

Norwegian University of Science and Technology
Faculty of Natural Sciences and Technology
Department of Physics

NTNU – Trondheim
Norwegian University of
Science and Technology

NTNU
Norwegian University of Science and Technology

Thesis for the degree of Philosophiae Doctor

Faculty of Natural Sciences and Technology
Department of Physics

ISBN 978-82-471-3731-4 (printed ver.)
ISBN 978-82-471-3732-1 (electronic ver.)
ISSN 1503-8181

Doctoral theses at NTNU, 2012:216

Printed by NTNU-trykk

I dedicate my dissertation work to my family. A special feeling of gratitude to my loving parents, Zahra and Mohammad whose words of encouragement and push for tenacity ring is in my ears.

I dedicate this work and give special thanks to my husband, Jafar, and my wonderful daughter, Armita, for being there for me throughout the entire doctorate program. Both of you have been my best cheer leaders.

I dedicate this work to my sister Mahboobeh and my brothers, Hossein and Mohsen who have never left my side and are very special.

Preface

This thesis is submitted in partial fulfilment of the requirements for the PhD degree at the Norwegian University of Science and Technology (NTNU) in Trondheim, Norway. The work presented in this thesis has been carried out at the Department of Physics, Faculty of natural science and Technology, in the period of May 2006 to August 2012 which included one year of teaching duties as a part of my PhD studies and about one year maternity leave within 2007-2008.

The work is a part of the KMB project "Advanced TEM in Catalysis" financed by the Research Council of Norway (NFR Project No. 169673/S10) and Statoil. This work has been done through the co-operation between the Physics and Chemical Engineering departments at NTNU, the Foundation of Scientific and Industrial Research (SINTEF) and Statoil.

The main objective in this project has been to obtain a detailed understanding of Fischer-Tropsch catalysts nanostructures by using advanced electron microscopy techniques. The Fischer-Tropsch process is the main part of the Gas to Liquid (GTL) Technology in which natural gas is converted into synthetic fuels. Supported cobalt materials are the main catalysts for this process and the work presented in this thesis focuses on the characterization of cobalt supported on α-Al_2O_3 and γ-Al_2O_3 substrates.

The main part of this thesis has been performed at NTNU at the Department of Physics through the application of several Transmission Electron Microscopy (TEM) techniques such as Scanning Transmission Electron Microscopy (STEM), Electron Tomography, Electron Energy Loss Spectroscopy (EELS) as well as conventional bright field and dark field imaging. For the cobalt catalysts, ex-situ TEM studies performed at NTNU using both a dedicated ex-situ reaction set-up and glove box to transfer the reduced material to the TEM. Some of the TEM studies were carried out through several visits to the Center for Electron Nanoscopy (CEN) at the Technical University of Denmark (DTU) using their Environmental TEM (ETEM) which has an image Cs corrector and Analytical TEM (ATEM) with probe C_S corrector. The development of electron tomography at NTNU was initiated through visiting the materials science group at Cambridge University and significant work was then done to establish the technique at NTNU. In cooperation with Chemical Engineering Department at NTNU, X-ray Diffraction (XRD) analysis, both with a home source and with a synchrotron source (Swiss-Norwegian beam line) were performed to characterize the catalysis materials. The catalysts materials for this project were provided by Statoil R&D centre in Trondheim.

Reduction of the catalysts materials was carried out at the Department of Chemical Engineering at NTNU. All of the TEM sample preparations and handling were carried out in the TEM Gemini centre.

Part of the PhD study was on the Ni catalyst for steam methane reforming. These catalysts materials provided by the Chemical Engineering department at NTNU and TEM studies performed at NTNU.

This thesis consists of two parts. The first part contains eight chapters. The theoretical introduction and literature review about the Fischer-Tropsch process and electron microscopy techniques are presented in chapters 1 to 3. Chapter 4 includes both the theoretical basics of the electron tomography technique and the results from the experimental work that has been done during this project. Chapter 5 is about the in-situ studies carried out at DTU and includes the details of Environmental TEM and part of the challenges encountered during these experiments. Chapter 6 describes the experimental procedure and typical results from the ex-situ experiments using an environmental reaction cell holder carried out at NTNU. Chapter 7 contains a list of conclusions in this work and Chapter 8 contains list of suggestions for further work.

The second part of the thesis includes a collection of the published and unpublished journal papers that have been obtained from the research listed below:

Paper I: "*In-situ reduction of promoted cobalt oxide supported on alumina by environmental transmission electron microscopy*"

R. Dehghan-Niri, T. W. Hansen, J. B. Wagner, A. Holmen, E. Rytter, Ø. Borg, J. C. Walmsley; Catalysis Letters, 141 (2011) 754-761.

Paper II: *"Electron microscopy study of γ-Al_2O_3 supported cobalt Fischer-Tropsch catalysts"*

Ø. Borg, J. C. Walmsley, **R. Dehghan**, B. S. Tanem, E. A. Blekkan, S. Eri, E. Rytter, A. Holmen; Catalysis Letters 126, 3-4 (2008) 224-230.

Paper III: "*Nano structural analysis of promoted cobalt phase supported on γ-Al_2O_3 by TEM and XRD"*

R. Dehghan-Niri, A. S. Voronov, N. Tsakoumis, A. Holmen, R. Holmestad, P. E. Vullum, Ø. Borg, E. Rytter, J. C. Walmsley;
(To be submitted)

Paper IV: "*TEM Study of spent supported cobalt catalysts used in Fischer-Tropsch process*"
R. Dehghan-Niri, N. Tsakoumis, M. Rønning, A. Holmen, E. Rytter, R. Holmestad, Ø. Borg, J. C. Walmsley;
(In preparation)

Paper V: "*Nanoconfinment of Ni clusters towards a high sintering resistance of steam methane reforming catalysts*"
R. Dehghan-Niri, J. C. Walmsley, A. Holmen, R. Holmestad, E. Rytter, P. Midgley, A. Hoang Dam, A. Hungria, J. C. Hernandez-Garrido, D. Chen;
(Accepted for publication in Catalysis Science and Technology)

Furthermore, I have also contributed to the following publications, which are not included in my thesis:

"Fischer-Tropsch Synthesis: Comparative study on alumina and carbon nanofiber supported cobalt catalysts"
Shreyas Rane, **Roya Dehghan-Niri,** John Walmsley, Øyvind Borg, Erling Rytter, Anders Holmen.
(To be submitted)

"A combined in-situ XAS-XRD-Raman study of Fischer-Tropsch synthesis over a carbon supported Co catalyst"
Nikolas E. Tsakoumis, **Roya Dehghan-Niri,** Rune Johnsen, Alexey Voronov, Wouter van Beek, John C. Walmsley, Øyvind Borg, Erling rytter, De Chen, Magnus Rønning, Anders Holmen.
Submitted to Catalysis Today

In addition to the journal papers, I have presented posters and oral presentations at several conferences.

1. *"Advanced TEM study of catalysts particles (ex-situ studies)"*
   R. Dehghan-Niri, J. C. Walmsley, A. Holmen, E. Rytter, Ø. Borg, R. Holmestad; Scandem Conference, 18-20 Jun 2007, Helsinki, Finland. [Poster]

2. *"TEM study of hydrotalcite derived Ni catalysts"*

   R. Dehghan-Niri, J. C. Walmsley, A. Holmen, P. A. Midgley, A. B. Hungria, J. C. Hernandez-Garrido, D. Chen; EuropaCat IX : Catalysis for a Sustainable World; September 30 – August 4, 2009, Salamanca, Spain. [Poster]

3. *"In-situ electron microscopy study of catalyst nanoparticles reduction"*
   R. Dehghan-Niri, J. C. Walmsley; NanoLab seminar, 12-13 May 2009, Trondheim, Norway. [Oral]

4. *"Advanced TEM study of Co Fischer-Tropsch catalyst"*
   R. Dehghan-Niri, J. C. Walmsley, T. W. Hansen, J. B. Wagner, A. Holmen, E. Rytter, Ø. Borg, R. Holmestad; NanoMat Seminar, 15-19 June, 2009, Lillehammer, Norway. [Poster]

5. *"Advanced TEM study of Co Fischer-Tropsch catalyst, (In-situ studies)"*
   R. Dehghan-Niri, T. W. Hansen, J. C. Walmsley, A. Holmen, E. Rytter, R. Holmestad, inGAP summer workshop, 22-26 June 2009. Trondheim, Norway. [Poster]

6. *"In-situ electron microscopy study of catalysts nanoparticle reduction"*
   R. Dehghan-Niri, T. W. Hansen, J. B. Wagner, A. Holmen, E. Rytter, Ø. Borg, J. C. Walmsley; Norwegian catalysis symposium, 30 November-1 December 2009, Trondheim, Norway. [Oral]

7. *"In-situ reduction of cobalt oxide supported on alumina in an aberration corrected environmental transmission electron microscope"*
   R. Dehghan-Niri, T. W. Hansen, J. B. Wagner, A. Holmen, E. Rytter, Ø. Borg, J. C. Walmsley; The Sixth Tokyo Conference on Advanced Catalytic Science and Technology (TOCAT6) and The Fifth Asia Pacific Congress on Catalysis (APCAT5), July 18-23, 2010, Sapporo Convention Centre, Japan. [Oral]

8. *"Using environmental transmission electron microscope to study the in-situ reduction of Co_3O_4 supported on α-Al_2O_3"*
   R. Dehghan-Niri, T. W. Hansen, J. B. Wagner, A. Holmen, E. Rytter, Ø. Borg, R. Holmestad, J. C. Walmsley; The 17th International Microscopy Congress (IMC17), September 19-24, 2010, Rio, Brazil. [Poster]

9. *"Advanced Transmission Electron Microscopy Study of reduced cobalt Fischer-Tropsch catalysts and the Re promoter"*
   inGAP Seminar, December 1-2, 2011, Trondheim, Norway. [Oral]

10. *"Reduction of promoted cobalt phase supported on γ-Al_2O_3 studied by Transmission electron microscopy"*
    R. Dehghan-Niri, A. S. Voronov, A. Holmen, R. Holmestad, Ø. Borg, E. Rytter, J. C. Walmsley; The 2nd International Symposium on Advanced Electron Microscopy for Catalysis and Energy Storage Materials, February 5-8, 2012, Berlin, Germany. [Poster]

Authors' Contribution

The author has performed all the work on which this thesis is based. All of the experimental work, data analysis and interpretation of the data have been done by the author except for the following;

In Paper I, the XRD experiments were performed by Julian Tolchard at Department of Materials Science and Engineering.

In Paper II, the author has done the TEM experiments and its related data analysis.

In Paper III, the reduction of the catalyst materials was performed by Alexey Voronov and the synchrotron XRD experiments and its data analysis have been done by Nikolas Tsakoumis, both at the Chemical Engineering Department at NTNU.

In Paper IV, the XRD experiments and related data analysis were performed by Nikolas Tsakoumis.

In Paper V, the catalytic testing has been done by Anh Hoang Dam at the Chemical Engineering Department at NTNU.

The author has written papers I, III-V and contributed in Paper II. Writing of paper V was done in close cooperation with Professor De Chen at the Chemical Engineering Department at NTNU.

Some of the experimental work for papers I and V was carried out during visits to the Danish Technical University and Cambridge University and experiments were conducted with assistance by co-authors from those institutions.

Acknowledgements

I had a long journey in my PhD and many people helped me in this journey to be where I am now, and I am sure the work presented here would not have come to the good end without their help and support.

First and foremost, I would like to thank my supervisor, Professor John C. Walmsley, for his magnificent guidance and helpful advice during all stages of this work. I appreciate him for helping me find solutions for many practical problems and also for contributing with many valuable ideas in my research work. Special thanks to him for always being patient, positive and helpful. He was available for my questions. He not only taught me the electron microscopy but also helped me to improve my English. John, I thank you for supporting me in all the moments of this journey!

I would like to thank my co-supervisor Prof. Randi Holmestad at the Department of Physics for being kind, friendly, and helpful. She has created an enjoyable environment in TEM group for me and for others.

I appreciate my co-supervisors, Prof. Anders Holmen and Prof. Magnus Rønning from the Chemical Engineering Department and Prof. Erling Rytter at Statoil R&D centre for their stimulating ideas and valuable comments and solutions to many problems.

My gratitude also goes to Professor De Chen in the Department of Chemical Engineering at NTNU for his great ideas and valuable scientific support.

I would also like to express my appreciation to Prof. Paul Midgley at the Department of Materials Science in Cambridge University and Dr. Anna B. Hungria and Dr. Juan C. Hernandez-Garrido, for their hospitality and motivating me to establish electron tomography at NTNU. I also appreciate them for their scientific advice. I am also very grateful to Prof. Rafal E. Dunnin-Borkowski, Dr. Thomas W. Hansen, Dr. Jakob B. Wagner, and Dr. Takeshi Kasama at the Center for Electron Nanoscopy at Danish Technical University (DTU) for their support, hospitality, many inspiring discussions, and their advice for the publications from this study. Gratitude is also given to Dr. Øyvind Borg and Dr. Sigrid Eri at Statoil R&D centre in Trondheim for both providing catalyst materials and excellent comments on the publications and thesis.

Special thanks to Mr. Heimir Magnusson and Mr. Bjørn G. Soleim for supporting me to work with the microscopes. Heimir was my first teacher in the TEM lab and taught me the basics of TEM application and Bjorn has helped me a lot to fix the problems in the microscopy sessions. I appreciate you for being available to answer my questions and for supporting me in the lab, even late in the evenings.

I thank all my colleagues at the Department of Physics who supported me in my PhD study. In particular I would like to thank Prof. Antonius T. J. Van Helvoort for his valuable advice and Dr. Ragnhild Sæterli for teaching me the EELS technique. I enjoyed of all the discussions that I had with you.

I also appreciate Dr. Bjørn Steinar Tanem for teaching me the sample preparation technique and Dr. Per E. Vullum at Sintef Materials and Chemistry for their assistance in the experimental work and data analysis.

I would also like to express my gratitude to Dr. Nikolas Tsakoumis and PhD student Alexey Voronov in the Department of Chemical Engineering for several good scientific discussions and for helping me in part of the experimental work. Nikolas, I appreciate you for giving the idea of using the Raman Cell to reduce my samples and also for synchrotron experiments. Alexey, I appreciate you for all of the long experiments that you have kindly done for me. Without these, my PhD would be quite different.

I would like to thank everyone at the TEM research group and specially those on the B4-corridor, Realfag, NTNU, (Wakshum (who is now in Stavanger), Ragnhild, Hanne, Jelena, Morteza, Ruben, Flemming, Malin, Jon) for their friendship throughout.

I thank all of my friends in Trondheim and around the world, who have supported me with their messages and sent me good wishes.

I would like to express my deepest gratitude to my parents and my siblings for their love and encouragement throughout all my years of study.

پدر بزرگوار و مادر عزیزم, از زحمات بی دریغ شما در طول این سالها سپاسگزارم.

Finally, I want to thank my husband, Jafar, and my daughter, Armita, for their love and support throughout all my years here at NTNU. They were a constant source of motivation and joy. Their endless support has been invaluable for the completion of this thesis.

I acknowledge the Research Council of Norway and Statoil for s financial support of this project. I would also like to express my appreciation to SINTEF, Statoil, Cambridge University and Center for Electron Nanoscopy at DTU for their valuable support and collaboration.

Notwithstanding the help I received, the present thesis is ultimately my responsibility, and I alone am to blame for any errors.

Trondheim, August 2012

Roya Dehghan-Niri

Abstract

Gas to Liquid (GTL) is a technology to produce synthetic fuels from natural gas. The importance of this technology for the environment is to produce clean-burning fuels and using the natural gas that would otherwise be flared and pollute the atmosphere. A main part of the GTL technology is the Fischer-Tropsch (FT) process in which the synthetic gas is converted into synthetic oil. The main catalysts for this reaction are supported cobalt materials.

The main objective of this thesis has been to characterize the supported cobalt catalysts by advanced Transmission Electron Microscopy (TEM) techniques and obtain detailed understanding of the catalysts nanostructure. Hence, several TEM techniques such as Scanning Transmission Electron Microscopy (STEM), High Resolution TEM (HRTEM), Electron Tomography (ET), and Electron Energy Loss Spectroscopy (EELS) were applied. The intention has also been to study the catalysts in conditions close to the FT process conditions. Since the cobalt is reactive on exposure to air, ex-situ and in-situ experiments were carried out to study the active phases. The results of this work are presented in the papers in Part II of this thesis. One of the milestones of the project was to establish the use of an ex-situ reaction cell for catalyst studies. This is also described. Electron tomography was established in the NTNU TEM lab during this project and a significant contribution has been made to achieve this and learn the necessary competence to apply the technique.

In paper I, the Re promoted cobalt oxide supported on α-Al_2O_3 was characterized during reduction by environmental TEM. The in-situ reduction was carried out in 3.4 mbar H_2 gas pressure and at 360˚C. Under these conditions, reduction of Co_3O_4 nanoparticles to metallic cobalt was observed. Both face centred cubic (fcc) and hexagonal closed pack (hcp) structures were present after reduction. During cooling to room temperature, re-oxidation of the cobalt nanoparticles was observed. Non-promoted similar catalysts were also studied to see the possible effect of promoter on the re-oxidation of cobalt nanoparticles during cooling. However, similar behaviour was observed for this catalyst both during reduction and during cooling.

In Paper II, a series of cobalt oxide supported on γ-Al_2O_3 with different pore sizes were studied. The influence of the support on the cobalt particle size and aggregation were studied by TEM, X-ray diffraction and hydrogen chemisorption in calcined state. It is observed that the Co_3O_4 is present in the aggregates of many small particles. The sizes of the small particles

correlate with the alumina pore diameter. These small particles in the aggregate tended to have a common orientation.

In paper III, the structure of cobalt oxide supported on γ-Al_2O_3 has been studied by Bright Field (BF) and Dark Field (DF) imaging, before and after reduction. The reduced material was transferred from a glove box to the TEM by using a glove bag for inert transfer. Electron diffraction, HRTEM and EELS were applied to confirm the state of the cobalt phases. Both fcc and hcp cobalt metal structures were observed in the reduced catalysts and fcc was the main component. It is observed that the continuous interlocking network of Co_3O_4 in the aggregate is separated into discrete particles. The size of the cobalt nanoparticles and cobalt crystallites were measured in the BF and DF images and the results were compared with X-ray measurements. A good correlation between the results from the two techniques was obtained for crystallite size. Planar faults associated with the fcc to hcp phase transition were observed in the structure of the cobalt nanoparticles and the mechanism of their formation is discussed.

In paper IV, a cobalt catalyst (20%Co/0.5%Re/γ-Al_2O_3) was studied before and after use in the FT process by in-situ XRD and TEM. The active catalyst before the FT process should be in a metallic state. However, for ease of experimental work, the sample was passivated. This leads to formation of a thin oxide layer in the cobalt nanoparticles which protects the rest of the particle. Both the passivated and utilised catalysts in the FT process were characterized with TEM. The TEM results show an increase in the cobalt nanoparticle size which is consistent with sintering as a deactivation mechanism for the cobalt nanoparticles spent in the FT process.

In paper V, a Ni/hydrotalcite catalysts for steam methane reforming was studied by TEM techniques in different stages of preparation. Electron tomography was applied to visualize the three dimensional structure of the catalyst. It was observed that Ni nanoclusters, after reduction, are confined in the porous structure of Mg-Ni-Al mixed oxides with connected pore channels, which provide good catalysts stability and proper access of the gaseous reactants. The novel catalyst structure is compared with a commercial catalyst.

List of abbreviations

Al_2O_3	alumina
α-Al_2O_3	Alpha alumina
γ-Al_2O_3	Gamma alumina
ATEM	Analytical Transmission Electron Microscope
BF	Bright Field
CEN	Center for Electron Nanoscopy
CNG	Compressed Natural Gas
Co	Cobalt
$CoAl_2O_4$	Cobalt aluminate
CoO	Cobalt monoxide
Co_3O_4	Cobalt oxide
DF	Dark Field
DME	Dimethylether
DP	Diffraction Pattern
DTU	Danish Technical University
EDS	Energy Dispersive Spectroscopy
EELS	Electron Energy Loss Spectroscopy
ETEM	Environmental Transmission Electron Microscope
EXAFS	Extended X-ray Absorption Fine Structure
FT	Fischer-Tropsch
GTL	Gas to Liquid
GTW	Gas to Wire
HAADF	High Angle Annular Dark Field
HRTEM	High Resolution Transmission Electron Microscopy
HT	Hydrotalcite
LNG	Liquefied Natural Gas
Re	Rhenium
SAD	Selected Area Diffraction
STEM	Scanning Transmission Electron Microscopy
TEM	Transmission Electron Microscopy
TPR	Temperature Programme Reduction
XRD	X-ray Diffraction

CONTENT

PART 1

PART 2

Part 1
Chapters

Chapter 1

General Introduction

A review over microscopy history reveals that the light microscope was the first developed instrument for magnifying objects. The first light microscope was invented by Anton van Leeuwenhoek, who is known as the father of microscopy. He discovered many things such as red blood cells and spermatozoa and helped to popularise microscopy as a technique [1,2]. In the 18th century, several technical innovations made microscopes better and easier to handle. Ernst Abbe in 1878 formulated a mathematical theory correlating resolution to the wavelength of light. His formula made calculations of the maximum resolution in microscopes possible [2].

Along with the developments in light microscopes in the 20th century, electron microscopes were invented and developed. The first electron microscope was constructed by the German physicist Ernst Ruska and his electrical engineer Max Knoll in 1931. Two years later, in 1933, Ruska built an electron microscope that exceeded the resolution attainable with an optical microscope [2]. He was awarded half of the Nobel Prize in Physics for his many achievements in electron optics in 1986 [2]. The first practical electron microscope was constructed in 1938 at the University of Toronto by James Hillier and Albert Prebus [3]. Siemens produced the first commercial Transmission Electron Microscope (TEM) in 1939 [4]. Electron microscopy has been developed significantly over the last decades, both in lenses improvement and capabilities. The new generation of electron microscopes, equipped with aberration corrected lenses, gives improved resolution, down to the sub-angstrom regime. In addition, the development of environmental transmission electron microscopes makes it possible to study the structure of materials while chemical reactions take place. Since in the present study TEM techniques are extensively applied to study catalysts materials, the principle of electron microscopy is reviewed in the following.

1.1 Principles of Electron Microscopy

The human eye is capable of distinguishing objects down to a fraction of a millimetre. When a light microscope is used, it is possible to distinguish objects down to sub-micron size, as illustrated in Fig. 1.1. At very high magnifications with transmitted light, point objects are seen as fuzzy discs surrounded by diffraction rings. The resolving power of a microscope is defined as the ability to distinguish between two closest sets of diffraction rings. The extent and magnitude of the diffraction patterns are affected by both the wavelength of light (λ), the refractive materials used to manufacture the objective lens and the numerical aperture (NA) of the objective lens [5]. The resolution *d* can be expressed as:

$$d = \frac{\lambda}{2NA} \tag{1.1}$$

The wavelength of visible light is in the range of 380-750 nm [5]. Therefore, the highest value of *d* obtainable in air (maximum NA≈1) is around 200 nm (Fig. 1.1).

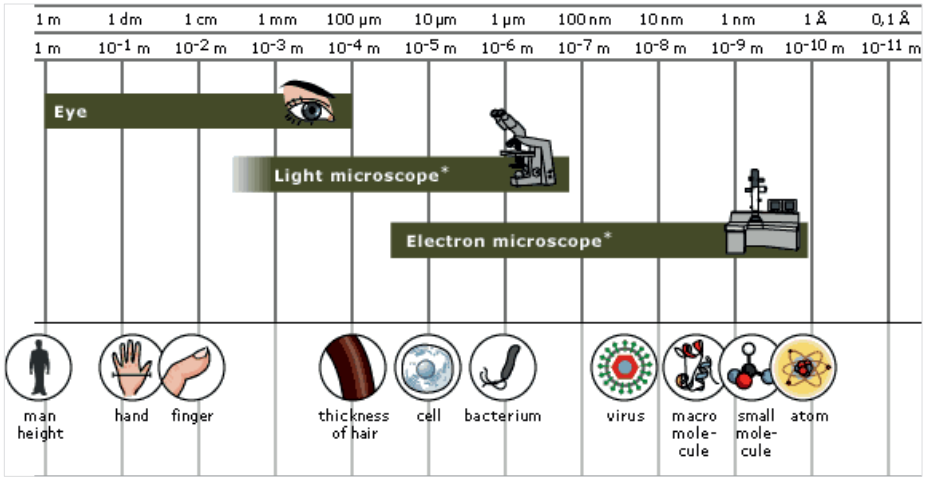

Figure 1.1: Comparison of the resolution power of human eye, light microscope and electron microscope. (*: Light microscope includes phase contrast and fluorescence microscopes. Electron microscope includes TEM) [2].

In the electron microscopes electrons are used for visualization of the objects instead of the photons in the light microscopes. Like all matter, electrons have both wave and particle properties. The wavelength of electrons, λ_e, is obtained by Eq. 1.2:

$$\lambda_e = \frac{h}{\sqrt{2m_eE\left(1+\frac{E}{2m_ec^2}\right)}} \tag{1.2}$$

Where h is Planck's constant m_e is the rest mass of an electron, E is the energy of an accelerated electron (eV), and c is the speed of light in vacuum [5]. Considering the constant values in Eq. (1.2) and with simplification, gives [5]:

$$\lambda_e = \frac{1.22}{\sqrt{E}} \qquad \text{[pm]} \tag{1.3}$$

This formula gives electron wavelengths of 3.86, 2.73 and 2.23 pm for 100, 200 and 300 keV accelerating voltages, respectively. The higher electron energies provide smaller electron wavelength and so higher accessible magnification. It has to be emphasized here that the resolution of electron microscopes in reality is less than the theoretical values calculated from the above equation. The microscope resolution is given by combination of Rayleigh criterion and the aberration error, which is mostly due to the spherical aberration of the electromagnetic lenses [4,5,6]. The Rayleigh criterion expresses that the overall intensity of two sources are resolved when central maximum of one source falls onto the first minimum of the other source [5]. Based on this combination, Hawkes [7] obtained a value for the resolution of the electron microscope:

$$r = \left(r_{th}^2 + r_{sph}^2\right)^{1/2} \tag{1.4}$$

where r_{th} is the radius of the fuzzy disk and r_{sph} contains errors from spherical aberration. The parameter r_{th} is defined as $r_{th}=0.61\lambda/\beta$ in which β is the objective lens semi-angle of collection. Parameter r_{sph} equals to $C_s\,\beta^3$ in which the C_s is spherical aberration coefficient. Re-writing Eq. (1.4) relative to the β gives:

$$r(\beta) = \left[\left(0.61\frac{\lambda}{\beta}\right)^2 + \left(C_s\beta^3\right)^2\right]^{1/2} \tag{1.5}$$

This formula gives the optimum value of β as:

$$\beta_{opt} = 0.77\frac{\lambda^{1/4}}{C_s^{1/4}} \tag{1.6}$$

Taking this optimum value of β into the r_{th} definition, a minimum value for resolution is obtained as:

$$\Delta r \approx 0.91(C_s\lambda_e^{\,3})^{1/4} \tag{1.7}$$

For example in a 200 kV microscope, with partly corrected spherical aberrations ("to the third order") with the C_s value about 1.4 mm the spatial resolution is 0.3 nm [5].

In TEM, electrons are usually generated in a process known as thermionic emission from a filament (usually LaB_6) or by field electron emission. An electric potential is used then to accelerate the emitted electrons along a column. This electron beam is focused by electrostatic and electromagnetic lenses onto the specimen as seen in Fig. 1.2. The transmitted beam from the sample contains information about electron density, phase and periodicity and it is used to form images of the sample [5]. More details about TEM and different TEM techniques used in the present research are described later in chapter 3 and 4.

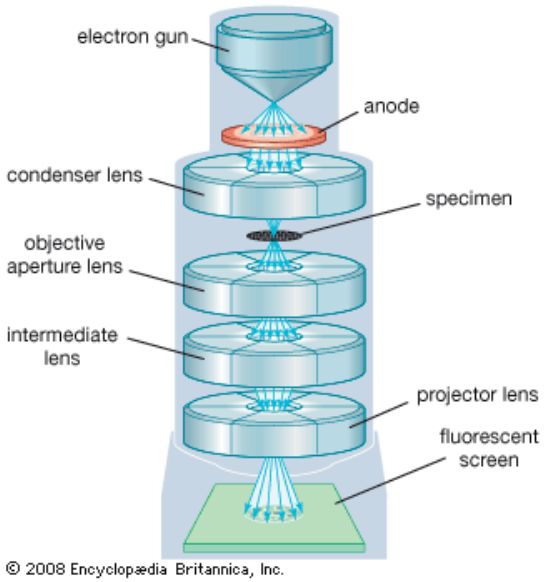

Figure 1.2: The schematic of the transmission electron microscope column [8].

1.2 Electron Microscopy of Fischer-Tropsch Catalysts

The FT process is an industrial procedure for converting natural gas into synthetic fuel. Supported cobalt nanoparticles are widely used as FT catalysts. The FT reaction with the presence of a cobalt-based catalyst supported on an alumina substrate is shown schematically in Fig. 1.3. A mixture of CO and H_2 is converted to hydrocarbon chains in the presence of the supported cobalt catalysts. Rhenium acts as promoter and increases the reducibility of the cobalt oxide phase.

To optimise the efficiency of the catalysts nanoparticles, and hence the FT process, fundamental understanding of the structure of these nanometre scale catalysts must be obtained. Hence, studying the dispersion, morphology and structure of the cobalt phases is crucial. Among the available characterization techniques, TEM is a powerful tool which provides the possibility to study these catalysts in high magnifications down to the nanometre

scale. FT catalysts have a complex microstructure. Electron tomography can provide three-dimensional information at the nanometre scale.

Metallic cobalt nanoparticles are rapidly oxidized during exposure to air. Hence, this kind of catalyst should be reduced prior the FT reaction. To gain better understanding of these catalysts, the TEM analysis must be performed on both oxide and the reduced catalysts. In-situ TEM studies give the opportunity to study the sample under reaction environment, with lower gas pressure than the normal laboratory or industrial conditions, inside the TEM [9]. Ex-situ studies are also practical in which the reaction is carried out outside the microscope and the sample is examined before and after the reaction.

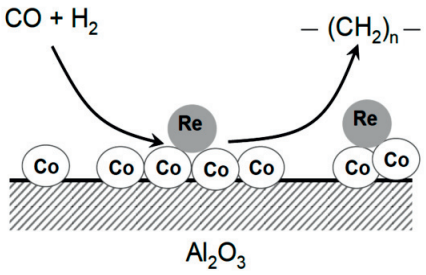

Figure 1.3: Schematic of the Co/0.5%Re/Al_2O_3 in a general FT reaction.

1.3 Scope of the Thesis

Having considered the above points, the present study is focused on electron microscopy investigations of the FT cobalt catalysts system. The effort is to get basic knowledge in different electron microscopy techniques and apply them to study the catalysts. This requires selection of appropriate TEM techniques such as Scanning Transmission Electron Microscopy (STEM), Electron Tomography (ET), Electron Energy Loss Spectroscopy (EELS) and Energy Dispersive X-ray Spectroscopy (EDS). This presents challenges both with the FT samples and the TEM techniques themselves.

TEM studies of the cobalt based catalysts are challenging, first due to the reactive nature of the cobalt nanoparticles, which re-oxidise in normal atmospheres, even with small amounts of oxidizing gas. A second challenge is sample damage by the electron beam. To overcome these difficulties specific considerations were required to gain the optimum conditions for effective TEM studies.

Although the present work covers many aspects of the catalysts materials investigation by advanced electron microscopy techniques, the main objectives of the thesis has been to:

1) Apply advanced TEM techniques to characterize and understand the structure of cobalt oxide nanoparticles.

2) Characterize and understand the structure of the metallic cobalt nanoparticles after reduction.

3) Initiate and establish the electron tomography technique at NTNU and apply it to investigate the three dimensional structure of catalysts nanoparticles.

4) Establish and apply the ex-situ set up and the dedicated ex-situ TEM sample holder at NTNU to study the catalysts before and after reaction.

Chapter 2

The Fischer-Tropsch Process

Fischer-Tropsch synthesis is a part of the Gas to Liquid (GTL) technology in which synthetic fuels are produced from natural gas. The main chemical reactions in this process take place in the presence of catalysts. The details of this process and the catalysts materials studied are described in the following.

2.1 Gas to Liquid Technology

Natural gas is regarded as one of the cleanest, safest, and most useful sources of energy in the world [10]. Natural gas is a combustible mixture of hydrocarbon gases and primarily is composed of methane. It can also include ethane, propane, butane and some other gases. The composition of natural gas can vary widely and a typical composition before refinement is shown in Table 2.1. Natural gas is always refined to remove impurities such as sulphur and nitrogen.

Table 2.1: Typical composition of natural gas before refining [10].

Methane	CH_4	70-90%
Ethane	C_2H_6	0-20%
Propane	C_3H_8	
Butane	C_4H_{10}	
Carbon Dioxide	CO_2	0-8%
Oxygen	O_2	0-0.2%
Nitrogen	N_2	0-5%
Hydrogen sulphide	H_2S	0-5%
Rare gases	Ar, He, Ne, Xe	trace

Natural gas is transported to the market in different ways as illustrated in Fig. 2.1. It is mainly transported through pipelines, liquefied natural gas (LNG) carriers, or compressed natural gas (CNG) tank trucks [11]. Moreover, natural gas can be processed, converted to other products and transported. For instance, when electricity is produced and transported by wires it is referred as gas to wire (GTW) transportation [11,12]. In the gas-to-liquid (GTL) process, natural gas is processed and converted into high-value liquids such as methanol, dimethylether (DME), and synthetic crude oil [13].

GTL technology is preferred over other transportation technologies when there is long distance between the gas resource and the market [11,13]. Another considerable advantage of GTL technology is that the diesel fuels produced from natural gas are cleaner than the fuels derived from the crude oil since they have lower content of nitrogen, sulphur, aromatics, and metals [11]. A main part of the industrial process for GTL is known as the FT synthesis process, which is described in the following.

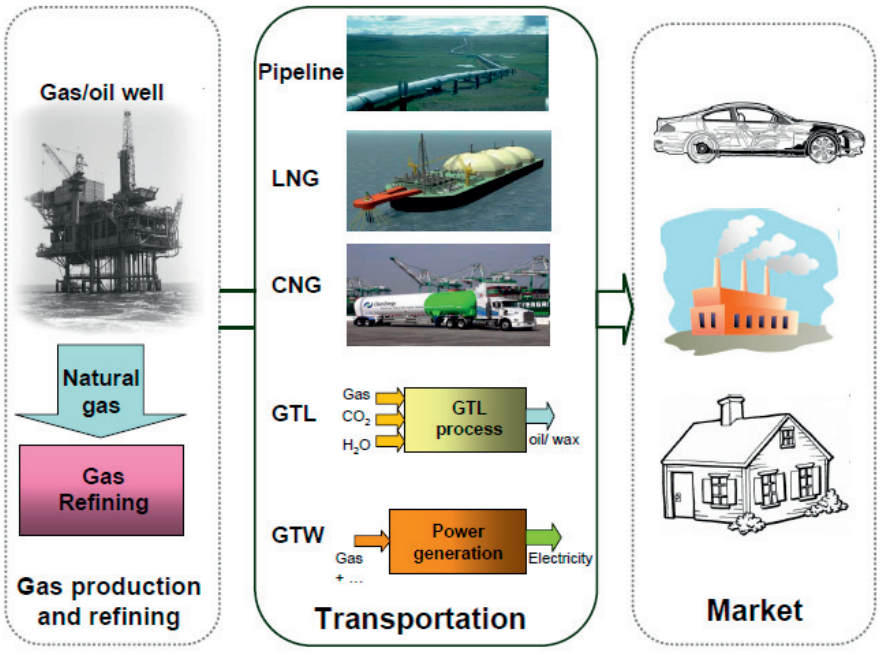

Figure 2.1: Main technologies for bringing natural gas to the market.

2.2 The Fischer-Tropsch Process

Fischer-Tropsch (FT) synthesis is a process that converts natural gas into synthetic fuels [14]. Historically, the synthesis of hydrocarbons from CO hydrogenation over transition metal catalysts was first discovered in 1902 when Sabatier and Sanderens produced CH_4 from H_2 and CO mixtures passed over Ni, Fe, and Co catalysts [15]. In 1923, Fischer and Tropsch reported the use of alkalized Fe catalysts to produce liquid hydrocarbons rich in oxygenated compounds — termed the Synthol process [14]. In 1925, they reported the synthesis of higher hydrocarbons at atmospheric pressure over group VIII metals [16]. This process and the related technologies have been extensively developed in the last century, however, converting CO and H_2 mixtures to liquid hydrocarbons over a transition metal catalyst is known as Fischer-Tropsch synthesis.

The whole FT process is schematically shown in Fig. 2.2 for the case of natural gas as the initial feedstock. Other sources such as biomass and petroleum coke can be used as feedstock to produce the synthesis gas. As seen in Fig. 2.2, the process consists of three main step; (1) synthesis gas (Syngas) production, (2) FT synthesis and (3) product refining. These three process steps are briefly described in the following.

2.2.1 Syngas Manufacture

The usual methods for syngas production are steam methane reforming, autothermal reforming and catalytic partial oxidation [14]. For FT plants that start with natural gas, such a reaction is necessary to convert the natural gas into synthetic gas. This process involves the following reaction which converts the methane into CO and H_2 [13,17,18]:

$$H_2O + CH_4 \rightarrow CO + 3H_2 \qquad \Delta H^o = 206 \text{ kJ/mol} \tag{2.1}$$

The reaction is strongly endothermic and is favoured at high temperatures, high steam-to-carbon ratio (S/C) and low pressures. The carbon monoxide produced from this reaction can further react with steam to produce more hydrogen via the water-gas shift reaction [14,18,19]:

$$CO + H_2O \rightarrow CO_2 + H_2 \qquad \Delta H^o = -41.2 \text{ kJ/mol} \tag{2.2}$$

Another important reaction in steam reforming is the overall reaction:

$$CH_4 + 2H_2O \rightarrow CO_2 + 4H_2 \qquad \Delta H^o = +165 \text{ kJ/mol} \tag{2.3}$$

CO_2 is not only produced via the gas shift reaction (2.2), but also directly via the steam reforming reaction (2.3). This implies that reaction (2.3) is not the 'overall reaction', despite the fact that in literature steam-methane reforming is often considered as a combination of reactions (2.1) and (2.2) [20].

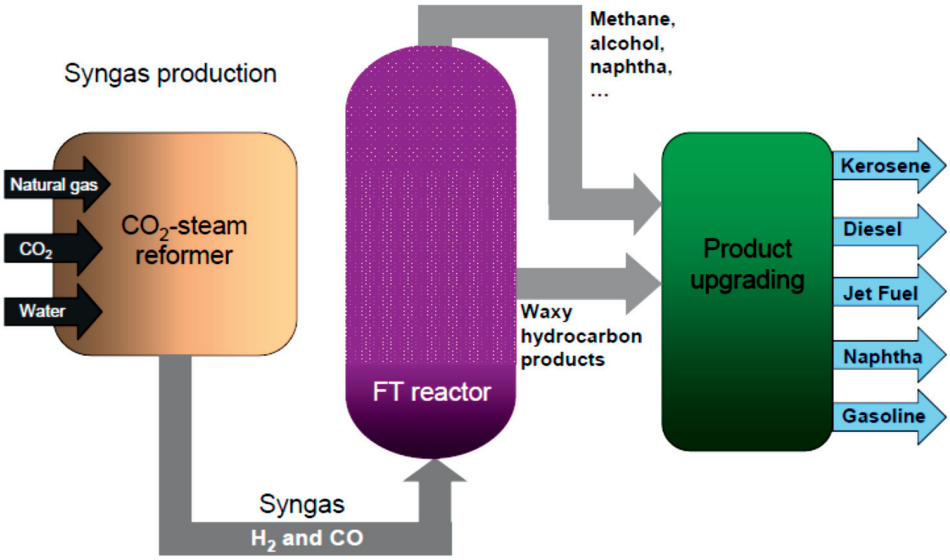

Figure 2.2: Natural gas conversion to liquid fuel through the FT process.

Steam Methane Reforming Catalyst

Steam methane reforming is a catalytic reaction and nickel-based catalysts are normally used in this process. The catalyst must sustain severe conditions including temperatures in the range of 750-900˚C and pressures up to 30 bar. Moreover, it must have sufficient activity, resistance to carbon formation and sintering in addition to high mechanical strength [21].

The Ni particle size is a very important factor for steam reforming yield. Smaller particles provide larger metal surface area and hence higher activity for the process reactions [22]. Among different precursors for Ni catalysts, hydrotalcite (HT) materials show high activity and stability and it seems a promising catalyst for steam methane reforming [23,24,25]. More details about characterization of this catalyst are in paper V.

2.2.2 The Fischer-Tropsch Synthesis

As stated above, FT synthesis is the main step in the GTL process. In this step, the syngas is converted to a large range of hydrocarbones through highly exothermic reactions. The chemical reactions for FT process and its related technologies are described in the following.

The Fischer-Tropsch Reaction

The FT reactions take place catalytically and the products range from methane to hard waxes. Small amounts of oxygenates exists also in the product [11]. Two major reactions in the FT synthesis reactor are [26]:

Formation of Paraffin: $$nCO + (2n+1)H_2 \rightarrow C_nH_{2n+2} + nH_2O \quad (2.4)$$

Formation of Olefin: $$nCO + 2nH_2 \rightarrow C_nH_{2n} + nH_2O \quad (2.5)$$

The water-gas shift reaction (2.2) is other main reaction in the FT process. The minor reactions in the FT reactor are:

Formation of Oxygenates: $$nCO + 2nH_2 \rightarrow C_nH_{2n+2}O + (n-1)H_2O \quad (2.6)$$

Boudouard reaction: $$2CO \rightarrow C + CO_2 \quad (2.7)$$

In the FT synthesis, the formation of one mole of -CH_2- releases -165 kJ/mol of heat. The industrial reaction conditions are 200-300˚C and 25-40 bar [13]. Since the present study is focused on the catalyst materials relevant to the FT synthesis, they are separately described in section 3.3.

The Fischer-Tropsch Reactors

Four types of reactor designs used over the years for FT synthesis are shown schematically in Fig. 2.3. Since the FT reactions are exothermic, the removal of a large amount of produced excess heat is very important for the reactor selection. Moreover, several problems may occur through overheating, for example catalyst deactivation due to carbon deposition and methane formation at higher temperatures [17,27].

In a **fixed-bed tubular reactor** many tubes are filled with the catalyst, immersed in boiling water for heat removal. Syngas is introduced into the top of the reactor and flows through the

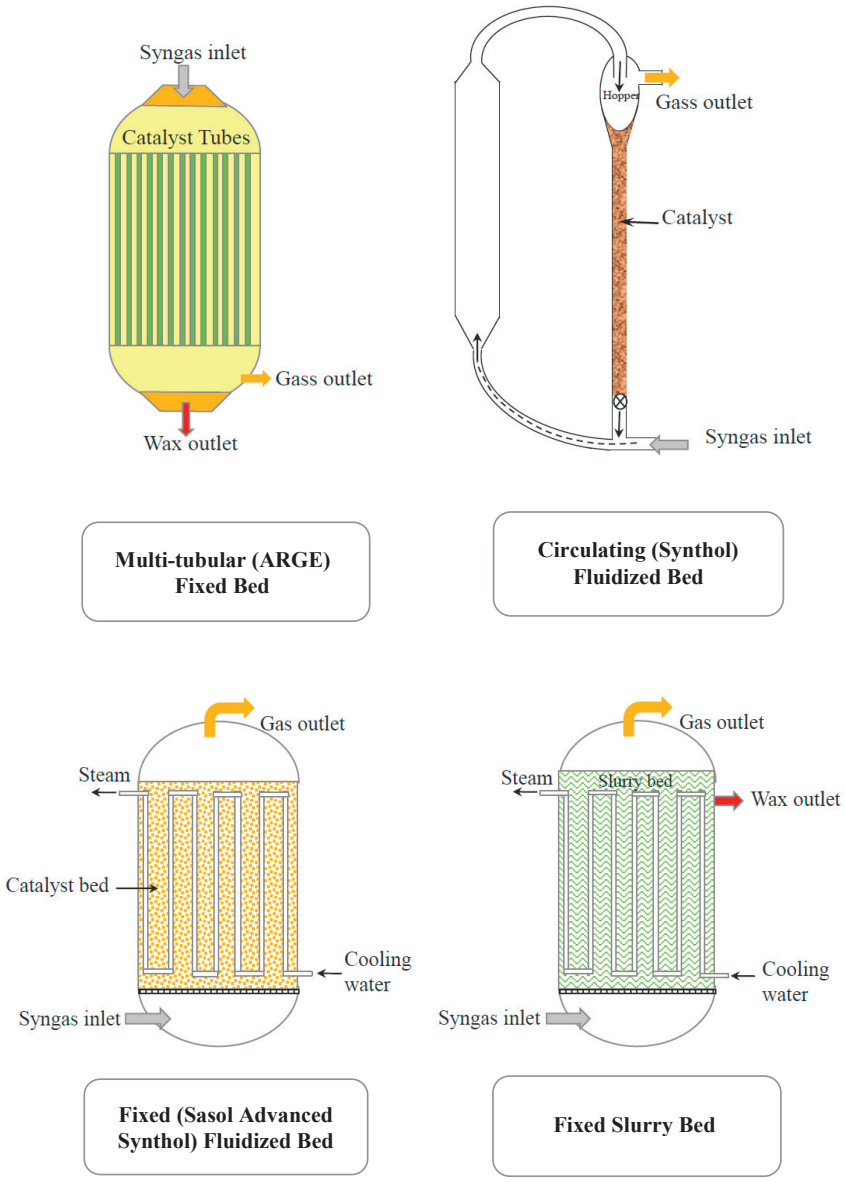

Figure 2.3: Fischer-Tropsch Synthesis Reactors, Rebuilt from Reference [27].

tubes. The products exit at the bottom of the reactor. The reactor is operated at 20-30 bar at a temperature of 220-260ºC. In a **circulating fluidized-bed reactor**, which is also known as a Synthol reactor, the syngas enters at the bottom of the reactor and is in contact with the catalyst that is flowing down the standpipe through the slide valve. The high gas velocity carries the catalyst into the reaction zone. The heat released in this zone is removed by heat exchangers. Product gases and catalysts are then transported into a large diameter catalyst hopper where the catalyst settles out and the product gases exit through a cyclone. The operational conditions of these reactors are 350°C and 25 bar. They have been developed for gasoline and light olefin production. In a **fixed fluidized bed reactor** gas is introduced through a distributor and the gas bubbles rise through a catalyst bed. Heat is removed by an internal heat exchanger immersed in the catalyst bed. Process conditions in the fixed fluidized bed reactors are similar to the Synthol reactors (350°C and 25 bar). In a **low-temperature slurry reactor**, solid catalyst particles are suspended and dispersed in a high thermal capacity liquid, which is often the FT wax product. Syngas is introduced from the reactor bottom and the distributed gas bubbles contribute to excellent contact with the catalyst while keeping the particles dispersed. The slurry reactors are optimized at low temperatures for high FT wax production with low methane production [17].

2.2.3 Product Refining

The hydrocarbon product mixture leaving the FT reactor is frequently referred to as synthetic crude oil. The product upgrading techniques that are used to refine oil are also suitable for upgrading of the FT synthesis product.

The FT process directly produces high quality waxes suitable for food applications, medicines and so on. The C_9-C_{15} olefins are very suitable for the production of bio-degradable detergents, whereas the paraffins are excellent lubricants. High selectivities towards fuels are obtained through hydrocracking of the wax. Hydrocracking converts heavy hydrocarbons into the C_4-C_{12} range with low selectivities to C_1-C_3. This directly produces a high quality gasoil (high combustion quality, low sulphur content, low aromatics) and kerosene (high paraffin content), which are very suitable as blending components to upgrade lower quality stocks. [13]. The product distribution of hydrocarbons formed during the FT process follows an Anderson-Schulz-Flory distribution, which can be expressed as:

$$W_n / n = (1-\alpha)^2 \alpha^{n-1} \tag{2.8}$$

where W_n is the weight fraction of hydrocarbon molecules containing n carbon atoms. α is the chain growth probability or the probability that a molecule will continue forming a longer chain. In general, α is largely determined by the catalyst and the specific process conditions [27]. Eq. (2.9) is graphically represented in Figure 2.4.

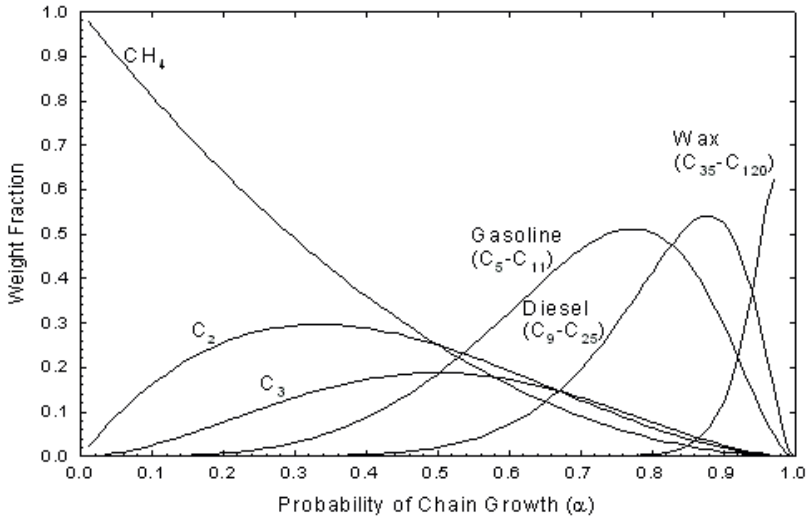

Figure 2.4: Anderson-Shulz-Flory Distribution [27].

Examining Eq. (2.9) reveals that methane is the largest single product; however the total amount of methane formed decreases with increasing α-value. In contrast, the formation of longer chain hydrocarbons increases with increasing α.

2.2.4 Fischer-Tropsch Catalysts

As mentioned in section 2.2, the chemical reactions in a FT reactor are performed catalytically. There are several catalyst candidates for FT reaction. Among them only cobalt, nickel, iron and ruthenium based catalysts have sufficient activity to be considered as commercially usable in the FT reaction [11,28]. The choice of catalyst depends on the desired end products and price of the active metals.

Ruthenium is the most active element for FT synthesis, however it is the most expensive compared to the other candidates and this limits its industrial application.

Nickel has powerful hydrogenation properties and produces a significant amount of methane. It also enhances the formation of volatile carbonyls (material composed carbon atom double-bonded to an oxygen atom) in the typical FT synthesis. These two properties make nickel unsuitable for FT synthesis [29].

Iron is suitable for synthesis gas with low H_2/CO ratio due to its high water-gas-shift activity [28]. Fe-based catalysts are selective for light olefins at high temperature (340˚C), with a low selectivity towards methane. This only seems possible with Fe-based catalysts, making them unique in this respect. It is worth noting that the application of Fe-based catalysts in the production of heavy wax is limited due to its tendency to form carbon, causing deactivation of the catalyst.

Cobalt is the main catalyst for FT synthesis at low temperatures. It is usually supported on metal oxide substrates such as Al_2O_3, SiO_2 and TiO_2 due to the high cobalt price, providing better catalyst stability and higher reactant surface area [11,28]. The tendency of the metallic cobalt (the active site) to form carbides at 200-300˚C and 25-40 bar is low [13]. The water-gas shift activity of Co-based catalysts is low and water is the main oxygen containing reaction product. This type of catalysts can be used to produce synthesis gas from natural gas due to low water-gas shift reactions [28]. Cobalt is generally poorly dispersed on metal oxide supports and Ru, Re, or Pt promoters are applied to enhance the reducibility of cobalt oxide phases [30]. Co-based catalysts are very suitable for wax formation in slurry columns and can operate at high conversions per pass. Regarding the point that Co-based catalysts are studied in the present work, they are described in more details in the following.

2.3 Cobalt based Fischer-Tropsch Catalysts

Cobalt-based FT catalysts contain three components; Cobalt metal as the primary active phase for the FT reaction, a high surface area oxide (Al_2O_3, SiO_2 or TiO_2) as support and a promoter metal. The procedure of Co-based catalysts preparation for the FT process, which is applied for the samples in the present study, and their reduction prior to FT synthesis are described in this chapter.

2.4.1 Preparation of Cobalt Catalysts

A common way to prepare the FT cobalt catalysts is incipient wetness impregnation of a metal oxide support (α-Al_2O_3, γ-Al_2O_3 or SiO_2) with an aqueous solution of cobalt nitrate

hexahydrate. In this study two α-Al_2O_3, γ-Al_2O_3 supports were studied. Before impregnation the supports are pre-sieved to 53-90 μm and pre-calcined in air at different temperatures for 10 h. The α-Al_2O_3 and γ-Al_2O_3 phases are pre-calcined at 770ºC and 500ºC, respectively. After impregnation the sample is dried and calcined in order to decompose the cobalt nitrate hexahydrate and obtain the cobalt oxide [11]. Prior to the FT reaction, the in-situ reduction transforms the inactive cobalt oxide aggregates to the active metallic cobalt phase. (α-Al_2O_3 or γ-Al_2O_3)

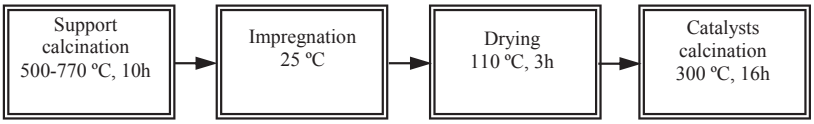

Figure 2.5: Catalysts preparation steps [11].

In the impregnation step in the laboratory, water is added drop-wise to the pre-calcined support until the pores are completely filled, which is the incipient wetness point. Then the same amount of adsorbed water (ml/g), as the specific volume of metal precursor is added to the approximately 30g of pre-treated support. The mixture is then mixed thoroughly to obtain homogeneity. Then it is dried for 3 hours at 110˚C in a furnace. During the drying period the sample is stirred gently every quarter-an-hour of the first hour and every half-an-hour for the last two hours. Then the dried sample is calcined under the air at 300˚C for 16 h in a fixed bed quartz reactor (inner diameter = 40 mm). The ramping rate of 2˚C /min is used to heat the samples from ambient temperature to 300˚C. The gas is directed through the samples at a flow rate of 0.2 L/(g.h). The flow rate is an important factor in the calcination. Low flow rate has negative affect on the dispersion of catalysts [31]. After calcination the catalyst is sieved to 53-90 μm [11]. Figure 2.5 shows the preparation steps.

Table 2.2: List of main FT samples studied in this thesis, identified with support and Co_3O_4 particle size measured by XRD.

Samples\Parameters	Alumina particle siz	Co_3O_4 particle size
12wt%Co/0.5wt%Re/α-Al_2O_3	94± 1nm	21± 0.5 nm
12wt%Co/α-Al_2O_3	94± 1nm	30± 2 nm
20wt%Co/0.5wt%Re/γ-Al_2O_3	6.10± 0.11 nm	13.27± 0.13 nm
20wt%Co/γ-Al_2O_3	6.7± 0.25 nm	14.14± 0.25 nm

In catalysts preparation through incipient wetness impregnation, the pore size distribution of the support plays an important role on the cobalt oxide particle size [32,33,34].

2.4.2 Reduction of Cobalt Oxide

The supported cobalt oxide particles are reduced to the metallic cobalt nanoparticles to make the active catalyst. The reduction of cobalt oxides and influencing parameters are described in this section

Reduction reaction

The reduction of cobalt oxide takes place in two steps through these reactions:

$$Co_3O_4 + H_2 \rightarrow 3CoO + H_2O \tag{2.10}$$

$$CoO + H_2 \rightarrow Co + H_2O \tag{2.11}$$

The standard reduction procedure applied for supported cobalt oxide in this research is 16 h under hydrogen flow at 360 ºC [11]. Different parameters influence the reduction procedure such as support structure, cobalt loading and promoter which are explained below.

Effect of the support material

The support material plays a significant role in design and catalytic performance of the cobalt FT catalysts. The principle function of the support is to disperse cobalt particles and to stabilize metallic cobalt particles after the reduction. A porous structure of the support can control the size of the supported cobalt particles. Supports with small pore sizes provide smaller cobalt crystal size [35]. Small particles have higher surface area, but they also have a stronger interaction with the support. Therefore, the probability of formation of cobalt-support mixed compounds increases with smaller particles. These compounds should be avoided since they do not produce active sites for the FT reaction. It has been reported that the metal-support interaction increases in the order γ-Al_2O_3 > TiO_2 >SiO_2 [11].

Effect of cobalt loading

Catalysts with different cobalt loadings interact differently with the support. At low loadings most of the particles interact strongly, causing formation of cobalt-support compounds, whereas high loading increases the cobalt phase dispersion and increases the crystal size of cobalt particles [11].

Effect of promoters

A promoter is a substance which increases the activity of the catalysts. Studies on cobalt FT catalysts have shown that an addition of small amounts of noble metals such as Re, Ru, Pt and Pb, or their oxides, enhances the FT activity [28, 36, 37]. The promoter is introduced through impregnation, as described above, and its presence has a strong impact on the structure and dispersion of cobalt species [28,36]. The main function of the promoter is to facilitate the reduction of cobalt oxide nanoparticles. As a consequence of this, it enhances the number of active sites for the FT reaction [28,37]. If the promoter is used as an oxide, it is reduced prior to the cobalt oxide and then it plays a catalytic role in the reduction of the cobalt oxides.

Morales et al. have divided the FT promoter elements into two groups, according to their intended functions; structural promoters and electronic promoters. Structural promoters influence the formation and stability of the active phase, while the electronic promoters directly affect the elementary steps involved in each turn-over on the catalysts [37]. They have suggested that the structural promotion may increase the stability and activity of the catalysts without influencing the selectivity. This is due to the fact that the structural promoter provides a higher number of active sites by avoiding formation of cobalt-support compounds or preventing the agglomeration and sintering. Electronic promotion, however, can be described in terms of ligands. The surrounding environment of an active Co site can be altered by the presence of a promoter. This leads to an electronic donation or withdrawal, leading to an increased intrinsic turn-over frequency or change in product selectivity [37].

Rhenium, which is the promoter in the present study, has been regarded as a structural promoter and earlier studies show that Re facilitates the cobalt oxide reducibility via the hydrogen spillover mechanism and, as a consequence, increases the number of active sites [37]. In the spillover mechanism, di-hydrogen molecules are adsorbed on the noble metal promoter and dissociate. Some hydrogen atoms remain attached to the metal phase, whilst others bind to the surface atoms and spill over to the cobalt, either on the support or directly from the noble metal to CoO, depending on the degree of contact between the components [38]. Hilmen et al. [38] applied Temperature Programme Reduction (TPR) to study the mechanisms of Re promotion. The results confirmed that Re promotes the reduction by a spillover mechanism and no direct contact between Re and cobalt was observed. Moreover, Jacobs et al. observed that Re promotes the reduction in the second step from CoO to Co and agreed with the spillover mechanisms. They also applied in situ Extended X-ray Absorption Fine Structure (EXAFS) which showed that direct contact between Re and Co atoms is

present in the catalysts, while Re-Re bonding was not observed. They reported that Re decreases the average cobalt cluster size and also promotes the reduction of small particles interacting with the support [39]. Borg et al. studied the effect of Re in a promoted and un-promoted cobalt catalyst supported on γ-Al_2O_3 and they concluded that Re promoted the reduction of CoO and influence the dispersion of the cobalt catalyst [40]

Effect of water

Water is one of the products in the FT synthesis. Several factors such as the conversion and the reactor system affect the amount of produced water in the reactor [11]. The water can affect the catalysts activity and product distribution and it may deactivate the catalysts [41]. Schanke et al. studied the effect of water on the deactivation of FT cobalt catalysts supported on alumina and suggested that the deactivation of the cobalt catalysts is due to the surface oxidation of a highly dispersed cobalt phase [42]. Hilmen et al. studied the effect of re-oxidation of the cobalt catalysts supported on alumina and observed that Re-promoted and non-promoted samples behaved differently [43]. They concluded that, in the presence of water, the promoted sample was easily re-oxidized. Moreover, they observed that the oxide formed during water treatment was more reducible than the oxide phase formed on the non-promoted catalysts [44]. Deactivation of cobalt based FT catalysts has recently been reviewed by Tsakoumis et al [45] and various deactivation routes have been evaluated [45]. One of the deactivation mechanisms considered in their review is re-oxidation. They reviewed different, contradictory, reports. Some have indicated that surface re-oxidation is a reason for deactivation in the FT reaction. However, some claimed that further reduction of catalysts occurs during FT synthesis [45]. Tsakoumis et al [45] concluded that several parameters, such as the experimental conditions and the catalyst properties, play roles in the experiments and that this is the cause of the wide range of results.

Chapter 3

Transmission Electron Microscopy

A brief overview of TEM was presented in chapter 1. In TEM, the results of the interaction of an electron beam with the object are used to get useful information from the object. Electron interactions with a specimen and the theories behind electron scattering are described briefly in this chapter. Since the sample preparation procedures for TEM are very important, a part of this chapter is, in particular, dedicated describing the TEM sample preparation applied during the work described in this thesis. The general TEM techniques for materials characterization such as Bright Field (BF) imaging, Dark Field (DF) imaging and diffraction are described. Moreover, the advanced TEM techniques of High Resolution TEM (HRTEM), Scanning Transmission Electron Microscopy (STEM), Electron Energy Loss Spectroscopy (EELS) and Energy Dispersive X-Ray Spectroscopy (EDS) are also described. Electron Tomography (ET), which has been widely used in the present work, is described in detail in chapter 4.

3.1 Electron Interaction with the Specimen

In TEM, electrons are accelerated through a high voltage potential into an essentially monochromatic beam and focused by electromagnetic lenses and passed through a thin specimen. The interaction between the high energy electrons and the specimen is used to characterize the specimen. Electrons are strongly scattered by the atoms and the scattered electrons carry much information about the specimen. Figure 3.1 shows schematically the different types of electron beam interactions with the specimen.

Electrons passing through a specimen can be categorized in two groups. The first group contains transmitted and elastically scattered electrons which do not suffer any energy loss during the passing. The second group contains inelastically scattered electrons with energy loss as a result of scattering.

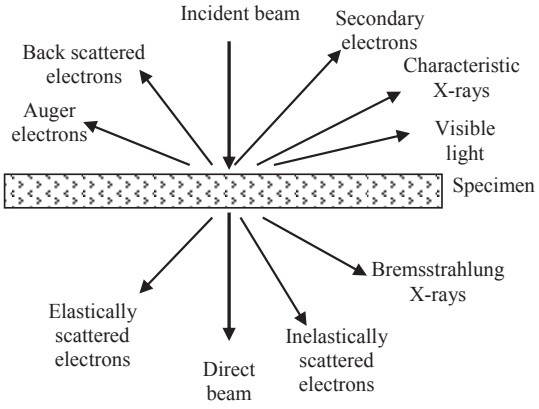

Figure 3.1: Electron beam interaction with specimen [46].

3.1.1 Elastic Scattering

Elastic scattering is the most important process which provides contrast in electron microscopy images. The incident electrons are elastically scattered by either of electrons or nucleus of the specimen atoms. The elastic electron-electron interaction results in low angle scattered electrons while the electrons interact with the Coulomb potential of the nucleus of the specimen atoms scattered to high angle. The scattering cross sections from these elastic scattered electrons are written as [47]:

$$\sigma_{electron} = \pi r_e^2 = \pi(\frac{e^2}{V\theta})^2 \tag{3.1}$$

$$\sigma_{nucleus} = \pi r_n^2 = \pi(\frac{Ze}{V\theta})^2 \tag{3.2}$$

in which the r_e and r_n are the radii of the electron cloud and the nucleus, respectively, e is electron charge, Z is atomic number, V is incident beam energy and θ is scattering angle. As seen in these formulas, $\sigma_{electron}$ is more a function of the incident electron beam, while for $\sigma_{nucleus}$ the Z becomes more important.

The simplest model for the differential cross section of the scattering of the charged particles in the unscreened electrostatic field of a nucleus is Rutherford scattering and can be written as:

$$\frac{d\sigma_n(\theta)}{d\Omega} = \frac{4\gamma^2 Z^2}{a_0^2 q^4} \tag{3.3}$$

where z is atomic number, γ is the relativistic factor equal to $(1-v^2/C^2)^{-1/2}$, a_0 is the Bohr radius equal to $a_0 = \frac{4\pi\varepsilon_0\hbar}{m_0 e^2}$, and q is the magnitude of the scattering vector, which is given by $q=2k_0 sin(\theta/2)$ in which $\hbar k_0=\gamma m_0 v$ is the momentum of the incident electron and $\hbar$ is the momentum transferred to the nucleus [48]. As seen from (3.1), the differential cross-section, $d\sigma/d\Omega$ is angular dependent and defines the flux of electrons scattering into a cone of angle $d\Omega$. It gives a reasonable estimate for electron scattering in high angle annular dark field (HAADF) imaging, but for typical TEM collection angles this equation overestimates the cross section because it ignores the screening effect. This is the effect of the electron cloud bound to the nucleus which reduces the Rutherford cross-section and the amount of scattering. This effect can be taken into account by using the Yukawa potential [48], in which the nucleus potential $V(r)$ is varying exponentially as a function of distance from the nucleus, r:

$$V(r) = (\frac{Ze}{4\pi\varepsilon_0 r})\exp(-r/r_0) \tag{3.4}$$

where e is the electron charge and ε_0 is permittivity of free space and r_0 is the screening radius. By considering the screening effect, the differential cross section is:

$$\frac{d\sigma_n}{d\Omega} = \frac{4\gamma^2}{a_0^2}\left(\frac{Z}{q^2 + r_0^{-2}}\right)^2 \tag{3.5}$$

Equation (3.3) is related to the values chosen for r_0. Lenz [48,49] has suggested an approximation for values of r_0 related to the atomic radius, which is used here:

$$r_0 = a_0 Z^{-1/3} \tag{3.6}$$

Using the Lenz approximation and integrating equation (3.3) over all angles, gives a total elastic cross section with a significantly reduced Z dependence:

$$\sigma_n = \frac{4\pi\gamma^2}{k_0^2} Z^{4/3} \tag{3.7}$$

The values for the cross section using the Lenz method gives inaccurate values for high *Z* elements, but allows a quick estimate of elastic scattering.

3.1.2 Inelastic Scattering

Through the electron interactions with the specimen, electrons have a probability of energy transfer, which is known as inelastic scattering. Inelastic scattered electrons carry information about the specimen which is useful for specimen characterization. For instance, Electron Energy Loss Spectroscopy (EELS) is one of the TEM techniques in which inelastically scattered electrons are detected in order to determine the elements in the specimen. This technique is described later in this chapter.

3.2 TEM Sample Preparation

Different techniques can be applied to prepare proper TEM samples. In this research the main samples were originally in powder form and only the two applied TEM sample preparation methods, dispersion and ultramicrotomy, are described.

3.2.1 Dispersion

In the dispersion method, small amounts of a crushed powder (catalyst) are suspended in a liquid such as ethanol. Then a drop of the suspension is dispersed on a TEM grid and left to dry. The choice of grid depends on the type of experiment. The most common TEM grids are copper with 200 or 300 bar/inch mesh that supports a holy carbon film [50].

The dispersed sample can also be prepared by dispersing the crushed powder directly onto a grid without using any liquid, which is called dry dispersion. The samples analysed in in-situ experiments and inert transfer, in this study (chapter 5 and 6) were mostly prepared by dry dispersion. The reason for choosing this sample preparation method for inert transfer analysis was to avoid any degradation of the glove box environment.

3.2.2 Ultramicrotomy

In the ultramicrotomy method, a very thin slice of material is cut by an instrument that contains two main parts, a mechanical mechanism and a blade. There are different blades, and

their application depends on the specimen and the desired thickness. Steel blades are used to prepare sections of animal and plant tissues for light microscopy studies. Glass knives are used to slice sections for both light microscopy and electron microscopy and they are also used for initial shaping of the sample before using a diamond blade. Diamond blades are generally used to slice all types of TEM samples including biological, polymer and hard materials. Diamond knives are formed from a single diamond crystal. The blades have a wedge so that the cutting edge is only a few atoms thick. Figure 3.2 shows the ultramicrotomy instrument and a type of diamond blade, which is used for the catalysts sample preparation.

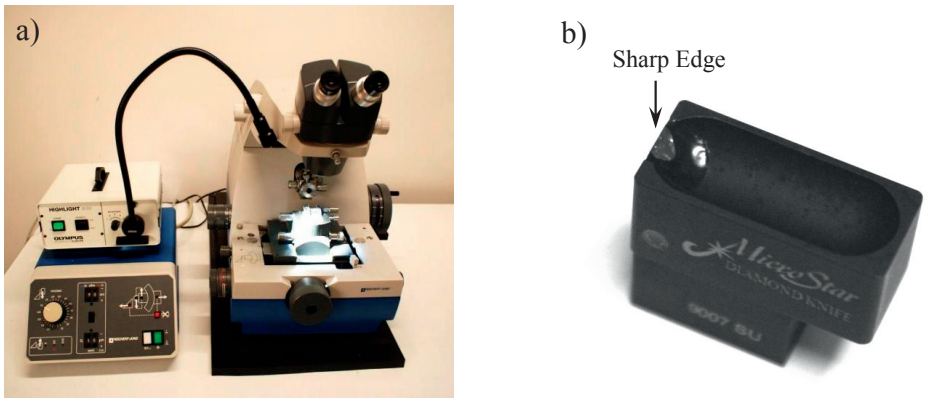

Figure 3.2: a) Ultramicrotomy instrument, b) Diamond blade

In order to prepare microtomed slices, a powder sample is embedded in a mixture of 15 part epoxy resin and 2 part hardener in a special capsule with truncated pyramid shape 1*1 mm at the face and left overnight. After removing the plastic capsule with a lab scalpel, the block is placed in a sample holder. The density of the catalysts is high at the tip. Glasses knives are used to trim the edges around the tip of the block (Figure 3.3). It is better to remove as much surrounding resin as possible. The knife glasses are made by cutting the glass bars (406 mm×25.4 mm×8mm) by glass knife maker. After making the sharp and fine edges, diamond blades are used to cut fine slices of the sample. The standard diamond knives, boat style, have a very small oval trough, which is filled with distilled water. This catches the thin slices which can be collected on a carbon grid (Figure 3.4).

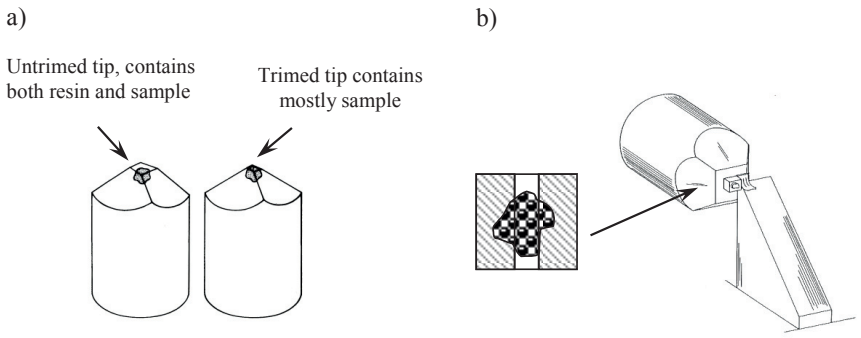

Figure 3.3: a) The microtomy block before and after trimming, b) application of the glass knife to trim the edges of the tip [50].

Figure 3.4: Floated microtomed slices are collected on TEM grid, which is handled by tweezers [50].

Table 3.1. Thickness of floated microtomed slices in the trough based on their colour [51].

Thickness (nm)	Colour
50	Gray
64-92	Silver
95-128	Gold
135-166	Reddish gold
200	Purple
239	Sky-blue
264	Yellow
278	Yellow-Green

The thickness of each cut can vary between 50-250 nm, however, thin slices are favourable for TEM analysis [51]. The thickness of the obtained sections through cutting can be estimated using the colour of floating slices in the trough and matching them with the available colour classifications listed in Table 3.1 [51].

3.3 General TEM Study

The general and advanced TEM techniques, which were applied in the present research, are described as follows.

3.3.1 Bright Field and Dark Field Imaging

Presence of a regular crystal specimen causes a phase difference between electrons scattered from atoms in a regular lattice and results in destructive and constructive interference. These destructive and constructive interferences produce minima and maxima in the profile intensity. The condition to fulfil the constructive interference from successive crystallographic planes can be described by Bragg's law:

$$\lambda = 2d \sin\theta_B \tag{3.8}$$

where λ is the wave length of the incident electrons, d is the distance between atomic planes and θ_B is the scattering angle or Bragg angle.

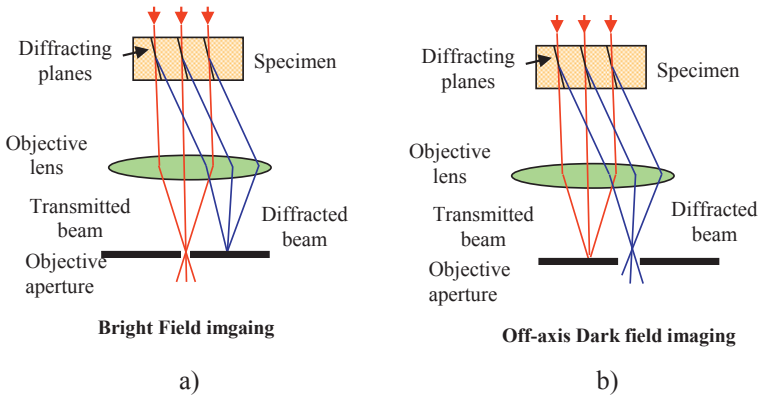

Figure 3.5: Ray diagram illustrating bright field (a) and dark field (b) imaging.

In the Bright Field (BF) mode of the TEM, an objective aperture is positioned in the back focal plane of the objective lens and allows only the direct beam to pass through it. Therefore, both mass thickness and diffraction contrast contribute to form the image, by removal electrons that are scattered off the optic axis. In BF images, thick areas and in zone axis crystalline areas appear dark and the thin and weakly diffracting areas appear bright.

In Dark Field (DF) mode, the electron beam is tilted in a way that one of the diffracting spots is passed through the objective aperture to transfer the information and form the image. The DF images have strong contrast. Figure 3.5 shows the mechanisms of BF and DF imaging in TEM and Figures 3.6a and c show an example of BF and DF images of cobalt oxide aggregate. The dark field image was produced by a (111) diffraction spot.

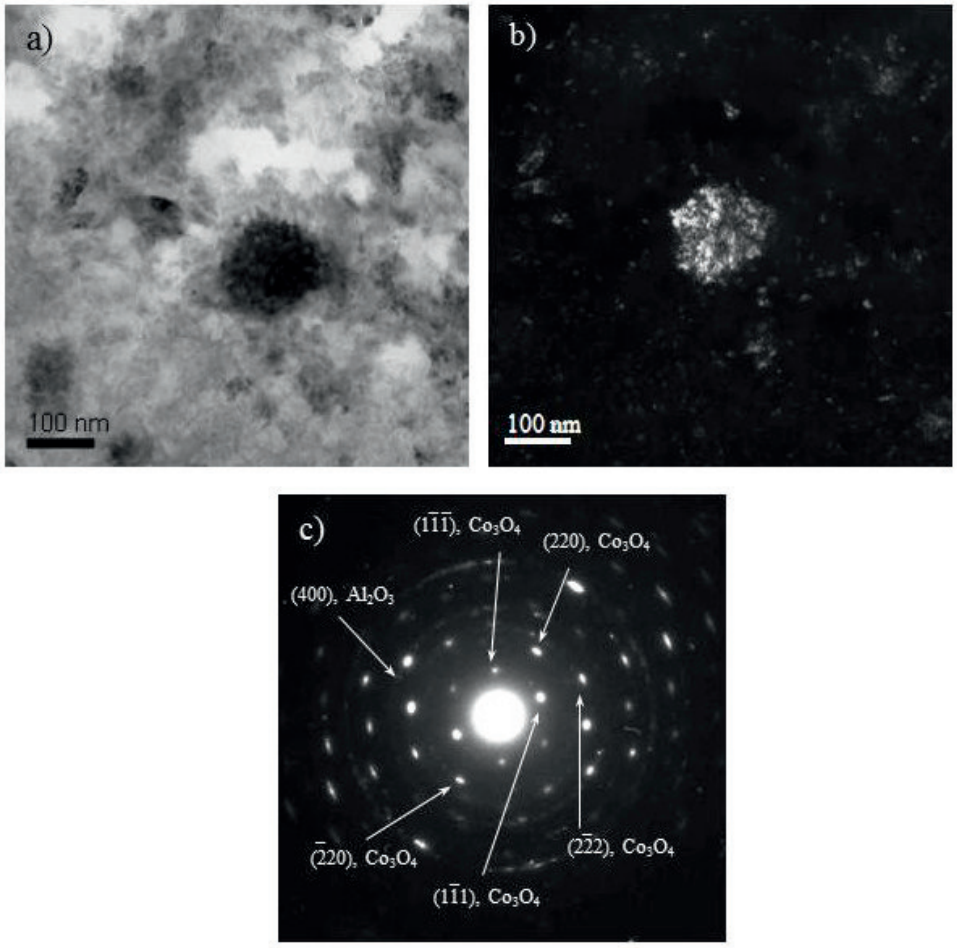

Figure 3.6: a) Bright field image, b) dark field image produced by (1$\bar{1}$1) reflection of Co_3O_4, c) diffraction pattern of cobalt oxide aggregate supported on γ-Al_2O_3, which is in [110] zone axis, The regular intense spots are from Co_3O_4 and the weak rings are from alumina.

3.3.2 Diffraction

Electron diffraction is a powerful tool to study the structure of the crystalline materials. The diffraction pattern is obtained in the back focal plane of the objective lens. Figure 3.7 shows a schematic view of the TEM column in diffraction mode compared to the imaging mode. To obtain the diffraction pattern from a particular part of the specimen, Selected Area Diffraction (SAD) apertures can be used. These apertures are located below the objective plane at a lower cross-over in the electron optical system. Figure 3.7 shows the position of the SAD apertures which goes into the first intermediate image plane. The effect of the SAD aperture is to block the whole electron beam except from the fraction which is passing through the aperture.

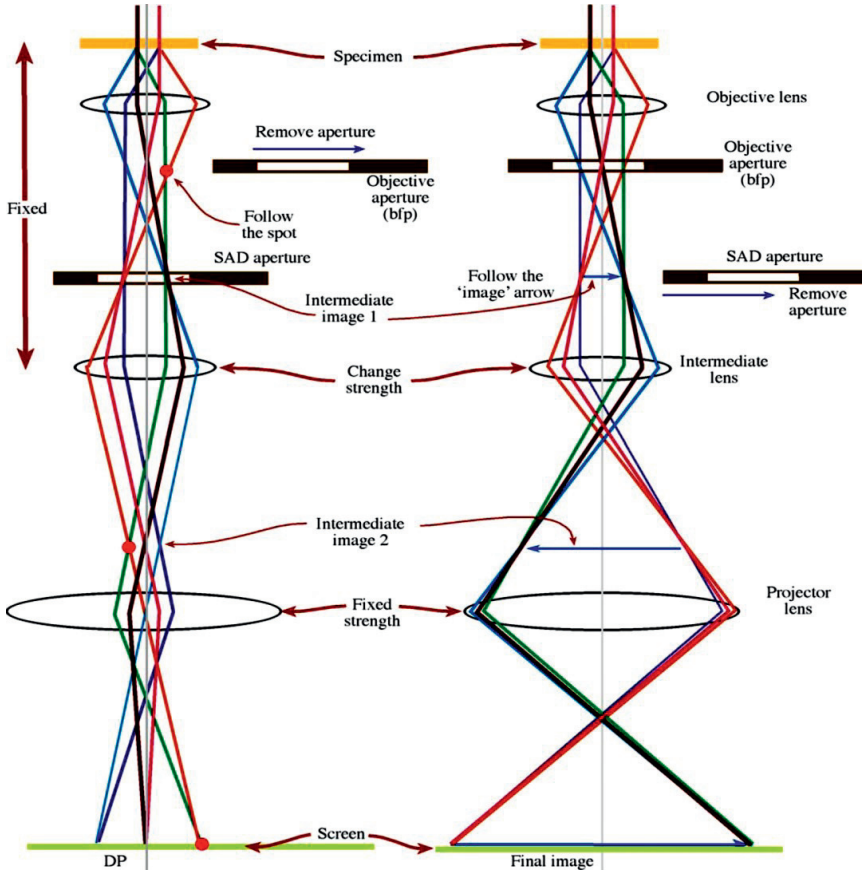

Figure 3.7: Schematic view of TEM in diffraction and imaging mode [46].

In diffraction patterns the strong intensities which satisfy the Bragg condition are known as Bragg peaks. Figure 3.6c shows the diffraction pattern from Co_3O_4 aggregates supported on alumina. Rings show the poor crystallinity alumina phase and the dots show the Co_3O_4 phase. Systematic rows of bright dots are related to a zone axis diffraction pattern in the Co_3O_4 aggregate. These phases are determined through the known d values for the atomic planes of different phases, as measured by XRD. The related tables for this study are presented in Appendix A.

3.3.3 High Resolution TEM

High Resolution TEM (HRTEM) mode allows imaging the structure of the specimen at the atomic scale. Atomic spacings can be measured directly in the images and the structure of the material can be determined.

In the HRTEM, the microscope transforms each point, (r), on the specimen into an extended region of the final image, g(r) [5]. The specimen is described by a specimen function, f(r), and the extended image is described as [5]:

$$\begin{aligned} g(r) &= \int f(r')h(r-r')dr' \\ &= f(r) \otimes h(r) \end{aligned} \tag{3.9}$$

In this formula, h(r) describes how a point spreads into a disk and it is known as point-spread function [5].
Taking the Fourier transform of this formula gives:

$$G(u) = F(u)H(u) \tag{3.10}$$

H(u) is Contrast Transfer Function (CTF) and is product of three parts:

$$H(u) = A(u)E(u)B(u) \tag{3.11}$$

A(u) is the aperture function and it relates to the applied objective aperture which cuts off spatial frequencies (u) greater than the aperture size [5]. E(u) is envelope function which shows the attenuation of the wave and is the property of the lens itself. B(u) is aberration function and is expressed as [5]:

$$B(u) = \exp(-i\chi(u)) \tag{3.12}$$

and the term χ(u) is written as:

$$\chi(u) = \pi\Delta f \lambda u^2 + \frac{1}{2}\pi C_s \lambda^3 u^4 \tag{3.13}$$

in which Δf is known as overfocus. This formula shows that the resolution in HRTEM images is influenced by C_s (the lens quality), λ (accelerating voltage), u (the spatial frequency) and Δf (the selected value of focus to form the image).

In order to obtain good quality of the images, several conditions should be fulfilled. First it is necessary to align the microscope accurately. Since the lenses aberration has significant influence on the HRTEM images, both focus and astigmatism should be adjusted carefully. Secondly, the sample should be as thin as possible and ideally tilted to the crystal zone axis orientation in which atomic planes are parallel to the electron beam [52]. Figure 3.8 shows an example of HRTEM image of cobalt oxide supported on γ-Al_2O_3. Image (a) in this figure shows the overview of the material at low magnification and (b) shows a cobalt nanoparticle indicated by the arrow in Fig 3.8a. In (b) fringes show *d* value of 1.94 Å which corresponds to the (101) atomic planes of hcp cobalt.

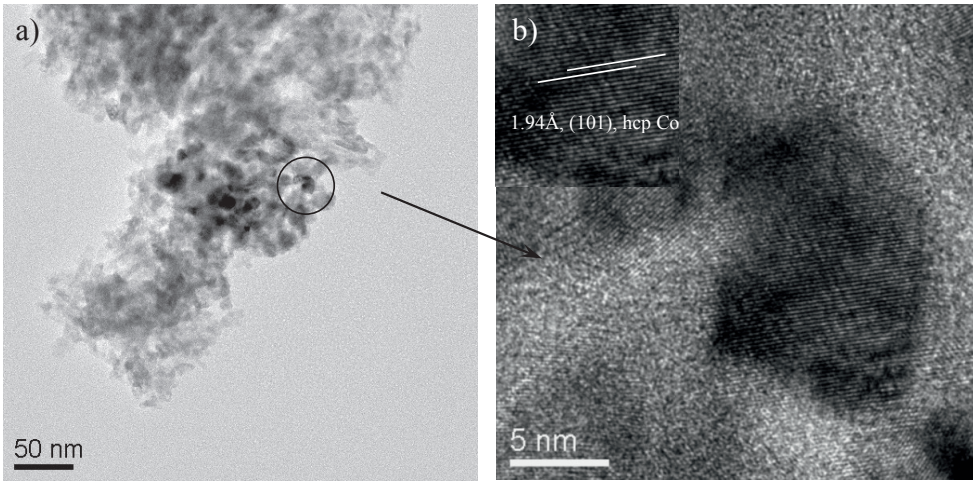

Figure 3.8: a) TEM image of 20%Co/0.5%Re/γ-Al_2O_3, b) HRTEM image of cobalt nanoparticles.

3.3.4 Scanning Transmission Electron Microscopy

Scanning Transmission Electron Microscopy (STEM) is a valuable technique for characterization of nanostructures. With the small probe used, we have also the ability to

measure elemental composition. The basic principles of image formation in STEM are different than those in TEM. In STEM, the electron beam is focused by the condenser lenses to a point on the specimen and the focused beam scanned across the sample by scanning coils. The STEM images are formed by collecting desired signals by appropriate detectors [46,53]. A variety of signals can be detected as a function of probe position. Figure 3.9 shows the schematic drawing of the STEM and possible detectors.

We consider three main imaging modes in STEM and the contrast in each mode depends on the angular range of the detector. In Bright Field (BF) a detector includes the transmitted beam so that holes in the sample appear bright in the formed images. In Dark Field (DF), an annular detector with small inner angle cut off is applied to collect the scattered electrons. The An Annular Dark Field (ADF) detector excludes the transmitted beam and therefore holes in the sample appear dark in DF images. The electrons that form BF and ADF images are scattered to low angles and contrast arises primarily from the Bragg diffraction, if the specimen is crystalline.

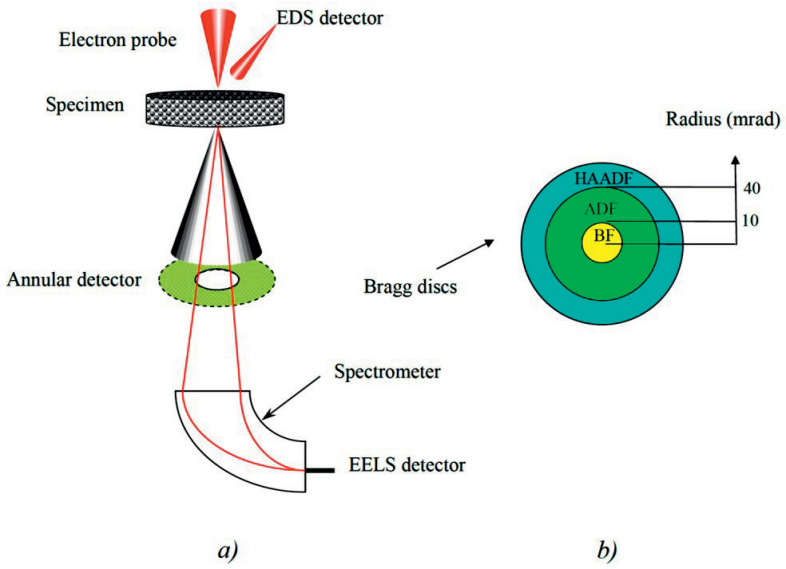

Figure 3.9: a) Schematic drawing of STEM and b) STEM detector geometry.

The third STEM imaging mode is High Angle Annular Dark Field (HAADF) imaging, in which electrons scattered elastically to high angles (75-150 mrad. at 200KV) are detected by an annular detector with higher inner-angle to form the images. The contrast in the HAADF images is sensitive to the atomic number (z) and it is approximately proportion to $Z^{3/2}$

[54,55,56]. Figure 3.10 shows examples of STEM images from two different types of catalysts. Figure 3.10a is a STEM image of Ni on hydrotalcite substrate in which the bright particles are Ni. Figure 3.10b is a STEM image of a microtomed cobalt oxide supported on α-Al_2O_3 catalyst.

An advantage of STEM imaging compared with TEM is that the magnification is not controlled by the lenses of the TEM but by changing scan dimension on the specimen. Therefore, the aberrations in the post specimen lenses do not influence the image quality, although the probe resolution is limited by the condenser lens aberrations. For example, if the scanned area on the specimen is 10μm × 10μm, and the resulted image has an area of 10^5μm $\times 10^5$μm, then the magnification is 10^4 times.

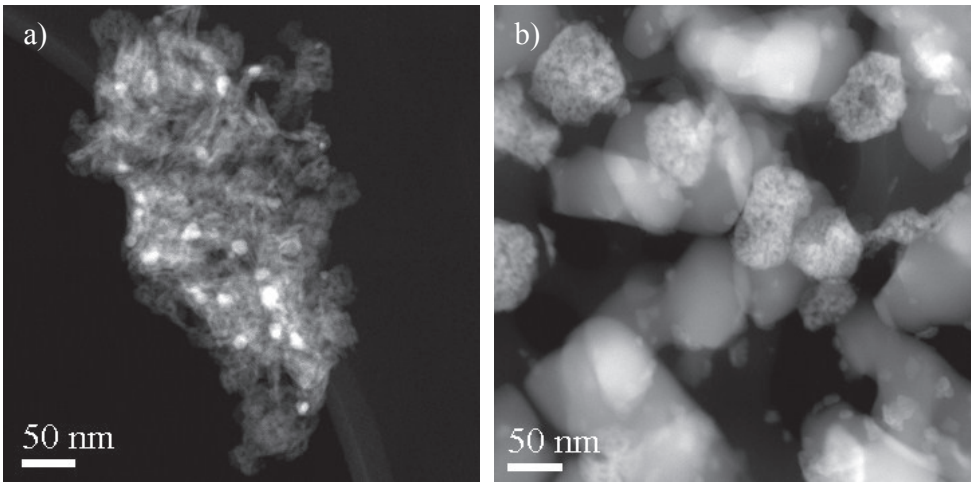

Figure 3.10: STEM images of a) The reduced 12%Ni/HT and b) the microtomed 12%Co/0.5%Re/α-Al_2O_3

Ronchigram

The beam alignment procedure in both analytical and high resolution STEM is important in order to obtain the highest possible resolution in the images. Often the alignment procedure in STEM is done by using the Ronchigram, or shadow image, around Scherzer defocus [57]. One of the involved parameters in the formation of Ronchigram is the spherical aberration. The apparent features of a Ronchigram are dependent on the structure of the sample. The intensity in the Ronchigram is:

$$I_R(K) = \left|\Phi(K) * P(K)\right|^2 \tag{3.14}$$

where $\Phi(K)$ is the object transmission function, K denotes the coordinates in reciprocal space, * represents a convolution integral and $P(K)$ is the probe function. $P(K)$ is determined by:

$$P(K) = A(K)\exp(i\chi(K)) \tag{3.15}$$

where $A(K)$ is the aperture function and $\chi(K)$ is the wave aberration function [58,59]. Wave aberration information, which is related to the alignment, is present in the Ronchigram. Figure 3.11 shows the Ronchigram. The apparent shape of the Ronchigram can be used to adjust the condenser lens astigmatism. The rings of the Ronchigram are circularly symmetric for correct astigmatism alignment. The Ronchigram also defines the coma-free axis, in which the correct size and position of the condenser aperture is determined [57].

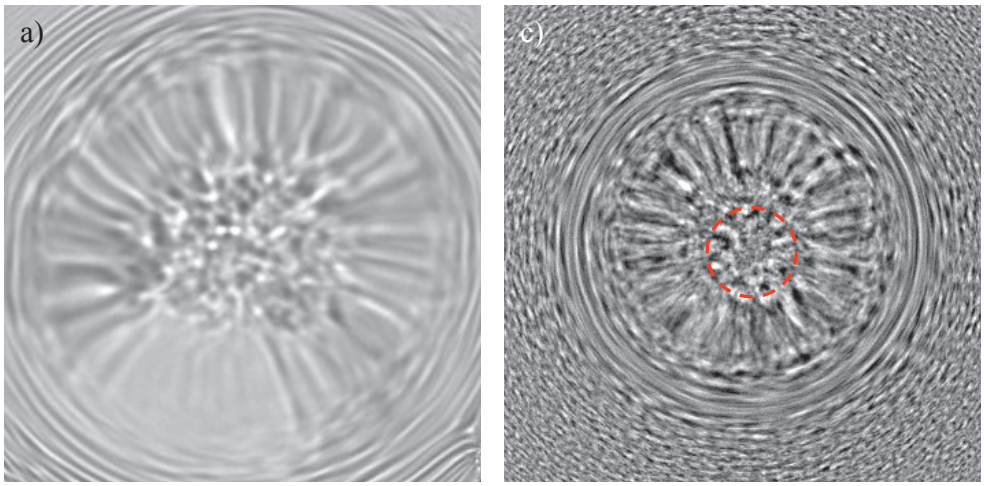

Figure 3.11: a) Ronchigram (small underfocus), from an amorphous specimen in analytical STEM mode, which is used to align the condenser aperture. b) Ronchigram (small underfocus), in HR-STEM mode, the dashed line shows the proper position of the condenser aperture.

In Fig. 3.11 the circle marks the position of the last spherical aberration ring. Application of a large condenser aperture forms a probe with higher convergence angle and its useable size is limited by spherical aberration. A small aperture results in a lower convergence angle. The optimum condition for the convergence angle is to position the aperture inside the last spherical aberration ring [60].

High Resolution STEM

In high resolution STEM (HR-STEM), the probe size is much finer and accurate alignment is needed [53,61]. The size of the probe is dependent on the spherical aberration coefficient of

the lenses forming the probe [62]. As explained above, a Ronchigram can be used to achieve the optimized electron probe [57]. In this study, high resolution STEM was applied to study the distribution of the promoter in the catalysts. Figure 3.12 shows an example of HR-STEM in which the experiments were performed in a probe aberration corrected microscope.

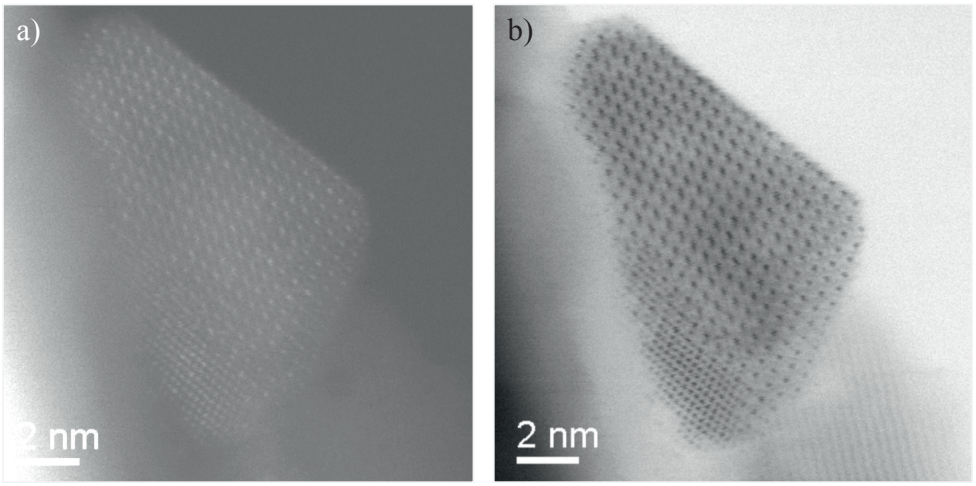

Figure 3.12: a) HAADF-STEM and b) corresponding BF-STEM image of a cobalt nanoparticle supported on α-Al_2O_3, taken at CEN-DTU on a Titan analytical 80-300 ST probe corrected instrument.

3.3.5 Electron Energy Loss Spectroscopy

Inelastically, scattered electrons which lose energy through interaction with the specimen, can give valuable information about the composition of the sample and other information about chemical and electronic properties. With Electron Energy Loss Spectroscopy (EELS), the energy spectrum of electrons can be analysed. This is done by an electron spectrometer and the amount of energy loss can be measured and interpreted in terms of what causes the energy loss. Inelastic interactions are [48,64]:

1- Plasmon excitations (collective excitations of valence electrons): less than 30 eV

2- Phonon excitations (lattice vibrations): less than 0.1 eV

3- Inter-band transition: less than 10 eV

4- Inner-shell electron excitation (core electron excitation): more than 13 eV

5- Excitation of free electron (secondary electron emission): less than 50 eV (background of spectrum)

6- Bremsstrahlung (emission of continuous X-rays): background of spectrum

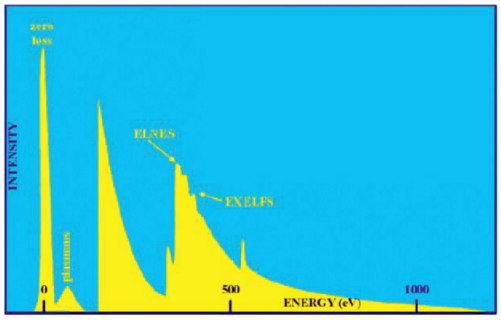

Figure 3.13: Schematic EELS spectrum showing main features [63].

Figure 3.13 shows a schematic representation of an EELS spectrum indicating the main features. The sharpest peak at the left of the spectrum is the zero loss which appears at 0 eV and its energy corresponds to the incident electron energy. In this schematic, the intensity of zero loss peak is shifted to have full peaks at the same spectrum. Near the zero loss peak, in the range of 15-60 eV are the Plasmon peaks, which results from plasmon excitations. Peaks which appear in the higher energy loss region such as Energy Loss Near Edge Structure (ELNES) and Extended Energy Loss Fine Structure (EXELFS) are related to the inner-shell excitation of the elements of the sample. The elements can be recognized from the energy values and intensity distribution [48,64]. Due to having better signal at lower energies, EELS is a suitable technique for characterization of light elements.

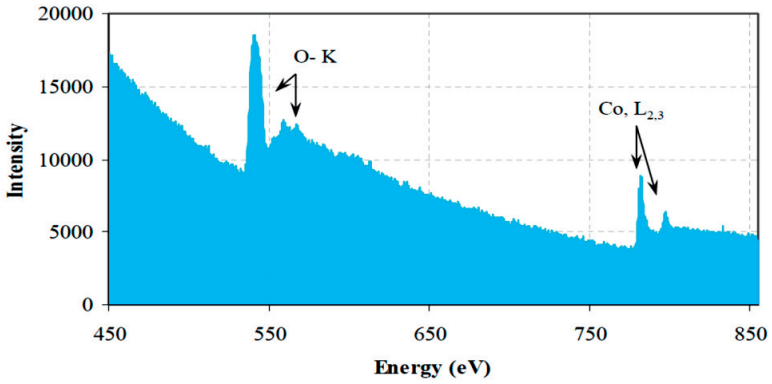

Figure 3.14: EELS spectrum of the cobalt oxide supported on alumina.

In this study EELS was used in both TEM and STEM mode to investigate the reduction procedure of the cobalt oxide particles. Fig. 3.14 shows a typical analysis, where peaks at energy 580 eV correspond to the O-K edge and peaks at 780 eV correspond to the Co-$L_{2,3}$ edge.

3.3.6 Energy Dispersive X-ray Spectroscopy

Energy dispersive X-ray Spectroscopy (EDS) is an analytical technique which gives the elemental composition of the sample. The electron beam causes an electron transition from an inner-shell to a higher energy level which leaves a hole in the inner-shell. When this hole is filled by an electron from a higher energy level, a characteristic X-ray with energy difference between those two energy levels is emitted. The characteristic X-rays have specific energy corresponding to each element. Therefore, the element can be identified from the peak energy and its level in a compound can be qualified from the intensity of the peak [46,64]. It is worth noting that the characteristic X-ray emission increases with increasing atomic number and it is therefore more useful for heavy elements. Figure 3.9 shows schematically the position of EDS detector in the TEM instrument just above the sample.

EDS analysis can be performed from a point or a selected area of the sample. Alternatively, a spectrum map can be acquired in which a spectrum is acquired from each pixel of a STEM map and resulting data can be processed to produce a composition map of the sample.

3.4 Microscope Facilities

The applied electron microscopes in the present work are briefly described in the following.

JEOL 2010F

A JEOL 2010F microscope at NTNU has been used extensively in this study for STEM, electron tomography, HRTEM and EELS analysis. It has a field emission gun source and is operated at 200 kV (Fig. 3.14a). The microscope point resolution is 0.21 nm and the information limit is 0.13 nm.

This microscope is equipped with STEM BF and ADF detectors. In all the STEM experiments in the present study, the ADF detector was used with camera lengths of 25 cm and 20 cm in both analytical and high resolution modes. With these camera lengths the inner and outer angles of the detector are in the range of 28-76 mrad and 36-96 mrad, respectively. The probe size was 0.7 nm with 70 mm condenser aperture size in analytical mode and 20 mm aperture size in high resolution mode. EELS experiments were carried out in both TEM and STEM mode using the GIF camera. EDS experiments were performed with an INCA EDS system from Oxford Instruments.

Philips CM30

This microscope is a 300 kV analytical TEM/STEM with a LaB_6 source (Fig. 3.14c) and located at NTNU. This instrument has been used for bright field, dark field and diffraction studies in this work. The microscope was operated at 200 kV and at this voltage has a point resolution of 0.27 nm.

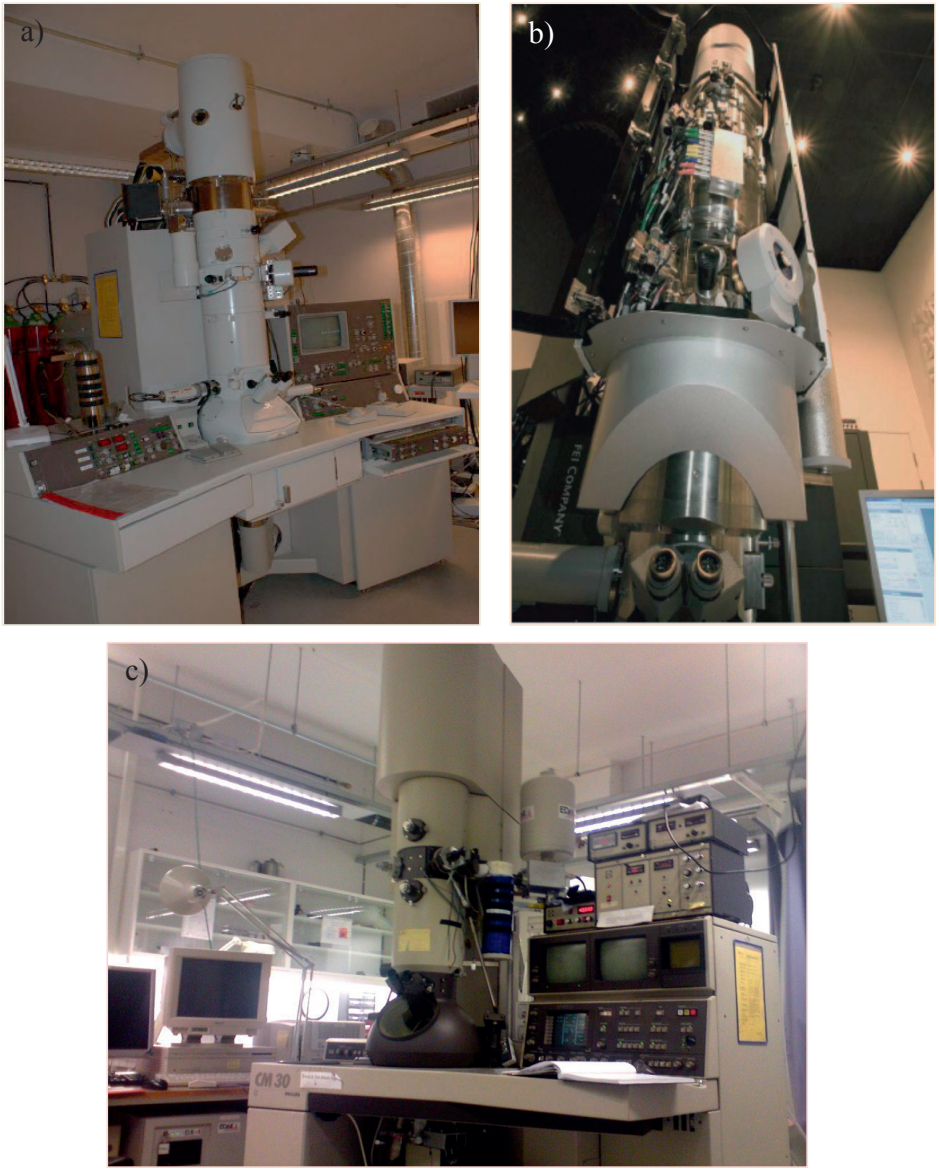

Figure 3.14: Transmission electron microscopes used in this study, a) JEOL 2010F (NTNU), B) Titan analytical probe corrected TEM (CEN), c) PHILIPS CM30 (NTNU).

FEI Titan Analytical 80-300ST-TEM

The Titan analytical is a 300 kV electron microscope equipped with a field emission gun, monochromator and a spherical aberration corrector on the condenser system. (Figure 3.14b) In this microscope, the TEM information limit is less than 0.1 nm and STEM resolution is about 0.08 nm. The microscope is probe corrected and, due to its small probe size, it is suitable for high resolution STEM and chemical mapping down to the atomic level. The mapping analysis is done by EDS with an energy resolution of 136 eV. This microscope is located at Center for Electron Nanoscopy (CEN) at Technical University of Denmark (DTU).

Titan E-Cell 80-300ST-TEM

This is an image C_s corrected transmission electron microscope with specialized vacuum system that is dedicated to in-situ studies and is located at CEN at DTU. More details about this microscope are given in chapter 5.

Chapter 4

Electron Tomography

In the area of science and technology, different techniques are used to characterise materials. Electron Tomography (ET) is an advanced TEM technique in which the structural information of nano scale materials is provided in three dimensions [65]. The word "*tomography"* literally means the visualization of slices [66].

With transmission electron microscopy (TEM), as described in the previous chapter, images of thin electron transparent objects are made in order to determine the materials properties. These images are two dimensional projections, but many materials have three dimensional structures at the nanometre scale and some information is lost in the TEM analysis. Electron tomography is a procedure by which a three dimensional structure can be reconstructed from a series of images taken at regular tilt intervals. [65,66,67].

Electron tomography enables the characterisation of complicated structures at nanometre scale resolution. The principles of electron tomography are described in this chapter and the focus is on the application of Scanning TEM (STEM) tomography for catalyst materials.

4.1 Theory Behind Electron Tomography

The physics of tomography, the basic mathematics formulations and image processing are described in the following.

4.1.1 The Radon Transform

The basic formulation of tomography was first described by Ron Bracewell in 1956 [68]. However, its foundation was outlined by Johann Radon in 1917 [69]. The Radon theory states

that a three dimensional object can be reconstructed by two dimensional projections. To describe the Radon transform, an object D described by *f(x,y)* is considered. *f(x,y)* here describes the variable density of the object. *f(x,y)* is an unknown function, where a parallel beam through the region of the object carries the information from the object and the aim is to know the object through this function.

In mathematics, the correspondent transform of line to numbers is given by the line integral over the object:

$$\begin{array}{c} L \rightarrow \int_L f(x,y) \\ \uparrow \qquad \uparrow \\ lines \quad numbers \end{array} \tag{4.1}$$

This correspondence shows the transformation of *f(x,y)* which is evaluated through all possible lines *L*. In the other word this transform is defined as the mapping of the function *f(x,y)*, by the projection, or line integral, through f , along all possible lines *L*:

$$\hat{f} = R_f(L) = \int_L f(x,y)ds, \tag{4.2}$$

where *ds* is the unit length of *L* [65,69]. Equation (4.2) is called the Radon transform and inverting the Radon transform gives the reconstruction of the object. Before inverting the Radon transform, it should be written in a particular coordinate system. The polar coordinate system seems suitable for this structure because it covers all possible lines. In this system each line through the regime is determined by *l,* which is the distance from the origin, and θ, which is the angle with the horizontal axis. Figure 4.1 shows the geometry.

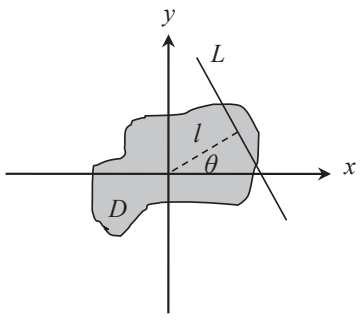

Figure 4.1: Line *L* through the object *D*.

The line integral of the object, Eq. (4.2), depends on the values of l and θ. Therefore, Eq. (4.2) can be rewritten as:

$$\hat{f}(l,\theta) = R_f(L) = \int_L f(x,y)ds, \tag{4.3}$$

If $\hat{f}(l,\theta)$ is known for all l and θ, then $\hat{f}(l,\theta)$ is the two dimensional Radon transform of $f(x,y)$. When $\hat{f}(l,\theta)$ is known only for certain values of l and θ, it is a sample of the Radon transform.

Using polar coordinates instead of Cartesian coordinates gives:

$$\begin{aligned} r &= \sqrt{x^2 + y^2} \\ \tan\varphi &= \frac{y}{x} \end{aligned} \tag{4.4}$$

Therefore, $f(x,y)$ which is a physical function at the geometrical point is described by $f(r,\varphi)$.

A set of coordinates l and z are also defined for easier understanding, for which l is perpendicular and z is parallel to the transform direction defined by the integral L (Fig. 4.2). The Radon transform converts the $f(r,\varphi)$ to $f(l,\theta)$ in Radon space. The Radon transform of $f(r,\varphi)$ is:

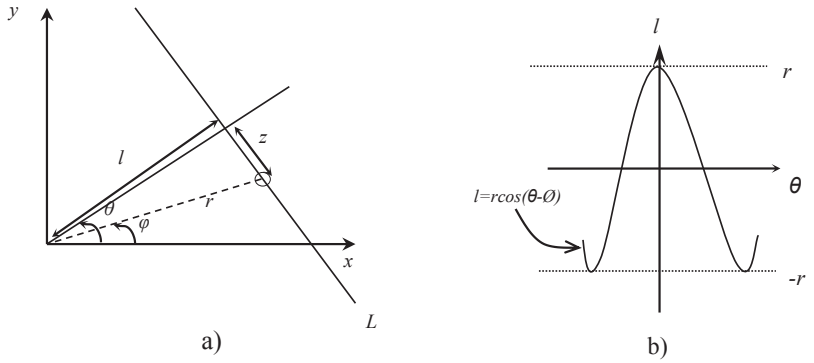

Figure 4.2: a) The relationship between real space *(r, φ)* and Radon space *(l,θ)*, b) The point in real space with the open circle is transformed to a line in Radon space with the equation of $l = rcos(\theta - \phi)$.

$$Rf(l,\theta)=\int_{-\infty}^{+\infty} f(\sqrt{l^2+z^2},\theta-\tan^{-1}(\frac{z}{l}))dz \qquad \text{if } l\neq 0$$

$$Rf(0,\theta)=\int_{-\infty}^{+\infty} f(z,\theta-\frac{\pi}{2})dz \qquad \text{if } l=0 \tag{4.5}$$

A point in real space, *(x,y)* or *(r,φ),* is a line in Radon space *(l,θ)* with the equation of $l=rCos(\theta-\phi)$ and a single projection of an object which is equivalent with a discrete sampling of the Radon transform produces a line at constant θ in Radon space [67]. Now the Radon transform is inverted to see the relation between this transform and the reconstruction of the object. Before that, it is worth mentioning that in this study only the parallel beam is considered and by definition a parallel beam has a common unit vector with different distances from the origin. Considering Fig. 4.1, line *L* in normal form is given by:

$$L=xcos\theta+ysin\theta \tag{4.6}$$

Now Eq. (4.3) is used to evaluate the $\int_L f(x,y)$ via a delta function. The property of the delta function is that, it gives zero for offline and infinity for online values and under integral it restricts the *f(x,y)* by the line. Then it gives:

$$\hat{f}(l,\theta)=R_L(f)=\int_{-\infty}^{\infty}\int_{-\infty}^{\infty} f(x,y)\delta(l-xCos\theta-ySin\theta)dxdy \tag{4.7}$$

Eq. (4.7) computes all values of $R_L(f)$ as a function of *l*. Therefore, taking one dimensional Fourier transform of this with respect to the *l* gives the inversion of the Radon transform. Inverting the Radon transform gives:

$$\begin{aligned} FR_f(l,\theta)&=\int_{-\infty}^{\infty} e^{-2\pi irl}R_f(l,\theta)dl \\ &=\int_{-\infty}^{\infty} e^{-2\pi irl}\left(\int_{-\infty}^{\infty}\int_{-\infty}^{\infty} f(x,y)\delta(l-xCos\theta-ySin\theta)dxdy\right)dl \\ &=\int_{-\infty}^{\infty}\int_{-\infty}^{\infty} f(x,y)\left(\int_{-\infty}^{\infty} e^{-2\pi irl}\delta(l-xCos\theta-ySin\theta)dl\right)dxdy \end{aligned} \tag{4.8}$$

The integral inside the parenthesis in the equation (4.8) gives:

$$\begin{aligned}&\int_{-\infty}^{\infty} e^{-2\pi irl}\delta(l - xCos\theta - ySin\theta)dl \\ &= e^{-2\pi ir(xCos\theta + ySin\theta)} \\ &= e^{-2\pi i(xrCos\theta + yrSin\theta)}\end{aligned} \tag{4.9}$$

To make it more simple two new variables are introduced here:

$$\begin{aligned}\xi_1 &= rCos\theta \\ \xi_2 &= rSin\theta\end{aligned} \tag{4.10}$$

Inserting the new variables in Eq. (4.9) and then the results in the Eq. (4.8), it gives:

$$\begin{aligned}FR_f(l,\theta) &= \int_{-\infty}^{\infty}\int_{-\infty}^{\infty} f(x,y)e^{-2\pi i(x\xi_1, y\xi_2)}dxdy \\ &= F^2 f(x,y) = G(\xi_1,\xi_2)\end{aligned} \tag{4.11}$$

Eq. (4.11) gives the two dimensional Fourier transform of *f(x,y)*, which is $G(\xi_1,\xi_2)$. It means to get *f(x,y)*, we need to do the inverse Fourier transform of $G(\xi_1,\xi_2)$:

$$f(x,y) = FT^{-1}G(\xi_1,\xi_2) \tag{4.12}$$

The inverse Radon transform is the basic principle of reconstruction algorithms and a sufficient number of projections can provide the reconstructed structure of the object. However, the Radon inversion formula relies on a complete and continuously sampled Radon space and any experimental projections will be discrete and therefore, their inversion will also be imperfect. One of the challenges with reconstruction algorithms is to achieve the best reconstruction of the object from experimental data.

4.1.2 *The Central Slice Theorem and Fourier Space Reconstruction*

The central Slice theorem, or projection slice theorem, states that the Fourier transform of a two dimensional projection of a three dimensional object corresponds to the central section of the three dimensional Fourier transform of the object [65,67,70]. For a better understanding of this theorem, it can first be described for a two dimensional object. The projection slice theorem in two dimensions, and in the form of operators, states that the results of the following two calculations are equal.

$$F_1 P = S F_2 \tag{4.13}$$

where F_1 and F_2 are one and two dimensional Fourier transform operators, respectively. P_1 is the projection operator which projects a two dimensional function onto a one dimensional line and S is a slice operator which extracts a one dimensional central slice from a function.
The projection of $f(x,y)$ on to the x axis is $p(x)$ where:

$$p(x) = \int_{-\infty}^{\infty} f(x,y)dy \tag{4.14}$$

The Fourier transform of $f(x,y)$ is:

$$F(u,v) = \int_{-\infty}^{\infty}\int_{-\infty}^{\infty} f(x,y)e^{-2\pi i(xu+yv)}dxdy \tag{4.15}$$

The slice is then $S(u)$:

$$\begin{aligned} S(u) = F(u,0) &= \int_{-\infty}^{\infty}\int_{-\infty}^{\infty} f(x,y)e^{-2\pi ixu}dxdy \\ &= \int_{-\infty}^{\infty}[\int_{-\infty}^{\infty} f(x,y)dy]e^{-2\pi ixu}dx \\ &= \int_{-\infty}^{\infty} p(x)e^{-2\pi ixu}dx = Fp(x) \end{aligned} \tag{4.16}$$

This formula can be extended easily to higher dimensions. Eq. (4.17) is another illustration of central slice theorem based on the Radon transform:

$$F_2 f = F_1 R f = F_1 \hat{f}, \tag{4.17}$$

where $\hat{f}$ is the Radon transform operator and F_1 and F_2 are one dimensional and two dimensional Fourier transforms, respectively.
Note that an intermediate interpolation is required between rectangular and polar coordinates in Fourier space since:

$$F_2 f(x,y) = \tilde{f}(u,v) \tag{4.18}$$

and

$$F_1 \hat{f}(l,\theta) = \tilde{\hat{f}}(k,\alpha) \tag{4.19}$$

Which after interpolation gives $k = \sqrt{u^2 + v^2}$ and $\alpha = \tan^{-1}\left(\frac{u}{v}\right)$. This result was first obtained
by Bracewell (1956) and applied in Radio astronomy [69]. The relationship between Fourier Transform and Radon transform is shown in Figure 4.3.

In reconstructions based on Radon transforms, the object is transformed to Radon space and then the Fourier transform of the transformed object provides sufficient data to reconstruct the object. It means that a series of projections at different tilt angles construct the object's Fourier transform and each projection corresponds to the part of object's Fourier transform.

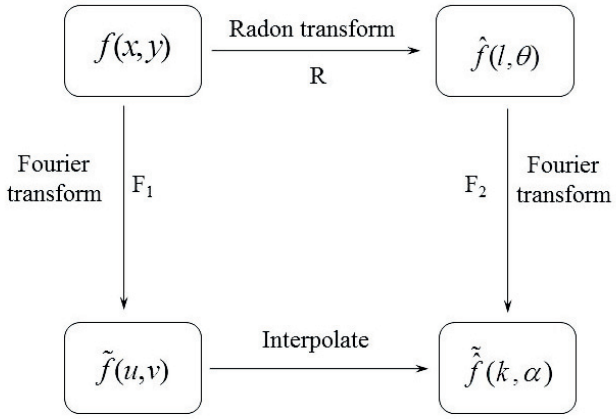

Figure 4.3: The central slice theorem, which is the relationship between Fourier transform and Radon transform [69].

Therefore, the three dimensional Fourier transform of the object can be built up plane by plane using transforms of different projections (central slice theorem). If a sufficient number

of projections are available, the object can be reconstructed by Fourier inversion of the resulting three dimensional transforms [69]. This method of tomographic reconstruction is known as direct Fourier reconstruction.

Unfortunately, the practical implementation of the Fourier transform is not easy due to sampling of the data at discrete angles. This causes regular gaps to be left in Fourier space, whereas the inverse Fourier transform requires a continuous function. It is possible to fill the gaps in Fourier space by radial interpolation, but the quality of the reconstruction is affected by the type of interpolation applied. Another disadvantage of Fourier reconstruction methods is that these are computationally intensive and difficult to implement. Therefore they have been replaced by real-space alternatives, which are faster and easier to implement [65,70,67].

This theory is important to understand the effect of sampling deficiencies in the original dataset. If projections are missing from an angular range, the Fourier transformed space is degraded and the reconstructed results will be distorted [67].

4.1.3 *Back Projection*

The term back projection was first introduced into tomographic reconstruction by Crowther et al. in 1970 [69]. They suggested that it is possible to reconstruct the object by a simple form of back projection [70]. The reason behind it is that any point in space is uniquely described by any three lines passing through it. For objects with more complexity more rays are needed to describe them. Each projection of the object is the inverse of each of those rays and describes part of the complexity of the object. Therefore, inverting the projections back into three dimensional space along the direction of projection gives a ray which describes the object in the projection direction [65,71,67,70] By having a sufficient number of projections at different angles and superimposing them, the three dimensional shape of the object is accessible. This reconstruction method is known as direct back projection [70,67,71]. Figure 3 shows a schematic view of the process. This figure illustrates the object which is sampled by projection in different angles, reconstructed by back projection of those projections at the original sampling angle into the reconstruction space [67,71].

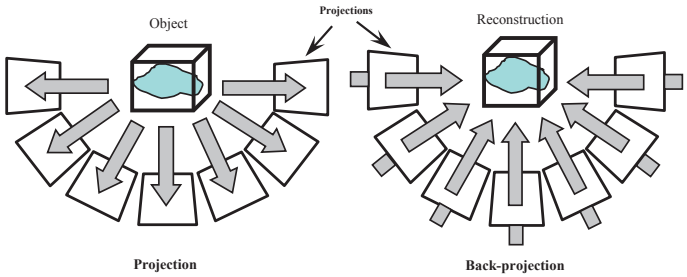

Figure 4.4: The procedure of back projection reconstruction [67,71]

In order to obtain the reconstruction, the inverse Fourier transform of the object has to be done:

$$f(x) = \int_{transform} \tilde{f}(u)\exp(-2\pi i x u)dx \tag{4.20}$$

For computational purposes, it is convenient to rewrite this integral as a summation:

$$f(x) = \delta u \sum_i F(u_i)\exp(-2\pi i x.u_i) \tag{4.21}$$

This equation shows that only transform values at a set of sampling points, u_i, are considered in the reconstruction. Crowther and co-workers argued that this summation is a valid representation of the inverse Fourier transform if the sample points are regularly spaced [70]. The inverse transform of a regular sampling function is periodic, and the origin peak is repeated at spacings inversely proportional to the sample spacings. This means that in the reconstruction from the sampled transform, the original single object is repeated periodically, with a period inversely proportional to the spacing of sample points in the transform [72]. It is easier to explain this in Radon Space. The data is a sample of Radon space *(l,θ)*, i. e. the projections, and so the reconstruction should return back the object in to the real space (r,φ). In each two dimensional slice, the intensity at a real-space pixel (*p*), from a single projection at angle θ, is related to the intersection of line $l = rcos(\theta - \phi)$ and θ in Radon space. This can be represented by the following integral [73, 69]:

$$\mathrm{B}f(r,\phi) = \int_0^{\pi} f[rCos(\theta-\phi),\theta]d\theta \tag{4.22}$$

B here is projection operator. The right side of this equation gives the value of *p,* using the Riemann sum; this integral is approximated as [73]:

$$\Delta\sum_{m=0}^{M-1} f(rCos(m\Delta-\phi), m\Delta) \tag{4.23}$$

where *m* is the number of projections and *Δ* is the angle between each increment, assuming an equal angular tilt increment. In real data sets, however, limited number of projections are available. Therefore, the sampling of the Radon space is limited and values for every solution of Equation (4.18) do not exist. This means that interpolation in Radon space is necessary to determine the unknown values. The quality of the back projection depends on the interpolation function that is applied [67,73]. The advantage of this reconstruction method is that the back projection is calculated for each pixel independently and is much faster than the Fourier transform method on the same data set [67,73].

4.1.4 Weighted Back Projection

Although reconstruction by back projection is efficient, the result is blurred. This is because the low frequency components are over emphasized compared to the high frequency components. This is due to the uneven sampling of spatial frequencies in the ensemble of projections which comes from the fact that the density of measurements in Fourier space is greater at lower frequencies. In two dimensions each of the projections provides a line intersecting the centre of Fourier space at zero frequency (central slice theorem). In practice, the zero frequency component is enhanced by a factor equal to the number of projections, while the components closer to the origin in Fourier space get more information from overlapping of different projections [65,67]. This causes the under sampling of the high spatial frequencies of the object and leads to blurring of the reconstruction [65,67].

To solve this problem, a high-pass filter is applied to the projections. This method of reconstruction after filtering is called weighted back projection or filtered back projection.

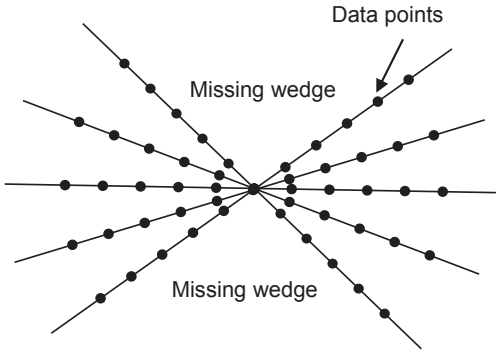

Figure 4.5: Display the non-uniform sampling of Fourier space causes by the acquisition of the tilt series. The angular increment between projections is θ and the maximum tilt angle is α.

4.1.5 Iterative Reconstruction

A back projection reconstruction is always imperfect due to the limited number of projections. In addition, the reconstruction gets worse if the number of projections is small or the signal-to- noise ratio (SNR) is low in the original projections. If the imperfect reconstruction is projected at the original projection angles, the re-projections will not be identical to the original projections. The difference between them is a characteristic of the deficiency of the reconstruction from an imperfect data set. This difference can be back-projected into reconstruction space (which makes a difference reconstruction), and can be used as a modification of the original reconstruction. The difference reconstruction constrains the reconstruction, to a degree, with the original projections. There are several ways to measure the difference and then improve the first reconstruction. The first proposed method known as the Algebraic Reconstruction Technique (ART), in which an algebraic procedure is used to corrects the reconstruction, projection by projection. Another technique is called the Simultaneous Iterative Reconstruction Technique (SIRT), in which all projections at each step are constrained to the reconstruction. This comparison operation is repeated iteratively until a best solution is reached [65,67,70].

4.2 Tomography in TEM

The principles of electron tomography have been mostly developed through biological science using Bright Field (BF) TEM tomography imaging [66,70]. Since the conventional TEM approach is not suitable for crystalline materials, its application has been limited in

material science. However, DF-TEM tomography has been applied to resolve the dislocation in crystalline materials using diffraction contrast by the group at Cambridge University [74,75]. HAADEF-STEM tomography has been also applied to study the crystalline materials such as cobalt FT catalyst by Arslan et. al [76].

4.2.1 Suitable Imaging Mode

A transmitted beam must satisfy assumptions to be suitable for tomographic reconstruction. The most important one is that the detected signal must be a form of projection through the structure and, in principle, a monotonically varying function is needed [77]. This is known as the projection requirement.

In BF TEM imaging the contrast arises due to the mass thickness contrast and diffraction contrast (Bragg contrast). BF tomography is based on the assumption that the mass thickness contrast due to atomic scattering is dominant. Therefore, the sample which is used in BF tomography must be thin and weakly scattering crystalline or amorphous [79,]. Biological specimens show all of the above characteristics and most of the development on tomographic reconstruction has been done on biological samples using BF TEM images.

In material science the specimens are primarily crystalline and therefore, the observed contrast is depended on the diffraction condition of the crystal and have no monotonic relationship with the amount of material which the beam passes through it. Therefore, BF images are not suitable for tomographic reconstruction of crystalline materials because it is not necessarily projections [79].

High Angle Annular Dark Field (HAADF) images show the similar contrast characteristic as mass thickness BF images. The intensity in HAADF images arises from both the atomic number of the scattering atom (Z) and the amount of material projected through. The suitability of HAADF for tomographic reconstruction of crystalline specimens is due to the high angle annular detector which exclude the most of Bragg scattered electrons beam [79].

In addition, tomographic acquisition requires a long acquisition time and that enhances the risk of beam damage. In STEM mode the total dose to the specimen is much lower than in conventional TEM imaging and the rastering nature of the probe allows dissipation of heat to the surrounding area. Therefore, in specimens where heating damage is dominant, STEM can

minimize the damage [5]. In specimens where inelastic knock-on damage is dominant, damage in STEM theoretically is greater due to the large current intensity in the probe.

4.2.2 STEM Tomography

As mentioned above, electron tomography in STEM mode is suitable for crystalline specimens. Using a sufficiently large inner radius, so called HAADF, detector to exclude Bragg-scattered electrons allows an image to form whose contrast is mostly to the thickness of material. This is called Z-contrast imaging and fulfils the projection requirements for tomography of crystalline specimens. Figure 3 shows the geometry of different detectors in STEM mode [78,79].

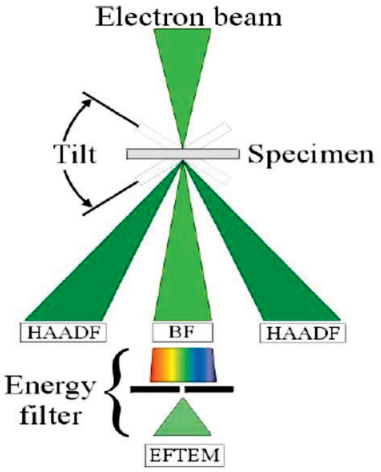

Figure 4.6: Schematic geometries of various signals that may be used for tomographic reconstruction in TEM [65].

In STEM there is no lens to form the images, instead STEM scanning coils raster a focused probe across a sample and the transmitted electron signal is monitored as a function of position to form the images. The STEM signal generated from any point of the specimen is detected and amplified and a proportional signal is displayed at an equivalent point on the screen.

4.2.3 Data Acquisition

Data acquisition is one of the major parts in the electron tomography analysis. Micrographs of the specimen recorded at different tilt angles with respect to the electron beam are collected. In practice, the acquisition steps are straight forward and the main thing is to tilt the sample

over a large range and record focused images of the area of interest at a series of tilt angles. It should be noted that the imaging conditions should remain constant during acquisition.

It is possible to acquire the data both manually and automatically. In the automated data collection, the position is controlled automatically with respect to a reference image and the focus is adjusted based on the high contrast level in each image, in each increment of tilt. In the manual collection the focus (Z-tracking) and the specimen drift are controlled in each increment. As the tilt series contain a large number of images, it is very challenging and time consuming to manually acquire a high quality series. In Manual collection the exposure time increases and therefore increases the probability of beam damage to the sample.

The beam damage and errors in focus are almost impossible to improve after the acquisition and they reduce the quality of the resulting reconstructions.

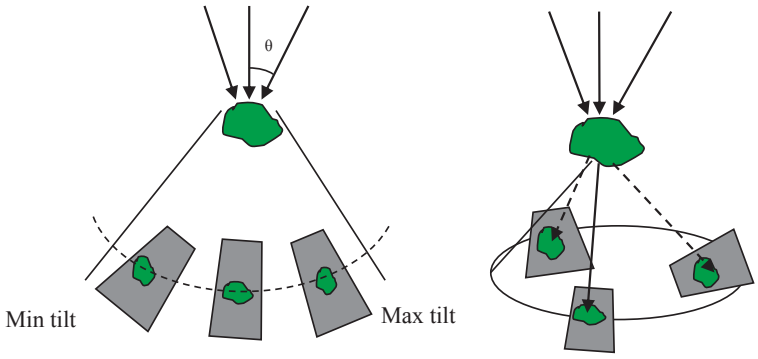

Figure 4.7: Different data collection geometries for electron tomography, a. single axis tilting, projections recorded at regular tilt increments, b. conical acquisition, projections recorded at a set of angles from zero to 360°.

Acquisition Geometries

As mentioned earlier, to reconstruct an object in three dimensions from electron micrographs, a number of projections of that object are required from different directions. These projections are acquired by tilting the specimen inside the microscope. Tilting the specimen is performed by the goniometer and images are recorded at each angular increment. Several tilting geometries have been developed such as single tilt, dual axis tilt and conical tilt as schematically shown in Fig. 4.7 [66].

Single axis tilting is the most straightforward and has been the most widely used. The specimen is tilted around the eucentric axis of the specimen holder, from one extreme to the other. The dual axis geometry is a development of the single axis tilting and involves the tilting of the specimen around two orthogonal axis and the reconstructions of two single axis tilt series are combined. In conical tilting, the specimen tilt angle remains constant while the stage is rotating in equal increments around the axis perpendicular to the specimen plane [66,67].

Acquisition Process

Prior to the series acquisition the microscope is well aligned and an object of interest (typically about 50-100 nm length) is selected. The selected area should not be too thick,

because at high angles the effective specimen thickness increases by the factor of $t/Cos\theta$, where t is the thickness of the object and θ is the tilt angle. This leads to a low Signal-to-noise ratio (SNR). Figure 4.8 shows the effect of thickness at angle of θ.

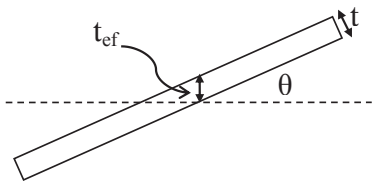

Figure 4.8: Shows the effective thickness of the object which is more than real thickness at higher angles.

The volume is selected close to the centre of the grid and it should be away from bar grids and other specimen regions to prevent the region of interest being obscured at high tilt angles. The selected area is then tilted to establish the possible extremes of the tilt that maybe reached and also check for correct eucentric height. If the possible tilt range is less than 130˚, an alternative area is chosen.

Limitation of Acquisition

The acquisition tilting range is limited by the physical structure of the sample holder and microscope. The size of the specimen holder with respect to the objective lens pole piece gap physically imposes a maximum tilt range [67]. Therefore, special holders are required which should have the possibility of tilting inside the pole-piece gap. Two different high tilt holders were used in this study. A high tilt Gatan tomography holder which provides up to ±80

degrees of tilt in the JEOL 2010F (Figure 4.9a) has a tip that is about 3mm wide (Figure 4.9b). The other is JEOL common specimen holder with high tilt retainer (EM-21311 HTR). Figure 4.9c shows the empty JEOL specimen holder rod and Figure 4.9d shows the rod with high tilt retainer.

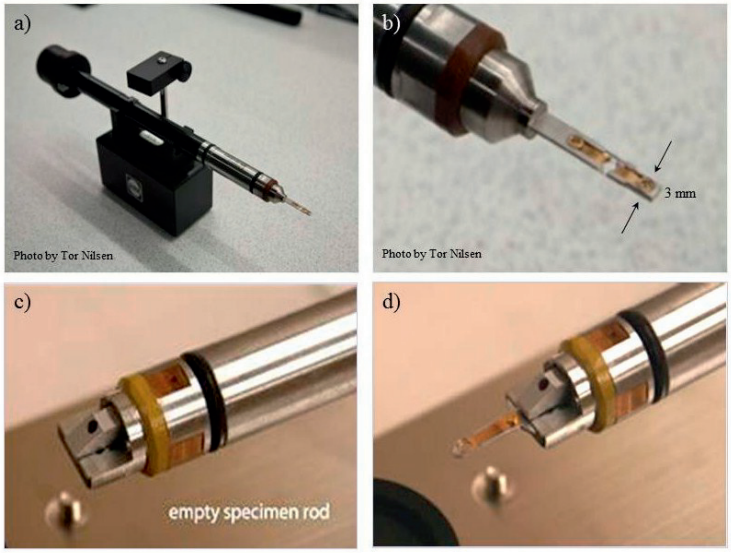

Figure 4.9: a) The Gatan tomography holder and b) its narrow tip, c) The JEOL common specimen rod and d) the JEOL rod with high tilt tip [80].

Another limitation is that when the specimen tilted, components of the holder or the sample itself or the grid obstruct the electron beam [65,67,66]. As mentioned before, the tomography holders permit tilting to angles ±80˚. In practice, however, acquisition cannot always be recorded up to the maximum 80˚, due to the specimen self-shadowing and the increased projected thickness of the specimen at high tilt angles [80]. The limitation on the maximum tilt range leads to the wedge of unsampled volume in Fourier space, the missing wedge, as described earlier. This causes the quality decrease in the reconstruction results. This problem has been improved by the development of dual axis and conical geometry acquisition as mentioned before.

One of the main factors in tomography is the resolution of the reconstructed images. In general, for the single axis tilt geometry the spatial resolution of the construction is anisotropic. The resolution *d* of a tomographic reconstruction is controlled by the number of projections, *N,* acquired in the tilt series and the diameter, *D,* of the volume to be constructed [65,67].

$$d = \frac{\pi D}{N} \tag{4.24}$$

Equation (4.24) assumes that the N projections have been done from $\pm$ 90, which is rarely the case. Due to this limitation the resolution in the direction of optic axis is decreased by an elongation factor, e, related to the range of angles, α, covered by the series. The elongation factor is described by Eq. (4.25):

$$e = \sqrt{\frac{\alpha + Sin\alpha Cos\alpha}{\alpha - Sin\alpha Cos\alpha}} \tag{4.25}$$

Hence, we may write the resolution in the direction of the optic axis (d_e) as:

$$d_e = d.e \tag{4.26}$$

Considering the above points, in order to provide maximum three dimensional information, as many projections as possible should be acquired over as wide range of tilting as possible.

4.2.4 Alignment Process

During acquisition, the area of interest is re-centred at each angular increment. However, it is not possible to do this perfectly as the goniometer control is not sufficiently accurate to shift the area to exactly the same position at each increment. Therefore, alignment of images after acquisition is required to avoid large misalignment in the reconstruction.

The direction of the tilt axis, which the specimen was tilted around, and the position of the tilt axis are very important for reconstruction because all the reconstruction algorithms are executed with reference to this axis. The alignment consists of two part, shift alignment and tilt axis alignment as described in the following:

Shift Alignment

There are two approaches to image shift alignment, an automatic approach and a manual one. These are both based on pair wise comparison of images. The difference is that in the automatic alignment the cross-correlation algorithm is applied to determine the relative offset

between them while in the manual approach each image should be positioned in an appropriate way to minimize the offset.

The Basics of Cross-Correlation Alignment

Two sequential projections, which are separated by a typical increment of few degrees will share many common features offset with the relative shift between two images. The cross-correlation alignment is applied to correct this and is based upon the use of the discrete 2D cross-correlation function which is defined as:

$$h(m,n) = \frac{1}{MN} \sum_{j=0}^{M-1} \sum_{k=0}^{N-1} f(j,k) g(j+m, k+n) \tag{4.27}$$

Where f and g denote the optical density measurements of two images and M and N denote their width and height, respectively [67]. If f and g are similar to each other up to a shift of $r_0 = (m_0, n_0)$, the cross-correlation array h will have a maximum at that location. The cross-correlation alignment principally means identifying these maximum locations pair wise for the images in the tilt series, and these locations are taken as the estimates of the relative shift parameters. Once the relative shift has been found for a sufficient number of image pairs, the image set can be aligned by identifying the relative shift between the reference view and each image, and then translating the images by the corresponding negative shift values so that the relative shifts become zero [66].

Alignment of Tilt Series by Fiducial Markers

During acquisition of the tilt series, the position of the object and its shape changes, depending on the angle of rotation and the tilt axis direction and its position. This information is necessary for alignment of the series. However, the shape of the object is usually unknown and, therefore, it cannot be used as a reference. One way to fix this problem is by adding a dispersion of colloidal gold nanoparticles solution to the grid. In this method a set of localized features are distributed in the sample. These particles are tracked in each projection and their measured position recorded as the tilt angle of the specimen changes. The positions are registered to correct the shifts afterwards [66,81].

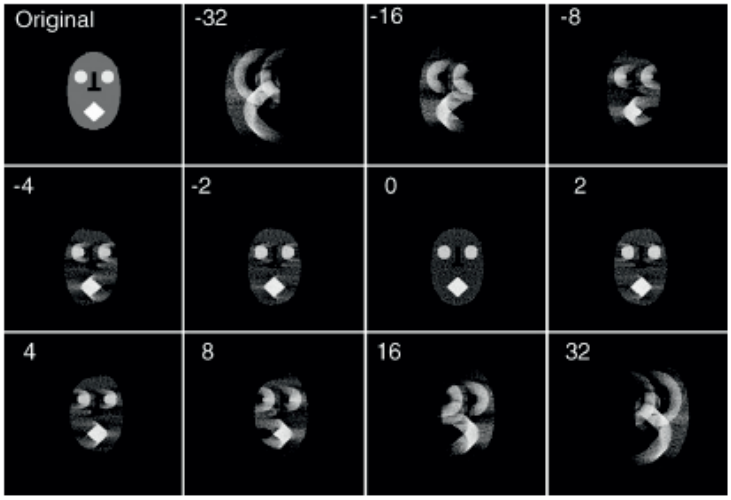

Figure 4.10: Display the effects of misalignment of the tilt axis on a reconstruction of a 'head phantasm', which is used as test object. The number indicates the pixel misalignment, perpendicular to the tilt axis. The head is 64 pixels wide [65,67].

Tilt Axis Determination

When the projections are acquired, alignment is necessary to define the position and angle of the tilt axis before reconstruction. The tilt axis should pass through the centre of each projection, at constant angle to the image axis. If the tilt axis is misplaced, artefacts are introduced into the reconstructed series. A misplacement of the tilt axis will spread the signal from a reconstructed object and produce arcs of intensity around the actual position of the tilt axis as illustrated in Fig. 4.10 [65,67]. The direction of this arc depends on the direction of misalignment away from the axis position and the size of the arc depends on the magnitude of misalignment [65]. Therefore, it is possible to adjust the tilt axis by shifting and rotating the projections in a way to minimize the arc shaped artefacts and see its effect on the 2D reconstructed slices through the whole series. After the alignment process the series is ready for reconstruction.

4.2.5 Visualization and analysis

A typical 3D volumetric dataset, as produced by tomographic reconstruction, gives significant challenges for visualisation. A large memory capacity for storage and manipulation is required. There are several main approaches to the visualisation of volume datasets. Among these, two dimensional slices, surface rendering, voxel projection (volumetric imaging) and segmentation are more applicable in material physics [78,79].

Slices are easily interpreted. However, the data displayed are extremely sensitive to the direction of the slices and it can be misleading if the wrong direction is chosen as representative of the whole.

It is possible to do quantitative measurements on the visualized object. In terms of catalysts the density and homogeneity of active sites are important factors for which tomography should be able to provide an accurate analysis [67,78].

Iso-surface Rendering

Surface rendering displays a reduced form of the whole dataset, usually from one or several different intensity levels. It generates a polygonal surface from the volumetric dataset which reduces a 3D volume into a geometrical description of its surface. It is done through the formation of a wire frame polygonal from volumetric data by joining the voxels with the same value of intensity. This value is determined by selecting a threshold intensity. Then the produced iso-surface is rendered by addition of depth, texture, perspective and shadow. This method of visualization shows distinct morphology and topology of material. The main draw-back is that the iso-surface is dependent on the choice of the threshold intensity and that can greatly influence the final conclusion [78,67,79].

Voxel Projection

Voxel projection is the simple re-projection of the 3D volume at any angle. The dataset has the same unit in all three dimensions. Each cubic volume element (voxel) from the dataset contains a density value. This value is described by two things, first the electron transparency of the corresponding material in the original sample which is known as the opacity factor (α=1/transparency) and second is the colour of every voxel. It is defined by using a RGBA (Red, Green, Blue, Alpha) transfer function which determines the RGBA value for every voxel. The Voxel visualization method is good for visualizing internal structure of the materials [67,78,79].

Segmentation

In the segmentation method, the region of the reconstructed volume is defined as an object and once the object is segmented, it can be individually visualized. Segmentation consists of two parts, recognition and delineation. Recognition is the process of roughly determining the boundaries of the object in the data. Delineation is the process that defines the precise special extent of the object. The latter is a complex process because the object may exhibit a

gradation of intensities as a result of reconstruction artefacts, blurring and background variations and also the homogeneity of the object [66,79].

There are several segmentation algorithms available to detect the edges of the volume of interest and recover its shape. Among them thresholding is the simplest method. In this method the pixel or voxels are selected with respect to their intensity above or below the user defined intensity [66]. It is also possible to do the manual segmentation by defining of the area of interest slice by slice through the whole volume of tomogram [66].

4.2.6 Software Packages

Several different software packages are available for acquisition and reconstruction of tilt series. Gatan Digital Micrograph is licensed software and has the ability of doing acquisition and reconstruction [82]. IMOD and ImageJ are freeware programmes which have different possibilities [83,84,85]. Avizo is licensed software for visualization of three dimensional reconstructed objects [86]. A description of these software packages is given in Appendix B.

4.3 Electron Tomography of Catalysis Materials

The application of tomography to materials science specimens is a relatively new field. However, as the ease of data acquisition increases, it will lead to more quantitative analysis of important parameters such as particle size, homogeneity and surface area to volume ratio becoming increasingly possible.

Tomography of catalyst materials is possible using tilt series of HAAD STEM images, which are sensitive to the atomic number. It allows the analysis of structural details and the direct imaging of defects such as agglomeration and a lack of homogeneity [67,78]. Applying the tomography technique for heterogeneous catalysis allows the determination of the three dimensional shape, volume, connectivity and location of meso and macro pores inside a support materials. Also size and location of metal particles inside the support material can be visualised.

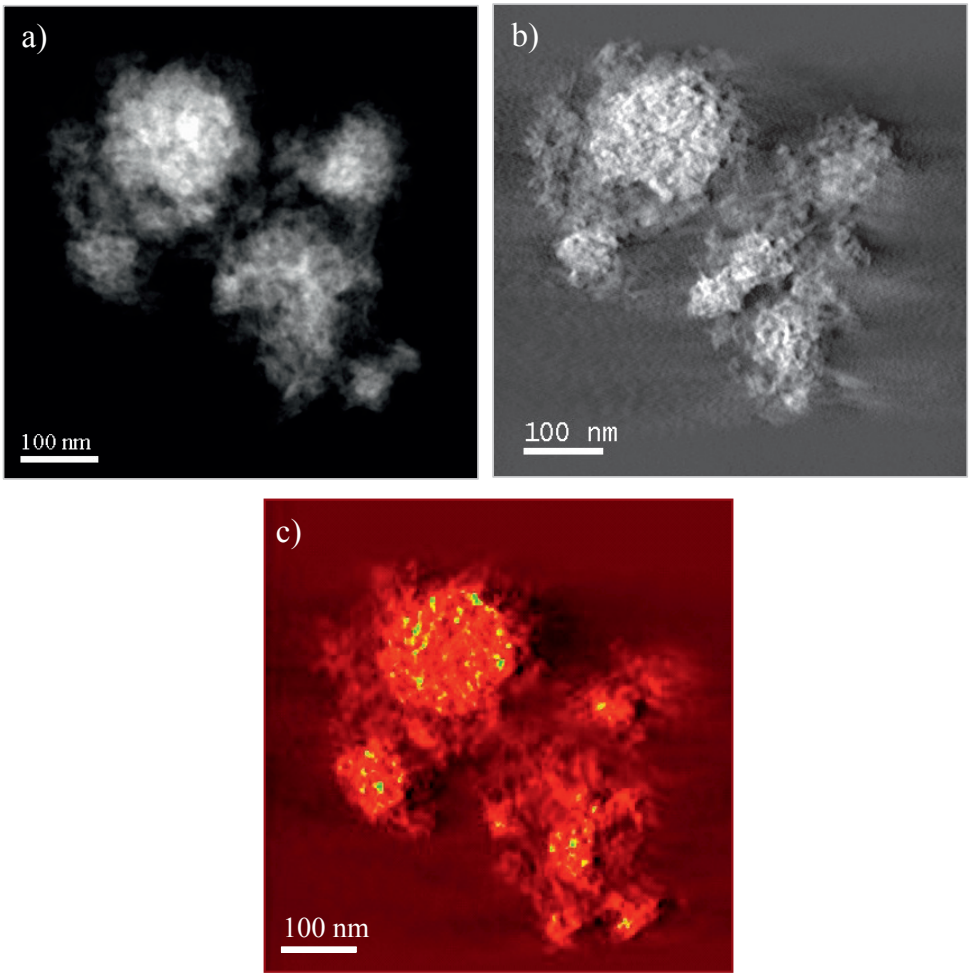

Figure 4.11: a) The STEM image of the sample at zero tilt angle, b) A section through the reconstructed results, c) A section through orthoslice visualization of the same reconstruction series.

4.3.1 Electron Tomography of Fischer-Tropsch Catalysts

Electron tomography was applied to study the cobalt FT catalyst supported on the α-Al_2O_3 and γ-Al_2O_3 substrates in both calcined and reduced states. Below is the brief explanation of experimental condition and results from each experiment.

Figure 4.11 shows an example of electron tomography on a calcined 20%Co%0.5%Re/γ-Al_2O_3 FT catalyst. The TEM sample was prepared by dispersion of crushed powder on carbon film. The acquisition was performed with a JEOL 2010F electron microscope, operating at

200kV. The tilt series were acquired with a high tilt Gatan tomography holder over tilting range of ±70 degrees. The acquisition was performed in high resolution STEM mode with manual control over the focus and shift corrections in each increment. The tilt series was aligned by the cross-correlation function in Digital Micrograph and reconstructed by using SIRT with the Gatan Digital Micrograph reconstruction software. Visualization was done using the Avizo software (Appendix B). The results show the degree of porosity in both cobalt oxide aggregate and γ-Al_2O_3 support. Although some pores are observed in the Co_3O_4 aggregate, No separation of the Co_3O_4 nanoparticles inside the aggregate is evident and it is consistent with the continuous mosaic structure of the oxide aggregate [87].

Figure 4.12 shows the tomography results from reduced 20%Co%0.5%Re/γ-Al_2O_3 catalyst. The TEM sample was prepared by dispersion of crushed powder on carbon film inside the glove box. The reduced material was transferred to the TEM by using the TEM holder cap and glove bag to protect the sample from air. The acquisition was performed with a JEOL 2010F electron microscope, operating at 200kV. The tilt series were acquired with a high tilt Gatan tomography holder over tilting range of ±72 degree. The acquisition was performed in STEM mode with manual control over the focus and shift corrections in each increment. The alignment and reconstruction were performed with the tomoj plugins in Imagej software. Visualization performed with Avizo 6.

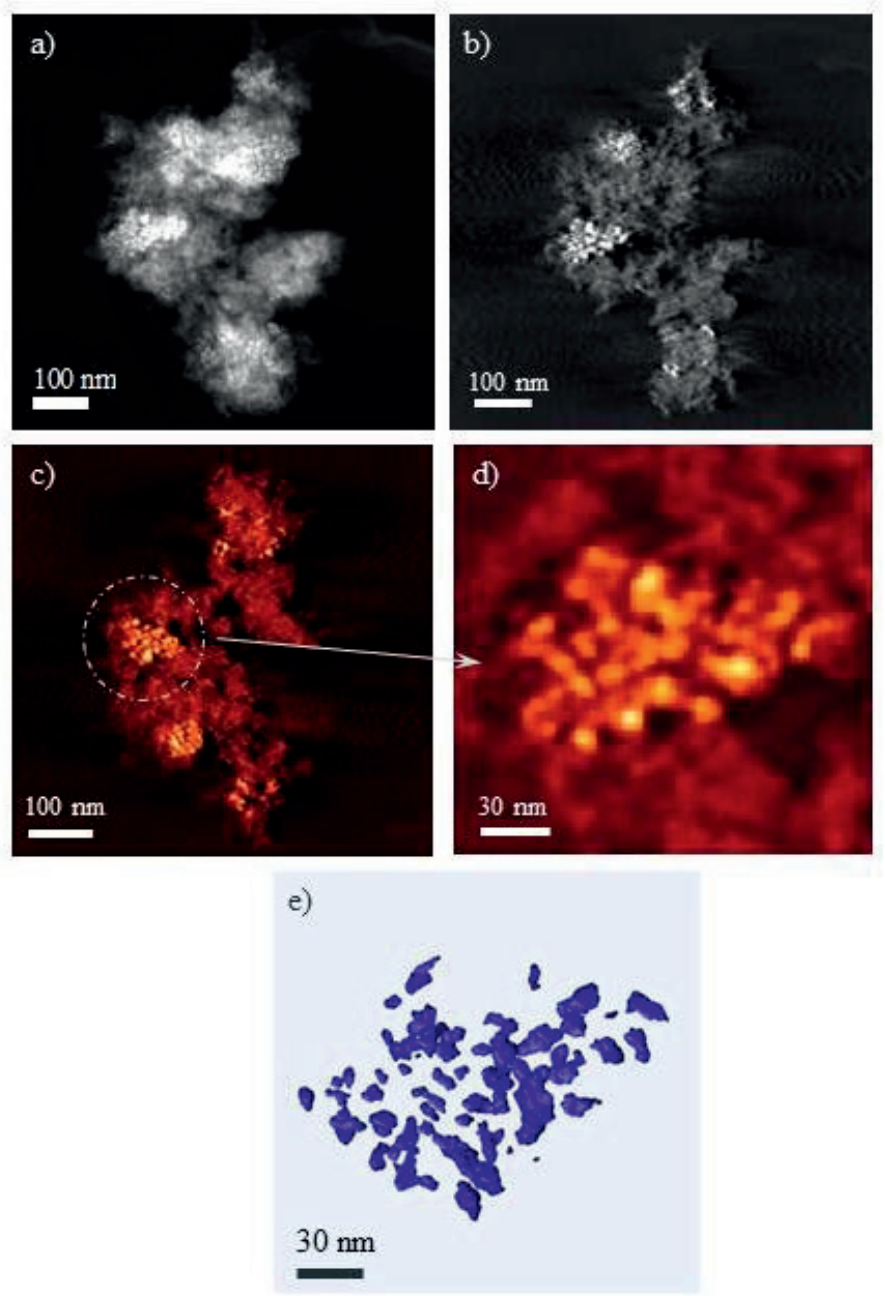

Figure 4.12: a) STEM image of the reduced cobalt supported on γ-Al_2O_3 at zero tilt, b) An orthoslice from the reconstructed results, c) A section through the same series visualized by voltex view, d) The magnified view of the indicated area in Fig. 4.12d, showing separation of the cobalt nanoparticles in the aggregate and e) A snapshot from segmented cobalt aggregate, showing the morphology of the metallic cobalt nanoparticles influenced by the shape of alumina pores.

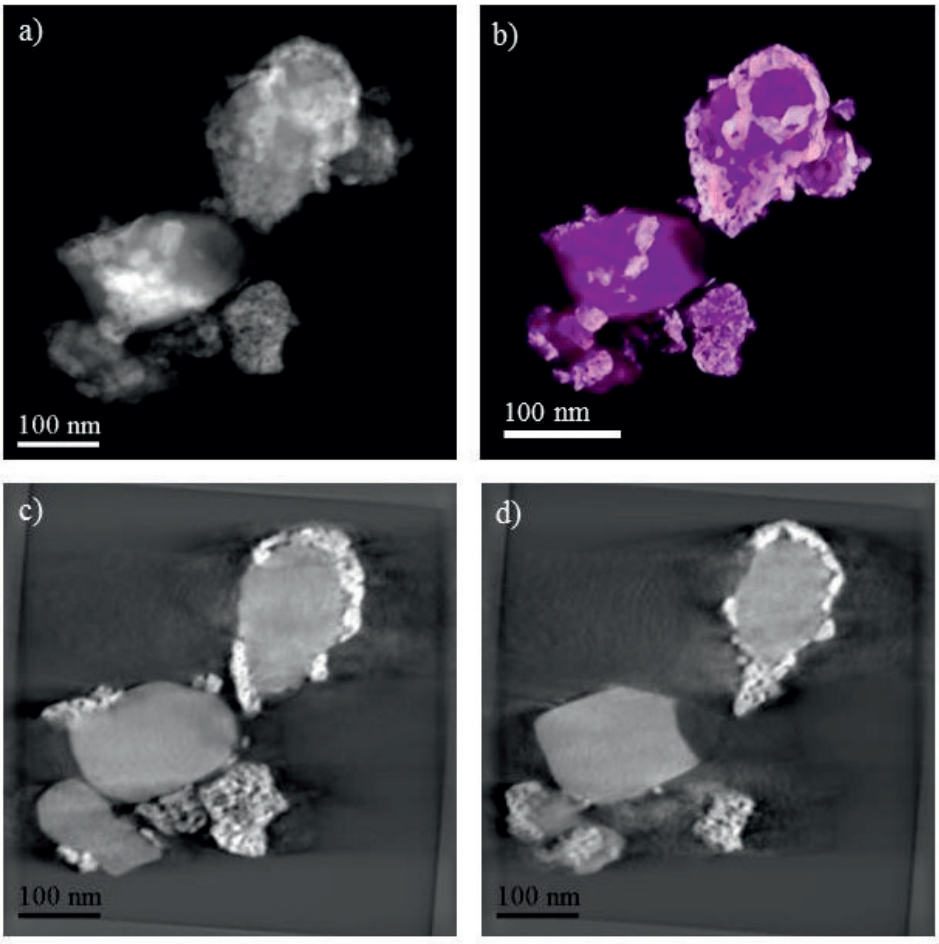

Figure 4.13 a) An orthoslide form 3D series of promoted cobalt oxide supported on α-Al_2O_3, b) Visualized voltex view of the same series, c) and d) two different orthoslices through reconstructed series.

Figure 4.12a shows a STEM image of the catalyst material at zero tilt. The reduction state of the material was confirmed by EELS as described later on. Figure 4.12b shows the reconstruction of the tomography series by SIRT. Figure 4.12c shows an orthoslice from the same reconstruction visualised by voltex view. Both Figure 4.12b and Figure 4.12.c shows that the cobalt nanoparticles are located in the aggregates and only a few of isolated cobalt nanoparticles distributed in the support. This is seen due to the high contrast between cobalt and substrate in the reconstructed file. . Figure 4.12d shows the enlarged area of the indicated aggregate in Fig. 4.12c. The separation of the particles in the aggregate due to the reduction is obvious. Figure 4.12e is the snapshot from the same aggregate as in Figure 4.12c, segmented through the whole volume. It shows the random morphology of the cobalt nanoparticles which reflects the influence of pore shape of alumina substrate on the cobalt phase growth. It

should be mentioned that due to the high contrast in the 3D series, it was difficult to distinguish the boundary of cobalt nanoparticles which are very closely separated. Therefore, some of the large cobalt nanoparticles observed in the segmented volume can be grouping of smaller adjacent nanoparticles. These results are discussed in more details in paper III.

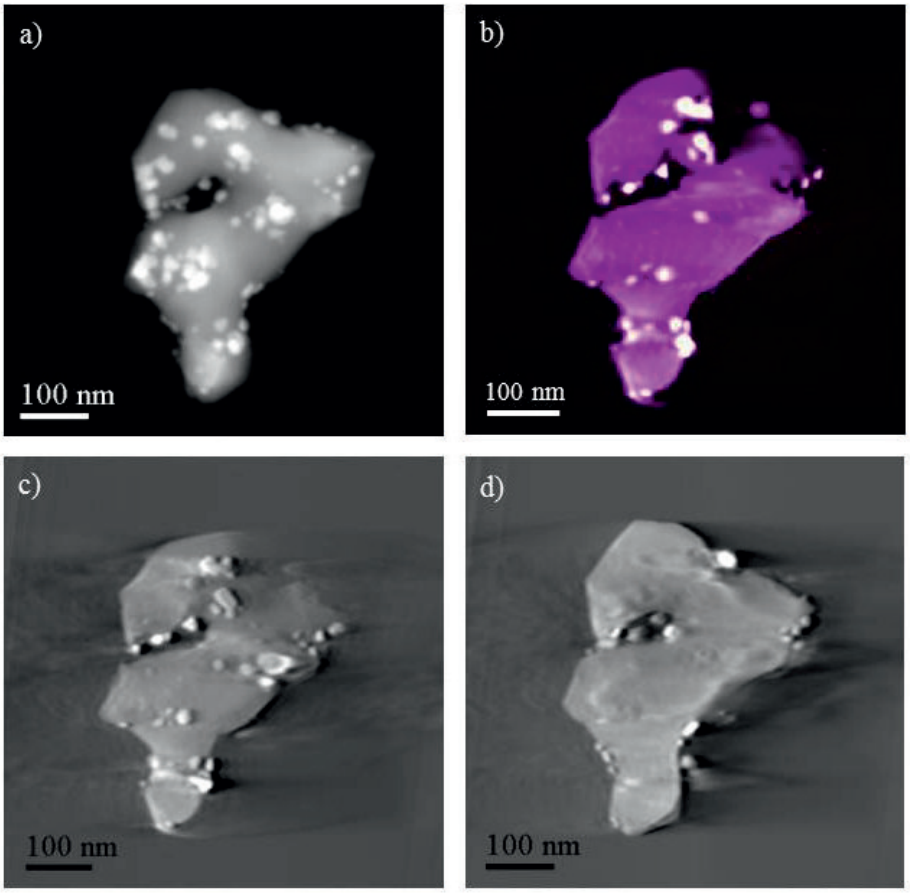

Figure 4.14: a) An slide form 3D series of reduced 12%Co/0.5%Re/α-Al_2O_3 catalyst, b) A snapshot from voltex view of reconstructed series, c) and d) Two different orthoslice from reconstructed series.

Figure 4.13 and Figure 4.14 show the electron tomography results from reconstruction of rhenium promoted cobalt catalyst on α-Al_2O_3 substrate before and after reduction, respectively. The reduced material was transferred from glove box to the TEM using glove bag. Figure 4.13a is a slide through the 3D series of clacined material before reconstruction and Figure 4.13b is voltex view of reconstructed series. It shows the distribution of cobalt oxide (white area) on the α-Al_2O_3 substrate (purple areas). Figure 4.13c and Figure 4.13d are two different orthoslices of the reconstructed series. Comparison of these two images show

that, there are features in Figure 4.13c, which are not present in Figure 4.13d and this is not recognized in the 2D TEM images. Figure 4.14a is one of the 2D images through the 3D series of the same material after reduction and Figure 4.14b is related voltex view in which the cobalt is in white colour and the α-Al_2O_3 substrate is in purple. Figure 4.13c and Figure 4.13d are two different orthoslices of the reconstructed series. Comparison of these two shows the importance of electron tomography for characterization of materials.

Visualization of the calcined and reduced catalyst shows that there are some porosities in the Co_3O_4 particles which are lost during reduction and the cobalt particle size has changed. It can be interpreted that due to the influence of the support, large cobalt oxide particles have been reduced to a few smaller particles.

Chapter 5

In-situ TEM study of Cobalt Catalysts

In general, TEM vacuum system works under high vacuum conditions. However, the interest for studying samples under dynamic conditions, in situ, has been led to the development of the environmental TEM (ETEM) [88,89]. Great attention has been paid to in-situ experiments in the area of catalysis in order to investigate materials under gas pressure and at elevated temperatures at atomic resolution [90]. In this chapter, a short review of TEM vacuum system is presented. Then the details of an ETEM instrument and its application for studying the FT catalysts are explained. The main results of this work have been published in a journal paper. However, more details of the experiments and unpublished results are presented in this chapter.

5.1 TEM Vacuum System

Standard TEM instruments operate with low pressure inside the column, typically 10^{-10} bar [5]. Ultra high vacuum TEM instruments have a pressure below 10^{-12} bar. The reason for running the TEM in high vacuum is the need to have a long mean free path for electron gas interactions. This allows reducing the collision frequency of the electrons with gas atoms to a negligible level.

A TEM is usually equipped with different types of pumps, each of which has different characteristics. A Rotary pump is a kind of mechanical pump and sucks air through an inlet valve into its chamber and expels it through an exit valve [91]. It operates in the range of atmospheric to 10^{-3} bar. Diffusion pumps and Turbo Molecular Pumps (TMP) are common type of pumps in the TEM instrument, to keep the vacuum at up to 10^{-10} mbar [5]. Diffusion pumps use a hot plate to boil oil, to form a series of concentric vapour jets. These jets drag air molecules out of the vacuum, then condense onto cold surface (water cooled walls) and leave the air molecules, which are extracted by a backing rotary pump [5]. Turbo molecular pumps

use a turbine to force gases from the vacuum chamber [91]. The type of pump generally used in the TEM to achieve ultrahigh vacuum is a Ion Getter Pump (IGP). The ion pump emits electrons from a cathode and these electrons move in a magnetic field and ionize gas molecules, which are attracted to a cathode which forms the internal surface of the pump [91]. The internal surface is made of Ti and molecules from the gas are embedded in the walls of the pump.

In most of the TEM instruments, cold fingers, or anti-contaminators, are used to provide an alternative site to condense the residual components around the specimen in the vacuum [91]. The cold surface efficiently removes the gas molecules from ambient pressure down to 10^{-9} bar. Liquid nitrogen is used to cool the device.

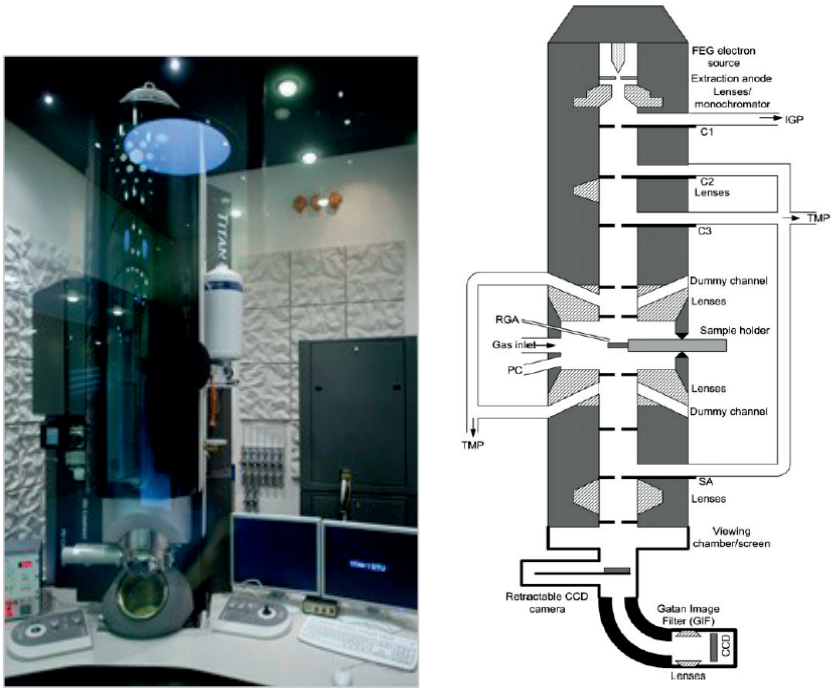

a) b)

Figure 5.1: a) Titan ETEM electron microscope, located at DTU CEN [92], b) Schematic view of the Titan microscope column [93].

5.2 Environmental TEM

In-situ experiments in this study were performed with dedicated Titan ETEM from FEI (Fig. 5.1) which is at the Centre for Electron Nanocopy (CEN) at the Technical University of

Denmark (DTU). It has the possibility to run at 80-300 kV accelerating voltage. Hansen et al. have reviewed the details of this microscope [93].

In TEM, an electron beam is focused by electromagnetic lenses, which exhibit both spherical aberration and chromatic aberration. Spherical aberration is caused by inhomogeneity of the lens field [94]. Electrons at different distances from the optic axis, focus on different points and causes a point to be imaged as a disk of finite size (Figure 5.2a). Overlapping of the disks degrades the resolution. Chromatic aberration relates to the wavelength and energy of the electrons. The lens cannot focus electrons with different energies to the same convergent point (Figure 5.2b). Both chromatic and particularly, spherical aberrations have been corrected to a high extent in recent electron microscopes [95,96].

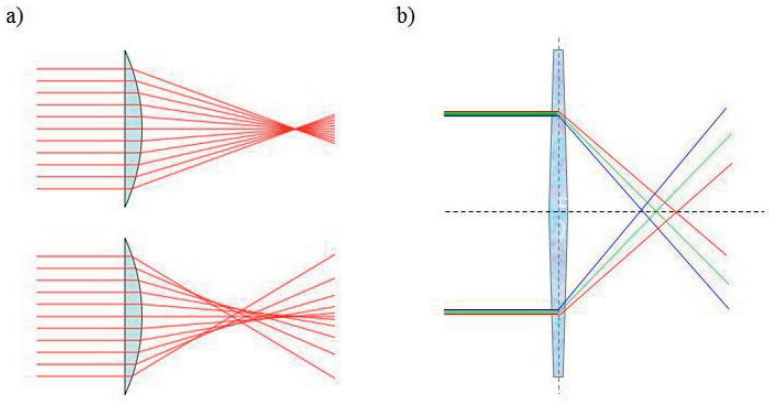

Figure 5.2: a) The effect of spherical aberration and b) the influence of chromatic aberration on the electron beam [97].

The ETEM is equipped with an image Cs corrector and monochromator. By operating at 300 kV, the point resolution and information limit without aberration correction is 0.2 nm and <0.1 nm, respectively. The Cs image corrector reduces the point resolution down to less than 0.1 nm at the same accelerating voltage [93]. A monochromator can provide an electron beam with a narrow wavelength range. By operating at 300 kV, the monochromator provides a measured energy spread of better than 200 meV. The ETEM has an EDS detector for elemental analysis, and Gatan GIF Tridiem which gives the possibility of doing EELS analysis with improved energy resolution [93]. Different gases such as H_2, N_2, CO and O_2 can be introduced into the TEM column, which makes it easy to choose the relevant gas for the experiment. The accessible pressure around the specimen is about 20 mbar. To monitor the gases surrounding the specimen, the microscope contains a capillary whose opening is inside

the objective lens and is in the vicinity of the sample. It can measure the gas composition using mass spectrometer (Residual Gas Analyser: RGA) [93]. The details of the RGA are described in appendix B.

The ETEM has the possibility to operate in two different modes, high vacuum conventional TEM or environmental TEM. The introduction of gases into the electron microscope column requires more pumping facilities. The TEM column is pumped by dedicated turbo-molecular and ion-getter pumps which maintain the high vacuum around the electron source. Each pumping stage is separated by additional apertures resulting in differential pumping. In ultra-high vacuum mode, the column is pumped by the standard ion getter pump and the turbo molecular pumps are sealed from the column by ultra-high vacuum compatible gate valves. Under these conditions the microscope operates as a conventional Cs image corrected monochromated TEM. In ETEM mode the pass ways to the ion getter pumps in the specimen area are closed and the valves to the turbo molecular pumps are opened to provide sufficient pumping capacity [93].

5.3 In-situ TEM Study of Cobalt Catalysts under Fischer-Tropsch Reaction

In this work, ETEM was applied to study cobalt Fischer-Tropsch catalysts behaviour under conditions relevant to the FT process. The industrial FT reaction condition i.e. 20-30 bar at 220˚C-240˚C is not accessible in ETEM, but the reaction with lower gas pressure (less than 20 mbar) is possible. Since cobalt oxide should be reduced prior to the FT reaction, the ETEM experiments were focused first on reducing cobalt oxide by H_2 and then mixture of H_2 and CO gases introduced to the metallic supported cobalt nanoparticles providing the FT reaction condition.

5.3.1 Cobalt Oxide Reduction

Samples used for reduction experiments were cobalt oxide supported on two different supports, α-Al_2O_3 and γ-Al_2O_3, which are standard samples, thoroughly studied in other part of the thesis. Since different behaviour was observed for these two different supports, the reduction experiments are described separately below.

Reduction of Cobalt Oxide Supported on α-Al_2O_3

Before TEM analysis, the dedicated sample holder and grids were cleaned using a plasma cleaner for 10-15 minutes. TEM specimens were prepared by dispersion of crushed powder onto steel grids. Several positions in the sample were analysed before reduction. In order to reduce the sample, H_2 was introduced to the system at 3.4 mbar. The temperature was then increased stepwise from room temperature to 360˚C. As a result of heating, materials in both the holder and the sample expand. Extension in the *x* and *y* dimensions leads to a drift of the examined region, whereas extension in the *z* dimension causes changes in the focus. Therefore, in order to follow a special particle during the reduction, it is crucial to increase the temperature stepwise to let the sample to stabilize after each step and have control over the changes.

Movie sequences were recorded from the sample during reduction after it had nearly stabilised, but evidence of drift was still clear in the movies. When the sample was stabilized at 360 ˚C, HRTEM and EELS analysis were applied and they confirmed the reduction of cobalt oxide to metallic cobalt. The analysis of the images in the movie showed the reduction of Co_3O_4 to CoO and then to metallic cobalt. Figure 5.3 shows HRTEM images of a cobalt nanoparticle before, after, and in the middle of reduction. Figure 5.3a is HRTEM image the cobalt nanoparticle before reduction, in which fringes show the d value of 4.72 Å corresponding to (111) planes of Co_3O_4. Figure 5.3b is HRTEM image of the same particle after reduction, and the fringes show the d value of 1.96 Å, which corresponds to hcp Co. Figure 5.3c is HRTEM image of the same particle, in the middle of reduction while both Co_3O_4 and CoO phases are present. Figure 5.3d shows the enlargement of indicated area in Figure 5.3c in which the fringes show the d value of 4.68 corresponding to (111) plane of Co_3O_4 and the d value of 2.48 corresponding to (111) plane of CoO.

In order to determine the accuracy of the measurements, lattice spacing measurements were made on about 20 recognizable particles in the HRTEM images of the α-Al_2O_3 and cobalt oxide phases on the images under the same focus conditions. The results give an average of ≈1% error on the fringe measurements. With this accuracy it is challenging to distinguish between similar spacings in fcc and hcp cobalt but is found to be possible.

After reduction, in order to get better resolution and in anticipation of introducing CO gas into the system, the temperature was decreased to ambient temperature while the sample was under H_2 flow. However, oxidation of the cobalt nanoparticles was observed at temperatures lower than 240˚C. The sample was re-reduced by increasing the temperature to 360˚C and its

reduction was again confirmed by HRTEM and EELS. Figure 5.4a shows TEM image of cobalt aggregate in which oxide layer started to grow and Figure 5.4b is the TEM image of the same particle after re-reduction at 360˚C.

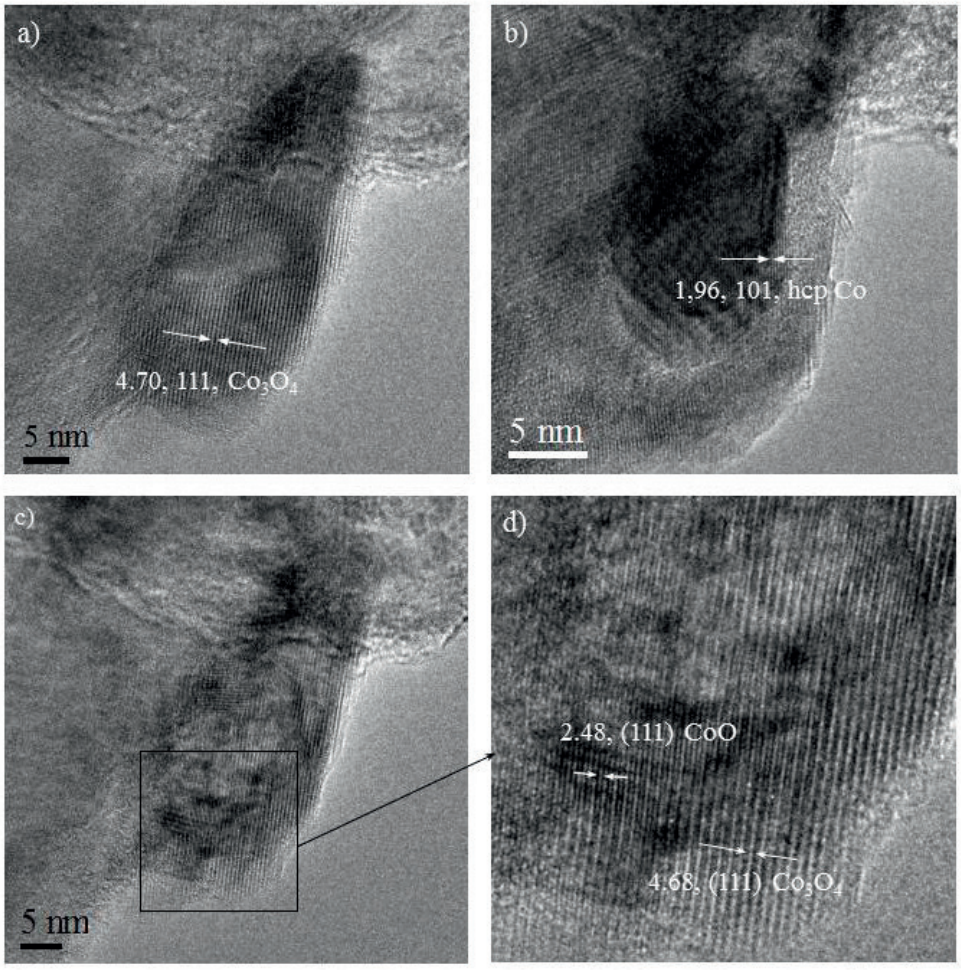

Figure 5.3: a) HRTEM image of Co_3O_4 nanoparticle before reduction, b) HRTEM image of the same nanoparticle as in Fig. 5.3a after reduction, c) HRTEM image of the same nanoparticle as in Fig. 5.3 in the middle of reduction, excluded from the acquired movie during reduction, and d) Enlargement of indicated area in Figure 5.3a. The fringes show the presence of both Co_3O_4 and CoO phases in this stage.

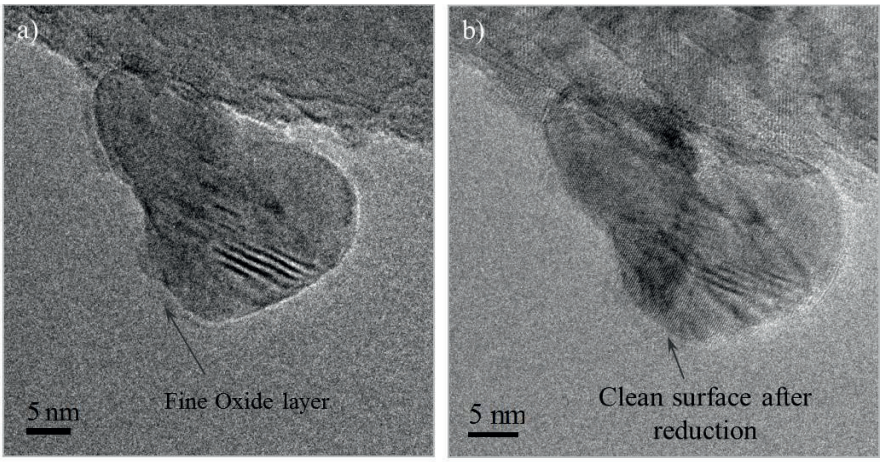

Figure 5.4: a) formation of an oxide layer on the surface of cobalt aggregate at T= 233°C, b) cobalt aggregate after re-reduction at T=360°C under H_2 gas.

The reduced sample was left overnight in the TEM vacuum and at the ambient temperature inside the microscope. The analysis performed on the day after showed partial oxidation of cobalt nanoparticles as illustrated in Figure 5.5. Both Figure 5.5a and Figure 5.5b show a layer of oxide around the cobalt nanoparticles. It is interesting to see that the metallic core in the Figure 5.5a contains the defects in the structure and it seems that the defects do not continue through the oxide shell.

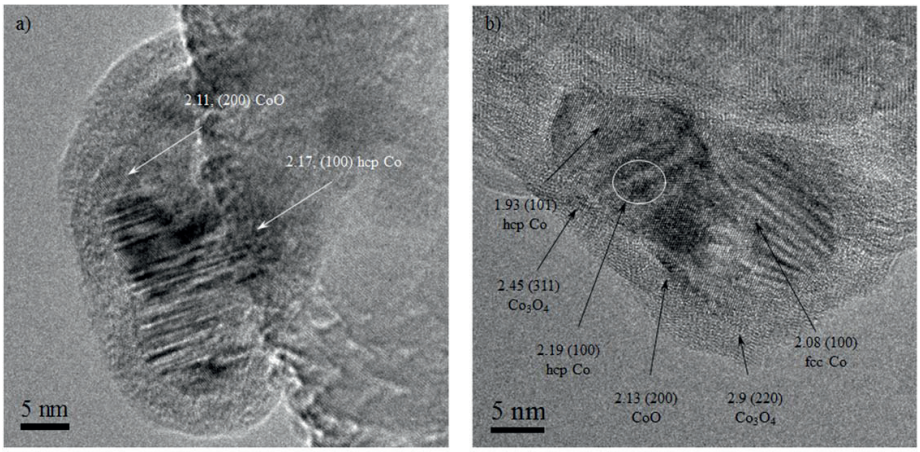

Figure 5.5: a) HRTEM image of the partially oxidized cobalt aggregate at room temperature and under H_2 flow, b) HRTEM image of cobalt aggregate while the sample was left overnight inside the microscope.

Different modifications to the ETEM configurations and operation were evaluated to prevent the re-oxidation of cobalt nanoparticles. Moreover, a residual gas analyzer was applied to monitor the components of the gas in the vacuum of the cell during the reduction experiment.

RGA Data Analysis

Analysis of RGA data is important in establishing the reason for re-oxidation of the cobalt metal particles at room temperature in the ETEM vacuum system. In the ETEM, RGA was used to measure the ion currents for about 10 different components. H_2O and O_2 can cause the re-oxidation. Therefore, here these two gases and H_2 as the input gas, are considered. Details are presented in appendix B. Detailed RGA data showed that with increasing the H_2 in the system the amount of H_2O increased proportionately, Fig. 5.6, while the level of O_2 in the vacuum was below the detector limit. The 6.5% level of H_2O with the H_2 gas, is concluded to be the reason for re-oxidation of the metallic cobalt as the temperature was reduced after reduction at 360C°. In general, the partial pressure of H_2O is high in the ETEM CELL due to the combination of water contamination from the goniometer, the gas inlet system and insufficient pumping of the ECELL in ETEM mode.

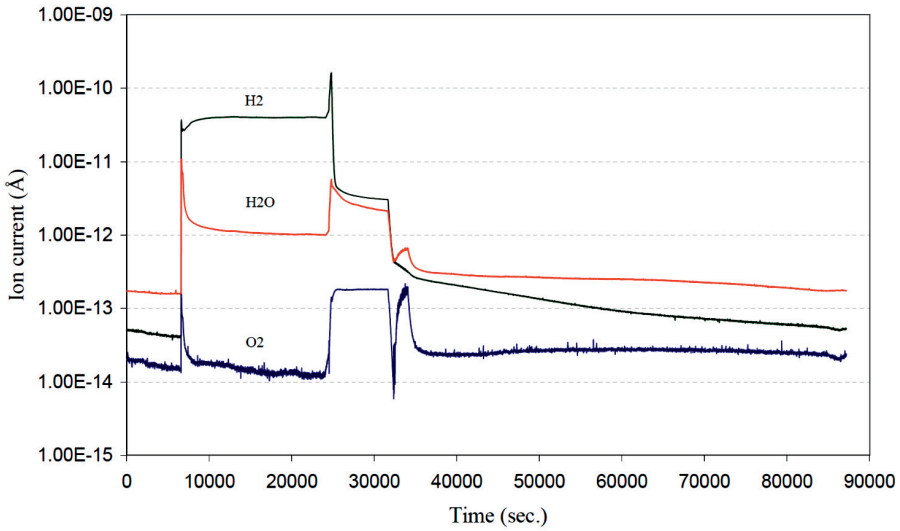

Figure 5.6: Ion current measured by RGA for H_2, H_2O and O_2 during and after reduction.

In the present study, attempts were made in order to decrease the H_2O content in the reducing gas. The H_2 gas supply is transported from a central gas system, which is about 30 meters far away from the microscope. In a subsequent experiment, a gas bottle was installed close to the

microscope and tested. No changes were observed in the level of H_2O in the RGA data measurements.

Table 5.1 Different applied ETEM operation procedures to control the re-oxidation.

Applied method\Temperature	Ambient Temperature	250 ˚C	360 ˚C
IGP and Cold Trap $\sim10^{-7}$ mbar	Metal	Metal	Metal
TMP (H_2 flow) $\sim10^{0}$ mbar	Oxide	Metal/Oxide	Metal
TMP+ Bypass open $\sim10^{-1}$ mbar	Oxide	Metal/Oxide	Metal

The contamination in the H_2 can also be due to the plastic pipes, which are used to connect the gas inlet into the microscope. Replacing them by metal pipes may give better results. However, there was not the possibility to try this in this study. In order to improve the vacuum operation and prevent the oxidation of cobalt particles at ambient temperature, different ETEM procedures were tried. Table 5.1 shows each method and the level of vacuum after its application.

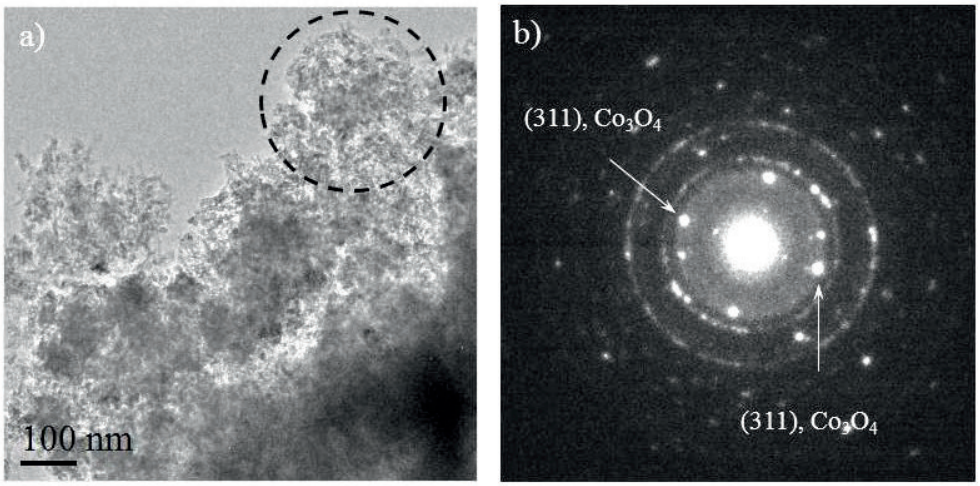

Figure 5.7: a) TEM image and b) diffraction pattern of the *20%Co/0.5%Re/γ-Al_2O_3* before reduction from the position indicated.

The only way that cobalt particles supported on α-Al_2O_3 stayed metallic at low temperature was under ultra-high vacuum and this level of vacuum was obtained by switching the microscope from ETEM mode to the ultra-high vacuum mode quickly after reduction.

Reduction of Cobalt Oxide Supported on γ-Al_2O_3

A sample with *20%Co/0.5%Re/γ-Al_2O_3* was analysed by HRTEM, STEM and EELS before reduction. Then the sample was reduced with the same procedure explained above; 3.4 mbar H_2 and at 360 C°. After reduction, the sample was analysed again by HRTEM, STEM and EELS, while it was still under reduction conditions. After analysis, the temperature was decreased to ambient temperature and the cobalt nanoparticles stayed reduced.

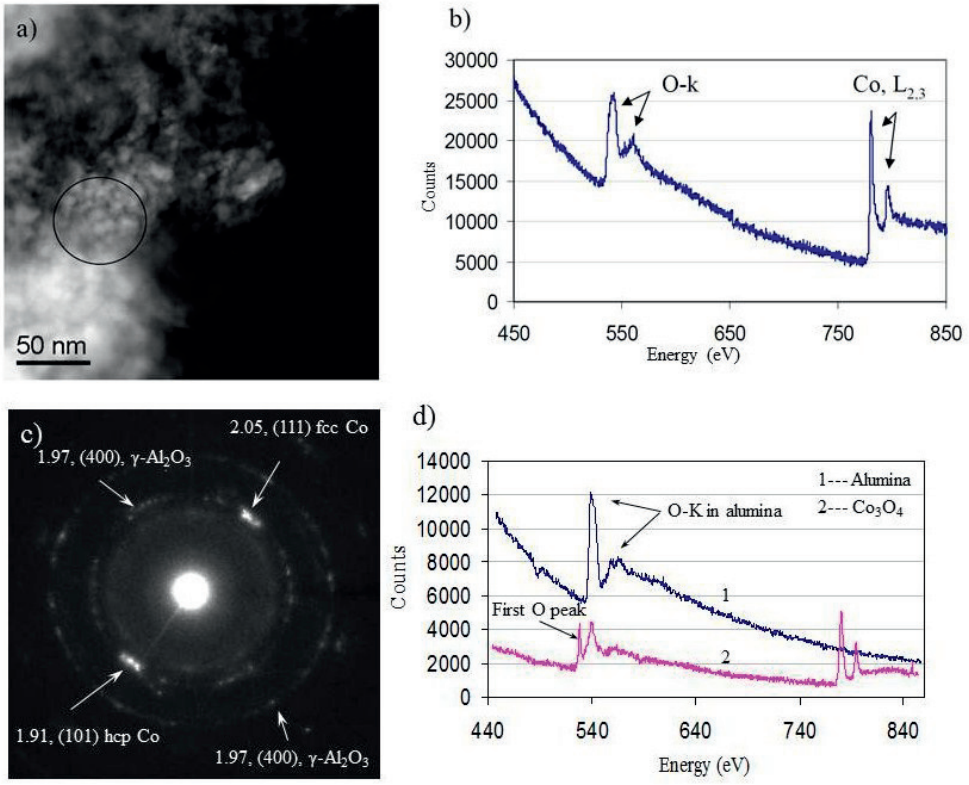

Figure 5.8: a) STEM image, b) EELS spectrum from indicated area after reduction at 200 °C and under vacuum in ETEM mode, c) diffraction pattern after reduction, confirming the presence of metallic cobalt, and d) Comparison of O-k edge from Co_3O_4 and γ-Al_2O_3.

Figure 5.7 shows a TEM image and its diffraction pattern before reduction. The diffraction pattern shows the presence of Co_3O_4 phase. Figure 5.8 shows STEM, corresponding EELS spectrum and diffraction pattern after reduction. The EELS spectrum was taken at 200 ˚C˚, while there was no gas in the system. Figure 5.8c compares the EELS Spectra obtained from alumina and Co_3O_4 in the same energy range. Spectrum 1 shows the O-K edge in alumina and spectrum 2 shows O-K and Co-$L_{2,3}$ edges in Co_3O_4. Comparison shows that the oxygen near edge fine structure obtained from Co_3O_4 and alumina is different. The first near edge peak (indicated in the spectrum) from Co_3O_4 is not present in the alumina spectrum [98,99]. Figure 5.8b shows that the oxygen fine edge related to the cobalt oxide is not present in this spectrum and the presented oxygen peak is due to the overlapping alumina, which confirms the reduction.

5.3.2 Preliminary Studies on Cobalt Catalyst under Fischer-Tropsch Condition

The Re promoted cobalt catalyst supported on γ-Al_2O_3 was reduced with H_2 at 360 ˚C in the ETEM and it was cooled down without H_2 flow to the ambient temperature. The sample stayed reduced at room temperature. Then FT reaction was tested for this catalyst, by increasing the temperature to 220 ˚C followed by introduction of mixture of H_2/CO=2. The gas pressure in the ETEM was about 6 mbar, which is far from the industrial FT pressure (20 bar). Under these conditions the sample stayed reduced and no oxidation was observed.

Figure 5.9 shows a TEM image of cobalt aggregate supported on γ-Al_2O_3 under FT reaction conditions. Figure 5.9a is TEM image of cobalt aggregates supported on alumina and Fig. 5.9b is a diffraction pattern from an indicated area in Fig. 5.9a. During CO/H_2 introduction, no significant changes were observed in the catalyst and stayed reduced. Rønning et al. [100] have studied similar catalyst with XRD and XANES and they did not observed any significant changes in the catalyst structure under FT condition (210 °C, 18 bar). However, at higher temperature, under methanation condition, (400 °C, 10 bar), they observed sintering of cobalt particles and further reduction of partially reduced particles. Sintering of cobalt nanoparticles may be related to the re-crystallization of faulted cobalt nanoparticles. It has been discussed in the paper III, that the fcc cobalt tends to transform to hcp Co and martensitic transformation occurs in the structure. Although the transition occurs in the faulted fcc/hcp

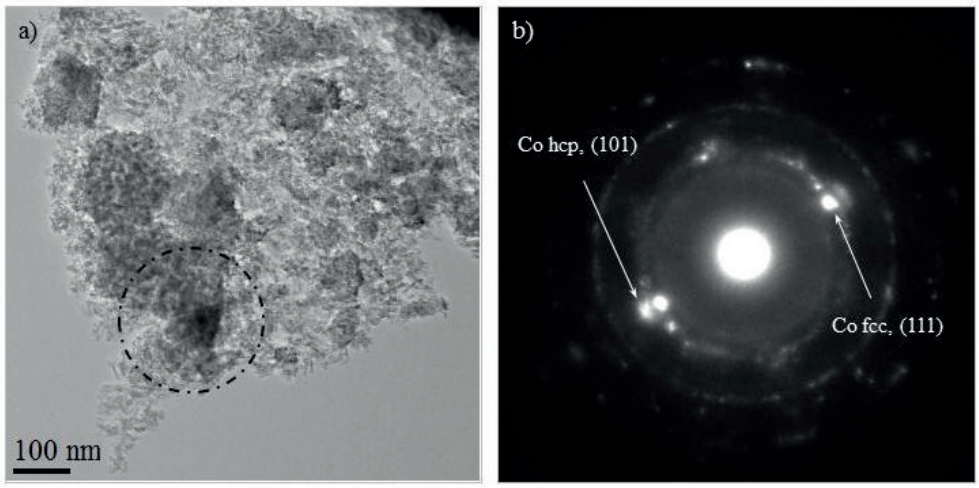

Figure 5.9: a) TEM image of 20%Co/0.5%Re/γ-Al_2O_3 under mixture of Co and H_2 with CO/H_2=2 and at 220 °C, b) diffraction pattern from indicated area, confirming the metallic state of the catalyst under these conditions.

nanoparticles, the small particles tend to keep their fcc structure even under FT reaction. To obtain definite conclusions, further ETEM experiments are needed.

5.4 Electron Beam Damage

The electron beam, which generates useful information in the TEM, has the drawback of damaging the sample. The amount of radiation damage is proportional to the electron dose [101]. The electron beam may damage the sample in two ways: Radiolysis and knock-on damage [5,95]. Radiolysis occurs as a result of ionization, in which inelastic scattering breaks the chemical bonds of certain materials. Knock-on damage is due to direct displacement of atoms from crystal lattices, which creates point defects. At high beam energies radiolysis is reduced while, the knock-on damage is dominant.

In ETEM, the electron beam may also influence the gas-solid interactions. Gas molecules can be ionized by high energy electrons in the beam or by low energy secondary electrons emitted from the specimen, changing their reactivity. Therefore, blank experiments (in the absence of the electron beam) are required to determine the beam effect. In the ETEM experiments in this study, the alumina substrates were nearly stable under the beam. However, beam damage was observed in the areas which were exposed for a long time. Figure 5.10 shows an example of occurrence of beam damage on the α-Al_2O_3 substrate. In figure 5.10a the substrate is starting to be damaged by the electron beam. In Figure 5.10b the substrate shows severe damage and has lost its crystallite structure.

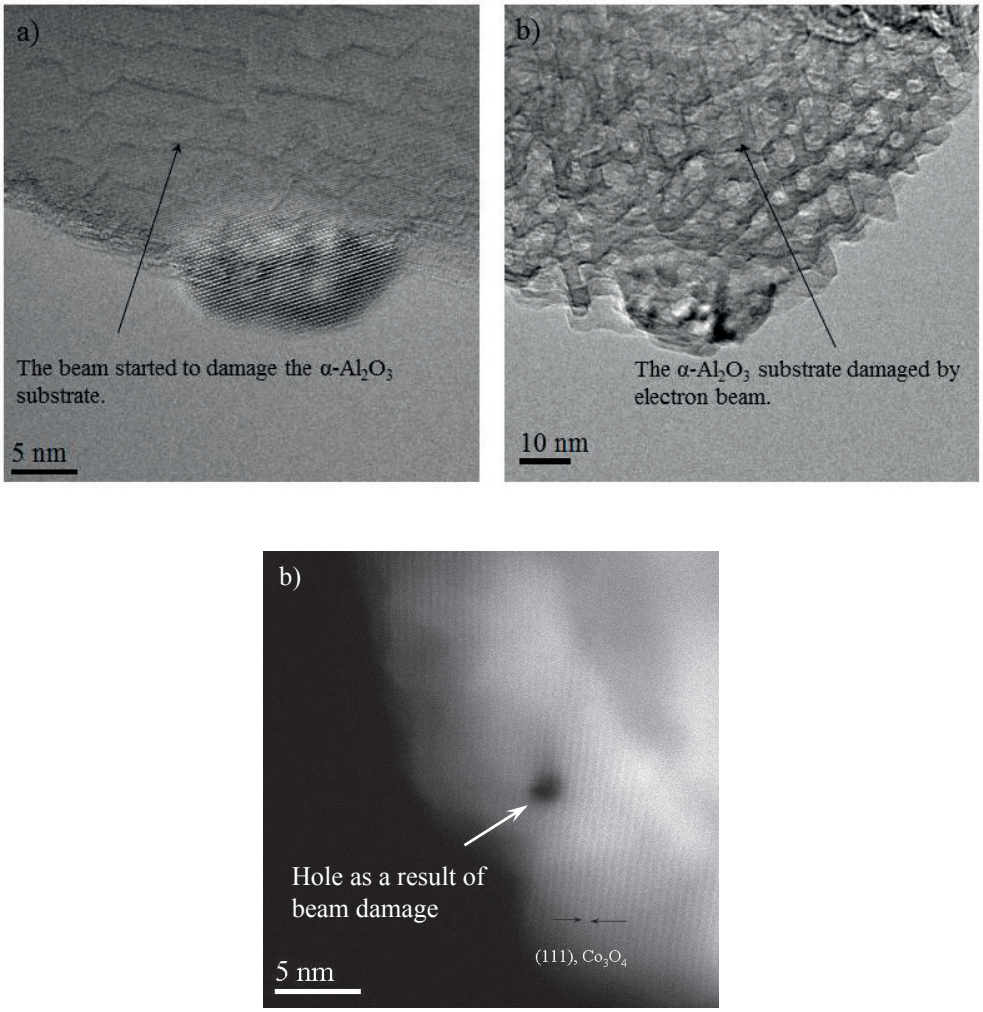

Figure 5.10: a) The α-Al_2O_3 substrate has started to be damaged by electron beam, b) The α-Al_2O_3 substrate exposed for a long time to the electron beam and damaged, images takesn by ETEM; and c) The hole in the cobalt oxide, due to beam damage which is generated after EDS point analysis in the ATEM.

In EDS point analysis with long exposure time in both TEM and ETEM, beam damage was observed in cobalt phases. As a result of beam damage, holes appeared in the examined area.

5.5 Influence of Image Correction on the Quality of TEM Image

As mentioned above, the presence of aberration corrections in the TEM instrument improves the spatial resolution significantly and reduces the image delocalization. Image delocalization means that the image details are displaced from their true location in the specimen. The

delocalization effect is easily observed in the interfaces, specimen edges or on surface of the nanoparticles [102,103]. This effect becomes more important in HRTEM images and makes the interpretation of the images difficult [102,104].

Figure 5.11 compares the results from two different, corrected and non-corrected, TEM instruments. Figure 5.11a shows the HRTEM image of a cobalt nanoparticle, which was taken in the ETEM with aberration correction (360 ˚C and under 3.4 mbar H_2 gas). Figure 5.11b is HRTEM image of similar cobalt nanoparticle at ambient condition taken in the non-corrected JEOL2010F. Comparison of these two images illustrates the delocalization effect around the surface of cobalt nanoparticle in the TEM image from non-corrected instrument. Although the

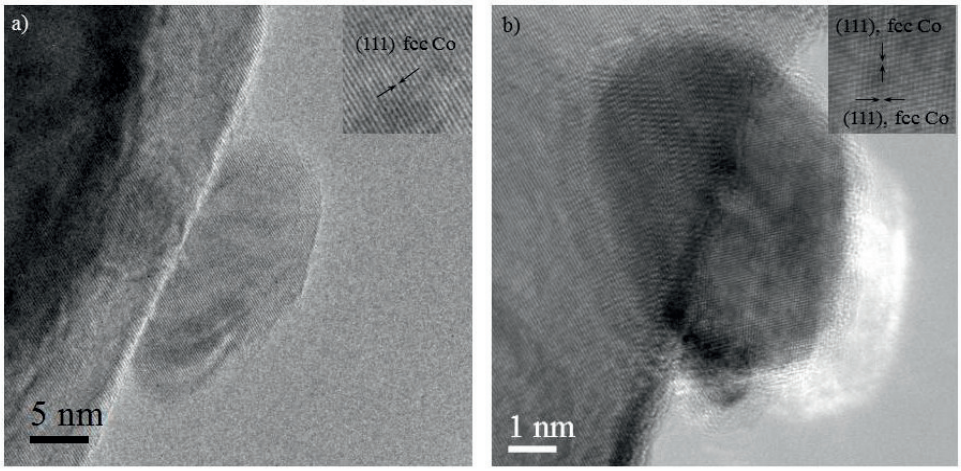

Figure 5.11: a) HRTEM image of cobalt nanoparticle at 360 ˚C and under 3.4 mbar H_2 taken by aberration corrected and monochromated ETEM instrument, b) HRTEM image of cobalt nanoparticle at ambient condition taken by JEOL2010F.

TEM image from the corrected instrument is under reduction condition, the edge of the cobalt surface is more clearly defined at the atomic scale.

5.6 Summary

Both cobalt oxide nanoparticles supported on α-Al_2O_3 and γ-Al_2O_3 are reduced under 3.4 mbar H_2 flow and at 360 ˚C in ETEM. Cobalt nanoparticles supported on α-Al_2O_3 did not stay reduced at room temperature, while the cobalt nanoparticles supported on γ-Al_2O_3 did. This is due to the reactive nature of cobalt nanoparticles but also it emphasizes that the α-Al_2O_3

support has a coarse pore structure. Therefore, the cobalt nanoparticles have higher chance to interact with the gases in the surrounding and oxidation are expected. By comparison, the γ-Al_2O_3 support has a much finer pore structure, which protects the sample from rapid re-oxidation by reducing the exposed surface area and limiting the access of oxidizing agent. The influence of different alumina supports on the Co_3O_4 reduction and on the FT synthesis performance have been studied by Borg et al [105].

Having the cobalt catalyst under the mixture of CO/H_2 at 220 and at low pressures (~ 6 mbar) in the ETEM did not show obvious changes in the catalyst.

Chapter 6

Ex-situ TEM Study of Cobalt Catalysts

In addition to the in-situ TEM technique described in chapter 5, ex-situ TEM methods can also be used to investigate the catalysis materials. Compared to in-situ analysis, the ex-situ study is less TEM time-consuming, with more simple microscope operation. Ex-situ TEM examination gives the opportunity to study the sample before and after chemical reaction, while the reaction is performed outside the TEM column. A special TEM sample holder and procedure are needed to keep the sample under reaction condition and then the transfer the sample to the microscope.

Two different ex-situ TEM methods have been considered in the present study. In the first, an environmental reaction cell holder was used to study the catalysts before and after reduction. In the second method the reduced catalysts samples were transferred to a glove box under inert gas (Ar) and were then transferred to the microscope using a normal TEM sample holder under inert conditions. In this chapter the details of both methods are explained and some of the obtained results are presented.

6.1 Ex-situ Reaction with Environmental Cell Holder

The ex-situ reduction of the supported cobalt oxide catalysts by using the environmental TEM holder are described in the following.

a)

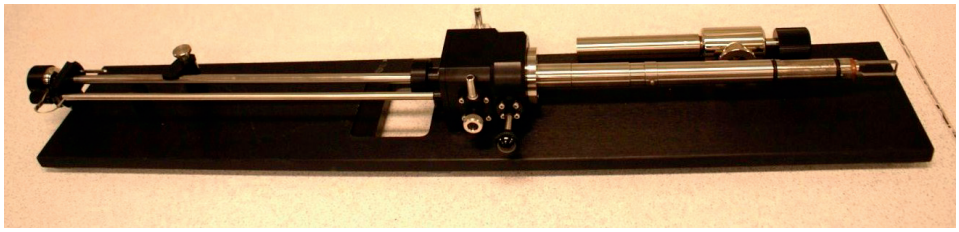

b)

1. Gas reaction chamber
2. Holder loading stand
3. Arm of holder loading stand
4. Support
5. Isolation gate valve
6. Socket for thermometer
7. Gas inlet
8. Gas outlet to the vacuum pump

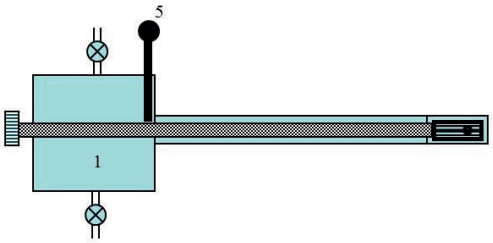

c)

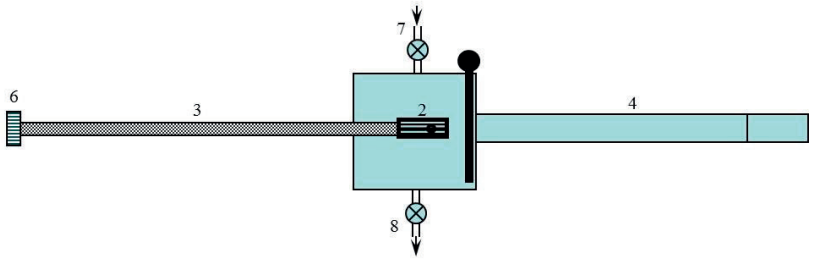

Figure 6.1: a) The environmental reaction cell holder, b) Schematic outline of the ex-situ reaction set up. The specimen is in TEM imaging position; c) The specimen is inside the chamber under gas purging.

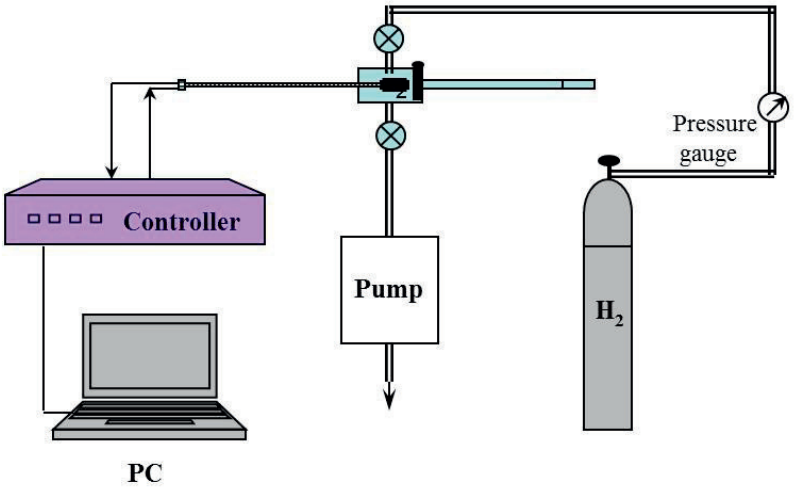

Figure 6.2: Schematic view of ex-situ reaction set-up

6.1.1 Experimental Set-up

The ex-situ reaction set-up consists of an environmental gas reaction holder, a control system for sample heating/cooling, a pumping system to evacuate the reaction chamber, and gas purging system.The details of experimental set-up and its components are described below.

Environmental reaction cell holder

The Gatan HHST 4004 environmental gas reaction holder shown in Fig. 6.1a is designed to hold the TEM sample in a sealed vessel. The reactions between the catalyst sample and the reacting gas take place inside the chamber under controlled pressure and temperature. The required reaction temperature is provided by a small heating element surrounding the sample cradle and the temperature is measured by a thermocouple.

The TEM sample, which has been dispersed on a TEM cupper grid, was located in the holder loading stand and retracted inside the chamber (Fig. 6.1). The chamber in the holder is equipped with a gate valve, a gas inlet and a gas outlet (Fig. 6.1). The gate valve is closed after retracting the sample inside the chamber in order to keep it under reaction environment or under vacuum. After pumping, the reducing gas is purged from the inlet into the chamber and it is pumped out from the outlet. This maintains a continuous flow of reducing gas over the sample under low pressure such as 4 mbar. Figure 6.2 is a schematic view of the ex-situ reaction set-up.

After reaction, the chamber is pumped to a good level (<10^{-5} mbar) of vacuum and then the holder is transferred to the TEM.

Pumping systems

Two pumps are used in the ex-situ set up; a rotary pump and turbo molecular pump. The single stage rotary pump (Pfeiffer BALZERS model) is first used to decrease the pressure and after reaching the suitable level, which is nominally 1×10^{-3} mbar, the turbo pump (ALCATEL-ANNECY) starts working. This pumping system can provide a high vacuum with pressures lower than 10^{-5} mbar. The vacuum level inside the chamber is measured by a penning gauge (PENNINGVAC PM 410).

Gas system

Diluted hydrogen gas with 10%H_2-90%N_2 composition was used as the reducing gas at the present work. The pressure of this gas during the reaction in the reaction holder was measured by a digital vacuum meter (Thyracont compact digital vacuum meter, VD 84m), which measures in the pressure in the range of 1000-0.001 mbar.

Heating/cooling system

The reaction temperature of the sample is controlled by an ITC503 temperature controller from Oxford instruments. This is controlled by Object Bench software. This is a general-purpose programme for controlling instruments from a computer system.

6.1.2 Ex-situ Cobalt Oxide Reduction

Ex-situ Reduction of Cobalt Oxide Supported on α-Al_2O_3

A cobalt oxide catalyst (12%Co/0.5%Re/α-Al_2O_3) was studied by TEM after reduction with the environmental reaction cell holder. The TEM sample was prepared by dispersion of the crushed catalysts powder on to a cupper grid supported by carbon film. The sample inserted into the TEM holder, retracted into the chamber, and transferred to the reaction set-up. For reduction, diluted H_2 was introduced to the chamber. When the pressure reached around 4 mbar, temperature increased to 360˚C with ramping rate of 1C/min. After holding the sample at this condition for 16 hours, the chamber was pumped and while the vacuum inside the chamber was better than 10^{-4} mbar the sample holder was transferred to the TEM goniometer. Then the pumping system was disconnected from the holder. The gate valve was opened and the sample moved into the TEM column.

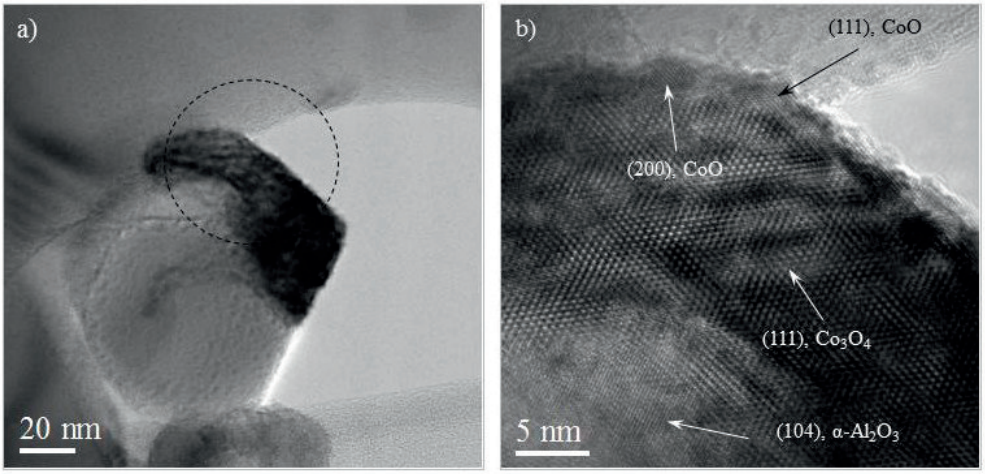

Figure 6.3: a) BF TEM image of 12%Co/0.5%Re/α-Al_2O_3 and b) HRTEM image of an edge of the indicated particle in Fig. 6.3a.

Figure 6.3 and Fig. 6.4 are examples of Re promoted cobalt catalyst supported on α-Al_2O_3. Figure 6.3a is a BF TEM image of the catalyst in low magnification and Fig. 6.3b is HRTEM image of the particle indicated in Fig. 6.3a. The HRTEM image shows a thick layer of Co_3O_4 surrounded by a fine layer of CoO. Phases were identified by direct measurement of inter planar spacings. This experiment performed with non-modified reaction cell holder in which only there was one entrance for gas and pumping.

Figure 6.4a shows a low magnification TEM image of a similar catalyst after reduction using the reaction cell holder after modification with two separate entrances for gas and pumping. Fig. 6.4b is HRTEM image of an indicated area in Fig. 6.4a. The fringes in HRTEM image, shows the d value of 1.92 Å corresponding to (101) planes of hcp cobalt. This image confirms the reduction of Co_3O_4 to Co. However, the diffraction pattern from a larger area including this particle shows the presence of a significant level of CoO in the catalyst after reduction.

These two examples indicate the partial reduction of cobalt oxide and suggest that the reduction time was not sufficient to complete the reduction procedure or the gas flow was not adequate during the reduction. Insufficient H_2 flow over the sample region can be due to having only one entrance on the cell. In the second example the modified cell provide better gas flow. However, it seems that the gas flow is not sufficient to reduce the bulk of the cobalt nanoparticles and this causes the surface reduction or reduction from Co_3O_4 to CoO.

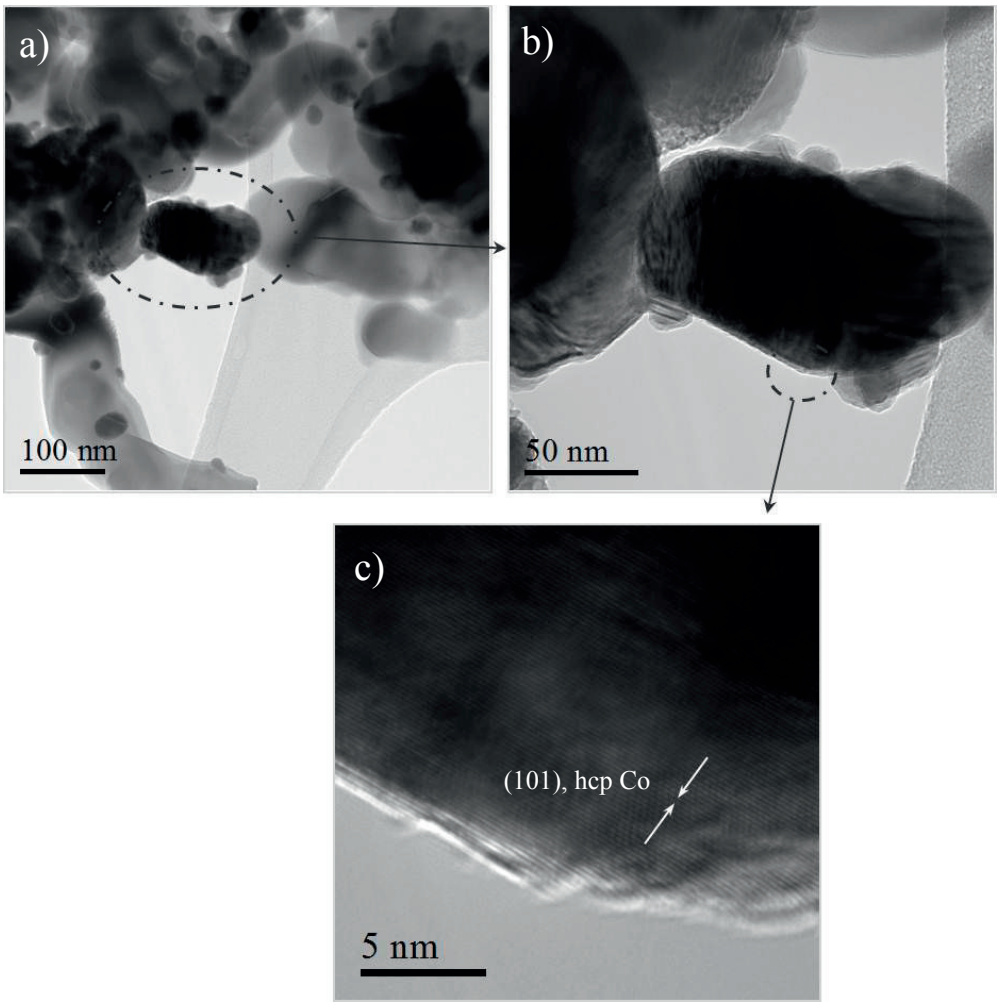

Figure 6.4: a) BF TEM image of the cobalt oxide supported on α-Al_2O_3 after being for 16 hours under reaction condition, b) BF TEM image of a large cobalt aggregate indicated in Fig. 6.4a and c) HERTEM image of indicated area in Fig. 6.4b.

Ex-situ Reduction of Cobalt Oxide Supported on γ-Al_2O_3

A cobalt oxide catalyst (20%Co/0.5%Re/γ-Al_2O_3) was studied after reduction by using the environmental reaction cell holder and with similar procedure as mentioned before in this chapter. The TEM sample was prepared by dispersion of the crushed catalysts powder on to a cupper grid supported by carbon film. After holding the sample under reduction condition for 16 hours, the hydrogen flow was stopped and glove bag was used to transfer the sample to the microscope for examination. The glove bag was connected to the TEM goniometer and filled

with Ar gas. More details about using the glove bag for transferring the sample holder to the TEM column will be described later in this chapter

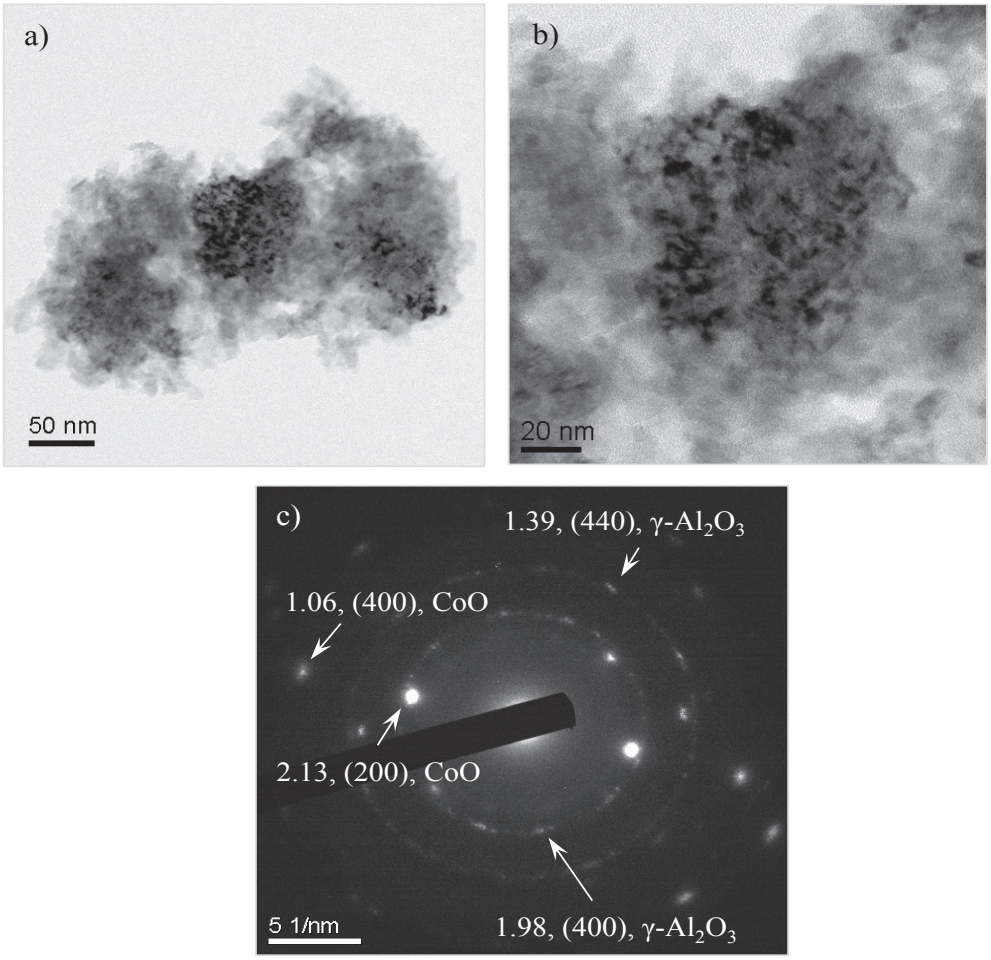

Figure 6.5: a) BF TEM image of the cobalt oxide supported on γ-Al_2O_3 after being for 16 hours under reaction condition, b) BF TEM image of the middle aggregate in Figure 6.5a in higher magnification. c) Diffraction pattern of the aggregate in Figure 6.5b where the diffraction pattern confirms the reduction to CoO.

Figure 6.5 shows an example of the results from TEM analysis of the catalysts after reduction. Figure 6.5a, is a BF TEM image of the catalyst particles, in which the dark gray areas are cobalt-containing phase and the light gray areas are the alumina support. Figure 6.5b shows the large cobalt oxide aggregate in the Figure 6.5a at higher magnification. It is seen in this image that the cobalt oxide nanoparticles started to reduce and as a result of shrinkage during reduction, they are visible individually in some areas. Figure 6.5c shows a diffraction pattern

from the same aggregate as in Figure 6.5b and the diffracting spots confirm the presence of CoO in the aggregate. There are weak spots in the diffraction pattern which may correspond to the metallic cobalt. However, the d values from cobalt oxide and metallic cobalt are close to each other and it is difficult to conclude the certain presence of metallic cobalt.
This explains that the most of the Co_3O_4 nanoparticles have been reduced to CoO but probably the reducing condition was not strong enough to reduce it further to metallic cobalt. Ozkaya et al. have also studied the reduction of similar un-promoted catalyst in an ex-situ gas reaction holder [106]. They have studied the reduction experiment at 400 ˚C with 4 mbar diluted H_2 after 1h and they observed the reduction of Co_3O_4 to CoO but not to metallic cobalt.

In order, to find the reason for limited reduction, the reduction procedure was compared with other successful lab reductions of similar material. For example; reduction in a Raman spectroscopy rig with the exact same temperature conditions and same ramping rate but with different H_2 flow at atmospheric pressure is successful. Since the temperature was the same as in the ex-situ experiments and the sample was left for the same period of time under reduction condition, the reason might be due to the lower hydrogen pressure. On the other hand, the in-situ reduction of the same material has been achieved by ETEM (Chapter 5) while the sample stayed for about 2 hours under 3.4 mbar diluted H_2 and at 360 ˚C.

With regard to the above discussion, the possible reasons for limited reduction of the catalyst are:

1- As explained earlier, the reaction cell holder has two entrances. The hydrogen is introduced to the sample from the inlet while it is pumped from the outlet. The pumping rate to some extent was controlled by the valve in the setup. However, having a constant flow of hydrogen gas, with high pumping rate, decrease the chance of H_2 molecules to react with the catalyst. It means that the pumping condition may affect the gas flow and influence the reduction procedure.
2- There might be leakage in the cell. Since the pressure inside the cell during reduction is lower than atmospheric pressure, any tiny leakage leads to the penetration of air into the chamber and cause the oxidation of active cobalt nanoparticles.
3- The thermocouple may not measure the temperature of the sample accurately since it is sitting on the grid.

6.2 Inert Sample Transfer to TEM

As mentioned earlier in the inert transfer method, the reduced sample is kept in the glove box and transferred to the TEM. Since the sample is sensitive to the air, the TEM specimen is prepared inside the glove box. The procedure followed was to insert the TEM grid in the holder outside the glove box, transfer the TEM holder into the glove box, and then disperse the crushed catalyst powder directly onto the grid. The TEM holder was then covered by the vacuum storage container to carry it to the microscopy room. Two different vacuum storage containers were used in this study. One is made by Fischione (model 9010) and the other made in the workshop at the NTNU physics department (Figure 6.6). In order to prevent exposure to air while inserting the sample to the microscope, a removable glove bag was placed around the goniometer and maintained with Ar/N_2 overpressure. Figure 6.7 shows a Picture of how the glove bag is connected to the TEM.

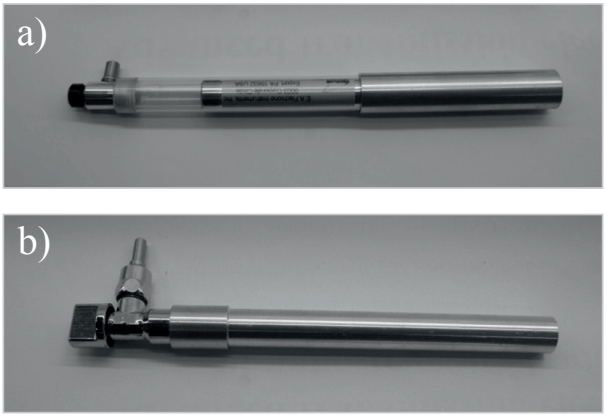

Figure 6.6: Vacuum storage container used to trasnfer the sample from glove box to the TEM, a) Fischione model 9010, b) Made in fabric in Physics department at NTNU.

The TEM holder with its vacuum storage container is placed inside the bag and the bag is filled with argon gas and evacuated manually several times in order to make argon prevailing environment inside it. TEM holder is then removed from the container and inserted into the TEM quickly. With this method, the supported cobalt nanoparticles are retained as metal and stay reduced in the TEM vacuum.

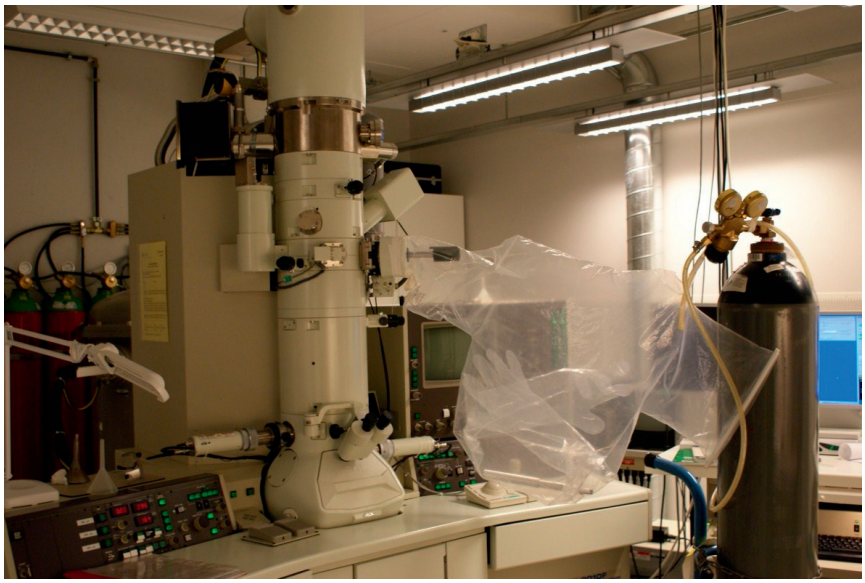

Figure 6.7: The connection of the glow bag to the TEM goniometer.

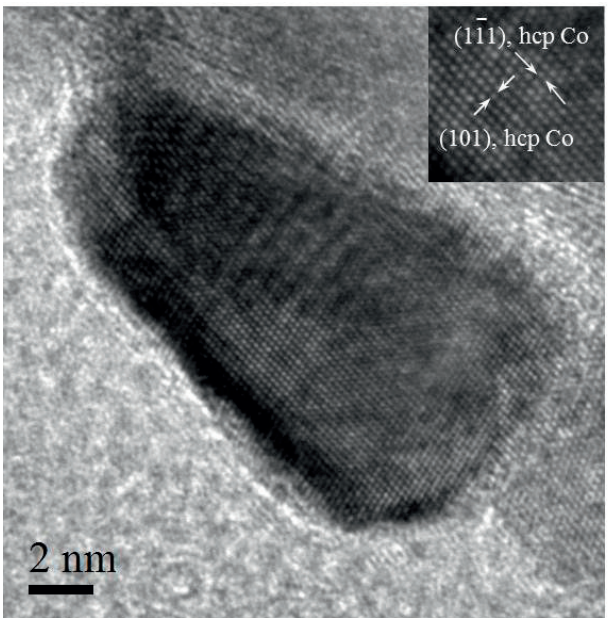

Figure 6.8: HRTEM image of cobalt nanoparticle after reduction, The two dimensional fringes corresponds to [121] zone axis of hcp cobalt.

Figure 6.8 shows HRTEM images of 12%Co/0.5%Re/α-Al_2O_3 that was transferred from a glove box to the TEM. Two dimensional fringes in this image show the *d* values of 1.89Å and 1.93Å, which corresponds to a [121] zone axis of the hcp cobalt structure.

The inert transfer method has earlier been applied successfully to prepare the air sensitive materials such as alanates for the TEM studies [107]. Here, this method was extensively used to study the structure of supported cobalt catalysts after reduction.

Chapter 7

Conclusions

The main scientific objective in this PhD study was to characterize catalyst for Fischer-Tropsch (FT) synthesis by Transmission electron microscopy (TEM). For this purpose, cobalt nanoparticles supported on two different α-Al_2O_3 and γ-Al_2O_3 substrates were selected and characterized by different TEM techniques such as STEM, HRTEM, EELS and electron tomography. The cobalt phase nanoparticles were studied in oxide form (after calcination) and in metallic form (after reduction). The analyses of the reduced material were carried out both through in-situ TEM analyses, with aberration corrected ETEM, and through ex-situ TEM analysis with a conventional FEG TEM. The secondary objectives of this project were to develop electron tomography at NTNU, and assemble reaction holder set up to study catalysts materials. Parallel with these objectives, Ni based on hydrotalcite, which is a catalyst for steam methane reforming was also studied. The conclusions from these studies are summarized in the following.

7.1 Cobalt FT Catalysts

a) Basic TEM analysis of calcined and reduced Co on γ-Al_2O_3 substrate

Basic electron microscopy techniques such as bright field and dark field on the calcined and reduced cobalt catalyst supported on γ-Al_2O_3 clarified the following points:

- The Co_3O_4 appears as aggregates in the alumina substrate and forms a continuous network with a common orientation in each aggregate.
- The cobalt aggregate size measurements, before and after, reduction indicate that the aggregate size did not change significantly due to reduction. The aggregates keep their

overall shape during reduction, while Co_3O_4 nanoparticles inside the aggregates are influenced by the reduction.

- After reduction the cobalt nanoparticles appear as separate particles inside the aggregate, which is due to 20% shrinkage in the diameter of the particles by reduction.
- After reduction, the common orientation in the aggregate is lost and the individual cobalt nanoparticles are more randomly orientated.
- The cobalt particle size and crystallite size were measured through the bright field and dark field images and the results are in good agreement with XRD data. Individual cobalt nanoparticles with 10.0 nm size contain crystallites with 5.4 nm in size. This describes the presence of crystal defects in the cobalt nanoparticles.
- In the reduced catalysts, both fcc and hcp metallic cobalt phases co-exist and the fcc is the dominant phase. The structure of the cobalt nanoparticles is size dependent. Small particles tend to have fcc structure, whereas, large particles have mostly hcp structure.
- Structural faults are present in the cobalt nanoparticles, which are proposed to be due to martensitic transformation, between Co fcc and Co hcp.

b) Electron tomography analyses

Scanning TEM (STEM) tomography was applied to study both calcined and reduced cobalt catalysts systems. The results give the following conclusions:

- Developing electron tomography was very challenging both for software selection and its application to series alignment and reconstruction.
- The electron tomography experiments were performed with JEOL2010F which made challenges, due to instability of the goniometer.
- Among different software packages, Digital Micrograph and Imagej were applied to process the data and it was found that each package has advantage and disadvantages.
- The 3D analysis of the calcined 20%Co/0.5%Re/γ-Al_2O_3 material confirmed that the cobalt aggregate has inter-grown in the alumina pores. The Co_3O_4 nanoparticles generally have common orientation in the aggregate and no physical separation of the Co_3O_4 particles in the aggregate was observed.
- The 3D results from the reduced 20%Co/0.5%Re/γ-Al_2O_3 catalyst shows the physical separation of the cobalt nanoparticles in the aggregate, due to the shrinkage of the Co_3O_4 particles during reduction. This is important from catalytic point of view as channels provide a path for gas penetration into the aggregate.
- The 12%Co/0.5%Re/α-Al_2O_3 catalyst has a different cobalt distribution compared to γ-Al_2O_3 catalyst, due to the coarse structure of α-Al_2O_3 and low porosity.

- The 3D data from 12%Co/0.5%Re/α-Al_2O_3 clarified that some of the Co_3O_4 nanoparticles have porous structure in the calcined condition.
- The above pores do not appear in the 3D data of reduced catalyst and a smaller cobalt particle size is observed compared to the calcined material and the cobalt nanoparticles appear fully dense.
- Due to long exposure of the specimen to the electron beam during tomographic acquisition, slight surface oxidation of the cobalt nanoparticles occurred in TEM sessions longer than a few hours. This is attributed to the electron beam interaction with any available H_2O molecules in the TEM column.

c) In-situ TEM studies

TEM studies by ETEM provided the following conclusions:

- It is possible to reduce Co_3O_4 supported on alumina in the ETEM. Phase transformation from Co_3O_4 to CoO, and then to metallic cobalt were observed in-situ.
- Oxidation of cobalt nanoparticles supported on α-Al_2O_3 was observed during cooling to room temperature. The rate of oxide formation increased under the electron beam. Slow oxidation was also observed for samples left in the TEM at ambient temperature overnight and about 3nm thickness of oxide layer formed around the cobalt nanoparticles.
- The cobalt supported on γ-Al_2O_3 stayed reduced at room temperature and even by leaving it overnight, it was still in metallic state. Different behaviour of the two catalysts during cooling is attributed to the different structure of the substrates. The γ-Al_2O_3 has a higher degree of porosity and cobalt nanoparticles are in the alumina pores. This protects them from re-oxidation.
- Under the electron beam, the re-oxidation of the cobalt nanoparticles on the γ-Al_2O_3 substrate was observed.
- Electron beam damage was observed on both α-Al_2O_3 and γ-Al_2O_3 substrates.
- CO gas introduction to the reduced 20wt%Co/0.5wt%Re/γ-Al_2O_3 catalyst at ambient temperature produced carbon contamination on the sample. This prevented from TEM analysis.
- Initial experiments on the Introduction of a mixture of H_2 and CO (1:2) at 220C° (close to FT conditions) to the cobalt supported on γ-Al_2O_3 produced no obvious changes in the structure of the cobalt nanoparticles.

d) Ex-situ TEM studies

The conclusions from ex-situ experiments performed with two different methods are summarized as follows:

- When the modified reaction cell holder was used to reduce the 12wt%Co/0.5wt%Re/α-Al_2O_3 catalyst material, the majority of the Co_3O_4 nanoparticles reduced to CoO. However, some particles were reduced to metallic Co.
- Using the reaction cell holder to reduce the 20wt%Co/0.5wt%Re/γ-Al_2O_3 catalyst, most of the Co_3O_4 nanoparticles reduced to CoO. There were a few weak spots in the diffraction pattern which can be related to the metallic cobalt. However, the d values from CoO and metallic cobalt are close to each other and it was difficult to conclude the certain presence of metallic cobalt.
- In inert transfer of the reduced catalyst from glove box to the TEM, cobalt stayed reduced in the TEM vacuum. However, leaving the sample overnight, or in the areas which were under the electron beam for a long time (a few minutes at high magnification), the formation of a fine oxide layer was observed around the edges of the cobalt nanoparticles.

e) TEM studies of Re promoter

TEM Probe corrected instruments were applied for preliminary study of the location of Re promoter in the catalysts structure with the following conclusions:

- In the Re promoted catalyst, no segregation of Re was observed.
- High resolution STEM images confirm the random distribution of a very fine bright spots in the structure of cobalt nanoparticles. It is proposed that these are related to the presence of Re small clusters or atoms in the catalyst.

7.2 Ni *Catalyst for Steam Methane*

Ni based on hydrotalcite material was studied by TEM techniques in different stages of preparation. The conclusions from the TEM results are summarized below:

- Before calcination, the catalyst has a compact structure of densely packed plate-shaped crystals.
- After calcination the hydrotalcite structure is transformed into the mixed oxides with well-developed layered structure. In this stage, NiO particles are not obvious in the structure.
- After reduction the phase separation occurs and a uniform distribution of Ni particles appeared in the structure.

- The 3D data analysis of the catalyst shows that the Ni nanoparticles are confined in porous nano-ribbons of mixed oxides with connected pore channels which provides good catalyst stability and access of gaseous reactants.
- The 3D microstructure of the catalyst can be related to its good selectivity and stability, providing a good example of the use of TEM for rational catalyst design.

Chapter 8

Recommendations for further Work

- Ultramicrotomy is a desirable sample preparation for TEM study of the calcined cobalt catalyst materials. It is suggested to mix the catalyst powder with resin and epoxy inside the glove box and leave it overnight. Quick ultramicrotomoy slicing outside the glove box may provide good TEM samples to investigate the structure of reduced materials. However, it may be necessary to enclose the whole process in a glove box to be effective.

- Preliminary in-situ TEM studies were performed on the 20%Co/0.5%Re/ γ-Al_2O_3 catalyst under CO/H_2 gas at 220 °C. However, due to the lack of time, in these experiments, the catalyst stayed for a short time (about 2 hours) under these conditions. It is interesting to examine the sample after being a longer time under these conditions.

- One challenge with studying the individual cobalt nanoparticles under reactant was a high porosity substrate such as γ-Al_2O_3. The porous substrate protects the cobalt nanoparticles from rapid re-oxidation, while makes it difficult to study their morphology. To understand the behaviour of these nanoparticles under gaseous reactant, it is suggested to use other small pore substrates such as $TiO_2/CeO_2/ZrO_2$, which are more stable towards reduction in the electron beam and individual cobalt nanoparticles are easily distinguishable.

- Application of fiducial markers in tomography of catalysts is recommended, which improve the alignment. Comparison of the results from fiducial marked samples with non-fiducial samples should be made. Au suspension can be mixed with the microtomy samples during preparation and it can be added to the dispersed sample after catalyst dispersion. Due to the lack of the time, in this study the focus was only on non-fiducial alignments.

- To study the location of Re in the catalyst structure, it is suggested to study the reduced material by probe corrected STEM. As glove bag can be used to transfer the reduced catalyst to the TEM.

- Image simulation for comparison with lattice resolution HAADF images to study the location of Re in the images of Cs probe corrected of the promoted cobalt catalyst is recommended. This can be extended to study the Co catalyst in reduced state.

References

1. www.vanleeuwenhoek.com

2. http://nobelprize.org

3. www.jameshillierfoundation.com/

4. P. Hawkes, The beginnings of Electron Microscopy, (Ed.), Academic Press, 1985.

5. D. B. Williams, C. B. Carter, Transmission electron microscopy, Plenium press, New York, 1996.

6. S. V. Kalinin, S. Jesse, J. Rodriguez, J. Shin, A. P. Baddorf, H. N. Lee, A. Borisevich, S. J. Pennycook; Spatial resolution, information limit, and contrast transfer in piezoresponse force microscopy; Nanotechnology 17 (2006) 3400-3411.

7. P. W. Hawkes, Electron optics and electron Microscopy, Taylor and Francis Ltd., London, England, 1972.

8. http://www.britannica.com

9. P. L. Gai, E. D. Boyes, Electron microscopy in hetereogeneous catalysis, Institute of Physics publishing, Series in microscopy in materials science, 2003.

10. http://www.naturalgas.org

11. Ø. Borg, Role of alumina support in cobalt Fischer-Tropsch synthesis, PhD thesis, NTNU, 2007:56.

12. www.power-hitachi.com

13. H. A. J. Van Dijk, The Fischer-Tropsch synthesis: A mechanistic study using transient isotopic tracing, Technical University of Eindhoven, NUGI, 2001, 813.

14. F. Fischer and H. Tropsch, the preparation of synthetic oil mixtures (synthol) from carbon monoxide and hydrogen, Brennstoff-Chem., 4 (1923) 267-285.

15. P. Sabatier and J. B. Senderens, New synthesis of methane, Compt. Rend. Acad. Sci., 134 (1902) 514-516.

16. F. Fischer and H. Tropsch, The synthesis of petroleum at atmospheric pressure from gasification products of coal, Brennstoff-Chem., 7 (1926) 97-104.

17. A. Heinzel, B. Vogel, P. Hubner; Reforming of natural gas—hydrogen generation for small scale stationary fuel cell systems; Journal of Power Sources, 105 (2002) 202-207.

18. E. O. Fernandez, CO2 acceptors for sorption-enhanced steam methane reforming, PhD thesis, NTNU, 2007:130.

19. C. A. Callaghan, PhD thesis, Kinetics and Catalysis of the Water-Gas-Shift Reaction:A Microkinetic and Graph Theoretic Approach Worcester Poly Technique institute, 2006.

20. P. Van Beurden, On the catalytic aspects of steam methane reforming, Report for Energy Research centre of Netherland, December 2004.

21. J. R. Rostrup-Nielsen, Production of synthesis gas, Catalysis Today, 18 (1993) 305-324.

22. M. A. Goula, A. A. Lemonidou and A. M. Efstathiou, Characterization of carbonaceous species formed during reforming of CH_4 with CO_2 Over Ni/CaO-Al_2O_3 Catalysts studied by various transient techniques; Journal of Catalysis 161 (1996) 626.

23. F. Cavani, F. Trifiro, A. Vaccari, Hydrotalcite-type anionic clays: Preparation, properties and applications, Catalysis Today, 11 (1991) 173-301.

24. E. Ochoa-Fernandez, C. Lacalle-Vila, K. O. Christensen, J. C. Walmsley, M. Rønning, A. Holmen and D. Chen, Ni catalysts for sorption enhanced steam methane reforming, Topics in catalysis, 45 (2007) 3-8.

25. L. He, H. Berntsen, E. Ochoa-Fernandez, J. C. Walmsley, E. A. Blekkan, D. Chen, Co-Ni Catalysts Derived from Hydrotalcite-like Materials for Hydrogen Production by Ethanol Steam Reforming, Topics in Catalysis, 52 (2009) 206-217.

26. J. M. Thomas, W. J. Thomas, Principles and practice of heterogeneous catalysis, VCH, 1997.

27. P.L. Spath and D.C. Dayton, Preliminary Screening: Technical and economic assessment of synthesis gas to fuels and chemicals with emphasis on the potential for biomass-derived syngas, Technical Report, National Renewable Energy Laboratory (NREL), US, NREL/TP-510- 34929, 2003.

28. A. Y. Khodakov, Fischer-Tropsch synthesis: Relations between structure of cobalt catalysts and their catalytic performance, Catalysis. Today, 144 (2009) 251-257.

29. M. E. Dry, The Fischer-Tropsch process:1950-2000, Catalysis Today, 71 (2002) 227-241.

30. F. Diehl, A. Y. Khodakov, Promotion effect of cobalt Fischer-Tropsch catalysts with nobel metals: a review, Oil. Gas Sci. Technol. -Rev. IFP, 64 (2009) 11-24.

31. J. Van de Loosdrecht, S. Barradas, E. A. Caricato, N. G. Ngwenya, P. S. Nkwanyana, M. A. S. Rawat, B. H. Sigwebela, P. J. van Berge and J. L. Visagie; Calcination of Co-based Fischer-Tropsch Synthesis Catalysts, Top. Catal. 26 (2003) 121-127.

32. A. Y. Khodakov, A. Griboval-Constant, R. Bechara and F. Villain; Pore-size control of cobalt dispersion and reducibility in mesoporous silicas. Journal of Physical Chemistry B, 105 (2001) 9805-9811.

33. A. M. Saib, M. Claeys and E. Van Steen; Silica supported cobalt Fischer-Tropsch Catalysts: effect of pore diameter of support; Catalysis Today, 71(2002) 395-402.

34. A. Y. Khodakov, R. Bechara and A. Griboval-Constant, Structure and Catalytic performance of cobalt Fischer-Tropsch catalysts supported by periodic mesoporous sillicas, Studies in Surface. Science and. Catalysis, 142 (2002) 1133-1140.

35. Ø. Borg, S. Eri, E. A. Belkkan, S. Storsæter, H. Wigum, E. Rytter and A. Holmen, Fischer-Tropsch synthesis over γ-Al_2O_3 supported cobalt catalysts: Effect of support variables, Journal of catalysis, 248 (2007) 89-100.

36 . A. Y. Khodakov, W. Chu and Pascal Fongarland; Advances in the developement of novel cobalt Fischer-Tropsch catalysts for synthesis of long-chain hydrocarbons and clean fuels, Chemical Reviews, 107 (2007) 1692-1744.

37. F. Morales and B. M. Weckhuysen, Promotion effect in Co-based Fischer-Tropsch catalysts, Catalysis, 19, (2006) 1-40.

38. A. M. Hilmen, Reduction and reoxidation of cobalt Fischer-Tropsch catalysts, PhD thesis, NTNU 1996:66.

39. G. Jacobs, J. A. Chaney, P. M. Patterson, T. K. Das, B. H. Davis, Fischer-Tropsch synthesis: study of the promotion of Re on the reduction property of Co/Al_2O_3 catalysts by in-situ EXAFS/XANES of Co K and Re LIII edges and XPS, Applied Catalysis., A, 264 (2004) 203-212.

40. Ø. Borg, N. Hammer, S. Eri, O. A. Lindvåg, R. Myrstad, E. A. Blekkan, M. Rønning, E. Rytter, A. Holmen; Fischer–Tropsch synthesis over un-promoted and Re-promoted γ-Al_2O_3 supported cobalt catalysts with different pore sizes; Catalysis Today, Vol. 142, No. 1-2, (2009) 70-77.

41. Ø. Borg, S. Storsæter, S. Eri, H. Wigum, E. Rytter and A. holmen, The effect of water on the activity and selectivity for γ-Al2O3 supported cobalt Fischer-Tropsch catalysts with different pore size, Catalysis. Letters, 107 (2006) 95-102.

42. D. Schanke, A. M. Hilmen, E. Bergene, K Kinnari, E. Rytter, E. Ådnanes and A. Holmen, Reoxidation and deactivation of supported cobalt Fischer-Tropsch catalysts, Energy Fuels, 10-4 (1996) 867-872.

43. A. M. Hilmen, D. Schanke, A. Holmen,TPR study of the mechanism of rhenium promotion of alumina supported cobalt Fischer-Tropsch catalysts, Catalysis. Letters. 38 (1996) 143-147.

44. A. M. Hilmen, D. Schanke, A. Holmen; Reoxidation of supported cobalt Fischer-Tropsch catalysts; Studies in Surface. Science and Catalysis, 107, (1997) 237-242.

45. N. E. Tsakoumis, M. Rønning, Ø. Borg, E. Rytter, A. Holmen, Deactivation of cobalt based Fischer-Tropsch catalysts: A review, Catalysis. Today, 154 (2010) 162-182.

46. D. B. Williams, C. B. Carter, Transmission electron microscopy, Plenium press, New York, 1996.

47. C. E. Hall, Introduction to Electron Microscopy, McGraw-Hill, New York, (1953) 229.

48. R. F. Egerton, Electron energy loss spectroscopy in the electron microscope, 2nd ed., Plenum press, New York, 1996.

49. L. F. Lenz, *Naturf.* a 9 (1954) 185.

50. M. A. Hayat, Principles and techniques of electron microscopy, Biological applications, 4th Ed., Cambridge University Press, 2000.

51. L. D. Peachey; Thin sections: Study of section thickness and physical distortion produced during microtomy; Biophysical and Biochemical Cytology, 4 (1958), 233-242.

52. M. Karlik, Lattice imaging in transmission electron microscopy, Materials and Structures, 8-1 (2001) 1-16.

53. N. D. Browning, E. M. James, K. Kishida, I. Arslan, J. P. Buban, J. A. Zaborac, S. J. Pennycook, Y. Xin and G. Duscher; Scanning transmission Electron Microscopy: An experimental tool for atomic scale interface science; Reviews on Advanced Materials Science; 1 (2000) 1-26.

54. S. J. Pennycook, Z-contrast STEM for materials science, UltraMicroscopy, 30 (1989) 58-69.

55. A. Howie, Image contrast and localized signal selection techniques, Journal of Microscopy, 117 (1979) 11-23.

56. N. D. Browning, M. F. Chisholm and S. J. Pennycook; Atomic-resolution chemical analysis using a scanning transmission electron microscope; Nature, 366 (1993) 143-146.

57. E. M. James, N. D. Browning; Practical aspects of atomic resolution imaging and analysis in STEM; Ultramicroscopy 78 (1999) 125-139.

58. J. M. Cowley; Coherent interference in convergent-beam electron diffraction and shadow imaging; Ultramicroscopy 4 (1979) 435-450.

59. J. A. Lin, J. M. Cowley; Calibration of the operating parameters for an HB5 STEM instrument; Ultramicroscopy 19 (1986) 31-42.

60. T. J. V. Yates, The development of electron tomography for nanoscale materials science applications, PhD thesis, Cambridge University, 2005.

61. N. Dellby, O. L. Krivanek, P. D. Nellist, P. E. Batson and A. R. Lupini; Progress in aberration-corrected scanning transmission electron microscopy, Journal of electron microscopy 50-3 (2001) 177-185.

62. A. V. Crewe, J. Wall and L. M. Welter, A high resolution scanning transmission electron microscope, Journal of applied Physics. 39-13 (1968) 5861-5868.

63. http://www.see.leeds.ac.uk/research/igt/people/lloyd/eels.htm

64. D. Shindo, T. Oikawa, Analytical electron microscopy for materials science, Springer, 2002.

65. P. A. Midgley, M. Weyland, 3D electron microscopy in the physical science: the development of Z-contrast and EFTEM tomography, Ultramicroscopy 96 (2003) 413-431.

66. J. Frank, Electron tomography, Three dimensional imaging with the transmission electron microscope, book, 1992.

67. M. Weyland, Two and three dimensional Nanoscale analysis: New techniques and applications, PhD thesis, University of Cambridge, England, December 2001.

68. R. N. Bracewell, strip integration in radio astronomy, Journal of Physics, Vol 9, 198-217, 1956a.

69. S. R. Deans, The Radon Transform and some of its applications, 2007.

70. R. A. Crowther, D. J. DeRosier, A. Klug; The reconstruction of a three-dimensional structure from projections and its application to electron microscopy; Proceedings of the Royal. Society of London. A. 317, 319-340 (1970).

71. P. A. Midgley, M. Weyland, T. J. V. Yates, I. Arslan, R. E. Dunin-Borkowski and J. M. Thomas, Nanoscale scanning transmission electron tomography, Journal of microscopy, Vol. 223(2006) 185-190.

72. F. Natterer; The mathematics of computerized tomography; Published by Wiley,1986.

73. G. T. Herman; Fundamentals of Computerized Tomography: Image Reconstruction from Projections; Published by Springer, 2009.

74. J. S. Barnard, J. Sharp, J. R. Tong, and P. A. Midgley; Three-dimensional analysis of dislocation networks in GaN using weak-beam dark-field electron tomography. Philosophical Magazine, 86, 29-31(2006) 4901-4922.

75. J. S. Barnard, J. Sharp, J. R. Tong, and P. A. Midgley; High-resolution three-dimensional imaging of dislocations; Science, 2006. 313(2006) 319-319.

76. I. Arslan, J. C. Walmsley, E. Rytter, E. Bergene, and P. A. Midgley; Toward three-dimensional nanoengineering of heterogeneous catalysts; Journal of the American Chemical Society, 2008. 130 (2008) 5716-5719.

77. P. W. Hawkes, The electron microscope as a structure projector, in Electron tomography: Three dimensional imaging with the transmission electron microscope, Frank J, Editor. 1992, Plenum press: New York; London, 1992.

78. M. Weyland, Electron tomography of catalysts, Topics in catalysis, Vol. 21, No. 4, 2002.

79. T. J. V. Yates, The development of electron tomography for nanoscale materials science application, PhD thesis, Cambridge University, England, 2005.

80. Gatan instruction manual, Model 916, high tilt tomography holder.

81. R. G. Hart, Electron microscopy of unstained biological material- Polytropic montage. Science, 159 (1968) 3822.

82. [http://www.gatan.com/software/

83. J. R. Kremer, D. N. Mastronarde and J. R. McIntosh, Computer visualization of three-dimensional image data using IMOD, Journal of structural biology, 116 (1996) 71-76.

84. IMOD was developed primarily by David Mastronarde, Rick Gaudette, Sue Held, Jim Kremer, and Quanren Xiong at the Boulder Laboratory for 3-D Electron Microscopy of Cells.

85. T. J. Collins, ImageJ for microscopy, Bio Techniques 43 (2007) 25-30.

86. http://www.vsg3d.com/avizo/standard

87. Ø. Borg, J. C. Walmsley, R. Dehghan, B. S. Tanem, E. A. Blekkan, S. Eri, E. Rytter, A. Holmen; Catal Lett. 126 (2008) 224–230.

88. P. L. Gai, E. D. Boyes; Advances in atomic resolution in situ environmental transmission electron microscopy and 1Å aberration corrected in situ electron microscopy; Microscopy Research and Technique. 72 (2009) 153–164.

89. Boyes ED, Gai PL; Environmental high resolution electron microscopy and applications to chemical science; Ultramicroscopy, 67 (1997) 219-232.

90. F. Banhart; In-situ electron microscopy at high resolution; World Scientific publishing, 2008.

91. J. A. Eichmeier, M. K. Thumm, Vacuum Electronics, components and devices, Speinger, Berlin Heidelberg, 2008.

92. Website of Center for Electron Nonoscopy at Technical University of Denmark (DTU Cen): http://www.cen.dtu.dk/English/Research/Instrumentation/TITAN_E-CELL.aspx

93. T. W. Hansen, J. B. Wagner, R. E. Dunin-Borkowski; Materials Science and Technology, No 11, Vol. 26, 1338-1344, (2010).

94. D. B. Williams, C. B. Carter, Transmission electron microscopy, Plenium press, New York, 1996.

95. B. Freitag, S. Kujawa, P. M. Mul, J. Ringnalda, P. C. Tiemeijer; Breaking the spherical and chromatic aberration barrier in transmission electron microscopy; Ultramicroscopy 102 (2005) 209-214.

96. C. Hetherington; Aberration correction for TEM; Materials Today, Review Feature, December 2004.

97. Wikipedia.org

98. R. Dehghan, T. W. Hansen, J. B. Wagner, A. Holmen, E. Rytter, Ø Borg, J. C. Walmsley; In-Situ Reduction of Promoted Cobalt Oxide Supported on Alumina by Environmental Transmission Electron Microscopy; Catalysis Letters, Vol. 141, No. 6 (2011) 754-761.

99. P. Li, J. Liu, N. Nag, P. A. Crozier; In Situ Synthesis and Characterization of Ru Promoted Co/Al_2O_3 Fischer-Tropsch Catalysts; Applied Catalysis A: General 307 (2006) 212-221.

100 . M. Rønning, N. E. Tsakoumis, A. Voronov, R. Johnsen, P. Norby, W. Van Beek, Ø. Borg, E. Rytter, A. Holmen; Combined XRD and XANES studies of a Re-promoted Co/γ-

Al_2O_3 catalyst at Fischer–Tropsch synthesis conditions; Catalysis Today, Vol. 155, No. 3-4, (2010) 289-295.

101. R. F. Egerton, P. Li, M. Malac, Radiation damage in the TEM and SEM, Micron 35 (2004) 399-409.

102. R. Erni; Aberration-corrected imaging in transmission electron microscopy; Published by Imperial College press, London, UK, 2010.

103. W. M. J. Coene and A. J. E. M. Jansen; Image delocalization and high resolution electron microscopy imaging with a field emission gun; Scanning Microscopy Supplement, 6 (1992) 379-403.

104. M. T. Otten, and W. M. J. Coene; High-resolution imaging on a field emission TEM; Ultramicroscopy, 48 (1993) 77-91.

105. Ø. Borg, S. Eri, E. Rytter, A. Holmen; Fischer-Tropsch synthesis over different alumina supported cobalt catalysts; Preprints American Chemical Society, Division of Fuel Chemistry, 51 (2006) 699-701.

106. D. Ozkaya, M. Lok, J. Casci and P. Ash; Reduction of Co/Al_2O_3 catalysts using and ex-situ gas reaction TEM holder; 16th International Microscopy Congress (IMC16), Sapporo, 2006.

107. C. M. Anderi, J. C. Walmsley, H. W. Brinkes, R. Holmestad, S. S. Srinivasan, C. M. Jensen, B. C. Hauback; Electron-microscopy studies of $NaAlH_4$ with TiF_3 additive: hydrogen-cycling effects; Applied Physics A: Materials Science &Processing 80-4 (2005) 237-249.

Part 2

Papers

Paper I

In-Situ Reduction of Promoted Cobalt Oxide Supported on Alumina by Environmental Transmission Electron Microscopy

Roya Dehghan[1*], Thomas W. Hansen[2], Jakob B. Wagner[2], Anders Holmen[3], Erling Rytter[4], Øyvind Borg[4], John C. Walmsley[1,5]

1. Department of Physics, Norwegian University of Science and Technology (NTNU), NO-7491 Trondheim, Norway.
2. Center for Electron Nanoscopy, Technical University of Denmark (DTU), 2800 Lyngby, Denmark.
3. Department of of Chemical Engineering, NTNU, NO-7491 Trondheim, Norway.
4. Statoil R&D, Research Centre, Postuttak, 7005 Trondheim, Norway
5. SINTEF Materials and Chemistry, 7465 Trondheim, Norway

Catalysis Letters, (2011) 141:754-761

Catal Lett (2011) 141:754–761
DOI 10.1007/s10562-011-0600-8

In-Situ Reduction of Promoted Cobalt Oxide Supported on Alumina by Environmental Transmission Electron Microscopy

Roya Dehghan · Thomas W. Hansen · Jakob B. Wagner · Anders Holmen · Erling Rytter · Øyvind Borg · John C. Walmsley

Published online: 2 May 2011

Abstract Reduction of 12wt.%Co/0.5wt.%Re/α-Al_2O_3 Fischer–Tropsch catalyst has been studied in-situ in an environmental transmission electron microscope. Reduction of Co_3O_4 to metallic cobalt was observed dynamically at 360 °C under 3.4 mbar H_2. Structural and morphological changes were observed by high resolution transmission electron microscopy and scanning transmission electron microscopy imaging. The cobalt particles were mainly face centred cubic while some hexagonal close packed particles were also found. Reoxidation of the sample upon cooling to room temperature, still under flowing H_2, underlines the reactivity of the nanoparticles and the importance of controlling the gas composition and specimen temperature during this type of experiment. Similar behaviour was observed for a non-promoted catalyst. Imaging and analysis of the promoted sample before and after reduction indicated a uniform distribution of the promoter.

R. Dehghan (✉) · J. C. Walmsley
Department of Physics, Norwegian University of Science and Technology (NTNU), 7491 Trondheim, Norway
e-mail: roya.dehghan@ntnu.no

T. W. Hansen · J. B. Wagner
Center for Electron Nanoscopy, Technical University of Denmark (DTU), 2800 Lyngby, Denmark

A. Holmen · E. Rytter
Department of Chemical engineering, (NTNU), 7491 Trondheim, Norway

E. Rytter · Ø. Borg
Statoil R&D, Research Centre, Postuttak, 7005 Trondheim, Norway

J. C. Walmsley
SINTEF Materials and Chemistry, 7465 Trondheim, Norway

Keywords Environmental transmission electron microscopy · Fischer–Tropsch · In-situ · Reduction · Cobalt

1 Introduction

Cobalt nanoparticles on a porous support, typically alumina, are widely used in Fischer–Tropsch (FT) processes to convert natural gas into synthetic fuel. To optimize the efficiency of these catalysts and the FT process, a fundamental understanding of the catalyst structure and behaviour must be obtained on the nanometre scale [1]. Dispersion, morphology and distribution of the particles are important in understanding the selectivity and activity of the catalyst. Among available techniques, Transmission Electron Microscopy (TEM) is a powerful tool for the direct study of catalyst systems. One challenge is to study the catalyst as close as possible to the condition in which it functions. While the industrial conditions at which FT synthesis takes place, 20–30 bar at 220–240 °C [2], are not accessible in the TEM, in-situ experiments can be conducted in Environmental TEM (ETEM) instruments [3–5]. Instruments with differentially pumped columns can provide operating pressures in the range up to 20 mbar [6]. Closed reaction cells with electron transparent windows have demonstrated pressures up to 1 bar [7].

Cobalt needs to be in the metallic state in order to be active in the FT process. The reduction sequence is from Co_3O_4 to CoO and to catalytically active metallic cobalt. The cobalt metal nanoparticles oxidize rapidly when exposed to the ambient atmosphere. The structures of Co_3O_4, CoO and cobalt are spinel, rock salt and hexagonal close packed (hcp) or face centred cubic (fcc), respectively [8, 9]. The corresponding volume decrease on going from Co_3O_4 to CoO is 12% and from Co_3O_4 to hexagonal or

Table 1

Co Hexagonal ($a_0 = 2.507$, $c_0 = 4.070$)	Co Cubic (Fm3m, $a_0 = 3.5447$)	CoO Cubic (Fm3m, $a_0 = 4.260$)	Co_3O_4 Cubic (Fd3m, $a_0 = 8.084$)	α-Al_2O_3 Trigonal (P63/mmc $a_0 = 4.758$, $c_0 = 12.991$)	Re Hexagonal ($a_0 = 2.760$, $c_0 = 4.458$)	$CoAl_2O_4$ Cubic (Fd3m, $a_0 = 8.103$)
2.16 (100)	2.05 (111)	2.46 (111)	4.67 (111)	3.47 (012)	2.38 (100)	4.68 (111)
2.02 (002)	1.77 (200)	2.13 (200)	2.86 (220)	2.55 (104)	2.23 (002)	2.86 (220)
1.91 (101)	1.25 (220)	1.51 (220)	2.43 (311)	2.08 (113)	2.10 (101)	2.44 (311)
1.49 (102)[a]	1.06 (311)	1.28 (311)	2.02 (400)	1.96 (202)	1.38 (110)	2.03 (400)
1.25 (110)	1.02 (222)	1.23 (222)	1.43 (440)	1.40 (124)	1.17 (112)	1.43 (440)

[a] This reflection is forbidden for metallic cobalt

cubic cobalt is 49%. At temperatures above 450 °C, bulk metallic cobalt has the fcc structure, while at lower temperatures the hcp cobalt structure is stable [10, 11]. Supported cobalt nanoparticles tend to form with both fcc and hcp cobalt structures at low temperatures, even below the bulk transition temperature [11, 12]. Lattice structures and major lattice spacings for the known cobalt phases and the alumina support are given in Table 1. Spacings for $CoAl_2O_4$ and metallic rhenium are also included. The formation of $CoAl_2O_4$ during reduction has been discussed by Jongsomjitt et al. [13].

Two TEM studies of in-situ and *ex-situ* reduction of Co_3O_4 supported on γ-Al_2O_3 have been reported. Li et al. [4] conducted experiments on 20wt.%Co/γ-Al_2O_3 and 20wt.%Co/2wt.%Ru/γ-Al_2O_3 in an in-situ TEM at 400 °C in 1.3 mbar of 10%H_2/90%N_2. Larger cobalt particles were reduced to CoO, while in the promoted sample small particles of metallic CoRu or pure Ru were also formed. Ozkaya et al. [14] used an *ex-situ* holder, in which a sample with 20%wt.Co/γ-Al_2O_3 was exposed to gas at elevated temperature in an integrated reaction cell so that the sample was not exposed to ambient atmosphere between reaction and observation. Reduction was conducted at 400 °C and 4 mbar of 10%H_2/90%N_2. The Co_3O_4 precursor was reduced to CoO but not metallic cobalt.

Here we report on the reduction of Co_3O_4 nanoparticles, observing changes in crystallography and morphology. We demonstrate in-situ TEM observations of the reduction of Co_3O_4 particles supported on α-Al_2O_3 to metallic cobalt.

2 Experimental

2.1 Sample preparation

The FT catalyst was synthesized through one-step incipient wetness impregnation of alumina support with an aqueous solution of cobalt nitrate hexahydrate, $Co(NO_3)_2{\cdot}6H_2O$, and perrhenic acid, $HReO_4$, to provide a rhenium promoter. The cobalt and rhenium loadings on the α-Al_2O_3 support were 12 and 0.5 wt%, respectively. The catalyst was dried at 110 °C for 3 h after impregnation. The dried sample was calcined in air at 300 °C for 16 h to form cobalt oxide particles with a composition 12wt.%Co/0.5wt.%Re/α-Al_2O_3. A ramping rate of 2 °C/min was used to heat the samples from ambient temperature to the final calcination temperature. XRD analysis of the sample gives an average crystallite size of 21 nm for the Co_3O_4 phase and 94 nm for the α-Al_2O_3. For comparison, some results from non-promoted catalyst are also presented. This was produced by the same route except that $HReO_4$ was not added to the precursor and the final composition was 12wt.%Co/α-Al_2O_3.

2.2 TEM analysis

TEM samples for in-situ experiments were prepared by dispersion of crushed powder directly onto stainless steel grids. This provides good thermal contact between grid and catalyst. TEM analysis was performed with an FEI TITAN ETEM operating at 300 kV. This microscope is equipped with a differential pumping system, making it possible to study materials under controlled gas flows and at elevated temperatures. The sample region is differentially pumped and the gas supply circuit is independent of the main vacuum system. Heating is by a thermal resistance heater in the sample holder and the temperature is measured by a thermocouple. The instrument has a C_S image corrector which increases the resolution of the instrument well into the sub-Angstrom regime [6]. The ETEM is equipped with a residual gas analyser (RGA) that allows the composition of the environment in the sample region to be monitored.

For each experiment, the sample was studied before introduction of H_2 and heating. Several positions were examined by High Resolution TEM (HRTEM), High Angle Annular Dark Field (HAADF) Scanning TEM (STEM) imaging and Electron Energy-Loss Spectroscopy (EELS). After initial observation, H_2 was introduced into

the region of the sample, to a stable pressure of 3.4 mbar and the temperature was gradually increased to 360 °C. The reduction reaction was monitored by recording TEM images of one of the selected regions of the sample at intervals of 0.8 s. These images were subsequently combined into movies showing the reduction process. After reduction the sample was analysed again by HRTEM, STEM and EELS. After analysis, the temperature was decreased to room temperature under continuous H_2 flow.

It is important to consider the possible influence of the electron beam on ETEM experiments. Beside ionisation and knock-on damage of the sample, the beam interaction with the gas consists of both incident high energy electrons and low energy secondary electrons which are emitted from the specimen and cause ionisation of the gas molecules [6]. To verify the influence of beam on the reduction experiment, blank reduction (with the absence of electron beam) was carried out and reduction was confirmed by EELS analysis.

Electron dose for acquisition at low magnification was about 10^2 e/nm^2 s and for acquisitions at high magnification was about 2×10^5 e/nm^2 s. Reduction was generally followed at low magnification, with the electron beam spread over a large area around one sample grid bar. Detailed examination of individual catalyst particles was then conducted after no further changes to the sample were observed. The reduction behaviour of catalyst particles which had not been exposed to the electron beam was confirmed by observing positions that had not been exposed to the electron beam during the initial reduction.

Energy Dispersive X-ray Spectroscopy (EDS) analysis was performed in a JEOL 2010F which is a Field Emission Gun (FEG) TEM and operates at 200 kV accelerating voltage. EDS was performed on both reduced and non-reduced promoted samples. Reduced material was transferred from glove box to the TEM by using glove bag. TEM samples for these experiments were prepared by dispersion of crushed powder on carbon film supported with copper mesh grid.

3 Results

The microstructure of the promoted sample before reduction is shown in Fig. 1. Figure 1a is a low magnification overview of the microstructure, showing the darker Co_3O_4 phase dispersed on the much coarser alumina grains. Some of the Co_3O_4 crystallites are grouped into aggregates, which are considerably larger than the 21 nm particle size measured by XRD. Examples of these are indicated by arrows. Figure 1b shows lattice resolution images of an enlarged area of Fig. 1a. Lattice spacings were measured directly from the image. In Fig. 1b the measured lattice spacings of 4.66 Å corresponds to the (111) planes of Co_3O_4, Table 1.

3.1 Movie of reduction

Figure 2a and b show the same area as Fig. 1a and b after reduction, respectively. Figure 2c shows a HRTEM image of a different cobalt particle after reduction. HRTEM images confirm that the reduction of Co_3O_4 to cobalt has been achieved successfully. Where overlap exists in spacings between cobalt metal and substrate, it is possible to distinguish the two phases on the basis of morphology and spatial distribution. According to Table 1, the features with lattice spacings of 1.91 and 2.16 Å are identified as hcp metallic cobalt and the features with lattice spacings of 2.05 Å (Fig. 2c) as fcc metallic cobalt. Lattice spacings of 2.02 Å could also be Co_3O_4. However, before reduction, the main lattice spacing representative of Co_3O_4 was 4.66 Å and in HRTEM images after reduction there is no evidence of that spacing in the images recorded. This strongly suggests that all the Co_3O_4 has been reduced to metallic cobalt.

Further confirmation of complete reduction of Co_3O_4 was provided by EELS. Figure 3 shows EELS spectra acquired from Co-phases before and after reduction. In spectrum 1, which was acquired from a Co_3O_4 particle before reduction, the O–K edges (at 532 eV) and Co-$L_{2,3}$ edges (at 779 eV) are present. Spectrum 2, acquired from a cobalt particle after reduction, shows only a Co-$L_{2,3}$ edge and no measurable signal from oxygen. Figure 4 compares the EELS Spectra obtained from alumina and Co_3O_4 in the same energy range. Spectrum 1 shows the O–K edge in alumina and spectrum 2 shows O–K and Co-$L_{2,3}$ edges in Co_3O_4. Comparison shows that the oxygen near edge fine structure obtained from Co_3O_4 and alumina is different. The first near-edge peak (indicated in the spectrum) from Co_3O_4 is not present in the alumina spectrum. Similar EELS spectra for Co_3O_4 and CoO were presented and discussed by Li et al. [4].

Figure 5 shows STEM images of the sample. Cobalt aggregates on the larger support grains show bright contrast relative to the substrate. STEM images are sensitive to atomic number and density and show the changes in morphology after reduction clearly. Figure 5a and b are images before reduction and Fig. 5c and d are images of the same area after reduction. Figure 5c and d show that the cobalt containing phase has become dense. Furthermore, the original Co_3O_4 aggregates show evidence of having separated into more distinct, individual, particles. This shrinking behaviour is consistent with the reduction in volume associated with the reduction process described in the introduction. This is also important from the catalytic

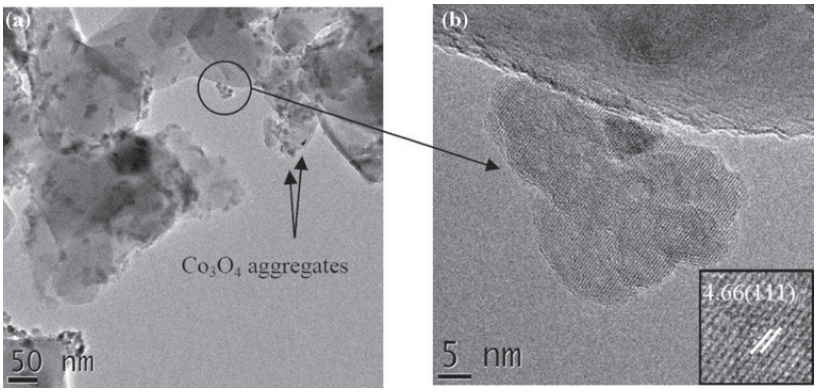

Fig. 1 Images of catalyst before reduction. **a** Low magnification image of Co_3O_4 on alumina support, *arrows* indicate Co_3O_4 aggregates. **b** HRTEM detail of a single Co_3O_4 aggregate

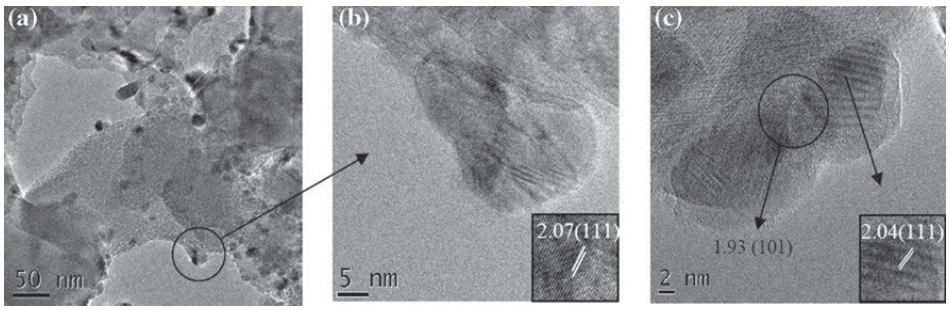

Fig. 2 Images of the catalyst after reduction. **a** Low magnification TEM image of catalyst, **b** HRTEM image of cobalt aggregate at T = 360 °C and in 3.4 mbar H_2 gas, which shows a lattice spacings for fcc cobalt **c** HRTEM image showing lattice spacing for both fcc and hcp cobalt

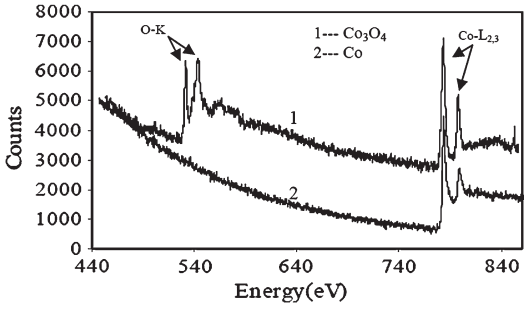

Fig. 3 EELS spectra recorded before and after reduction

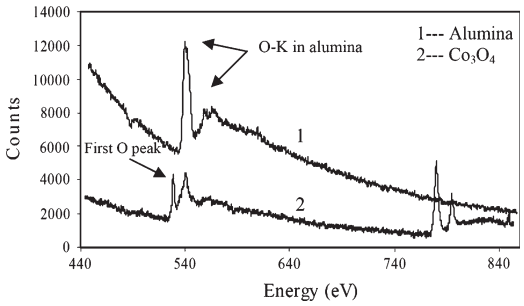

Fig. 4 EELS spectra of alumina and Co_3O_4

point of view as it provides a larger surface area of metal than if the particles were to coalesce.

After reduction the sample was allowed to cool down to room temperature in H_2. It was found that the cobalt nanoparticles had partially re-oxidized. Figure 6a shows a cobalt aggregate after reduction, some minutes after cooling to room temperature and still under H_2 flow. In this image some areas show lattice spacings of 2.86 Å, which corresponds with (220) planes of Co_3O_4, and some parts show lattice spacings of 2.13 Å which corresponds with (200) planes of CoO.

After analysis, the sample was kept inside the microscope overnight, without H_2 flow and the result was further

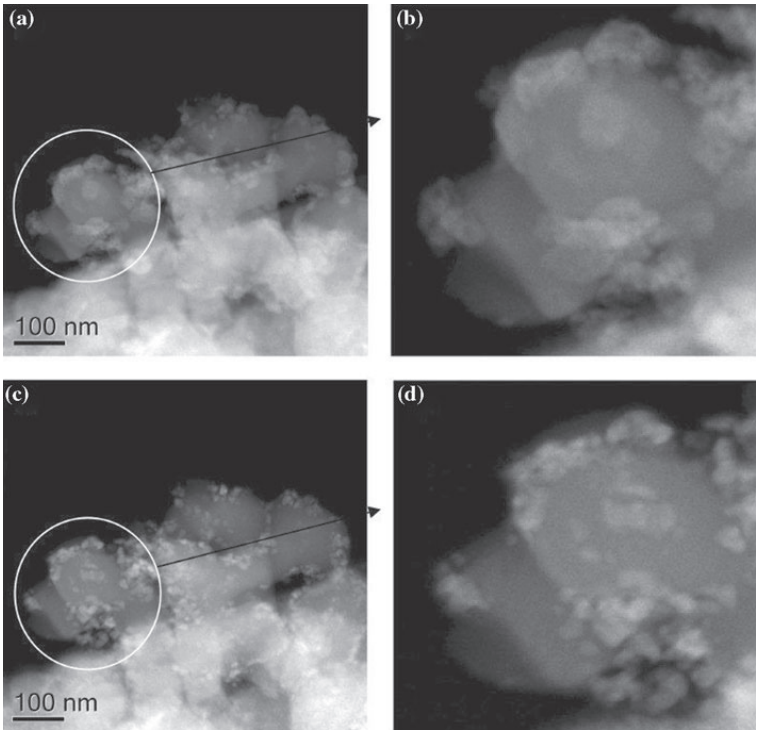

Fig. 5 STEM images before and after reduction. **a** Before reduction. **b** Magnified area of **a**. **c** The same area as **a** after reduction. **e** Magnified area of **d**

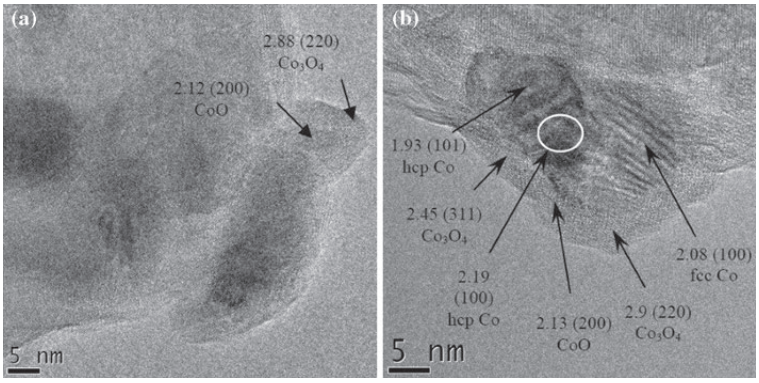

Fig. 6 **a** HRTEM image showing reoxidation. **a** Image of cobalt aggregate at room temperature and under H_2 flow. **b** HRTEM image of particle shown in Figs. 1**b** and 2**b** after being left overnight in the TEM vacuum

partial oxidation of cobalt. Figure 6b shows a layer with approximately 3 nm thickness of oxide around a cobalt particle. Lattice fringes confirm that the outer layer of oxide contains the characteristic *d* values of 2.86 Å, 2.46 Å for Co_3O_4 and 2.13 Å for CoO, respectively. The fringes in the inner layer show the *d* value of 1.91 Å, 2.16 Å, which correspond with (100) and (101) planes of hexagonal cobalt and 2.05 Å which corresponds with (111) planes of fcc cobalt. Generally, a structure with the most oxygen-rich oxide on the outside and the metal in the centre is seen. This is consistent with slow oxidation of the particles, which requires transport of oxygen through the stable outer layer of Co_3O_4.

As described above, areas in the sample that had not been previously exposed to the electron beam were examined after reduction. Figure 7 shows analysis from such an area. Figure 7a shows STEM image and Fig. 7b shows an EELS spectrum from that area in which the oxygen signal is absent. After reduction the structure of these cobalt nanoparticles was similar to that observed in

the areas observed at low magnification under the electron beam during reduction, confirming that electron beam irradiation did not have a significant influence on the reduction process. However, in the areas of the specimen which were under the beam for repeated heating and cooling and where single particles were examined at higher magnification, and correspondingly higher beam current density, some beam damage of the sample was observed.

No distinct rhenium particles were observed during examination of the promoted sample, either from measurements of characteristic lattice parameters from Table 1 or from strong contrast in HAADF images that would be expected from the large difference in atomic number with cobalt. It is not possible to perform EDS in the sample heating holder that was used for the reduction experiments, due to the furnace of the heating element. In addition, rhenium is not easily studied by EELS as the major edge, $O_{2,3}$ at 35 eV, overlaps with peaks from other elements and the $M_{4,5}$ at $\sim$1900 eV with a delayed maximum, is at too high an energy for efficient analysis. Li et al. [4] were able to use EELS to study the distribution of Ru catalyst in a promoted Co/γ-Al_2O_3 catalyst and found that the promoter was concentrated in small Ru or bimetallic RuCo particles alongside larger CoO particles after in-situ reduction of the catalyst.

EDS analysis was performed on the reduced promoted sample, 12wt.%Co/0.5wt.%Re/α-Al_2O_3, and same analysis was performed on the same sample before reduction. The results were not reproduced here. However, in both cases analysis showed the presence of a weak Re signal, consistent with the overall stoichiometry of the sample. No local concentration of Re was observed, either with cobalt or as separate particles.

Figure 8 shows analysis of cobalt particles in the non-promoted sample after reduction. Figure 8a shows fcc metallic lattice fringes with spacing of 2.05 Å in the particles, corresponding to fcc metallic cobalt. Figure 8b shows the EELS spectrum from a reduced particle. The very weak oxygen edge can be attributed to a small contribution from the alumina substrate and in spectra where the oxygen peak was stronger the pre-edge structure associated with Co-oxide was absent.

4 Discussion

ETEM experiments allow in-situ study of the morphology of catalysts cobalt nanoparticles during exposure to a reducing gas. This can have an important role in understanding the reduction mechanisms, interface interaction and regeneration of supported metal catalysts [15].

The results show that it is possible to reduce the cobalt oxide particles at 360 °C with H_2 gas in-situ in the ETEM and to follow the particles during reduction**.** The availability of spherical aberration correction on the objective lens system gives a significant improvement in the level of information that can be obtained from samples. For example, minimising image delocalisation, especially near the edges of the particles makes it easier to interpret the surfaces and facets structures and reduces the electron dose to the sample for the same amount of information [6, 16].

It is of interest to know the crystal structure of the metallic cobalt particles and to know the distribution of fcc and hcp cobalt between them. The main lattice spacing which confirms the presence of fcc cobalt is 2.05 Å, which is close to the lattice of 2.02 Å spacing for hexagonal cobalt. In order to determine the accuracy of the measurements, measurements were made on about 20 recognizable spacings on the HRTEM images of the α-Al_2O_3 and cobalt oxide phases on the images from the same session or similar sessions. The results give an average of $\approx$1% error on the fringe measurements. With this accuracy it is challenging to distinguish between similar spacings in fcc and hcp cobalt but it is possible. The results indicate that small aggregates (7–20 nm) have only fcc structure after reduction, while the aggregates with the size between 20 and 30 nm have a mixture of hcp and fcc structure. One large particle, with a size of 30 nm, gave spacings consistent with being hcp. The in-situ TEM analyses were done at 360 °C, which is lower than the limit for the

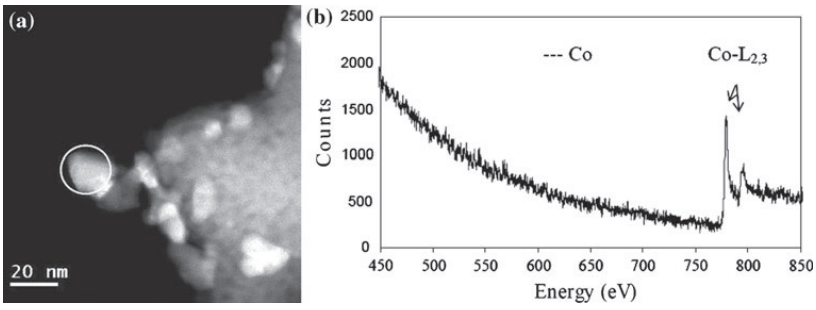

Fig. 7 Analysis of a particle that was not exposed to the electron beam during reduction. **a** STEM image. **b** EELS spectrum

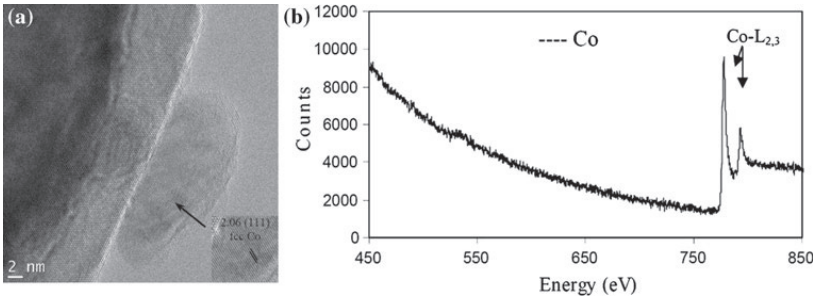

Fig. 8 Reduced Co particle in non-promoted material. **a** HRTEM image. **b** EELS spectrum

transition between fcc and hcp in the bulk. The literature clearly shows a size effect for cobalt nanoparticles. The in-situ XRD reduction of Co-oxide supported on γ-Al_2O_3 which has done by Bulavchenko et al. [12] showed that reduction occurred through the formation of CoO and then the metallic fcc cobalt phase. The temperature for the onset of reduction from Co_3O_4 to CoO was 180 °C and metallic cobalt appeared at 260 °C. The average particle size for fcc cobalt was 7 nm. Kitakami et al. [17] has also reported that the cobalt structure is particle size dependent. Particles smaller than 20 nm were fcc, those larger than 40 nm were hcp, while the particles with the size about 30 nm were a mixture of both fcc and hcp. An increased activity for CO conversion in FT conditions for hcp as opposed to fcc cobalt supported on γ-Al_2O_3 has been reported [11].

Bulavchenko et al. [12] reported a high concentration of stacking faults, according to analysis of x-ray diffraction peaks. By contrast, the level of planar stacking observed in the metallic cobalt particles observed here was low.

The catalysts particles and support can be distinguished from their morphology, even where their lattice spacing may overlap with other phases. According to Table 1, there is a potential overlap of metallic cobalt spacings with the $CoAl_2O_4$ phase (400) spacing. Cobalt aluminate formation has been reported in the presence of H_2O. Jongsomjit et al. [13] detected surface-formation of $CoAl_2O_4$ phases by Raman spectroscopy. The volume of catalyst present in the ETEM is orders of magnitude smaller than is present at laboratory or commercial reduction process and it is not considered that enough H_2O would be liberated to produce $CoAl_2O_4$ phases. Furthermore, EELS showed the presence of pure cobalt when effects due to overlapping of the support were avoided and no evidence of the formation of $CoAl_2O_4$ due to residual H_2O in the vacuum was observed.

The transitional CoO was not observed during reduction here, presumably due to the fact that it reduces rapidly. CoO was observed as a reoxidation product during cooling, as the cobalt nanoparticles reoxidized. It is interesting to note that they are not readily passivated by a uniformly thin oxide layer. The reason for the reoxidation is believed to be the presence of H_2O in the vacuum system, as observed by residual gas analysis. These trace amounts can enter the system via O-ring seals in the microscope.

As mentioned in the introduction, earlier TEM studies on the *ex-situ* and in-situ reduction of cobalt oxide particles showed the reduction of Co_3O_4 to CoO, but not to metallic Co [4, 14]. For a ruthenium promoted catalyst, the distribution of the promoter was not homogeneous and smaller Ru and Ru-Co bimetallic particles were reduced, but not larger cobalt particles [4]. In the case of rhenium promoter, the formation of small bimetallic particles in 4.6wt.%Co/2wt.%Re was observed by Rønning et al. using EXAFS [18]. In contrast, measurable direct Re–Re bonding in a 15wt.%Co/1wt.%Re on γ-Al_2O_3 supported catalysts after reduction was not observed by Jacobs et al. [19]. It has been suggested that an intimate contact between Re and Co is not necessary to obtain the promoting effect [20]. In the present study, no evidence of an inhomogeneous distribution of rhenium in the promoted material was observed, either in reduced or non-reduced conditions. This suggests that the observed reduced particles were essentially cobalt particles. This behaviour was confirmed in a similar non-promoted sample, where the catalyst particles are known to be pure cobalt.

In the earlier studies the cobalt oxide particles were supported on γ-Al_2O_3, which has significantly different pore characteristics from α-Al_2O_3. The nanoparticles interact more readily with the support [21] making them more difficult to reduce. Preliminary reduction experiments performed on γ-Al_2O_3 catalysts in the ETEM, confirmed that they were more difficult to reduce and that the degree of reduction was not so easy to establish due to the more complicated microstructure.

Recent TEM studies report on the observation of metallic cobalt nanoparticles regularly dispersed in a polymer matrix [22, 23]. In these studies decomposition of organometallic precursors in the presence of a reactive gas produced metallic cobalt nanoparticles. In another study cobalt nanoparticles were obtained by evaporation of cobalt foil at $\sim$1500 °C in a small high vacuum chamber followed by condensation to ultrafine powders [24]. The powders were then oxidized by small doses of O_2 giving a

layer of oxide surrounding the cobalt bulk and then the powder was collected on a Cu substrate. In all these cases, the cobalt metal surface was protected from oxidation.

The observation reported here illustrate both the high reactivity of the clean cobalt metal surface and the importance of strong control of the gas composition in order to study the kinetics of the interaction with gas compositions that are relevant to the FT process at the atomic scale.

5 Conclusions

TEM studies of 12wt.%Co/0.5wt.%Re/α-Al_2O_3 and 12wt.%Co/α-Al_2O_3 catalysts show that it is possible to study the reduction process of the samples in-situ at ~3.4 mbar. The reduction behaviour of the promoted and non-promoted catalysts was generally similar. High resolution images combined with EELS and HAADF imaging confirm the presence of metallic cobalt and show clearly the changes in morphology of the catalyst nanoparticles and their aggregates. HRTEM gives information about the nanoparticles crystallography, while STEM gives good morphological detail. On reduction, metal particles tend to separate, keeping a large relative surface area. It is shown that careful measurements of lattice parameters allow fcc and hcp metallic cobalt to be distinguished. Measurements of lattice spacings suggested that the majority of particles had the fcc cobalt structure and confirms the suppression of hcp crystal structure for small nanoparticles. It was also found that the levels of planar faults were low.

Reoxidation of the particles underlines the high reactivity of cobalt nanoparticles. The clean cobalt metal surface is extremely sensitive to trace gases present in the vacuum system. Qualitatively similar observations are made for a similar non-promoted catalyst. The distribution of the Re in the promoted catalysts appeared to be quite uniform. The methods used are promising for the future in-situ studies of cobalt-based FT systems.

Acknowledgments The financial support from Research Council of Norway and Statoil is greatly acknowledged. This publication forms a part of the inGAP Centre of Research-based Innovation, which receives financial support from the Norwegian Research Council under contract no. 174893. The ETEM experiments were done at the Center for Electron Nanoscopy at the Technical University of Denmark (DTU). The A. P. Møller and Chastine Mc-Kinney Møller Foundation is gratefully acknowledged for their contribution towards the establishment of the Center for Electron Nanoscopy. Rafal E. Dunin-Borkowski is gratefully acknowledged for valuable discussion. Julian Tolchard is gratefully acknowledged for doing XRD experiments.

References

1. Khodakov AY (2009) Catal Today 144:251–257
2. Dry ME (2002) Catal Today 71:227–241
3. Boyes ED, Gai PL (1997) Ultramicroscopy 67:219–232
4. Li P, Liu J, Nag N, Crozier PA (2006) Appl Catal A Gen 307:212–221
5. Gai PL, Boyes ED (2009) Microsc Res Techniq 72:153–164
6. Hansen TW, Wagner JB, Dunin-Borkowski RE (2010) Mater Sci Technol 26(11):1338–1344
7. Giorgio S, Joao SS, Nitsche S, Chaudanson D, Sitja G, Henry CR (2006) Ultramicroscopy 106:503–507
8. Smith WL, Hobson AD (1973) Acta Cryst B29:362–363
9. Powder diffraction file, Inorganic phases, International centre for diffraction data, (1986), p 532, 538, 680, 1049
10. Troiano AR, Tokich JL (1948) Trans AIME 175:728
11. Ducreux O, Rebours B, Lynch J, Roy-Auberger M, Bazin D (2009) Oil Gas Sci Technol Rev IFP 64:49–62
12. Bulavchenko OA, Cherepanova SV, Malakhov VV, Dovlitova LS, Ishchenko AV, Tsybulya SV (2009) Kinet Catal 50(2): 192–198
13. Jongsomjit B, Panpranot J, Goodwin JG Jr (2001) J Catal 204:98–109
14. Ozkaya D, Lok M, Casci J, Ash P (2006) IMC16 Sapporo, vol 3. p 1561
15. Gai PL, Boyes ED (2003) Electron microscopy in heterogeneous catalysis. Institute of Physics Pub, London
16. Freitag B, Kujawa S, Mul PM, Ringnalda J, Tiemeijer PC (2005) Ultramicroscopy 102:209–214
17. Kitakami O, Sato H, Shimada Y (1997) Phys Rev B 56(21):13849–13854
18. Rønning M, Nicholson DG, Holmen A (2001) Catal Lett 72(3–4):141–146
19. Jacobs G, Chaney JA, Patterson PM, Das TK, Davis BH (2004) Appl Catal A 264:203–212
20. Hilmen AM, Schanke D, Holmen A (1996) Catal Lett 38:143–147
21. Borg Ø, Walmsley JC, Dehghan R, Tanem BS, Blekkan EA, Eri S, Rytter E, Holmen A (2008) Catal Lett 126:224–230
22. Verelst M, Ely TO, Amiens C, Snoeck E, Lecante P, Mosset A, Respaud M, Broto JM, Chaudret B (1999) Chem Mater 11:2702–2708
23. Respaud M, Broto JM, Rakoto H, Fert AR, Thomas L, Barbara B, Verelst M, Snoek E, Lecante P, Mosset A, Osuna J, Ely TO, Ameniens C, Chaudret B (1998) Phys Rev B 57(5):2925–2935
24. Sayagues MJ, Rojas TC, Fernandez A, Dunin-Borkowski RE, Doole RC, Hutchison JL (2002) Microsc Microanal 8:403–411

Paper II

Electron Microscopy Study of γ-Al_2O_3 Supported Cobalt Fischer–Tropsch Synthesis Catalysts

Øyvind Borg[1], John C. Walmsley[2,3], Roya Dehghan[3], Bjørn S. Tanem[2], Edd A. Blekkan[1], Sigrid Eri[4], Erling Rytter[4], Anders Holmen[1*]

1. Department of Chemical Engineering, Norwegian University of Science and Technology (NTNU), NO-7491 Trondheim, Norway.
2. SINTEF Materials and Chemistry, 7465 Trondheim, Norway
3. Department of Physics, NTNU, 7491 Trondheim, Norway.
4. Statoil R&D, Research Centre, Postuttak, 7005 Trondheim, Norway

Catalysis Letters, (2008) 126:224-230

Catal Lett (2008) 126:224–230
DOI 10.1007/s10562-008-9650-y

Electron Microscopy Study of γ-Al_2O_3 Supported Cobalt Fischer–Tropsch Synthesis Catalysts

Øyvind Borg · John C. Walmsley · Roya Dehghan · Bjørn S. Tanem · Edd A. Blekkan · Sigrid Eri · Erling Rytter · Anders Holmen

Received: 5 June 2008 / Accepted: 8 September 2008 / Published online: 2 October 2008

Abstract Three supported catalysts containing 20 wt% cobalt and 0.5 wt% rhenium were subjected to electron microscopy studies in their calcined state. The catalysts were prepared by incipient wetness impregnation of γ-Al_2O_3 supports of different pore characteristics with aqueous solutions of cobalt nitrate hexahydrate and perrhenic acid. The influence of the support on the Co_3O_4 crystallite size and distribution was studied by X-ray diffraction and electron microscopy. There was a positive correlation between the pore diameter of the support and the post calcination Co_3O_4 crystallite size. On all three γ-Al_2O_3 supports, Co_3O_4 was present as aggregates of many crystallites (20–270 nm in size). Cobalt oxide did not crystallise as independent crystallites, but as an interconnected network, with a roughly common crystallographic orientation, within the matrix pore structure. The internal variations in crystallite size between the catalysts were maintained after reduction. Fischer–Tropsch synthesis was carried out in a fixed-bed reactor at industrial conditions ($T = 483$ K, $P = 20$ bar, $H_2/CO = 2.1$). Although the cobalt-time yields varied significantly (4.6–6.7 $\times$ 10^{-3} mol CO/mol Co s), the site-time yields were constant (63–68 $\times$ 10^{-3} s^{-1}) for the three samples. The C_{5+} selectivity could not be correlated to the cobalt oxide aggregate size and is more likely related to the cobalt particle size and chemical properties of the γ-Al_2O_3 support.

Keywords Fischer–Tropsch synthesis · Cobalt · Rhenium · TEM · Pore diameter · Porosity

Ø. Borg · E. A. Blekkan · E. Rytter · A. Holmen (✉)
Department of Chemical Engineering, Norwegian University of Science and Technology, 7491 Trondheim, Norway
e-mail: anders.holmen@chemeng.ntnu.no

Present Address:
Ø. Borg · S. Eri · E. Rytter
Statoil R&D, Research Centre, Postuttak, 7005 Trondheim, Norway

J. C. Walmsley · B. S. Tanem
SINTEF Materials and Chemistry, 7465 Trondheim, Norway

R. Dehghan
Department of Physics, Norwegian University of Science and Technology, 7491 Trondheim, Norway

1 Introduction

Cobalt is favoured for the synthesis of long-chain hydrocarbons from natural gas-based synthesis gas because of its high activity, high selectivity to linear paraffins, high resistance towards deactivation, and low water-gas shift activity. In order to maximise the exposure of cobalt to gaseous reactants, it is normally dispersed on a high surface area support. Common supports include γ-Al_2O_3, SiO_2, and TiO_2. The choice of support is important for the final Fischer–Tropsch synthesis catalyst. However, site-time yields on supported cobalt catalysts are traditionally considered independent of support identity and cobalt dispersion [1–7]. Thus, the catalyst productivity can be predicted directly from the number of cobalt atoms deposited on the surface. Iglesia et al. [1–3] found constant site-time yield for the cobalt dispersion range 0.45–9.5%, which includes most of the typical low-dispersion cobalt Fischer–Tropsch catalysts. This cobalt dispersion range corresponds to a particle size range from 10 nm to 210 nm if cobalt oxide can be completely reduced to metal. However, for cobalt supported on carbon nanofibers, it has recently been shown that the site-time yield is lower for particles smaller than 8 nm in size [8].

While the influence of the support on Fischer–Tropsch activity is reasonably well-established, the impact on product selectivity is not equally clear. Many investigations [7, 9–12] have reported a strong influence of pore diameter on the C_{5+} selectivity. Iglesia et al. [1, 13, 14] proposed that the differences in selectivity observed for cobalt on different supports are due to variations in the extent of α-olefin re-adsorption. Neither the cobalt particle size, support, nor bimetallic effects are considered to influence the intrinsic chain growth probability on cobalt surfaces [1, 13, 14]. Shi and Davis [15], on the other hand, reported that diffusion limitations for the α-olefin products and their subsequent re-incorporation as chain initiators do not have a major impact on the product distribution. Bezemer et al. [8] recently reported a strong influence of the cobalt particle size on the performance in Fischer–Tropsch synthesis. At 35 bar, the C_{5+} selectivity decreased from 85% to 51% when the cobalt particle size was reduced from 16 nm to 3 nm. However, the C_{5+} selectivity was not calculated at the same CO conversion level for all five catalysts. A range in CO conversion between 13% and 84% provided the basis for the selectivity calculations. There is, however, a strong correlation between CO conversion and C_{5+} selectivity. Also, the experiments were conducted at two different temperatures.

To conclude, no unequivocal explanation seems to exist for the role of the support in the literature. However, like Bezemer et al. [8], we recently suggested that the particle size plays an important role for the product selectivity [10]. However, our study was silent about a possible impact of cobalt distribution. This paper, therefore, presents transmission electron microscopy images of selected catalysts from our recent investigation and relates these to the catalytic performance. Three catalysts that gave significant variations in C_{5+} selectivity were chosen. In order to reveal the microstructures as clearly as possible, samples were prepared for electron microscopy by ultramicrotomy [16].

2 Experimental

2.1 Catalyst Preparation

Three supported catalysts containing 20 wt% cobalt and 0.5 wt% rhenium were prepared by one-step incipient wetness co-impregnation of different Al_2O_3 supports (Sasol GmbH Puralox series) with aqueous solutions of cobalt nitrate hexahydrate and perrhenic acid. The supports (53–90 μm) were pre-calcined in flowing air at 773 K for 10 h prior to impregnation. A heating rate of 1 K/min was used to heat the samples from ambient temperature to 773 K.

All catalysts were dried at 393 K for 3 h after impregnation. Calcination at 573 K for 16 h in flowing air completed the preparation process. The temperature was increased by 2 K/min from ambient temperature to 573 K. Finally, the catalysts were sieved and the 53–90 μm fractions collected. Further treatment was done in situ.

The supports were named according to their pore sizes: "NPA" (narrow pore alumina), "MPA" (medium pore alumina), and "WPA" (wide pore alumina). After cobalt and rhenium impregnation, the catalyst nomenclature was "CoRe/NPA", "CoRe/MPA", and "CoRe/WPA".

The Fischer–Tropsch synthesis activity and selectivity of these catalysts have been presented previously [10].

2.2 Support and Catalyst Characterisation

2.2.1 Nitrogen Adsorption/Desorption

Nitrogen adsorption–desorption isotherms were measured on a Micromeritics TriStar 3000 instrument at liquid nitrogen temperature, 77 K. The samples (0.3 g, 53–90 μm) were outgassed at 573 K overnight prior to measurement.

The surface area was calculated from the Brunauer–Emmett–Teller (BET) equation [17], while the total pore volume and pore size distribution were found applying the Barrett–Joyner–Halenda (BJH) method [18]. The nitrogen desorption branch was chosen for pore size analysis.

2.2.2 X-ray Diffraction

X-ray diffraction patterns were recorded for all the supports and catalysts at ambient temperature on a Siemens D5005 X-ray diffractometer using Cu$K\alpha$ radiation. The samples were crushed prior to measurement. The scans were recorded in the 2θ range between 10 and 90° using a step size of 0.04°. Peaks were identified by comparison with standards in a database.

The average cobalt oxide crystallite thickness was calculated from the Scherrer equation [19] using the (311) Co_3O_4 peak located at $2\theta = 36.9°$. A K factor of 0.89 was used in the Scherrer formula [19]. Lanthanum hexaboride was used as reference material to determine the instrumental line broadening.

2.2.3 Hydrogen Chemisorption

Hydrogen adsorption isotherms were recorded on a Micromeritics ASAP 2010C unit. The samples (0.5 g, 53–90 μm) were evacuated at 313 K for 1 h, and then reduced in situ in flowing hydrogen at 623 K for 16 h. The temperature was increased by 1 K/min from 313 to 623 K. After reduction, the samples were evacuated for 1 h at 603 K, and for 30 min at 373 K before cooling to 313 K. The adsorption isotherm was recorded in the pressure interval ranging from 20 to 510 mmHg. The amount of

chemisorbed hydrogen was determined by extrapolating the straight-line portion of the isotherm to zero pressure. Furthermore, in order to calculate the dispersion, it was assumed that two cobalt surface atoms were covered by one hydrogen molecule [20], and that rhenium did not contribute to the amount of hydrogen adsorbed.

The apparent cobalt metal particle size ($d(Co^0)_{uncorrected}$) can be calculated from the cobalt dispersion (D) by assuming spherical, uniform cobalt metal particles with site density of 14.6 at./nm^2 [21]. These assumptions give the following formula:

$$d\left(Co^0\right)_{\text{uncorrected}}(\text{nm}) = \frac{96}{D(\%)} \quad (1)$$

Since the reducibility of metal oxide supported cobalt catalysts can be low, it is necessary to correct Eq. 1 for the degree of reduction (DOR). Thus, the corrected cobalt particle size is:

$$d\left(Co^0\right)_{\text{corrected}}(\text{nm}) = \frac{96}{D(\%)} \cdot DOR. \quad (2)$$

2.2.4 Electron Microscopy

For ultramicrotomy TEM sample preparation, small amounts of the catalysts were embedded in a two component epoxy resin and stored overnight at room temperature. Thin slices (nominally $\sim$50 nm) were obtained by cutting the embedded catalyst with a diamond knife using a Reichert-Jung ultramicrotome and collected on a standard perforated carbon support Cu mesh grid. TEM analysis was performed using a JEOL 2010F instrument operating at 200 kV equipped with an Oxford Instruments X-ray detector for energy dispersive spectroscopy (EDS) composition analysis. Conventional TEM was performed under bright-field diffraction contrast conditions. For EDS, the microscope was operated in scanning transmission electron microscopy (STEM) mode with a nominal probe diameter of $\sim$0.7 nm. STEM images were acquired using an annular dark field detector which provides contrast that has a strong dependence on atomic number. This is particularly useful for distinguishing higher atomic number catalyst particles, which appear relatively bright, from a lower atomic number support.

2.3 Fischer–Tropsch Synthesis

Fischer–Tropsch synthesis was performed in a fixed-bed reactor (stainless steel, 10 mm inner diameter). The samples (1.0 g, 53–90 μm) were diluted with inert silicon carbide particles (20.0 g, 75–150 μm) in order to improve the temperature distribution along the catalytic zone.

The samples were reduced in situ in hydrogen at 1 bar while the temperature was increased at 1 K/min to 623 K. After 16 h of reduction, the catalysts were cooled to 443 K. The system was then pressurised to 20 bar and synthesis gas of molar ratio $H_2/CO = 2.0$ (and 3% N_2 as internal standard) was introduced to the reactor. To avoid run-away and catalyst deactivation at start-up, the temperature was increased slowly to the reaction temperature 483 K.

Each experiment was divided into two periods which lasted for 24 and 76 h, respectively. The following conditions were used:

Period 1: Synthesis gas at a flow rate of 250 N mL/min.
Period 2: Synthesis gas at an adjusted flow rate to give a target CO conversion of 50%.

Heavy hydrocarbons were collected in a heated trap (363 K) and liquid products were removed in a cold trap (298 K). The effluent gaseous product was analysed for hydrogen, nitrogen, carbon monoxide, carbon dioxide, water, and C_1 to C_9 hydrocarbons using an on-line Agilent 6890 gas chromatograph equipped with a thermal conductivity detector and a flame ionisation detector.

Activity is reported as cobalt-time yield (mol CO/(mol Co s)). The C_{5+} selectivity was calculated by subtracting the amount of C_1–C_4 hydrocarbons and CO_2 in the product gas mixture from the total mass balance.

3 Results and Discussion

3.1 Support and Catalyst Characterisation

3.1.1 N_2 Adsorption/Desorption

Nitrogen adsorption/desorption isotherms showed that three types of hysteresis loops and, therefore, three types of pore geometries were represented by the three supports. In the absence of a universal model, the Barrett–Joyner–Halenda model was chosen for calculation of pore sizes. Figure 1 gives the pore size distributions of the γ-Al_2O_3 supports and the corresponding impregnated samples. Although the starting support in all cases was γ-Al_2O_3, the physical parameters varied significantly. Impregnation, drying, and calcination did not significantly modify the pore size distributions, but reduced the nitrogen uptake. Table 1 gives surface areas and pore size data.

3.1.2 X-ray Diffraction

X-ray diffraction patterns of all the calcined catalysts confirmed the presence of crystalline phases γ-Al_2O_3 and Co_3O_4 [10]. However, the line width of the Co_3O_4 peaks was different for the various catalysts. Thus, the Co_3O_4 crystallite size varied. The third column of Table 1 and the second column of Table 2 indicate that the Co_3O_4

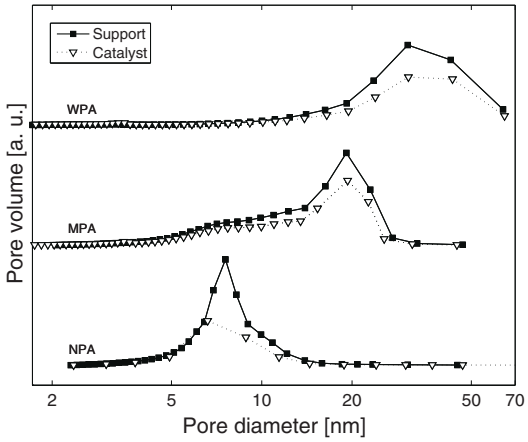

Fig. 1 Support and catalyst pore size distributions calculated from the nitrogen desorption branches using the Barrett–Joyner–Halenda method (filled symbol = support, open symbol = catalyst)

Table 1 Nitrogen adsorption/desorption data

Sample	BET surface area (m^2/g)	Average pore diameter (nm)	Pore volume (cm^3/g)	Porosity
NPA	184	7.4	0.48	0.66
CoRe/NPA	143	7.1	0.30	0.55
MPA	191	11.6	0.78	0.76
CoRe/MPA	149	11.6	0.51	0.67
WPA	114	26.7	0.96	0.78
CoRe/WPA	92	23.7	0.57	0.69

The experimental error ($\pm 2\sigma$) is ± 5 m^2/g for the surface areas, ± 0.2 nm for the average pore diameters and ± 0.02 cm^3/g for the pore volumes. The uncertainty is based on three independent runs of all the samples

crystallite size could be correlated with the support pore diameter. Largest Co_3O_4 crystallites were found in the support of widest pores. The same relationship has previously been demonstrated for a series of 10 other γ-Al_2O_3 supported cobalt catalysts [10]. Table 2 also shows that the corrected cobalt metal particle size after catalyst activation was related to the post calcination Co_3O_4 crystallite size.

For two of the catalysts (CoRe/NPA and CoRe/MPA), the average Co_3O_4 crystallite size was larger than the calculated average support pore diameter. Thus, the majority of the crystallites were apparently located on the exterior of these supports. However, comparison of pore diameter and Co_3O_4 crystallite size for location of the crystallites should be done with care. In fact, we believe that the crystallites were located inside the pore system and relate the conflicting results to the choice of pore geometry model. The Barrett–Joyner–Halenda model assumes presence of only cylindrical pores and absence of pore networks. In reality, no simple pore geometry exists as demonstrated by Rytter et al. [22]. Transmission electron microscopy images of the Co/γ-Al_2O_3 interphase showed that the alumina crystallites were entangled into each other in what appeared to be a chaotic fashion. The cobalt aggregates stretched over a number of alumina crystallites and so-called pores. To conclude, the calculated Co_3O_4 crystallite size can very well be larger than the calculated pore size even though the crystallites actually are located inside the pores.

3.1.3 Electron Microscopy

Before continuing, it is important to bear in mind that the electron microscopy observations were made on the cubic Co_3O_4 phase, after impregnation, drying, and calcination, but before reduction. During reduction, the cubic oxide phase will transform to the hexagonal metallic phase. Some fine-scale changes in the catalyst particle morphology are to be expected during the reduction process. Nevertheless, Fig. 2 shows a dark-field STEM micrograph and complementary mapping of catalyst CoRe/MPA. In Fig. 2a, Co_3O_4 appears as bright, spherical aggregates embedded in the surrounding amorphous γ-Al_2O_3 support. The support appears grey relative to the Co_3O_4 because of its lower relative atomic number. The distribution of the phases shown in the STEM image was confirmed by EDS mapping of Co, Re, Al and O in the same field of view (Fig. 2b–e). The Re EDS signal has a very poor signal-to-noise ratio because of the low concentration (0.5 wt%). As the EDS

Table 2 Cobalt particle size data

Catalyst	Co_3O_4 crystallite size (nm)	Dispersion (%)	$d(Co^0)_{uncorrected}$ [a] (nm)	Degree of reduction (%)	$d(Co^0)_{corrected}$ [b] (nm)
CoRe/NPA	12.0	8.7	11.1	63	6.9
CoRe/MPA	14.6	7.9	12.2	74	9.1
CoRe/WPA	21.1	6.5	14.9	76	11.4

The experimental error ($\pm 2\sigma$) is less than ± 1 nm for the Co_3O_4 crystallite sizes calculated from X-ray diffraction and less than ± 0.5 nm for the cobalt metal particle sizes calculated from hydrogen chemisorption data. The uncertainty is based on three independent runs of all the catalysts

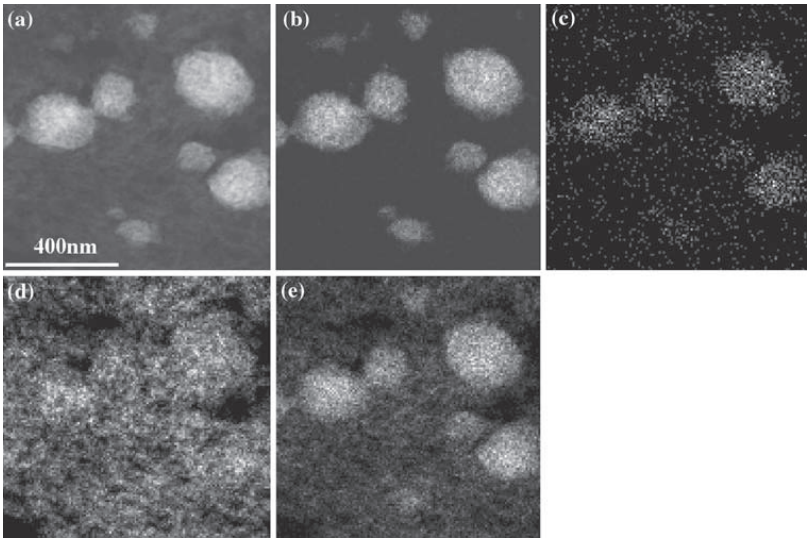

Fig. 2 Dark-field STEM micrograph and complementary composition mapping of catalyst CoRe/MPA. (**a**) STEM image. (**b**) Co EDS map. (**c**) Re EDS map. (**d**) Al EDS map. (**e**) O EDS map

background signal increased in the region of Co_3O_4 aggregates, the Re map alone is not reliable evidence of the localisation of this element. However, EDS spectra extracted from the mapping data at the positions of the Co_3O_4 aggregates showed weak, but clear, characteristic Re peaks. Similar spectra extracted from the area of the γ-Al_2O_3 support showed no Re peaks, indicating that most or all of the Re was associated with the Co_3O_4.

Bright-field TEM micrographs of catalyst CoRe/MPA is shown in Fig. 3. Due to the higher density and stronger diffraction from the more crystalline Co_3O_4 crystallites relative to the γ-Al_2O_3 support, the Co_3O_4 aggregates are black and the alumina support grey. Lower magnification images included a sufficient number of aggregates to allow measurement of a reliable average aggregate size. The aggregate diameter measurements were corrected for underestimation of the true value due to cutting of the aggregates at the bottom and top surfaces of the sample. Diameters of around 100 aggregates from each sample were measured and divided into bins of 5 nm. A correction was then calculated to correct for the finite thickness of the sample [23]. The latter was taken to be 50 nm, the nominal thickness for the microtomed slices studied, although this was not measured exactly. As shown in Table 3, there were some differences in the average Co_3O_4 aggregate sizes between the three materials. While the average aggregate size of CoRe/NPA was 83 nm, the corresponding sizes of catalysts CoRe/MPA and CoRe/WPA were similar and close to 120 nm.

More detailed analysis of the Co_3O_4 aggregates shows that these can tend to grow with crystallites roughly aligned in a common crystallographic orientation. This is

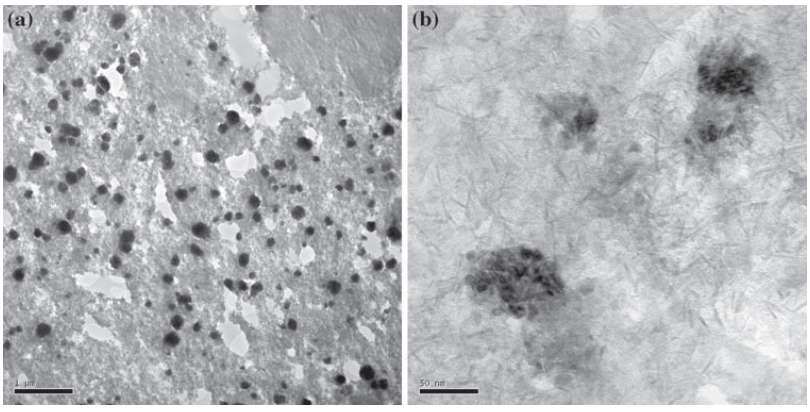

Fig. 3 Bright-field TEM micrographs of catalyst CoRe/MPA (sample at low magnification (**a**), structure of the support and cobalt aggregates in finer detail (**b**))

Table 3 Corrected average Co_3O_4 aggregate size

Sample	Aggregates between (nm)	Corrected average aggregate size (nm)	Numbers of aggregates measured
CoRe/NPA	20–230	87	100
CoRe/MPA	30–270	134	185
CoRe/WPA	30–250	113	175

The uncertainty in the average aggregate size is approximately ±15 nm

illustrated in Fig. 4 which shows bright-field (a), and dark-field (b), images of a single cluster and the diffraction pattern obtained from it (c). The dark-field image shows bright contrast over the whole cluster, suggesting a common diffraction condition for most of the crystallites in the aggregate. This is confirmed by the diffraction pattern that was recorded from an area in the sample including the entire aggregate. It shows a quite clean systematic row based on the (220) Co_3O_4 reflection. Other details in the diffraction pattern are due to discrete, randomly oriented, Co_3O_4 crystallites in the aggregate and the alumina support. Arslan et al. [24] have recently used electron tomography to show the detailed three dimensional morphology of a Co_3O_4 aggregate in a similar γ-alumina supported catalyst. The Co_3O_4 and support were found to form a dense interlocking network, with the former filling the pores of the latter. The electron tomography results were not sensitive to crystallographic orientation and the observation in Fig. 4 is complementary showing an overall crystallographic alignments of the crystallites within the aggregate. Since cobalt crystallised as an interconnected network, the aggregate size (Table 3) was lower for the catalyst with lowest porosity (Table 1), CoRe/NPA, than catalysts CoRe/MPA and CoRe/WPA. Storsæter et al. [16] also attributed the larger aggregates present on SiO_2 than on γ-Al_2O_3 to the higher porosity of the SiO_2 support. Feller et al. [25] related the size of the clusters to the size of the cobalt nitrate droplet during the drying process.

3.2 Fischer–Tropsch Synthesis

Cobalt and site-time yields recorded after 8 h on stream are given in Table 4. Although the cobalt-time yields varied (4.6–6.7 $\times$ 10^{-3} mol CO/mol Co s), the site-time yields were constant (58–64 $\times$ 10^{-3} s^{-1}). It should be mentioned that Bezemer et al. [8] found cobalt particles smaller than 8 nm in size to be less active than larger particles. No such difference was found in this investigation. However, note that only one catalyst had an average particle size below 8 nm in size (CoRe/NPA) and that the calculated particle size is dependent on the H_2 chemisorption and O_2 pulse titration measurement conditions. Also, the cobalt particle size distribution is unknown. Thus, there is not sufficient data to draw any conclusions about a possible particle size effect on the cobalt intrinsic activity.

Significant variations in C_{5+} selectivity were observed. At constant CO conversion level, the numbers were 81.7, 83.4, and 84.9% for catalysts CoRe/NPA, CoRe/MPA, and CoRe/WPA. These numbers can be positively correlated to both the pore diameter and the particle size. However, we [10] indicated in our previous investigation that the pore diameter most likely plays a minor role for the selectivity. This was later confirmed by Rytter et al. [22]. In the

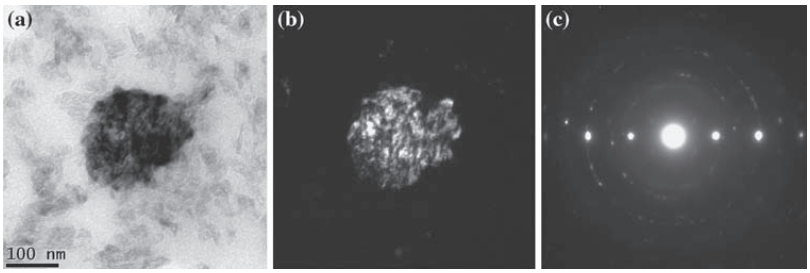

Fig. 4 Bright-field and dark-field image and a diffraction pattern recorded from an aggregate in catalyst CoRe/MPA

Table 4 Cobalt-time yields and site-time yields calculated after 8 h on stream (T = 483 K, P = 20 bar, H_2/CO = 2.1 and GHSV = 15 Nl/(g_{cat} h)) and C_{5+} selectivity recorded at 43–44% CO conversion

Catalyst	Initial cobalt-time yield $\times$ 10^3 (mol CO/(mol Co s))	Initial site-time yield $\times$ 10^3 (s^{-1})	C_{5+} selectivity (%)
CoRe/NPA	6.7	63	81.7
CoRe/MPA	6.2	64	83.4
CoRe/WPA	4.6	58	84.9

The experimental error ($\pm 2\sigma$) is $\pm 5 \times 10^{-3}$ s^{-1} and ±0.5% for the site-time yield and C_{5+} selectivity, respectively

present work, there was an apparent close correlation between the selectivity level and the cobalt particle size in the range 7–11 nm. Bezemer et al. [8] also found the particle size to impact the C_{5+} selectivity, but only for particles between 3 nm and 8 nm in size. Although the data of the present investigation indicate that their results can be extended to larger particles, we also believe that the chemical properties of the γ-Al_2O_3 support are important for the variations in selectivity. Furthermore, there are no indications that the Co_3O_4 cobalt distribution (e.g. aggregate size) plays an important role for the C_{5+} selectivity level as evident from Tables 3 and 4. Nevertheless, it should be mentioned that Storsæter et al. [16] observed that when Co_3O_4 appeared as single crystallites on α-Al_2O_3 and TiO_2, the C_{5+} selectivity was high. For γ-Al_2O_3, Co_3O_4 was located in aggregates and the selectivity to long-chain hydrocarbons was lower.

4 Conclusions

Catalyst particle size and distribution was studied in three γ-Al_2O_3 supported cobalt catalysts having different pore characteristics. X-ray diffraction showed that the dominant cobalt phase after calcination was Co_3O_4. Electron microscopy images showed that Co_3O_4 appeared in aggregates, intergrown through the support pore structure, of many individual Co_3O_4 crystallites. The size of the aggregates was found to correlate with the porosity of the samples. X-ray diffraction crystallite size data indicated a positive correlation between the Co_3O_4 crystallite size and the average pore diameter of the support. The starting support had a great impact on the final Fischer–Tropsch catalyst and performance. Further work is required to characterise the microstructural features obtained by TEM and to more accurately correlate these with the catalyst performance.

Acknowledgments The financial support from the Research Council of Norway and Statoil is greatly acknowledged.

References

1. Iglesia E, Soled SL, Fiato RA (1992) J Catal 137:212
2. Iglesia E (1997) Appl Catal A 161:59
3. Iglesia E (1997) Stud Surf Sci Catal 107:153
4. Oukaci R, Singleton AH, Goodwin JG Jr (1999) Appl Catal A 186:129
5. Bertole CJ, Mims CA, Kiss G, Joshi P (2001) Stud Surf Sci Catal 136:369
6. Bertole CJ, Mims CA, Kiss G (2004) J Catal 221:191
7. Storsæter S, Borg Ø, Blekkan EA, Holmen A (2005) J Catal 231:405
8. Bezemer GL, Bitter JH, Kuipers HPCE, Oosterbeek H, Holewijn JE, Xu X, Kapteijn F, van Dillen AJ, de Jong KP (2006) J Am Chem Soc 128:3956
9. Saib AM, Claeys M, van Steen E (2002) Catal Today 71:395
10. Borg Ø, Eri S, Blekkan EA, Storsæter S, Wigum H, Rytter E, Holmen A (2007) J Catal 248:89
11. Xiong H, Zhang Y, Wang S, Li J (2005) Catal Commun 6:512
12. Song D, Li J (2006) J Mol Catal A 247:206
13. Iglesia E, Soled SL, Fiato RA, Via GH (1993) J Catal 143:345
14. Iglesia E, Soled SL, Fiato RA, Via GH (1994) Stud Surf Sci Catal 81:433
15. Shi B, Davis BH (2005) Catal Today 106:129
16. Storsæter S, Tøtdal B, Walmsley JC, Tanem BS, Holmen A (2005) J Catal 236:139
17. Brunauer S, Emmett PH, Teller E (1938) J Am Chem Soc 60:309
18. Barrett EP, Joyner LG, Halenda PP (1951) J Am Chem Soc 73:373
19. Scherrer P (1918) Göttingen Nachrichten 2:98
20. Reuel RC, Bartholomew CH (1984) J Catal 85:63
21. Jones RD, Bartholomew CH (1988) Appl Catal 39:77
22. Rytter E, Eri S, Skagseth TH, Schanke D, Bergene E, Myrstad R, Lindvåg A (2007) Ind Eng Chem Res 46:9032
23. Andersen SJ, Holme B, Marioara CD (2008) Ultramicroscopy 108:750
24. Arslan I, Walmsley JC, Rytter E, Bergene E, Midgley PA (2008) J Am Chem Soc 130:5716
25. Feller A, Claeys M, van Steen E (1999) J Catal 185:120

Paper III

Nano Structural Analysis of Fischer-Tropsch Catalyst, Promoted Cobalt Phase Supported on γ-Al_2O_3, by TEM and XRD

R. Dehghan[1], A. Voronov[2], N. Tsakoumis[2], A. Holmen[2], R. Holmestad[1], P. E. Vullum[3], Ø. Borg[4], E. Rytter[4], M. Rønning[2], J. C. Walmsley[1,3]

1. Department of Physics, Norwegian University of Science and Technology (NTNU), NO-7491 Trondheim, Norway
2. Department of Chemical Engineering, NTNU, NO-7491 Trondheim, Norway
3. SINTEF Materials and Chemistry, NO-7465 Trondheim, Norway
4. Statoil R&D, Research centre, Postuttak, NO-7005 Trondheim, Norway

To be submitted

Paper IV

TEM and XRD Study of supported cobalt catalysts spent in Fischer-Tropsch process

R. Dehghan-Niri[1], N. Tsakoumis[2], M. Rønning[2], A. Holmen[2], E. Rytter[3], Ø. Borg[3], R. Holmestad[1], J. C. Walmsley[1,4]

1. Department of Physics, Norwegian University of Science and Technology (NTNU), NO-7491 Trondheim
2. Department of Chemical engineering, (NTNU), NO-7491 Trondheim, Norway
3. Statoil R&D, Research centre, Postuttak, NO-7005 Trondheim, Norway
4. SINTEF Materials and Chemistry, NO-7465 Trondheim, Norway

In preparation

TEM and XRD Study of supported cobalt catalysts spent in Fischer-Tropsch process

R. Dehghan[1], N. Tsakoumis[2], M. Rønning[2], A. Holmen[2], E. Rytter[3], Ø. Borg[3], R. Holmestad[1], J. C. Walmsley[1,4]

1. Department of Physics, Norwegian University of Science and Technology (NTNU), NO-7491 Trondheim
2. Department of Chemical engineering, (NTNU), NO-7491 Trondheim, Norway
3. Statoil R&D, Research centre, Postuttak, NO-7005 Trondheim, Norway
4. SINTEF Materials and Chemistry, NO-7465 Trondheim, Norway

Abstract

A Re promoted cobalt Fischer-Tropsch catalyst supported on γ-Al_2O_3 was studied by Transmission Electron Microscopy (TEM) and X-ray Diffraction (XRD) before (fresh) and after (spent) FT synthesis. TEM Particle size measurements on the cobalt nanoparticles of fresh and spent catalyst showed the average of 11.5±3.5 nm and 16.9±5.3 nm, respectively. XRD analysis showed the sintering of the cobalt nanoparticle and further reduction of catalyst under FT synthesis.

Keywords: Transmission Electron Microscopy, Cobalt catalyst, Fischer-Tropsch,

1. Introduction

Fischer-Tropsch (FT) synthesis is a process to convert mixture of carbon monoxide and hydrogen into clean hydrocarbon fuel [1]. A key element in the FT process is the application of a stable catalyst with high activity and high wax selectivity. Cobalt nanoparticles dispersed on porous substrate, typically alumina, are one of the favourable catalysts for the FT reaction as they provide high activity and high selectivity to produce long chain waxes and also show low water gas shift activity [2]. The activity of the catalysts is proportional to the number of available active sites. However, the catalyst is deactivated over time under reaction conditions. Many studies have been made on the deactivation of the cobalt based FT catalysts and different mechanisms have been proposed for its deactivation such as sintering, poisoning, attrition and re-oxidation of the cobalt phase [3,4,5]. Tsakoumis et al. have reviewed different deactivation mechanisms for supported cobalt FT catalyst [6].

To improve the performance of the cobalt catalyst it is crucial to gain proper understanding of the catalysts at the nano scale. Suitable characterization techniques are required to study the

individual components of the catalysts. Moreover, to characterize the catalysts properties relevant to its catalytic performance, it should be ideally studied as close as possible to working condition. Since cobalt is rapidly oxidized in the air and its metallic phase is considered as the active phase in the FT process, therefore, in-situ experiments are required. Several in-situ studies have been done to characterize the supported cobalt catalysts materials [5,7,8]. However, the in-situ instruments are not easily available and the exact reaction conditions may not access. To characterize the reduced metal catalyst, one method is passivation in which a thin layer of protective oxide is formed by controlled and moderated oxidation environment [9].

Here the aim is to study the 20%Co/0.5%Re/γ-Al_2O_3 catalysts in both fresh and after FT reaction by TEM and XRD. The fresh catalyst was passivated in order to be in close condition to the industrial catalyst. The spent catalyst has been about a month under the FT process and removed from the reactor. Rønning et al. have done similar studies on the rhenium promoted Co/γ-Al_2O_3 at FT condition by X-Ray Diffraction (XRD) and X-ray Absorption Near Edge Structure (XANES) and they did not observed any changes in the catalysts under the FT condition; however, at higher temperature, methanation condition, they observed the sintering of the cobalt particles and further reduction of partially reduced catalysts particles [5].

Here the intention was to apply TEM techniques to observe any possible changes in the dispersion and shape of the cobalt nanoparticles and compare the results with the XRD data.

Experimental procedure

The details of the Fischer-Tropsch catalyst preparation and the application of TEM and XRD techniques for its characterization are described bellow.

2.1 Catalyst preparation

The FT catalyst was synthesized through one-step incipient wetness impregnation of the alumina support with an aqueous solution of cobalt nitrate hexahydrate, $Co(NO_3)_2.6H_2O$, and perrhenic acid, $HReO_4$, to provide a rhenium promoter. The cobalt and rhenium loadings on the γ-Al_2O_3 support were 20wt% and 0.5wt%, respectively. After impregnation, the catalyst was dried at 110 °C for 3 hours and then calcined in air at 300°C for 16 h to form cobalt oxide particles with a composition 20wt%Co/0.5wt%Re/γ -Al_2O_3. A ramping rate of 2 °C/min was used to heat the sample from ambient temperature to the final calcination temperature. The sample was reduced with a heating rate of 3 °C/min up to 350 °C under 100 ml/min H_2 flow

at atmospheric pressure and then kept for 16 h under these conditions. Then the reduced sample was embedded in wax, to protect from air. The de-waxed catalyst was used for TEM analysis.

The fresh catalyst was run in a slurry bed reactor at industrial FT conditions for approximately one month.

2.2 TEM

TEM experiments were performed with a JEOL 2010F equipped with field emission gun, operating at 200 kV accelerating voltage. TEM samples were prepared by dispersion of the crushed catalysts powder on a carbon supported Cu mesh. TEM data analyses were performed with Digital Micrograph.

2.3 XRD

The catalyst was characterized by High-resolution X-ray powder diffraction (HR-XRD) before and after reduction. The measurements were performed at the BM01B station of the Swiss-Norwegian Beamlines (SNBL). The X-ray beam was adjusted with the use of Si (1 1 1) monochromators to the energy of 24.698 eV, corresponding to a wavelength of 0.502 Å. The applied slits provided an X-ray beam spot of 4 mm horizontal size and 1 mm vertical size at the sample position. The diffractometer is equipped with an X-ray detector consisting of six independent counting chains, each made of a Si (1 1 1) analyser crystal and a NaI scintillation counter. Data were collected in a 2θ range from 9^o to 33^o before and after reduction.

Catalyst reduction and characterization by XRD were done *in- situ* at 400°C and under 2.5 ml/min pure hydrogen flow. In particular, 7-10 mg of the sample was loaded into quartz capillary 1mm in diameter and stabilized by quartz wool plugs. The cell design and experimental set up is described in detail elsewhere [5]. The sample was heated from ambient temperature to 400 °C at a rate of 3°C /min at ambient pressure. When the desired set point reached, the temperature was held for 4 h before switching to a He flow of 5 ml/min and ramp down to room temperature.

Data analysis was done using the Bruker EVA and Topas v4.2 software. This provided both structural and particle size information. For the full profile fitting of the diffraction data the Pawley method [10] was used.

3. Results

Figure 1a is a TEM image of the passivated catalyst and Figure 1b is a HRTEM image of a cobalt aggregate. The two dimensional fringes in the Figure 1b shows the d value of 1.92 corresponding with [121] zone axis of the hexagonal cobalt structure. This confirms that the cobalt particle is fully reduced and any oxide layer is not seen around the particle.

Figure 2a is the TEM image of cobalt catalyst after FT synthesis and Figure 2b is HRTEM image of a cobalt nanoparticle. The fringes in this image, show the d value of 1.92, which corresponds to the (101) planes of hexagonal metallic cobalt. There is no evidence of oxide in the cobalt nanoparticles.

The average size of the particles was measured from TEM images. Since the fresh catalyst was passivated, makes it possible to measure the particles size. TEM measurements give an average value of 11.5±3.5 nm for fresh catalyst and 16.9±5.3 for the spent catalyst. Figure 3a and 3b shows the distribution of cobalt nanoparticle size in the fresh and spent catalysts, respectively.

Figure 4 shows comparison of XRD spectra from fresh and spent catalysts. Spectrum 1 is from the catalyst treated under reduction condition with H_2 and spectrum 2 is from the catalyst being for a month under FT synthesis condition. The comparison of two spectra shows that the cobalt particle size has increased and further reduction of cobalt oxide occurred in the catalyst.

4. Discussion

Comparing the average particle size of the fresh and spent catalysts shows that the particle size has increased after the FT process. This is consistent with some sintering of the cobalt nanoparticles.

References

1. B. H. Davis, M. L. Occelli, Advances in Fischer-Tropsch synthesis, Catalysts and catalysis,
2. A. Y. Khodakov; Fischer-Tropsch synthesis: Relation between structure of cobalt catalysts and their catalytic performance, Catal. Today, 144, issue 3-4, (2009) 251-257.
3. J. A. Moulijn, A. E. van diepen, F. Kapteijn, Appl. Catal. A, General, 212 (2001) 3-16.
4. P. J. van Berge, J. van de Loosdrecht, S. Barradas, A. M. van der Kraan, Cata. Today, 58 (2000) 321-334.

5. M. Rønning, N. E. Tsakoumis, A. Voronov, R. E. Johnsen, P. Norby, W. Van Beek, Ø. Borg, E. Rytter, A. Holmen; Catal. Today, vol. 155, issue 3-4, (2010) 289-295.
6. N. Tsakoumis, M. Rønning, Ø. Borg, E. Rytter, A. Holmen, Catal. Today, Vol. 154, issue 3-4, (2010) 162-182
7. R. Dehghan, T. W. Hansen, J. B. Wagner, A. Holmen, E. Rytter, Ø Borg, J. C. Walmsley, Catal. Lett. Vol. 141, No 6, (2011) 754-761.
8. P. Li, J. Liu, N. Nag, P. A. Crozier, Appl. Catal. A: General 307 (2006) 212-221.
9. F. Huber, Z. Yu, S. Logdberg, M. Rønning, D. Chen, H. Venvik, A. Holmen, Catal. Lett. Vol. 110, No. 3-4, 2006.
10. G.S. Pawley, Journal Of Applied Crystallography 14 (1981) 357-361.

List of Figures:

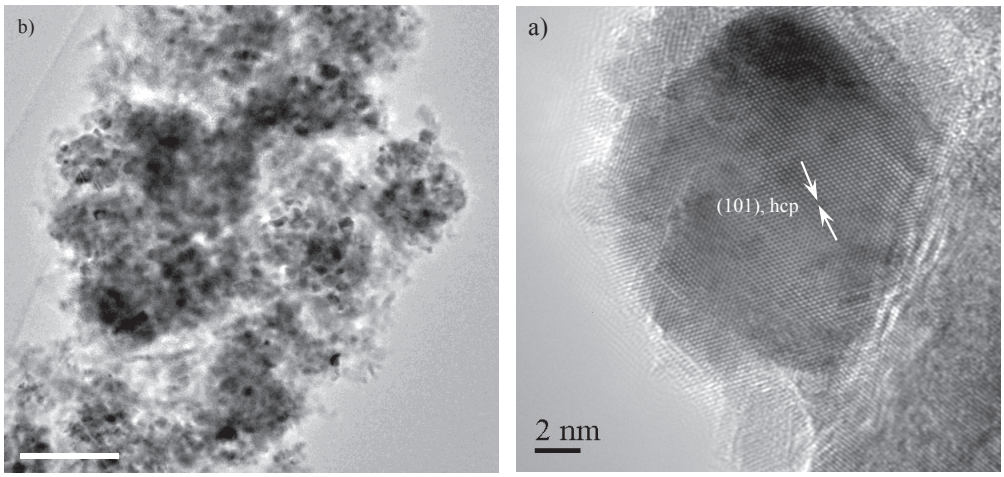

Figure 1a) TEM image of passivated Co/0.5%Re/Al_2O_3, b) HRTEM image of cobalt nanoparticle.

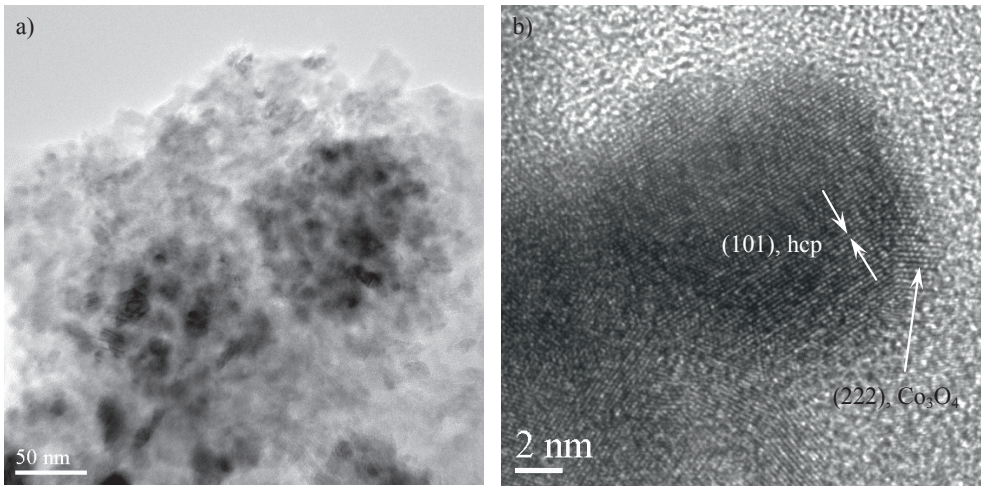

Figure 2a) TEM image of Co/0.5%Re/Al_2O_3 catalyst spent in the FT process, b) HRTEM image of a cobalt nanoparticle.

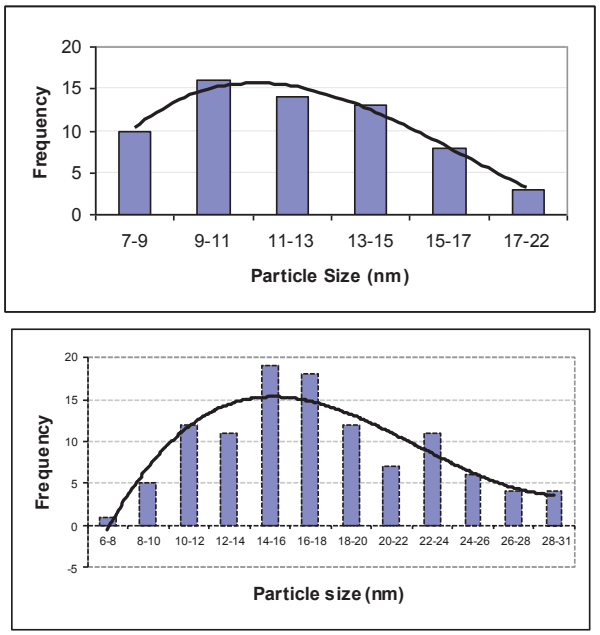

Figure 3a) Particle size distribution for passivated catalyst, b) for spent catalyst.

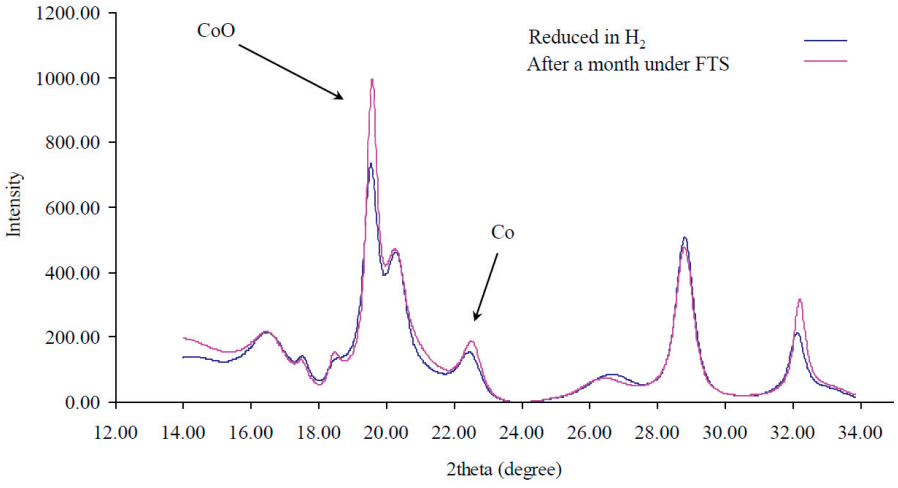

Figure 4) Comparison of in-situ XRD spectra of the catalyst treated in reduced state and treated after a month under FT synthesis.

Paper V

Nanoconfinement of Ni Clusters towards a High Sintering Resistance of Steam Methane Reforming Catalysts

Roya Dehghan-Niri[1], John C. Walmsley *[1,2], Anders Holmen[3], Paul A. Midgley[4], Erlying Rytter[5], Anh Hoang Dam[3], Ana B. Hungria[4,6], Juan C. Hernandez-Garrido[4,6], De Chen*[3]

1. Department of Physics, Norwegian University of Science and Technology (NTNU), NO-7491 Trondheim, Norway.
2. SINTEF Materials and Chemistry, NO-7465 Trondheim, Norway.
3. Department of Chemical Engineering, (NTNU), NO-7491 Trondheim, Norway.
4. Department of Materials Science and Metallurgy, University of Cambridge, Pembroke Street, CB23QZ, Cambridge, United Kingdom, England.
5. Statoil R&D, Research Centre, Postuttak, NO-7005 Trondheim, Norway.
6. Departamento de Ciencia de los Materials, Ingenieria Metalurgicay Quimica Inorganica, Facultad de Ciencias, Universidad de Cadiz, Rio San Pedro s/n, Puerto Real, 11510, Spain

Submitted to Catalysis Science and Technology

Journal Name

Dynamic Article Links ►

Cite this: DOI: 10.1039/c0xx00000x

www.rsc.org/xxxxxx

ARTICLE TYPE

Nanoconfinement of Ni Clusters towards a High Sintering Resistance of Steam Methane Reforming Catalysts

Roya Dehghan-Niri[a], John C. Walmsley *[a,b], Anders Holmen[c], Paul A. Midgley[d], Erlying Rytter[e], Anh Hoang Dam[c], Ana B. Hungria[d,f], Juan C. Hernandez-Garrido[d,f], De Chen*[c]

Received (in XXX, XXX) Xth XXXXXXXXX 200X, Accepted Xth XXXXXXXXX 200X
DOI: 10.1039/b000000x

This study reports an improvement of steam reforming catalyst stability at typical pre-reforming conditions by enhanced stabilization of Ni nanoparticles through spatial confinement in a mixed oxides matrix. We revealed a simple approach of three dimensional engineering of Ni particles by means of self-assembly of Ni atoms inside the nanoribbon of hydrotalcite derived mixed oxides. Taking advantage of transmission electron microscopy (TEM), together with electron tomography, the three dimensional (3D) structure of the catalyst was investigated at a nanometer scale, including Ni particle size, shape, location and spatial distribution, as well as pore size and morphology of the mixed oxides. Porous nano-ribbons were formed by high temperature treatment, adopting the layer structure of the hydrotalcite-like materials. Ni particles formed by selective reduction of mixed oxides embedded in the nano-ribbons with connected pore channels, allowing good access for the reactants. These spatially confined and well distributed Ni particles increased catalyst stability significantly compared to the Ni particles supported on the support surfaces in commercial catalysts during the steam methane reforming.

Introduction

Rational design of catalysts has played an increasing role in developments of new catalysts and radical improvements of the existing industrial catalysts.[1] In addition to the surface composition, particle size and, shape of nanoparticles, the hierarchical structure of the catalysts has an important implication for catalytic activity, selectivity and stability.[2-3] Great efforts have been devoted to design catalysts with a high stability without compromising high activity. Steam methane reforming is the most promising reaction for synthesis gas production, which is of great importance for large scale production of methanol, ammonia, and hydrogen.[4-5] Ni catalyst is still a preferred selection as the industrial catalyst due to its relatively low price and high abundance. Ni is also a typical catalyst for pre-reforming, which is conventionally used to convert heavy hydrocarbons to methane and syngas at relatively low temperatures to reduce the coking potential at of the steam reforming at high temerpatures.[6-7] In addition, Ni catalysts have drawn increasing attention for hydrogen production from biomass derived compounds at relatively low temerpatures.[8] However, there has long been a challenge to increase the resistance to carbon formation and sintering of the Ni catalysts. Enormous efforts have been made in the fundamental investigation of surface elementary reaction steps, including carbon formation, effects of the surface composition and the Ni particles size on the activity and stability.[9-17] These fundamental insights make it possible to rationally design Ni based catalyst with respect to high activity, high resistances to carbon formation and sintering, [11, 16, 18] which is essential for the reforming reactions at relatively low temperatures, such as pre-reforming and reforming of biomass derived compounds. Manipulating the surface composition is a prevalent principle in rational catalyst design to reduce surface carbon concentration by reducing methane decomposition rate.[16, 18] However, the most promising strategy to achieve a high carbon resistance but without compromising high activity is to use Ni nanoparticles with smaller size.[17] As a consequence, the greatest challenge is how to stabilize the Ni nanoparticles at relatively high temperatures in the presence of steam.

Conventional metal nanoparticles are typically deposited on the surface of the supports and sintering is unavoidable at high temperatures due to their mobility. Approaches involving embedded catalysts, where the small metal particles are isolated by the porous support shell, have shown a promising potential to suppress sintering of the metal effectively. The porous structure of the support shell ensures the access of reactant molecules to the active sites.[3] Several approaches have been employed to isolate individual nanoparticles, such as embedding in sol-gel matrices and metal@support core shell catalysts.[3]. In addition high hydrothermal stability of the support is a strong requirement for steam reforming catalysts. Spinels, such as $MgAl_2O_4$ and $CaAl_2O_4$ have been long used as the industrial catalyst supports, due to their high stability and mechanical strength. Moreover, high Ni activity requires highly porous catalysts with a relatively large pore size to reduce mass transport resistance. However, it remains a challenge to prepare small sized Ni nanoparticles

isolated in highly stable, suitably porous support.

Hydrotalcite derived materials has been long used as sorbents and catalysts.[19-21] The general formula for hydrotalcite (HT) materials is shown as:

$$\left[M_n^{2+}M_m^{3+}\left(OH\right)_{2(n+m)}\right]^{m+}A_{m/x}^{x-}.yH_2O \qquad (1)$$

Where M^{2+} and M^{3+} are metal cations, x is the charge of the anion, $n>m$ and y is the number of interlayer water molecules. The most common HT contains Mg and Al. The structure of HT is basically brucite, $Mg(OH)_2$, in which octahedral of Mg^{2+} ions (6-fold coordinated to OH^-) share edges to form infinite sheets. These sheets are stacked on top of each other and are held together by hydrogen bonding. When Mg^{2+} ions are substituted by a trivalent ion such as Al^{3+} to form HT, a positive charge is generated in the hydroxyl sheets. This positive charge is compensated by CO_3^{2-} anions which lie in the inter-layer region between two brucite sheets. Water of crystallization is also located in the free space of this inter layer region. [9, 22-23] Partially replacing Mg^{2+} with Ni^{2+} can form Ni containing hydrotalcite materials.

It is demonstrated that the hydrotalcite derived Ni catalysts possess a superior activity and stability with respect to a commercial reforming Ni catalysts. The hydrotalcite-derived Ni catalysts provide small Ni particles, high resistance to carbon formation and excellent stability.[9, 23] However, a detailed understanding of the catalyst structure and properties responsible for such superior catalytic performance is still missing. Here we combine Transmission Electron Microscopy (TEM) and High Angle Annular Dark Field (HAADF) Scanning TEM (STEM) imaging to study the development of the structure, including three dimensional structures of pores, Ni or Ni oxide particle size, shape and distribution in each treatment steps starting from the hydrotalcite like materials. Taking advantage of electron tomography in heterogeneous catalyst and related nanomaterials, [24-29] we reveal for the first time that the three dimensional structure of the porous oxide ribbons, where the individual Ni particles were isolated by the oxide shell makes them stable. These new fundamental insights provide prevalent principles in rational catalyst design of nanomaterials highly stable at high temperatures.

Experimental Procedure

Catalyst Preparation and Characterization

Hydrotalcite like materials containing Ni catalysts were prepared by co-precipitation of $Mg(NO_3)_2{\cdot}6H_2O$ and $Al(NO_3)_3.9H_2O$ and $Ni(NO_3)$ to obtain 12.5wt% catalyst (12.5%Ni/HT), as described previously.[9] The catalyst was dried overnight under vacuum at 343 K and calcined at 873 K for 6 h with a heating rate of 5 K/min in air. The materials were characterized by different techniques including TEM, chemisorption and X-ray diffraction (XRD). XRD spectra clearly indicate the pure structure of hydrotalcite of the synthesized catalyst, composed of 12.5wt%Ni and the ratio of the Ni:Mg:Al are as (0.38:2.62:1).[9]

A portion of the calcined sample was reduced in H_2 flow (50% H_2 in Ar) from 273 K to 943 K with a heating rate of 10 K/min and then kept for 10 hours. Passivation of the reduced Ni catalyst was performed at 305 K with 1% O_2 in Ar before the ex-situ TEM characterization.

Transmission Electron Microscopy (TEM)

TEM samples were prepared in two different methods; dispersion and ultramicrotomy. In the first method, a dispersion of crushed catalysts powder in ethanol solvent is dried on a carbon support Cu mesh grid. For ultramicrotomy, a small amount of catalyst powder is embedded in a resin and stored overnight at room temperature. Thin uniform slices (~50nm thick) are then obtained by cutting the embedded catalyst with diamond blade, using a commercial ultramicrotome. The slices are collected on a carbon support Cu mesh grid.

Conventional TEM and STEM images were taken by a JEOL 2010F Field Emission Gun (FEG) instrument operating at 200 kV acceleration voltage. Electron Tomography was used to reconstruct the three dimensional structure of the catalysts sample. Electron tomography series were acquired with a FEI Tecnai F20 FEG electron microscope operating at 200 kV. Tomographic acquisition of two dimensional images of the calcined and reduced 12.5%Ni/HT samples were performed in STEM mode over the tilt range of ±72°, with 2° increments, using a dedicated high-tilt sample holder. Image acquisition was undertaken using the FEI software package Xplore 3D. Alignment of the image stack and tomographic reconstructions were performed with FEI software package Inspect 3D using the Simultaneous Iterative Reconstructive Technique (SIRT) routine. Reconstructed volumes were then processed with ImageJ. Avizo6 software from Mercury Computer systems was used to visualize the 3D data volume by voltex view and segmentation. In the voltex view the re-projection of the 3D volume at each angle is produced from the intensity value of each voxel. In the segmentation method, the area of interest in the 3D volume is selected through the whole volume and visualized separately. Thresholding of feature edges was done manually within the visualization software.

Volumetric Hydrogen Chemisorption

Hydrogen adsorption of the Ni catalysts was measured at 308 K using a Micromeritics ASAP 2010C apparatus. The catalyst was loaded in a U-shaped quartz reactor heated by an electric furnace. The samples were initially evacuated at 308 K for one hour and then reduced in H_2 flow at 943 K for 10 hours with heating rate of 10 K/min. After reduction, the samples were evacuated for 30 minutes at 943 K, followed by 60 minutes at 308 K. An adsorption isotherm was constructed at 308 K, based on the adsorbed amount of hydrogen at 10 different pressures in the range 4-310 mmHg. After pumping for 30 minutes, a second isotherm was measured in order to separate strongly and weakly bonded hydrogen. The difference between the two isotherms represents the chemisorbed amount of H_2. The monolayer capacity was determined by extrapolating the linear part of the different isotherms to zero pressure.

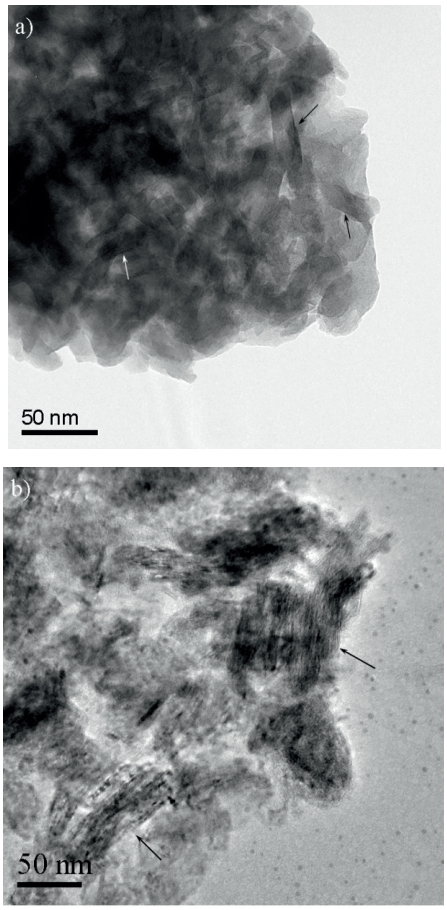

Fig. 1. BF-TEM images of 12.5%Ni/HT, **a)** before calcination and **b)** after calcination, respectively. Likely plates, viewed approximately edge-on are indicated in Figure 1a. Particles where the layer structure is viewed approximately edge-on are indicated in Figure 1b.

Nitrogen Adsorption

Nitrogen adsorption-desorption isotherms for the Ni catalysts were performed in a CoulterTM SA 3100 instrument and the data were collected at liquid nitrogen temperature. Prior to the measurements the samples were dried under vacuum at 423 K for 1 h. The surface area was calculated from the Brunauer-Emmett-Teller (BET) equation and the total pore volume and the average pore size were calculated applying the Barrett-Joyner-Halenda (BJH) method. [30-31] BJH pore size distribution was estimated from the adsorption branch of the N_2 adsorption isotherm, to avoid the possible tensile strength effect.[32]

Catalyst Testing

Catalysts activity and deactivation has studied in a fixed-bed reactor at atmospheric pressure. 10 mg of Ni catalyst diluted with 100mg of inert α-Al_2O_3 was heated from ambient temperature to 943 K at 2K/min in a mixture of 1:1 H_2/Ar and held at these conditions for 10 h to reduce. The catalyst stabilized at 923 K, steam to carbon ratio: S/C=3 and 50 cm^3/min of CH_4. Total gas flow of 100 cm^3/min obtained by using Ar and H_2 as diluents.

Results

Properties of Ni Catalysts

Figure 1 shows the microstructural changes at different stages of the processing of the catalyst preparation. Figure 1a shows that the synthesized materials have a compact structure of densely-packed, plate-shaped, crystals. Due to the overlapping of particles in the aggregate, the morphology of the individual particles is not obvious. Closer inspection reveals individual particles showing contrast that is consistent with the plate-like morphology that is expected for this material. Several examples are indicated by arrows. The uncalcined material was unstable under the electron beam and this prevented three dimensional analyses. After treatment at 873 K, XRD revealed that the hydrotalcite structure was transformed into mixed oxides, where the Ni-Mg/Al oxide solid solution is possibly formed, although MgO, NiO, Al_2O_3 and Ni-Mg oxide solid solutions could not be distinguished in the XRD spectra.[9]

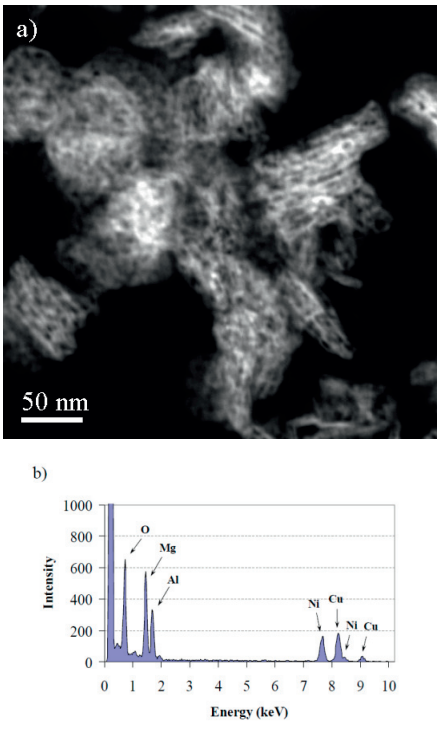

Fig. 2a) A HAADF-STEM image of 12.5%Ni/HT after calcination, without reduction and **b)** EDS spectrum of the calcined material.

TEM image in Figure 1b shows a more well-developed layered structure of the homogeneous mixed oxides than the hydrotalcite like material. The morphology of the calcined sample shows good contrast in the STEM images (Figure 2a), in which contrast

depends on the atomic number (Z). The dark areas are holes and the gray bright areas show the catalyst materials. The white contrast in the Figure 2a is due to the thickness of the sample.

A layered ribbon structure is seen in the calcined material, which appears to be derived from the plate morphology of the hydrotalcite-like material. The morphology of the calcined material is described further in the next section. The length of the ribbons in the calcined material is larger than that of the original hydrotalcites, suggesting that a solid-state reaction occurred between the layered hydrotalcite like layers in calcination. More interestingly, the STEM image, (Figure 2a) reveals the rather characteristic pore structure of the ribbons in which the pores are roughly aligned in layers parallel to the ribbons`surface. The calcination process obviously transforms the dense layer structure to the structure with a higher level of porosity and no obvious NiO particles are visible. The STEM contrast indicates that the Ni is homogeneously distributed in the oxide ribbons. Energy Dispersive Spectroscopy (EDS) analysis of several different positions in the sample gave all Ni peaks with similar intensities relative to Mg and Al. Figure 2b shows the EDS spectrum, which was taken from one of the examined areas similar to the one in Figure 2a. The presence of a strong Cu peaks is an artifact due to secondary flourescence of the mesh grid used to support the carbon film.

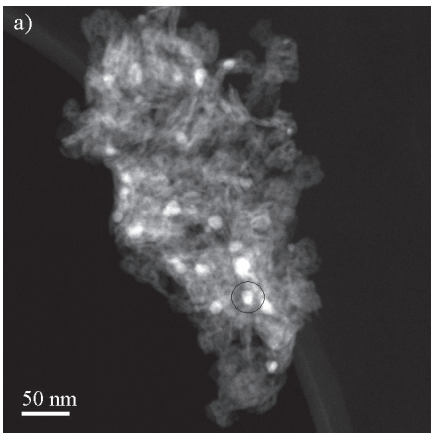

Fig. 3a) A HADF STEM image of 12.5%Ni/HT after reduction treatment, and **b)** EDS spectrum from a Ni particle indicated in Fig. 3b.

By contrast, phase separation clearly occurred during the reduction and the Ni particles were formed from the mixed oxides. This is seen by comparison of Figure 2a and Figure 3a. Figure 3a is a STEM image of 12.5%Ni/HT after reduction.

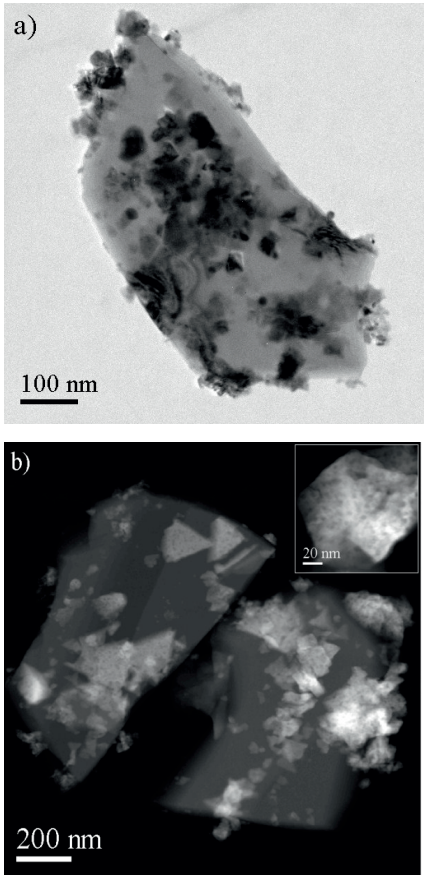

Fig. 4a) BF-TEM and **b)** HAADF-STEM images of commercial $Ni/\alpha Al_2O_3$ catalyst. The TEM image on the right corner of Fig. 4b is detail of Ni oxide region in which its porosity is clear.

The ribbons have smaller size after reduction. The Ni particles appear as bright features, which are embedded in the porous support and their composition was confirmed by EDS. The EDS spectrum in Figure 3b was recorded from the Ni particle indicated in Figure 3a, in which Ni has a peak with higher relative intensity than Mg and Al peak which is seen in Figure 2b, consistent with the particle being Ni surrounded by Mg/Al oxide.

The BET surface area was measured by N_2 adsorption. Ni dispersion and Ni particle size were measured by H_2 chemisorption and the results are summarized in the Table 1. The properties of the commercial Ni catalyst supported on α-Al_2O_3 used as reference catalyst are also listed in the Table 1. Both BET surface area and Ni dispersion are much higher for the hydrotalcite derived catalyst, which results in a higher steam methane reforming activity than the commercial Ni catalyst. The

catalyst stability was examined by the deactivation function of 1-r_{25}/r_0 (Table 1), where r_0 and r_{25} are the reaction rate at 0 and 25 hours of the time on stream, respectively. Interestingly, the stability of the hydrotalcite derived Ni catalysts is much better, as indicated by a much lower deactivation rate, than for the commercial Ni catalyst, although the Ni particle size is much smaller. Our previous results have indicated that a S/C of 3 is far beyond the coking threshold, and carbon formation should not be the cause of the deactivation.[11] The improvement of stability of Ni catalysts derived form hydrotalcite like materials has been further evident from a comparative study between the hydrotalcite derived Ni catalysts with several Ni loadings (12.5, 40 and 77.5) and the Ni (12 wt.%) catalysts supported on hydrotalcite materials prepared by impregnation. [9] Kinetic study illustrated also a much slower sintering kinetics of hydrotalcite derived Ni catalysts compared to Ni supported on α-Al_2O_3 and $CaAl_2O_4$ spinels, although the Ni particles sizes are much larger on two late supports.[17] Moreover, a large body of the literature consistently showed a better stability against heat treatment [21, 33-35] and good stability in steam reforming of ethanol.[23]

Sintering has been identified as the main cause of the deactivation at the condition studied.[17] Both atomic and crystallite migration are important mechanisms for sintering.[30] The better stability of the hydrotalcite derived Ni catalysts could be ascribed the different morphology and location of Ni particles in, or on, the supports (Figure 3b) comparing to one on the commercial catalyst, studied in calcined state, shown in Figure 4. The large porous triangular shaped Ni particles were found on the blocky α-Al_2O_3 surfaces (Figure 4) in the commercial Ni catalysts. Deposition of the metal particles on the support surfaces is the typical particle location for the conventional oxide supported catalysts prepared by impregnation. It is very different from the Ni particle location derived from hydrotalcite materials as shown in Fig. 3a, which will be analyzed by the electron tomography in the next section.

Catalyst	BET surface area $m^2.g_{cat}^{-1}$	Ni surface area $m^2.g_{cat}^{-1}$	Ni dispersion %	d_{Ni}[a] nm	r_0 mmol $(g_{Ni},s)^{-1}$	D[b] $(1-r_{25}/r_0)$
12.5% Ni/HT	229[d]	9.1	11.4	8.9	7.8	0.04
CC[c]	5.5	1.3	1.5	65	2.4	0.51

Table 1. Properties of the Ni catalysts and their initial activities and deactivation rates in steam methane reforming.

[a]: calculated from H_2 chemisorption, $d_{Ni}(nm) = \frac{101}{D(\%)}$, D: dispersion

[b]: Deactivation rate at time on stream after 25 h where r_0 is the initial activity and r_{25} is the activity measured at time on stream of 25 hours, steam reforming of CH_4 at 923 K, 28.5 cm^3/min CH_4, 20 cm^3/min H_2, 5.1 g/h H_2O, 9 cm^3/min Ar and 1 bar. [9]

[c]: commercial Ni catalyst, 12.5 wt% Ni/α-Al_2O_3.

d: BET surface area was measured on reduced and passivated 12.5 %Ni/HT

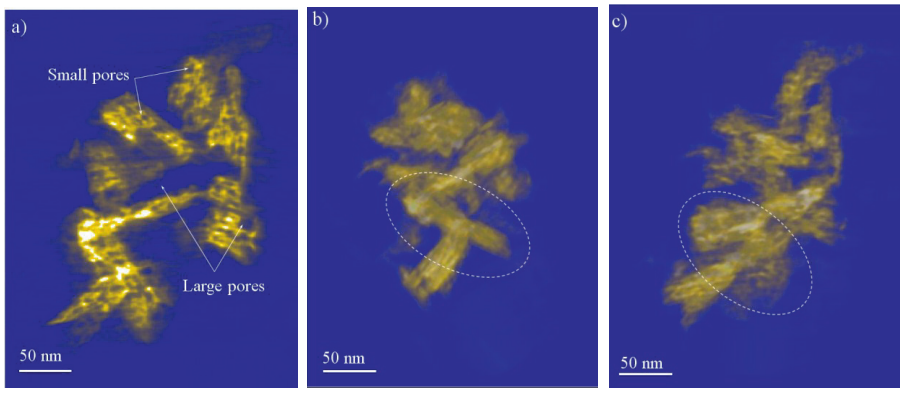

Fig. 5a) An orthoslice through the 3D reconstructed series of calcined material, which shows the ordered porosity in the ribbons, **b)** 3D voltex of the same reconstructed series, viewed in a direction in which one ribbon is viewed edge-on and **c)** The same voltex rotated so that the same ribbon is viewed more obliquely.

Three dimensional visualization analysis

For the hydrotalcite-derived catalyst, two dimensional images could not reveal the detailed three dimensional structures including pore structure and network, Ni particle size, shape and location and distribution in this embedded Ni catalysts. Electron tomography is applied to determine the three dimensional structure.

Figure 5a shows an orthoslice through a 3D reconstruction of the calcined material. Figure 5b and Figure 5c are snapshots of the voltex view of the same reconstruction from two different views. In Figure 5b the reconstruction is tilted in a direction in which at least one ribbon is viewed edge-on, showing its thickness to be 15.8 nm. The average thickness of the ribbons in the analyzed volume was 15.2±2.8 nm. In Figure 5c the same ribbons is seen obliquely and shows much weaker contrast. The size of the rectangular ribbon marked in Figure 5b is 12.4 nm ×51.5 nm × 15.8 nm. The results illustrate an interesting feature of the hydrotalcite derived catalysts, that the rather regular 3D nanometer-scale rectangular ribbon structure can be produced by the calcination of layered hydrotalcite structure. Moreover, Figure 5 shows the arrangement of regular, small pores inside the ribbons. These internal pores have a roughly rectangular morphology and are regularly distributed within the plates. The internal pores with the average size of 4.3±1.0 nm are formed parallel to the ribbon sheets. Beside the internal pores inside the structure of the catalysts, external pores are present in its microstructure which were formed in the junction of layered planes and generally have larger size than the internal pores. An average external pore size was found to be about 17.4±5.1 nm. internal pores with the average size of 4.3±1.0 nm are formed parallel to the ribbon sheets. Beside the internal pores inside the structure of the catalysts, external pores are present in its microstructure which were formed in the junction of layered planes and generally have larger size than the internal pores. An average external pore size was found to be about 17.4±5.1 nm.

The dual pore size distribution obtained by electron tomography is consistent with the measurements of low temperature N_2 adsorption, which is shown in Figure 6. In this Figure, two types of pores were identified, with average pore sizes of 2.8 nm and 18 nm, respectively. However, electron tomography provides also the pore structure and the location. There is slight difference between the average of small pore size measured by electron tomography and low temperature N_2 adsorption technique. The reason for this is believed to be that the resolution in the electron tomography series is not high enough to resolve the smallest pores in the structure and measure them accurately. However, these pores are observed in two dimensional TEM images and measurements on these images give the average of 3.5±0.9 nm for the small pores, in agreement with low temperature N_2 adsorption data.

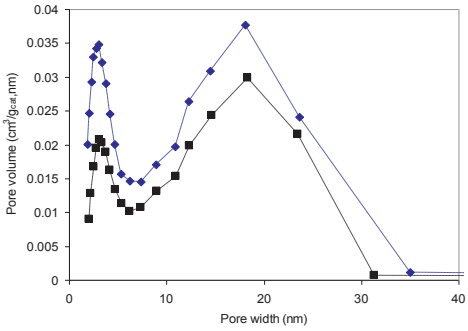

Fig. 6 Pore size distribution of calcined (■) and reduced (♦) hydrotalcite derived samples.

The Ni nanoparticles location is shown in Figure 7, where Figure 7a shows an orthoslice of the 3D reconstructed series of the reduced materials and Figure 7b is its voltex view. The bright features in Figure 7 are Ni particles, which located inside the oxide ribbon matrix. A movie of the voltex view of reduced sample can be found at the following link: Movie of reduced material. Figure 7c and Figure 7d show segmentation of the indicated Ni particle (yellow) and its surrounding oxides (red) from two different views. The morphology of the Ni nanoparticle without its surrounding is shown in Figure 7e. A movie for segmentation of the Ni particle can be found at the following link: Movie of Ni particle segmentation. Segmentation shows that the Ni particle is embedded in the support structure but open channels are present, which makes it accessible to the reactant gases.

The Ni particles shape and 3D distribution are illustrated in Figure 8, through segmentation of some of the Ni particles observed in the reconstructed series of reduced sample, which is also shown in the movie at the following link Movie of Ni Particles segmentation. Figure 8a shows the distribution of the Ni particles viewed from the x direction. Figure 8b and Figure 8c show the particles rotated for 20 degree and 40 degree relative to the Figure 8a, respectively. A few of the particles are labeled in each figure to make it easy to follow them after rotation. Figure 8d and Figure 8e show the morphology of a Particle, P2, and Figure 8f and Figure 8g show the morphology of the P3, in two different views. Both figures and movie show that most of the Ni particles are elongated in a direction along the ribbon axis and a few of them have roughly spherical shape. All the Ni nanoparticles are constrained inside the rectangular ribbons.

Journal Name

Dynamic Article Links ►

Cite this: DOI: 10.1039/c0xx00000x

www.rsc.org/xxxxxx

ARTICLE TYPE

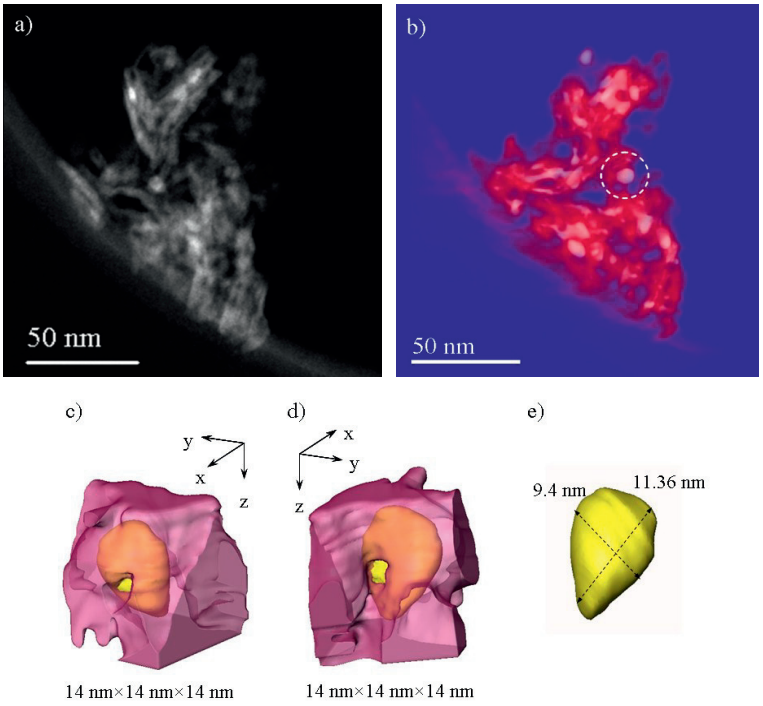

Fig.7a) An orthoslice from the reconstructed series of reduced 12.5%Ni/HT, **b)** a snapshot of the reconstruction in voltex view in the same orientation, **c)** and **d)** Segmented volume of catalyst contain Ni (yellow) and its surrounding mixed oxides (red) in two different directions, **e)** The segmented Ni particle showing its morphology.

The catalyst particles are typically measured by hydrogen chemisorption, where metal particles are assumed to be spherical shape. The Ni particle size of 8.9 nm measured by chemisorption is obviously only a mean size.

An attempt was made here to compare the mean size, which is estimated based on the 3D particle shape, to the one measured by chemisorption. Firstly, the size was measured in three directions for each particle, and the volume of each particle was estimated by assuming an ellipsoid shape. The mean size (2r) of Ni particles can then be estimated from the equivalent spherical volume with a radius as the volume measured. In this way, an average particle size of 7.5±2.1 nm was obtained. The particle size measured on 2D images from several areas give an average of 8.9±2.4 nm, which is similar to the Ni particle size measured by H_2 chemisorptions, which was estimated by an assumption of ideal spherical Ni particles, Table 1. In the 2D particle size measurements of the oval shape particles, the averages of maximum and minimum dimensions were considered. Since the measurements were made on several region of the sample it is regarded as more reliable than particle size from 3D visualization. It is interesting to note that the Ni particle size is larger than the pore size measured in the calcined samples. The pore size distributions in the calcined and reduced samples are unchanged, This is seen by the comparison of STEM images in Figure 2a and 3a. The results from low temperature N_2 adsorption in Figure 6 confirm this, quantitatively. This indicates that the Ni particles nucleate and grow inside the oxide sheets, becoming enclosed in localized cages within the pore structure. This is consistent with the tomographic reconstruction of oxide ribbon sheet containing Ni particles.

Spatial Confinement of Ni Clusters and Catalyst Stability

Sintering is often the main cause of catalyst deactivation at high temperatures. Sintering occurs either through atomic migration from one crystallite to another, by diminishing small crystallites in size and increasing the larger ones, or via crystallite migration

Cite this: DOI: 10.1039/c0xx00000x

www.rsc.org/xxxxxx

ARTICLE TYPE

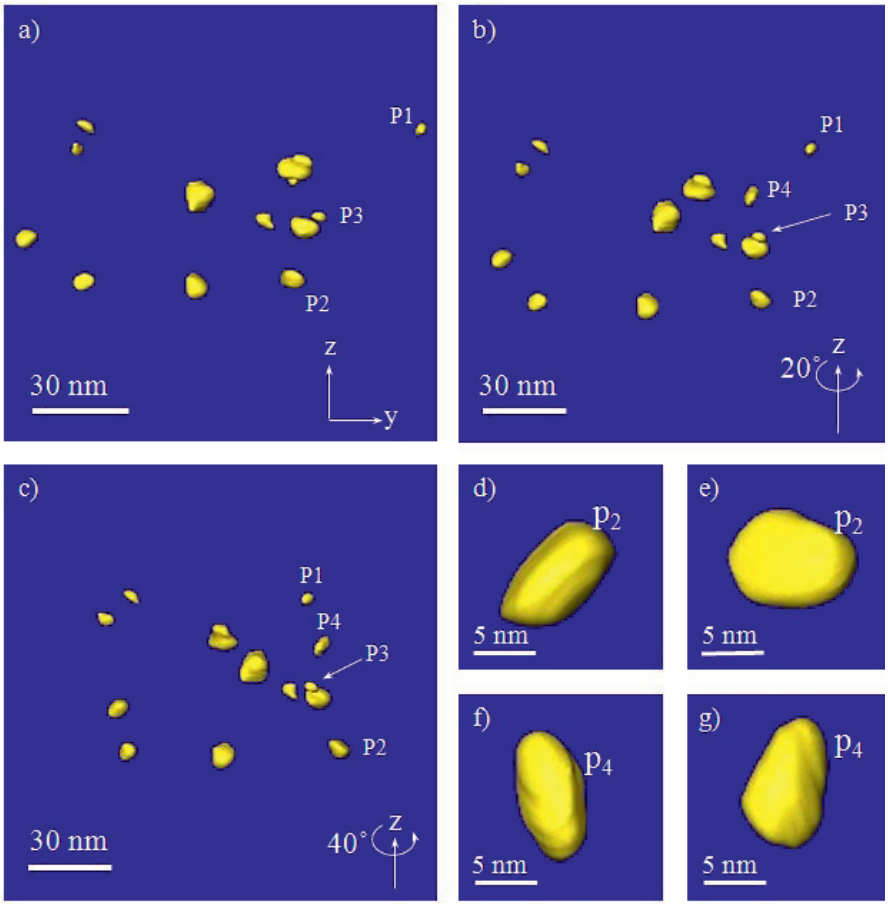

Fig. 8 Segmentation of several particles in three different direction, **a)** View parallel to the x direction, **b)** Rotated around z for 20 degree **c)** Rotated around z for 40 degree, **d)** and **e)** showing the morphology of the particle 2, (P2), in two direction, and **f)** and **g)** showing the morphology of particle 4, (P4), in two directions.

along the support surface, followed by collision and coalescence of two crystallites. The resistance to crystallite migration depends on the particle size and small sized crystals are mobile, thus having a low resistance for the migration.[17, 36-37] This leads to a great challenge in stabilization of nanoparticles at high temperatures. Industrial steam reforming catalysts typically use very large Ni particles supported on the low surface area of supports, as illustrated in Figure 4. However, the particle migration resistance also depends on the support surface roughness, and maybe also the surface energy.[37] The present work clearly illustrates that a large Ni particle size cannot guarantee the stability. The deactivation rate of Ni/α-Al_2O_3 (commercial catalysts) is still relatively high even though the Ni particle size is as high as 65 nm, Table 1.

This study details a strategy for stabilizing the Ni nanoparticles through spatial confinement. The confinement is clearly demonstrated in Figure 7c and Figure 7d, where a Ni nanoparticle is confined inside a cage in porous ribbons, (The segmented cube is 14nm*14nm*14nm in size). In contrast to the deactivation of the large Ni particles on α-Al_2O_3, the confined catalyst is very stable during the steam methane reforming (Table 1). Very stable reaction rate with time on stream indicated very little changes in Ni dispersion. It might suggest that the confinement of Ni particles increases the resistance for the crystal migration. Moreover, 3D volume measurements provide the distance

between the closest neighboring Ni nanoparticles as shown in Figure 8, which was determined to be 38 nm. The nanoconfined Ni nanoparticles and combined with a relatively long distance between adjacent particles provide a significant increase in the resistance to sintering, which results in a much lower deactivation rate compared to the commercial Ni catalyst, as indicated a much lower deactivation function in Table 1. To find out more details of the catalyst stability with respect to sintering, it would be interesting to study the deactivated catalyst in 3D and compare it with the results from the fresh catalyst. This will be addressed in a future study.

Conclusions

The approach for improving the stability of the Ni nanoparticles catalyst for the steam methane reforming process has been elucidated through nano scale analysis. Three dimensional information from the structure of the catalyst was provided by electron tomography; the distribution, size, shape and location of the Ni nanoparticles were determined. In addition, the pore size, spatial shape and the thicknesses of the nano-ribbons in the Mg-Ni-Al mixed oxides substrate were measured. Good consistency between the results and the determined properties of the catalyst by chemisorption and low temperature N_2 adsorption was observed. The combination of bulk property measurements with direct nanometer-scale observation is essential in understanding of the structure at a nanometer level, providing a principle for rational design of the system reforming catalysts towards a better stability. The results reveal that rather regular rectangular shaped ribbons of Ni-Mg-Al mixed oxides were formed through calcination of layered hydrotalcites. The reduction resulted in a formation of Ni particles confined in the porous nano-ribbons of Mg-Al mixed oxides with connected pore channels which provided good catalyst stability and proper access of the gaseous reactants. Relatively long distances between the Ni particles, further increases the resistance to crystal migration, and this may reduce the deactivation rate.

Acknowledgment

The work is done through "NANOMAT and RENERGI Projects" financed by the Research Council of Norway and Statoil (NFR Project No. 169673/S10 and 178190). The financial support from the European Union under the Framework 6 program under a contract for an Integrated Infrastructure Initiative, Reference 026019 ESTEEM and financial support from the ERC under grant number 291523 3DIMAGE is greatly acknowledged.

Notes

[a] *Department of Physics, Norwegian University of Science and Technology (NTNU), Hogskoleringen 5, 7491, Trondheim, Norway,*
[b,*] *SINTEF Materials and Chemistry, Hogskoleringen 5, 7491, Trondheim, Norway. E-mail: John.Walmsley@sintef.no*
[c,*] *Department of Chemical Engineering, Norwegian University of Science and Technology (NTNU), Sem Sælands vei 4, Trondheim, Norway, Fax: +47 7359 5047;Tel: +47 48222428; E-mail: chen@nt.ntnu.no.*
[d] *Department of Materials Science and Metallurgy, University of Cambridge, Pembroke Street, CB23QZ, Cambridge, United Kingdom*
[e] *Statoil R&D, Research centre, Postuttak, NO-7005 Trondheim, Norway*
[f] *Departamento de Ciencia de los Materials, Ingenieria Metalurgicay Quimica Inorganica, Facultad de Ciencias, Universidad de Cadiz, Rio San Pedro s/n, Puerto Real, 11510, Spain*

† Electronic Supplementary Information (ESI) available: Three supplementary videos included in this article show the visualized reconstruction of reduced 12.5%Ni/HT material, the segmented nanoparticle with surrounding mixed oxide and the segmentetaion of Ni nanoparticles. The content of movies were explained in the text. See DOI: 10.1039/b000000x/

References

1. **J. H. Larsen and I. Chorkendorff, *Surface Science Reports*, 1999, 35, 165-222.**
2. **G. A. Somorjai and J. Y. Park, *Chemical Society Reviews*, 2008, 37, 2155-2162.**
3. **C.-J. Jia and F. Schuth, *Physical Chemistry Chemical Physics*, 2011, 13, 2457-2487.**
4. **J. R. Rostrup-Nielsen and R. Nielsen, *Catalysis Reviews-Science and Engineering*, 2004, 46, 247-270.**
5. **J. R. Rostrup-Nielsen, J. Sehested and J. K. Norskov, in *Advances in Catalysis, Vol 47*, 2002, pp. 65-139.**
6. **T. S. Christensen, *Applied Catalysis a-General*, 1996, 138, 285-309.**
7. **T. Sperle, D. Chen, R. Lodeng and A. Holmen, *Applied Catalysis a-General*, 2005, 282, 195-204.**
8. **D. Chen and L. He, *Chemcatchem*, 2011, 3, 490-511.**
9. **E. Ochoa-Fernández, C. Lacalle-Vilà, K. Christensen, J. Walmsley, M. Rønning, A. Holmen and D. Chen, *Topics In Catalysis*, 2007, 45, 3-8.**
10. **H. S. Bengaard, J. K. Norskov, J. Sehested, B. S. Clausen, L. P. Nielsen, A. M. Molenbroek and J. R. Rostrup-Nielsen, *Journal of Catalysis*, 2002, 209, 365-384.**
11. **D. Chen, R. Lodeng, H. Svendsen and A. Holmen, *Industrial & Engineering Chemistry Research*, 2011, 50, 2600-2612.**
12. **D. W. Blaylock, T. Ogura, W. H. Green and G. J. O. Beran, *Journal of Physical Chemistry C*, 2009, 113, 4898-4908.**
13. **F. Abild-Pedersen, J. K. Norskov, J. R. Rostrup-Nielsen, J. Sehested and S. Helveg, *Physical Review B*, 2006, 73.**
14. **F. Besenbacher, I. Chorkendorff, B. S. Clausen, B. Hammer, A. M. Molenbroek, J. K. Norskov and I. Stensgaard, *Science*, 1998, 279, 1913-1915.**
15. **D. Chen, K. O. Christensen, E. Ochoa-Fernandez, Z. X. Yu, B. Totdal, N. Latorre, A. Monzon and A. Holmen, *Journal of Catalysis*, 2005, 229, 82-96.**
16. **E. Nikolla, A. Holewinski, J. Schwank and S. Linic, *Journal of the American Chemical Society*, 2006, 128, 11354-11355.**
17. **K. O. Christensen, D. Chen, R. Lødeng and A. Holmen, *Applied Catalysis A: General*, 2006, 314, 9-22.**
18. **D. Chen, E. Bjørgum, R. Lødeng, K. Omdahl Christensen and A. Holmen, in *Studies In Surface Science And Catalysis*, eds. B. Xinhe and X. Yide, Elsevier, 2004, pp. 139-144.**
19. **S. Kannan, *Catalysis Surveys from Asia*, 2006, 10, 117-137.**

20. M. R. Othman, Z. Helwani, Martunus and W. J. N. Fernando, *Applied Organometallic Chemistry*, 2009, 23, 335-346.
21. K. Takehira and T. Shishido, *Catalysis Surveys from Asia*, 2007, 11, 1-30.
22. F. Cavani, F. Trifirò and A. Vaccari, *Catalysis Today*, 1991, 11, 173-301.
23. L. He, H. Berntsen, E. Ochoa-Fernandez, J. C. Walmsley, E. A. Blekkan and D. Chen, *Topics in Catalysis*, 2009, 52, 206-217.
24. P. A. Midgley, E. P. W. Ward, A. B. Hungria and J. M. Thomas, *Chemical Society Reviews*, 2007, 36, 1477-1494.
25. J. C. González, J. C. Hernández, M. López-Haro, E. del Río, J. J. Delgado, A. B. Hungría, S. Trasobares, S. Bernal, P. A. Midgley and J. J. Calvino, *Angewandte Chemie International Edition*, 2009, 48, 5313-5315.
26. K. P. de Jong and A. J. Koster, *ChemPhysChem*, 2002, 3, 776-780.
27. H. Friedrich, P. E. de Jongh, A. J. Verkleij and K. P. de Jong, *Chemical Reviews*, 2009, 109, 1613-1629.
28. O. Ersen, J. Werckmann, M. Houllé, M.-J. Ledoux and C. Pham-Huu, *Nano Letters*, 2007, 7, 1898-1907.
29. J. M. Thomas and P. A. Midgley, *Chemical Communications*, 2004, 1253-1267.
30. E. P. Barrett, L. G. Joyner and P. P. Halenda, *Journal of the American Chemical Society*, 1951, 73, 373-380.
31. S. Brunauer, P. H. Emmett and E. Teller, *Journal of the American Chemical Society*, 1938, 60, 309-319.
32. J. C. Groen, L. A. A. Peffer and J. Pérez-Ramírez, *Microporous and Mesoporous Materials*, 2003, 60, 1-17.
33. Z. X. Yu, D. Chen, M. Ronning, B. Totdal, T. Vralstad, E. Ochoa-Fernandez and A. Holmen, *Applied Catalysis a-General*, 2008, 338, 147-158.
34. Z. X. Yu, D. Chen, M. Ronning, T. Vralstad, E. Ochoa-Fernandez and A. Holmen, *Applied Catalysis a-General*, 2008, 338, 136-146.
35. K. Takehira, *Journal of Natural Gas Chemistry*, 2009, 18, 237-259.
36. C. H. Bartholomew, *Applied Catalysis A: General*, 1993, 107, 1-57.
37. E. Ruckenstein and D. B. Dadyburjor, *Journal of Catalysis*, 1977, 48, 73-86.

Unpublished Results

Unpublished Results

Investigation of Re promoter in Fischer-Tropsch cobalt catalysts by aberration corrected scanning transmission electron microscopy

1. Introduction

Supported cobalt materials are important catalysts for Fischer-Tropsch reaction, which is a process to convert natural gas, biomass, and coal in to the synthetic fuels. Including small amount of noble metals such as Re, Ru or Pt to the catalysts has strong impact on the structure and dispersion of cobalt species and enhances the activity and may influence the selectivity of the catalyst [1]. The main role of the promoter is to facilitate the reduction of cobalt oxide and hence increase the number of active sites [1]. The promoter elements are divided in two groups according to their intended functions; the structural which effects the formation and stability of the active phase, and the electronic promoters which affect the local electronic structure of an active metal by adding or withdrawing electron density near the Fermi level in the valence band of the metal leads to the changes in the chemisorption properties of the active metal.

Rhenium is regarded as a structural promoter and it has been reported in the literature that Re increases the reducibility of the cobalt oxide phases through the spill over mechanism [2,3,4]. Several studies have been made earlier to understand the mechanism of the promoter in the cobalt FT catalysts [5,6,7,8]. It is very important to know the location and distribution of the promoter. Transmission Eletcron Microscopy (TEM) is a powerful technique to observe the atomic structure of the materials. A very small amount of promoter is present in the catalyst However, Scanning Transmission Electron Microscopy (STEM) imaging in which the heavier elements are appeared brighter than lighter elements seems to be a suitable technique to locate the promoter in the catalysts structure due to its relatively high atomic number. Aberration corrected (STEM) has been applied to image different promoters in the cobalt supported on γ-

Al_2O_3 by Shannon et al. [9]. They have examined the calcined and passivated catalysts and they concluded that Re is distributed as isolated atoms. Here, we study a simpler catalyst with coarser structure in precise experiments with aberration corrected STEM instrument. In the present study aberration corrected TEM is applied to study the location of Re in the catalysts with 12%Co/0.5%Re/α-Al_2O_3 in calcined condition. The un-promoted similar catalyst is also studied for comparison.

2. Experimental

The applied experimental procedure in the present work is described as follows.

2.1 Catalysts Preparation

The cobalt catalyst for FT process was synthesized through one-step incipient wetness impregnation of the alumina support with an aqueous solution of cobalt nitrate hexahydrate, $Co(NO_3)_2.6H_2O$, and perrhenic acid, $HReO_4$, to provide a rhenium promoter. The cobalt and rhenium loadings on the α-Al_2O_3 support were 12wt% and 0.5wt%, respectively. After impregnation, the catalyst was dried at 110 °C for 3 hours and then calcined in air at 300°C for 16 h to form cobalt oxide particles with a composition 12wt%Co/0.5wt%Re/α -Al_2O_3. A ramping rate of 2 °C/min was used to heat the sample from ambient temperature to the final calcination temperature. The sample was reduced with a heating rate of 3 °C/min up to 350 °C under 100 ml/min H_2 flow at atmospheric pressure and then kept for 16 h under these conditions. The reduced material was kept inside a capillary until it was used for TEM analysis.

2.2 TEM Experiments

TEM experiments were performed with Titan analytical 80-300ST located in the Center for Electron Nanoscopy (CEN) at the technical university of Denmark (DTU). The microscope operates at 300 kV and is equipped with field emission gun, monochromator and spherical aberration corrector on the condenser system. Due to its small probe size it is suitable for high resolution scanning transmission electron microscopy and chemical mapping at the atomic level. The mapping analysis is done by energy dispersive spectroscopy (EDS) with resolution of 136 eV. TEM samples were prepared by dispersion of crushed powder of the catalysts on to Cu grids supported by carbon film.

3. Results

Figure 1 shows the high resolution dark field and bright field STEM images of a cobalt oxide nanoparticle supported on α-Al_2O_3. In Figure 1.a two dimensional fringes are clear and the atomic planes are observed as bright spots. In the bright field STEM image of the same cobalt nanoparticle (Fig. 1.b) the atomic columns appear dark.

Figure 2 is another example of STEM images from a cobalt oxide nanoparticle. As mentioned above, in the dark field STEM image (Figure 2.a) the atomic columns appear bright. However, there are few spots with higher contrast than the atomic column. These bright spots can be an evidence of atomic Re in the cobalt oxide nanoparticle.

Figure 3 shows the dark field and bright field high resolution STEM images of the cobalt oxide supported on α-Al_2O_3 in un-promoted catalyst.

Figure 4 shows the EDS spectrum taken on the cobalt oxide nanoparticles in promoted (blue) and un-promoted nanoparticles (pink) and EDS of the alumina area in the catalyst. The spectrum presented here are exactly similar data obtained in the microscope. This Figure shows that in the spectrum from promoted catalyst, there are very weak peaks can be related to the Re. However, the peaks are very small and to get certain conclusion, precise quantitative data analyses are required.

4. Discussion

The applied rhenium precursor in this catalyst is perrhenic acid, $HReO_4$, which has a close structure related to the Re_2O_7. The structure of Re_2O_7 with octahedral and tetahedrals is similar to the Co_3O_4 structure and therefore during preparation it goes randomly with the Co_3O_4 structure onto the pores of the alumina support. The phase diagram from Re also proof the solid solution of Re in cobalt. Therefore, Re atoms go into the cobalt phase structure. This suggests that the Re atoms have been dispersed uniformly in the cobalt oxide areas. This confirms with the EDS mapping from alumina area. Although the signal in the promoted catalyst is very weak, however, this weak signal is not present in the EDS from alumina area.

During cobalt oxide reduction, rhenium oxide is reduced after reduction of Co_3O_4 to CoO and before reduction of CoO to Co and its role is to facilitate the reduction of CoO to metallic cobalt [1]. The rhenium oxide is reduced to the hexagonal metallic rhenium earlier than CoO and due to its shrinkage during reduction; it produces the free space around it. This free space

act similar to a channel and provides a rapid diffusion path for hydrogen. The volume of atom per unit cell for both Re_2O_7 and Re is obtained as following:

$$V_{Re_2O_7} = \frac{(12.5 \times 15.26 \times 5.45)}{8 \times 2} = 65.08$$

$$V_{Re} = \frac{\sqrt{3}(2.76)^2 \times (4.458)}{2 \times 2} = 14.43$$

The volume change during the reduction of Re_2O_7 to hexagonal Re is:

$$\frac{V_{Re_2O_7} - V_{Re}}{V_{Re_2O_7}}\% = \frac{65.08 - 14.43}{65.08}\% = 77.83\%$$

Therefore, by existence of Re in the structure, the reaction rate is increased and this is consistent with the spillover mechanism. It is also suggested that by the presence of hexagonal Re in the catalyst during reduction, the metallic cobalt tend to form in hexagonal structure than fcc which may affect the activity or selectivity of the catalysts.

5. Conclusion

It is concluded that Re phase is included in the sample with cobalt phase during impregnation and due to solid solution phase for Re, it is dispersed evenly in the cobalt oxide phase. During the reduction, Re2O7 is reduced before the reduction of CoO to metallic cobalt and due to a high shrinkage during the reduction; it produces channels into the cobalt oxide nanoparticles and enhances the reducibility of cobalt oxide nanoparticles.

6. Acknowledgement

This research has been done through the grant from The Nordic Network for Transmission Electron Microscopy (NORTEM net).

List of Figures

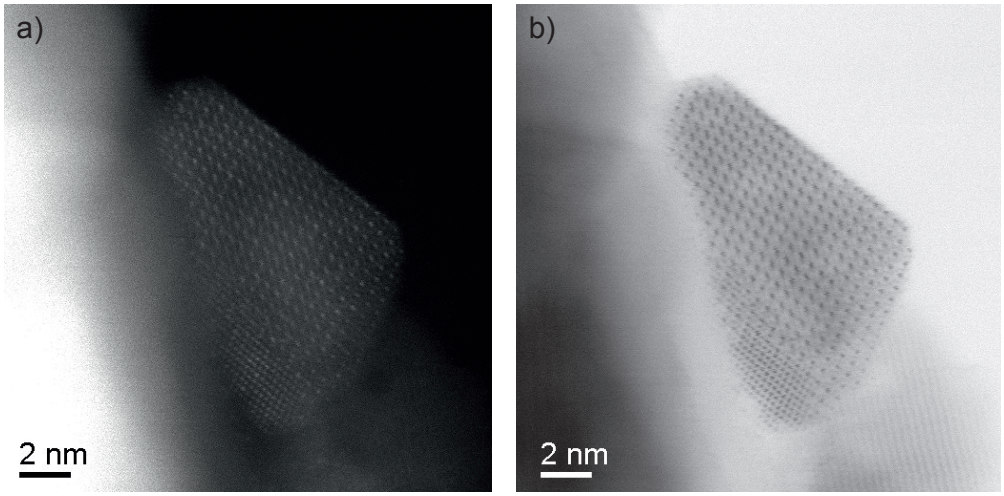

Figure 1.a: Dark field and b: Bright field STEM image of the Re promoted cobalt oxide supported on α-Al_2O_3.

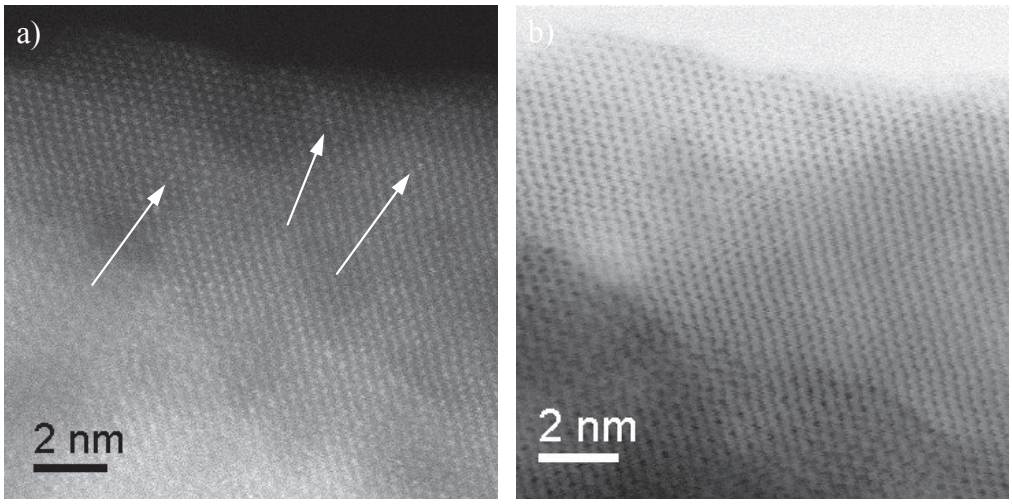

Figure 2.a: DF STEM and b: BF STEM images of the Re promoted cobalt oxide supported on α-Al_2O_3.

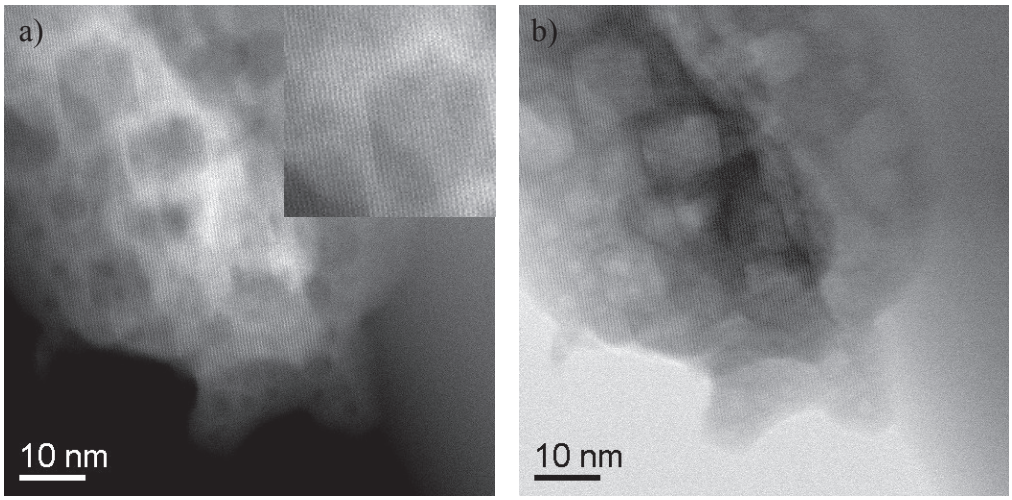

Figure 3a: BD STEM and b: BF STEM images of cobalt oxide supported on α-Al_2O_3.

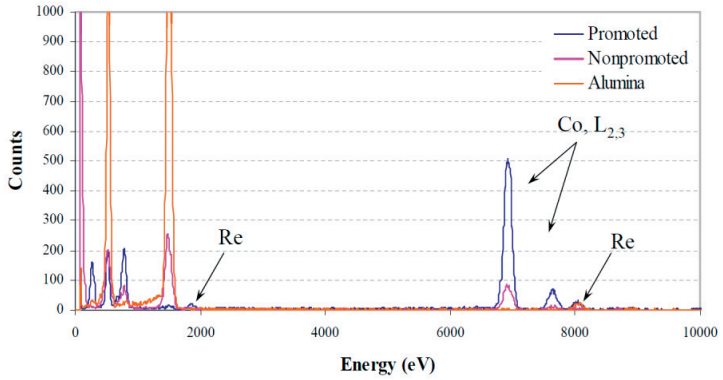

Figure 4: shows the EDS mapping of the cobalt oxide area in the promoted catalyst (blue) and un-promoted catalyst (pink), and EDS mapping of the alumina area (orange).

7. References

1. F. Morales and B. M. Weckhuysen, Catalysis, 19 (2006) 1- 40.
2. A. M. Hilmen, D. Schanke and A. Holmen, Catal. Lette., 38 (1996) 143-147.
3. G. Jacobs, J. A. Chaney, P. M. Patterson, T. K. Das, B. H. Davis, Appl. Catal. A, General, 264 (2004) 203-212.
4. M. Rønning, N. Tsakoumis, A. Voronov, R. E. Johansen, P. Norby, W. Van Beek, Ø. Borg, E. Rytter, A. Holmen; Catal. Today, 155 (2010) 289-295.
5. A.M. Hilmen, D. Schanke, A. Holmen, Stud. Surf. Sci. Catal., 1997, 107, 237.
6. A.M. Hilmen, D. Schanke, K.F. Hanssen, A. Holmen, Appl. Catal. A: General, 1999, 186, 169.
7. M. Ronning, D.G. Nicholson, A. Holmen, Catal. Lett., 2001, 72, 141.
8. L. Guczi, L. Takacs, G. Stefler, Z. Koppany, L. Borko, Catal. Today, 2002, 77, 237.
9. M. D. Shannon, C. M. Lok, J. L. Casci, Journal of catalysis, 249 (2007) 41-51.

Appendices

Appendix A

Properties of cobalt catalysts compounds

The physical properties of different applied compounds in the catalysts are described in this section. The main possible materials in the cobalt Fischer-Tropsch catalysts are categorized in three different groups. The first group contains different cobalt phases including cobalt oxide (Co_3O_4), cobalt monoxide (CoO) and two metallic cobalt phases. The second group include the alumina substrates containing α-Al_2O_3, γ-Al_2O_3 and the third group is Rhenium as promoter.

Cobalt oxides (Co_3O_4, CoO)

Cobalt oxide (Co_3O_4) is a black antiferromanetic solid. It has spinel crystal structure with a lattice constant of a_0=8.080 Å. There exist two types of ions in its crystal structure, Co^{2+} ions, which are tetrahedrally coordinated and Co^{3+} ions that are octahedrally coordinated with the ratio of Co^{2+}/Co^{3+}:1/2.

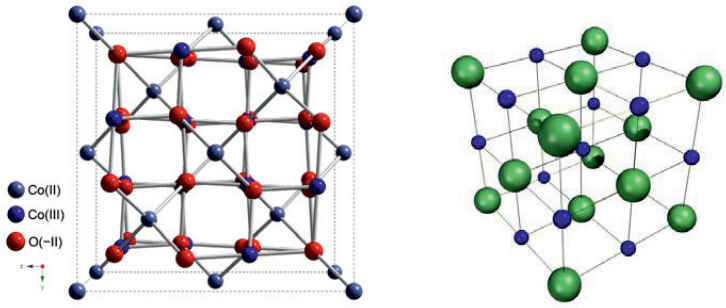

Figure A.1: Location of cobalt and oxygen atoms in a) Co_3O_4 and b) CoO structures.

Table 1. The main d values for Co3O4 [Page 538].

Co_3O_4(cubic) ***a_0=8.084, FD3M***		
d Å	***I/I_1***	***hkl***
4.669	20	111
2.860	40	220
2.438	100	311
2.333	12	222
2.021	25	400
1.650	12	422
1.556	35	511
1.429	45	440

Cobalt monoxide (*CoO*) is an inorganic compound which has rocksalt structure consists of two interpenetrating fcc sublattices of Co^{2+} and O^{2-} ions. The lattice constant of *CoO* is 4.260Å and each cubic unit cell has four Co^{2+} and four O^{2-} ions. The structure of Co_3O_4 and *CoO* are illustrated in Figure A.1. Moreover, the d values and related atomic planes are listed in Table 1 and 2 respectively.

Table 2. The main d values (Å) for CoO phase [532].

CoO (fcc) ***a_0=4.26, FM3M***		
d Å	***I/I_1***	***hkl***
2.46	75	111
2.13	100	200
1.506	50	220
1.2846	20	311
1.2298	16	222

Cobalt structures

Cobalt is a transition metal with atomic number of 27 and metallic gray colour. Two metallic phases exist for cobalt, which are called α-cobalt and β-cobalt (Figure A.2). The α-cobalt has hexagonal closed pack (hcp) structure with a_0=2.507 and c_0=4.070 and is the stable phase at room temperature. The β-cobalt has face centred cubic (fcc) structure with a_0=3.545 and is stable at temperatures above 420˚C [2]. However, in supported cobalt materials both metallic cobalt phases have been observed at room temperatures. The details about the structure of these two phases are in Table 1.

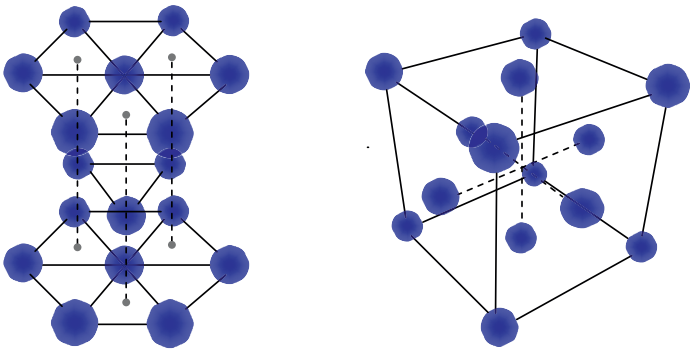

Figure A.2: Location of cobalt atoms in the a) hexagonal and b) cubic cobalt structures

Table 1. The atomic plane for two metallic phases.

Co(hcp) ***a_0=2.507, c_0=4.070***			***Co (fcc)*** ***a_0=3.545***		
d Å	***I/I_1***	***hkl***	***d Å***	***I/I_1***	***hkl***
2.165	20	100	2.046	100	111
2.023	60	002	1.77	40	200
1.91	100	101	1.25	25	220
1.48	-	102	1.07	30	311
1.25	80	110	1.023	12	222

As oxygen atoms are eliminated from the Co_3O_4 structure, it is first transformed to cobalt monoxide (CoO) with a face centred cubic (fcc) structure [1]. In the CoO, the cobalt atoms are located on the corners and the sides of the cubic unit cell, while the oxygen atoms are located on the edges and centre of the cube. With further reduction the CoO is converted to fcc or hexagonal closed pack (hcp) metallic cobalt. The oxygen elimination causes structural shrinkages in the reduction steps; 12.2% from Co_3O_4 to CoO, 42.4% from CoO to cubic cobalt, and 42.7% from CoO to hexagonal cobalt. According to the literature, bulk metallic cobalt has the hcp structure at temperatures below 420 ºC, while at temperatures above that the fcc cobalt is stable [2,3]. In supported cobalt materials, however, both fcc and hcp cobalt structures have been observed at lower temperatures, even below the transition temperature [3,4, 5].

Alumina (Al_2O_3)

Alumina is an important support for FT catalysts due to its high porous structure and high surface area. Normally γ-Al_2O_3 is produced through calcination of boehmite (γ-AlOOH) at 500°C in air and by further calcination at 1130°C it transforms to the more thermodynamically stable α-Al_2O_3 phase [6]. During calcination the structural changes occur and γ-Al_2O_3 with fcc structure transforms to α-Al_2O_3 with trigonal structure. It causes that γ-Al_2O_3 is lost its porosity via sintering and the final α-Al_2O_3 product has coarser structure than γ-Al_2O_3 [7].

Table 4. The main d values (Å) for γ-Al_2O_3 structure.

γ-Al_2O_3 (fcc) ***a_0=7.90, FD3M***		
d Å	***I/I_1***	***hkl***
4.56	40	111
2.80	20	220
2.39	80	311
2.28	50	222
1.977	100	400
1.520	30	511
1.395	100	440

Table 5. The main d values (Å) for α -Al_2O_3 structure.

α-Al_2O_3 (Trigonal) ***a_0=4.758, D^6_{9D}-R3C***		
d Å	***I/I_1***	***hkl***
3.479	75	012
2.552	90	104
2.379	40	110
2.165	<1	006
2.085	100	113
1.964	2	202
1.740	45	024
1.601	80	116

Rhenium (Re)

Rhenium is a transition metal with atomic number of 75 and has silvery-white colour. This element is used as promoter in the cobalt Fischer-Tropsch cobalt based catalysts. The main d values for this element is listed in Table 6.

Table 6. Main d values (Å) for Re with hexagonal structure.

Re (hexagonal) ***a_0=2.760, c_0=4.458***		
d Å	***I/I_1***	***hkl***
2.388	32	100
2.226	34	002
2.105	100	101
1.629	11	102
1.380	22	110
1.262	16	103
1.173	20	112

Appendix B

Software application

As mentioned in chapter 4, several software can be used for acquisition and reconstruction of tilt series. In the present thesis, four software packages were extensively used and therefore they are shortly described in the following.

ImageJ

ImageJ is a Java based image processing programme developed at the National Institute of Health in US [8]. This software supports a wide range of file types and has different types of plugins for different purposes which easily can be installed through internet. It has special plugins for projection alignment and reconstruction, which is called TomoJ. The disadvantage of working with this software is that the storage memory is limited and some times there are problems with running the reconstructions, especially when the images are acquired at high resolution.

IMOD

IMOD is a set of image processing programmes used for tomographic reconstruction of electron microscopes series and also for optical sections [9]. This programme was developed as Unix based software and for full functionality on the windows, it requires installation of Unix toolkit called Cygwin. The eTomo programme for building tomograms requires a Java run-time environment. This programme supports number of file types and it is a good candidate for doing alignment and reconstruction on fiducially marked datasets.

Avizo

Avizo is a powerful tool for visualization, processing and analysis of three dimensional reconstructed data. It was developed by VSG-Visualization Science Group and was originally designed and developed by the Visualization and Data Analysis Group at Zuse-Institute Berlin (ZIB) under the name Amira [10, 11].

Gatan Digital Micrograph

Gatan Digital Micrograph is electron microscopy software which provides a complete package to acquire process and analyse the images and spectrums [12]. It also offers the license for alignment and reconstruction. The ease of this software is that the whole tomographic procedure is done at the same software with no need to convert the files between different software. In addition, the tilt axis determination is manually which some how is better to understand the alignment procedure.

Diffraction process

Diffraction process is a free computer programme to process electron diffraction patterns from poly crystalline or amorphous materials. In this programme, first the exact position of non-scattered beam is identified by visual image manipulation and then the average intensities of each ring are obtained as a function of the radius of the ring. This programme gives the advantage of quantified intensities, good angular resolution, easy and fast operation [13].

Appendix C

RGA data analysis

The Titan ETEM used in the present study for the in-situ experiments is equipped with a Residual Gas Analyser (RGA) as described shortly in chapter 5. This system and the considerations on its measurements in this thesis are described in the following.

Residual Gas Analyser

The determination of the gas composition is important in vacuum systems and typically is measured by a compact mass spectrometer known as Residual Gas Analyzer (RGA). RGA is a small capillary mass spectrometer, which is designed to measure the currents of present elements in the vacuum and then detect the level of impurities in the vacuum systems. It is necessary to have low pressure around capillary to be able to measure the composition. Figure C.1 shows the schematic view of the quadropole mass spectrometer [14].

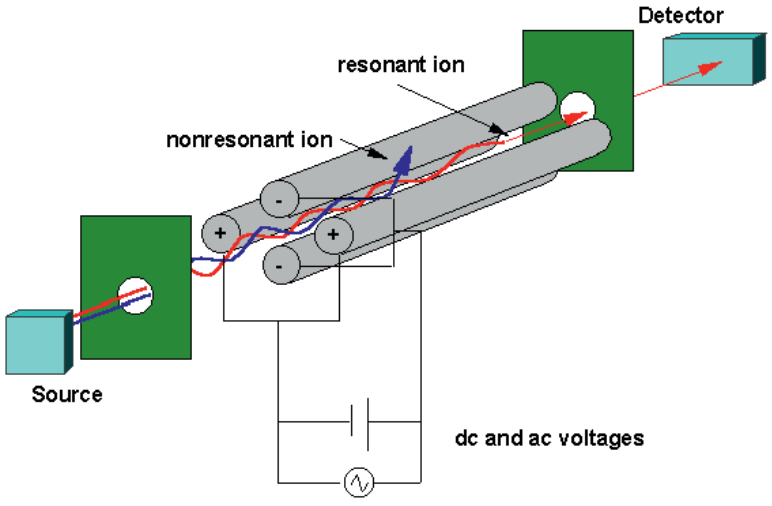

Figure C.1: Shematic view of the quadropole mass spectrometer.

Mass spectrometer is consisted of three parts, a hot cathode extractor ionization gauge, an quadropole analyzer (electrostatic mass filter) and the ion collector. In the mass spectrometer, an electric field accelerates ions out of the source region and into the quadrupole analyzer. The analyzer consists four parallel rods with approximately 6 mm diameter and 100- 150 mm length. As the ions travel through the quadrupole they are filtered according to their mass to charge ratio (*m/z).* Electric field applied to the rods and ions are separated in qudropoles based on the stability of trajectories in the oscillating electric filed. The *m/z* value is determined by the Radio Frequency (RF) and Direct Current (DC) voltages that applied to the electrodes. These voltages produce an oscillating electric field that act as a band-pass filter to transmit the selected *m/z* value.

RGA measurements in ETEM

RGA capillary in ETEM is installed next to the sample and measures directly the ECELL environment. However, the pressure around the capillary should be reduced more than ECELL pressure in order to enable RGA to measure the composition along the capillary. The output of RGA measurements are currents from different ions. However, having these numbers in pressure gives better idea about the level of impurity in the vacuum system. Equation (C.1) converts the measured currents to the partial pressure of elements:

$$I = M^T p \tag{C-1}$$

where, I is the current, p is the individual pressure and M is a coefficient matrix and is equal with:

Comp.\Mas.	2	4	14	16	18	28	32	40	44	55	57
Ar	0	0	0	0	0	0	0	1	0	0	0
CO_2	0	0	0	0	0	0.2	0	0	1.5	0	0
H_2	3	0	0	0	0	0	0	0	0	0	0
H_2O	0	0	0	0	1	0	0	0	0	0	0
C_xH_y	0	0	0	0	0	0.03	0	0	0	0.25	0.25
N_2/CO	0	0	0.1	0	0	1	0	0	0	0	0
O_2	0	0	0	0.1	0	0	0.8	0	0	0	0
He	0	0.3	0	0	0	0	0	0	0	0	0

In order to find the partial pressures, it has to be converted to a 8*11 matrix, which is complicated. However, by some tricks, it is possible to solve it. The elements that are

effective in reduction and re-oxidation process are H_2, H_2O and O_2. Thus, the currents for these elements are written as:

$$\begin{aligned} I_2 &= M_{2,H_2} P_{H_2} = 3P_{H_2} \\ I_{18} &= M_{18,H_2O} P_{H_2O} = 1P_{H_2O} \\ I_{32} &= M_{32,O_2} P_{O_2} = 0.8P_{O_2} \end{aligned} \qquad \text{(C-2)}$$

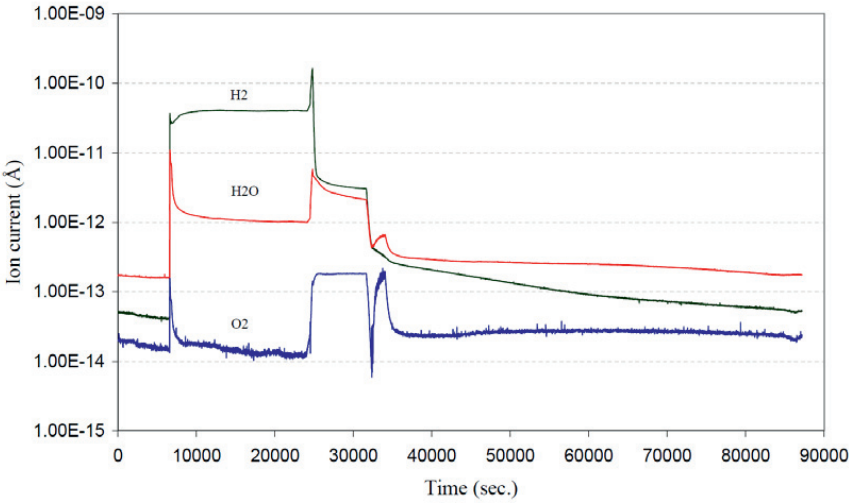

Figure 2: Ion current measured by RGA for H_2, H_2O and O_2 during and after reduction.

Estimating the base current (zero current) and subtracting it from the measured values has to be done. Figure C.2 shows the graph of different currents, which were measured by RGA during H_2 exposure in the ETEM. As seen in the Fig. C.2, the ion currents before H_2 exposure can be used as based current to calculate the Partial pressure of H_2, H_2O and O_2 during and after reduction. The average of the ion currents for these three phases before H_2 exposure is:

$$\begin{aligned} I_{H_2} &= 4.54 \times 10^{-14} \quad A \\ I_{H_2O} &= 1.64 \times 10^{-13} \quad A \\ I_{O_2} &= 1.74 \times 10^{-14} \quad A \end{aligned} \qquad \text{(C-3)}$$

The average value after H_2 introduction is:

$$
\begin{aligned}
I_{H_2} &= 4.03\times10^{-11} \quad A \\
I_{H_2O} &= 1.10\times10^{-12} \quad A \\
I_{O_2} &= 1.52\times10^{-14} \quad A
\end{aligned}
\tag{C-4}
$$

I_{O2} is lower after gas introduction and indicates that the oxygen level is below the detection limit. Therefore, it does not play a main role in the re-oxidation of metallic cobalt. The relative pressure of H_2 and H_2O is then:

$$
\begin{aligned}
P_{H_2} &= \left(\frac{4.03\times10^{-11} - 4.54\times10^{-14}}{3}\right) = 1.34\times10^{-11} \\
P_{H_2O} &= \left(\frac{1.10\times10^{-12} - 1.64\times10^{-13}}{1}\right) = 9.36\times10^{-13}
\end{aligned}
\tag{C-5}
$$

This gives about 6.5% H_2O in the H_2 gas, which is high and apparently causes the re-oxidation of metallic cobalt at room temperature. In general, the pressure of H_2O is high in the ETEM CELL. This is due to the combination of water contamination from goniometer and gas inlet system and from insufficient pumping of ECELL in ETEM mode. However, the RGA data analysis shows that with increasing the H_2 in the system the amount of H_2O is increased and that means the H_2 gas reached to the CELL was not clean enough.

References for Appendices

1 . Powder diffraction file, Inorganic phases, International centre for diffraction data, (1986), Pages 538, 532.

2. Troiano AR, Tokich JL, Trans. AIME 175 (1948) 728.

3. Ducreux O, Rebours B, Lynch J, Roy-Auberger M, Bazin D, Oil Gas Sci Technol, Rev. IFP, 64 (2009) 49-62.

4. Bulavchenko OA, Cherepanova SV, Malakhov VV, Dovlitova LS, Ishchenko AV, Tsybulya SV, Kinet Catal, (2009), Volume 50, Number 2, 192-198.

5. R. Dehghan, T. W. Hansen, J. B. Wagner, A. Holmen, E. Rytter, Ø Borg, J. C. Walmsley, Catal. Lett. DOI: 10.1007/s10562-011-0600-8.

6. Ø. Borg, Role of alumina support in cobalt Fischer-Tropsch synthesis, PhD thesis, Norwegian University of Science and Technology (NTNU), 56 (2007).

7. S. H. Cai, S. N. Rashkeev, S. T. Pantelides and K. Sohlberg, Phase transformation mechanism between γ- and θ-alumina, Phys. Rev. B 67 (2003) 224104.

8. T. J. Collins, ImageJ for microscopy, Bio Techniques 43, 25-30, 2007.

9. J. R. Kremer, D. N. Mastronarde and J. R. McIntosh, Computer visualization of three-dimensional image data using IMOD, Journal of structural biology, 116, 71-76, 1996.

10. http://www.vsg3d.com/avizo/standard

11. http://en.wikipedia.org/wiki/Avizo_(software)

12.http://www.gatan.com/software/

13 . Janos L. Labar, "Process diffraction": A computer programme to process electron diffraction patterns from polycrystalline or amorphous samples, EUREM,12, Brno, Czech Republic, (9-14 July 2000) 1379-1380.

14. S. E. Van Bramer, An introduction to mass spectrometry, Widener University, Department of Chemistry, 1997.